The Secret Lives of Star Clusters: Formation and Dynamical Evolution

Dissertation

zur

Erlangung der naturwissenschaftlichen Doktorwürde
(Dr. sc. nat.)

vorgelegt der

Mathematisch-naturwissenschaftlichen Fakultät

der

Universität Zürich

von

Elena Gavagnin

aus

Italien

Promotionskommission

Prof. Dr. George Lake (Vorsitz)
Prof. Dr. Romain Teyssier
Prof. Dr. Lucio Mayer

Zürich, 2017

Abstract

Stars are social animals, like humans. Indeed, they are mostly found in groups, called star clusters. Since star formation is a collective process and a group of stars forms together from the same molecular cloud, star clusters are firstly nursery for stellar objects. Moreover, once formed, stars interact gravitationally with each other, hence a star cluster is the smallest gravitational entity where we can study stellar dynamics. On a bigger scale, star clusters are bricks of galaxies, therefore understanding how their formation and evolution work is of fundamental relevance for various field of research in astrophysics. However, the detailed transition from dense gaseous cloud to star cluster is still an open question with a lot of partial answers and observations tell us that 'star cluster' is a broad term which comprises completely different objects, such as globular clusters, open clusters, associations, young star cluster, nuclear star cluster, which differ in terms of number, masses, ages, sizes and therefore densities, stellar populations and distribution. Every subcategory presents unique features, which wait to be explained. Moreover, an eventual connection between all these forms of star clusters or the determination of the conditions under which one type or another forms, are still missing.

In this thesis, I focus on two big open questions. First I study the formation and emergence of a star cluster from its parent cloud. Using radiation hydrodynamical simulations, I analyse the collapse and dispersal of the cloud due to the photoionising radiation emitted by the newborn stars. We want to understand how feedback affects the structure and dynamical status of the young cluster. The results suggest that photoionisation is very effective in disrupting the cloud and producing a gas-free collection of stars. Feedback has a huge impact on the star cluster characteristics, reducing the stellar density and hence allowing the formation of structures in virial equilibrium. Without feedback, the high values of density reached increases the frequency and strength of close encounters between stars, which cause a progressive disruption of the cluster. Feedback is also responsible for stopping accretion onto massive stars. Survival of substructures and the extent of mass segregation are found to be higher in the model with the strongest feedback, which compares positively with observations. Multiple systems of stars and the number of high-velocity escapers also exhibit a dependence with feedback, which provides an in-

teresting check for simulations on galactic scale.

The second topic of research looks at the interaction between already formed gas-free globular clusters as an explanation of their multiple populations and rotation. Using N-body simulations, I study whether merging of star clusters could explain these two characteristics in the specific case of iron-complex globular clusters. Iron-complex globular clusters exhibit both large star-to-star light elements abundance variations and, surprisingly, also Fe abundance variations. The globular clusters within this category show some unusual aspects in the metal-rich/metal-poor number ratio and relative concentration, not explained by the existing self-enrichment models for multiple populations. Moreover, rotation has been observed in several globular clusters, but there is not yet a general consensus for its origin. The key parameters explored are the initial mass and density ratio of the progenitors. The results indicate that the relative concentration of the two progenitors in the final merger output strongly depends on these two parameters. In particular, when the progenitors have similar initial densities, the more massive progenitor dominates the central part of the merger remnant and the less massive progenitor forms an extended population. To be more centrally concentrated, the low mass progenitor needs an initial density higher by roughly the mass ratio. The merger remnants show solid body rotation in the inner parts, becoming differential in the outer parts. Rotation velocity and ellipticity show agreement with models for oblate rotators with isotropic dispersion. The density ratio is found to have an impact on the rotation profile of the remnant in case of unequal mass mergers. This signature is a useful observational test for this model.

Zusammenfassung

Sterne könnten in gewissem Sinne als soziale Tiere betrachtet werden, wie Menschen auch. In der Tat treten Sterne zumeist in Ansammlungen auf, auch Sternhaufen genannt. Da die Sternentstehung im Grunde ein kollektiver Prozess ist und eine Ansammlung von Sternen zusammen aus der selben Molekülwolke entsteht, sind Sternhaufen als Erstes Kinderstube für stellare Objekte. Ausserdem interagieren Sterne, sobald enstanden, untereinander durch Gravitation, daher ist ein Sternhaufen die kleinste Struktur, in der es möglich ist, die Dynamik der Sterne zu untersuchen. Auf grsserem Massstab knnen Sternhaufen als Bausteine von Galaxien betrachten werden, deshalb ist das VerstŁndnis ihrer Entstehung und Entwicklung für viele Forschungsfelder in der Astrophysik von grundsätzlicher Bedeutung. Jedoch ist der genaue Übergang von einer dichten Gaswolke zum Sternhaufen immer noch eine offene Frage mit vielen Teilantworten, und Beobachtungen zeigen, dass der Begriff "Sternhaufen" breit definiert ist, der so verschiede Objekte beinhaltet wie Kugelsternhaufen, Offene Sternhaufen, Sternassoziationen, Junge Sternhaufen, oder Kernsternhaufen, welche sich in ihrer Anzahl, Masse, Alter, Grösse und damit Dichte, Sternpopulation und Verteilung unterscheiden. Jede dieser Unterkategorien zeigt eindeutige Charakteristiken, welche darauf warten erklärt zu werden. Desweiteren ist eine etwaige Verbindung zwischen diesen Formen von Sternhaufen und die Ermittlung von Voraussetzungen für ihre Entstehung immer noch ungeklärt.

In dieser Doktorarbeit adressiere ich zwei grosse offene Fragen dieses Gebietes. Zuerst wende ich mich der Untersuchung von Entstehung und Hervortreten von Sternhaufen aus ihrer Molekülwolke zu. Mit Hilfe von Strahlungs-Hydrodynamiksimulationen analysiere ich Kollaps und Ausbreitung der Wolke durch von neugeborenen Sternen emittierte photoionisierende Strahlung. Das Interesse liegt hierbei in der Bestimmung, wie jene Rückkopplung Struktur und Dynamik des Jungen Sternhaufens beeinflusst. Meine Resultate zeigen, dass Photoionisation sehr effektiv darin ist, die Wolke zu zerreissen und eine gaslose Ansammlung von Sternen zu erzeugen. Die Rückkopplung hat grosse Auswirkung auf die Charakteristik von Sternhaufen, wobei die Sterndichte reduziert wird und dadurch die Entstehung von Strukturen in virialem Gleichgewicht erlaubt. Ohne diese Rückkopplung erhöht sich durch die hohe Dichte die Häufigkeit

und Stärke von Nahbegegnungen zwischen Sternen, was eine fortlaufende Zerstörung des Haufens bewirkt. Rückkopplung ist auch für das Aufhalten von massiver Sternakkretion verantwortlich. Die Überlebensrate von Substrukturen und das Ausmass der Massentrennung zeigen sich höher im Fall, dass die Rückkopplung am stärksten ist, was sich mit den Observations-Ergebnissen deckt. Vielfach-Sternsysteme und die Anzahl an schnell-entkommenden Sternen zeigen auch eine Abhängigkeit von der Rückkopplung, was eine gute Möglichkeit zur Überprüfung von Simulationen auf galaktischem Massstab darstellt.

Die zweite Forschungsfrage dreht sich um die Interaktion zwischen schon entstandenen gaslosen Sternhaufen und Unterscheidungskriterien von Kugelsternhaufen, nämlich Vielfach-Populationen und Rotation. Mit Hilfe von N-Körper-Simulationen untersuche ich, ob die Verschmelzung von Sternhaufen diese beiden Charakteristiken im speziellen Fall von Eisen-komplexen Kugelsternhaufen erklären könnte. Eisen-komplexe Kugelsternhaufen sind Objekte mit grossen Variationen der Menge sowohl an leichten Elementen als auch von Fe. Kugelsternhaufen dieser Kategorie zeigen unübliche Anzeichen vom Verhältnis Metall-reiche zu Metall-arme Sterne und von ihrer relativen Konzentration, welche nicht durch das Selbstanreicherungs-Modell von Vielfach-Populationen erklärt werden können. Ausserdem wurde in einigen Kugelsternhaufen eine Rotation beobachtet, für deren dynamischen Ursprungsmechanismus noch keine Einigkeit besteht. Die Hauptparameter der vorliegenden Untersuchung sind die initiale Masse und Dichteverhältnis der beiden Vorgänger. Die Ergebnisse deuten darauf, dass die relative Konzentration der Vorgänger im Ergebnis der Verschmelzung stark von diesen zwei Parametern abhängt. Insbesondere wenn die Vorgänger ähnliche Anfangsdichten haben, wird der massivere der Beiden den zentralen Teil des Verschmelzungsrestes dominieren und der Andere eine ausgebreitete Population darstellen. Um auch zentraler konzentriert zu sein, muss der kleinere Vorgänger genenüber dem grösseren eine ungefähr dem umgekehrten Massenverhältnis entsprechendes Dichteverhältnis haben. Die Überbleibsel der Verschmelzung weisen in der inneren Region starre Rotation auf, in der äusseren hingegen differenzielle Rotation. Die Rotationsgeschwindigkeit und die Elliptizität sind in Übereinstimmung mit Modellen von abgeflachten Rotatoren mit isotroper Dispersion. Das Dichteverhältnis hat offenbar Einfluss auf das Rotationsprofil im Überbleibsel, wenn die Massen ungleich sind. Diese Signatur könnte einen nützlichen Test dieses Modelles durch Beobachtungen darstellen.

The Secret Lives of Star Clusters: Formation and Dynamical Evolution

Elena Gavagnin

Elena Gavagnin
Institute for Computational Science
Universität Zürich
Winterthurerstrasse 190
CH-8057 Zürich
Switzerland

Contents

Preface **xi**

1 Introduction **1**

2 Star Clusters: a Family Portrait **11**
2.1. Globular clusters 11
2.2. Open clusters 25
2.3. Young star clusters 32
2.3.1. Stellar associations 32
2.3.2. Young massive clusters 34
2.3.3. Embedded star clusters 41
2.4. Nuclear star clusters 44

3 Star and Star Cluster Formation **49**
3.1. Molecular clouds 51
3.2. Gravitational collapse 57
3.2.0.1. Free-fall timescale 59
3.2.1. Jeans' Mass and Length 61
3.2.2. Virial theorem 65
3.2.2.1. Virial equilibria 68
3.3. Feedback mechanisms 69
3.3.1. Stellar winds 70
3.3.1.1. Protostellar outflows 70
3.3.1.2. Massive hot stars 72
3.3.2. Radiation-gas interaction 73
3.3.2.1. Radiation pressure 73
3.3.2.2. Photoionisation 75
3.3.3. Supernovae 76

4 Dynamical Evolution of Stellar Systems **79**
4.1. Star cluster equilibrium models 80
4.1.1. Size scales 85
4.2. The granularity of the gravitational field: Two-body relaxation 85
4.2.1. Timescales 87
4.2.2. Evaporation 91

4.2.3. Gravothermal instability . . . 92
4.2.4. Equipartition and mass segregation . . . 93
4.3. Post collapse: Binaries &Co. . . . 94
4.4. Additional perturbations . . . 95

5 Star Cluster Formation & Photo-Ionisation: a Love Story 97
5.1. Introduction . . . 98
5.2. Numerical Methods . . . 104
5.2.1. Initial Conditions . . . 104
5.2.2. Refinement strategy . . . 105
5.2.3. Sink Particles . . . 105
5.2.4. Radiative Processes . . . 106
5.3. Analysis . . . 107
5.3.1. Virial properties . . . 108
5.3.2. Mass function . . . 112
5.3.2.1. Comparison to observations . . . 112
5.3.2.2. Slope of the mass function . . . 115
5.3.3. Mass segregation . . . 118
5.3.4. Stellar dynamics . . . 125
5.3.4.1. Escaping stars . . . 125
5.3.4.2. Multiple systems . . . 129
5.4. Summary and Discussion . . . 133

6 Can Merging Explain Iron-Complex Globular Clusters? 139
6.1. Introduction . . . 140
6.2. Methods and simulations . . . 143
6.3. Results . . . 146
6.3.1. Relative Concentration . . . 146
6.3.2. Rotation . . . 151
6.4. Discussion and Conclusions . . . 158

7 Conclusions and Outlook 163

A Numerical Methods 165
A.1. Starlab . . . 165
A.2. Ramses . . . 170

Bibliography 175

Acknowledgements 202

Preface

This thesis is the fruit of the achievements, failures and experience gathered during my PhD. The result is part of a dazzling story, whose origins are lost in the past.

This journey started very early in the morning, on a raft, on the shore of an unknown island, probably close to Gibraltar. With the eyes to the sky, a legendary hero (or maybe just a common man) was trying to search for some reference point to come back home. From there, centuries of eyes starring at the sky, studied the same stars and discovered that these are much more numerous than initially thought, and that they cluster together.

The pursuit of knowledge has the terrible characteristics of being never enough, and therefore star clusters were found to be more than a thousand, distinguished in different categories, characterised by disparate ages, structures, or colours. All this amount of information and doubts claim for an explanation, which will bring us to explore the theory behind the formation of these objects and the study of their dynamics.

The scientific research is affected by something I would call "negative question-capacity" (in analogy with another negative capacity typical of gravitational systems, how it will be clear in Chapter 4), which means that for the number of questions which find an answer, always new questions pop-up. Therefore, the theoretical framework described, explains many properties of the star clusters and at the same time still leaves tons of doubts about them.

Much of the life of a star cluster is indeed *secret*, meaning we do not really see what they are doing live. We have just a collection of pictures and from there we reconstruct what happened in the moments (or million years) before the picture was taken. Our story will end trying to describe two secret moments, which are the birth of a new cluster and interaction between two of them. This will hopefully serve to solve some doubts and raise new exciting questions.

Elena Gavagnin

1

Introduction

γηθόσυνος δ'οὔρῳ πέτασ' ἱστία δῖος Ὀδυσσεύς.
αὐτὰρ ὁ πηδαλίῳ ἰθύνετο τεχνηέντως
ἥμενος· οὐδέ οἱ ὕπνος ἐπὶ βλεφάροισιν ἔπιπτε
Πληϊάδας τ' ἐσοπῶντι καὶ ὀψὲ δύοντα Βοώτην
Ἄρκτον θ', ἣν καὶ ἅμαξαν ἐπίκλησιν καλέουσιν,
ἥ τ' αὐτοῦ στρέφεται καί τ' Ὠρίωνα δοκεύει,
οἴη δ' ἄμμορός ἐστι λοετρῶν Ὠκεανοῖο·
τὴν γὰρ δή μιν ἄνωγε Καλυψώ, δῖα θεάων,
ποντοπορευέμεναι ἐπ' ἀριστερὰ χειρὸς ἔχοντα.

Homer, *Odyssey*, V Book, vv 269-277, VIII b.C.

Gladly then did goodly Odysseus spread his sail to the breeze;
and he sat and guided his raft skilfully with the steering-oar,
nor did sleep fall upon his eyelids,
as he watched the Pleiads, and late-setting Bootes,
and the Bear, which men also call the Wain,
which ever circles where it is and watches Orion,
and alone has no part in the baths of Ocean.
For this star Calypso, the beautiful goddess,
had bidden him to keep on the left hand as he sailed over the sea.

translation by T.Murray, (Homer, 1919)

After seven years prisoner of the beautiful nymph Calypso, Odysseus is finally allowed to leave. His only desire is to come back to his island Itaca. He builds himself a raft, spreads the sail and starts his journey (which will be still long until he reaches his beloved kingdom). To reach Greece, sailing in the night, the point of reference are stars and in particular a very specific star cluster, the Pleiades. The hero had probably to travel towards East in order to reach Greece, that's why the nymph suggests to keep the Ursa Major ("the Bear", "the Wain "), indicating the North, always to the left and the Pleiades, rising in the East, in front of him.

The Pleiades are the star cluster for which we found oldest reference in western history. These verses from the Odyssey are definitely one of the oldest mentions dated ∼VIII century b.C. Almost 3000 years later we are still observing and studying the same star clusters, as fundamental guiding point not only for sailing but also for the advancement of astrophysical research.

Clearly, between Odysseus and us a lot happened and a lot has been discovered. In the ancient world the Pleiades were thought to be only 7 stars, until Galileo Galilei started observing the sky with the *Perspicillum*, the original name of what we know as telescope, and observed more than 40 extra stars being part of the Pleaides, as it is evident from Figure 1.1 (Galilei, 1610).

Galileo, after finding similar evidence for other group of stars which were before thought to be a single star, concluded that *"Est enim GALAXIA nihil aliud, quam innumerarum Stellarum coacervatim consitarum congeries" (Galilei, 1610)*, i.e. the Galaxy is in fact nothing else, than a collection of innumerable stars planted in heaps.

With the new telescope Giovanni Battista Hodierna discovered several systems of stars in 1654, classified as *Luminosae*, *Nebulae* and *Occultae*, whether it was possible to distinguish some members at naked eye (Luminosae), or had a fuzzy appearance at naked eye but could be resolved with the telescope (Nebulae) or they appeared as covered by a cloud (Occultae) (see Figure 1.2).

The results of his study were published in Hodierna (1654) and include the observations of the open clusters later identified as M6, M36, M37, M38, M41, M47, NGC 2362, NGC 6231 and the HII region M8. Among the others he produced the first telescopic image of the the Orion Nebula (M42) (probably one of the most observed object by now), being able to detect the Trapezium cluster within it and the nebulosity surrounding it (Fodera-Serio et al., 1985), see Figure 1.3 .

Starting from the Galileian discovery, what were thought to be "nebu-

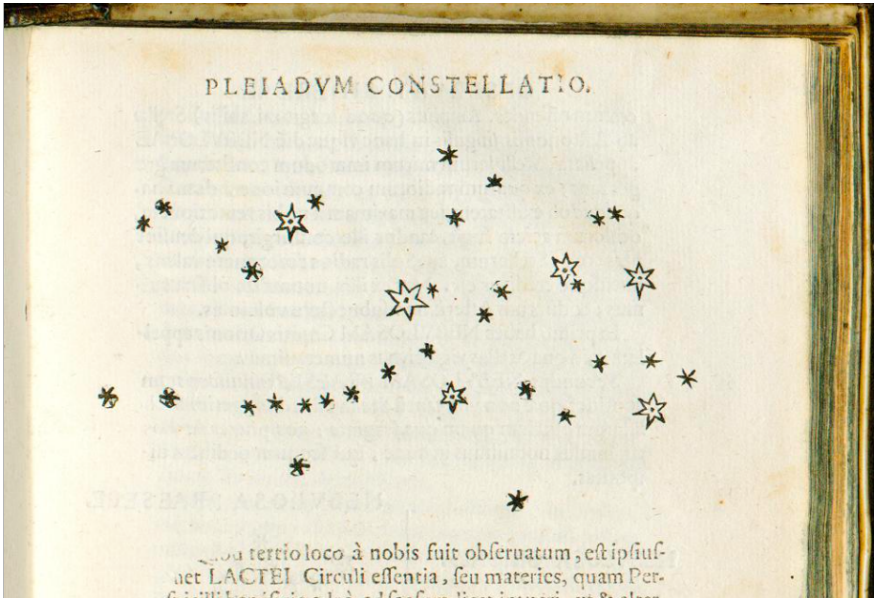

Figure 1.1: The Pleiades star cluster as observed by Galileo Galilei. The more luminous stars are depicted bigger in size. The revolutionary use of the telescope allowed the discovery of about other 40 stars. From Galilei (1610).

Figure 1.2: Graphical representation of examples of Luminosae, Nebulosae and Occulatae systems of stars. From Hodierna (1654).

Figure 1.3: The Orion Nebula (M42) as seen by Hodierna (1654) (*Top*) and by M.McCaughrean et al., ESO Very Large Telescope (*Bottom*), composite near-infrared image, the field of view is ~ 1 pc across. At the centre of both images is visible the Trapezium cluster.

lous object" (nebulae) or single stars were recognised actually as "congeries Stellarum", star clusters. Hodierna set also another fundamental milestone for astronomy. He established that the coexistence of Luminosae, Nebulosae and Occultae systems of stars is possible only if we assume that the stars have different distance from us[1] . In this way, the author manages to justify why some stars appear very bright while some other fuzzier and dimmer. A related problem he deals with in the final part of Hodierna (1654), *Problemata nonnulla*, is the consequent theory of star formation (see Fodera-Serio et al., 1985, for a detailed analysis).

To explain why the more luminous stars appear usually isolated, while the less bright are found in groups, he claims that stars form from the condensation of *lux primogenita*, therefore the biggest stars collect lux from a bigger region. At the end of the star formation process, this region will be empty of lux, no other stars will form nearby and the star will shine visibly (Hodierna, 1654, p. 53). In the Nebulosae, many small stars form closer from smaller cores, resulting in fainter luminosity and less resolvability at naked eye[2](Fodera-Serio et al., 1985). Moreover according to Hodierna, this process of star formation is still active and it could be possible to observe new stars anytime[3](Fodera-Serio et al., 1985).

It interesting to notice how, even with its own incorrectness, this theory identify some sort of condensation phenomenon, which shapes the final properties of stars. If we would substitute the concept of lux primogenita, with molecular gas, and the lux-deprived region with gas-free region due to feedback, the theory starts looking quite modern.

A substantial step forward in the observation of star clusters was the work of Charles Messier. The first globular clusters were observed between mid-XVII century and mid-XVIII, but it was not until 1764 that some *nebulae* were distingushed in individual stars by Messier (M4). The fundamental work by Messier translated into the first *Catalogue of Nebulae and Clusters*

[1] *"Stellas Mundo coevas, quae in Aetheris eminentissimi profunditate, innata sibi luce, adinstar Solis huius, praefulgent, nequaquam omnes, ac singulas in eadem Sphaericitate Mundi coordinatas, et circumpositas esse, ita ut omnes, ac singulae è Terris, aequidistent"* (Hodierna, 1654, p. 25).

[2] *"An quia lux primogenita dùm ab initio quando dixit Deus fiat lux Mundu universu circumambiens per Aethera expandetur, ad nutum deinde Imperii divini qaundo fecit Deus Stellas, & posuit eas in firmamento Caeli in varios, ac diversae magnitudinis Globus, undique defluens involveretur, ubi ad maioris molis globos constituendos, maior eiusdem substantiae portio conspirasset, maius etiam Aetheris spatium denudatum necessario relinqueretur at ubi in maiores atque minores involutus fuerit orbilculos, angustiora spatia denudata paterent"* (Hodierna, 1654, p. 53).

[3] *"Nam ex eadem substantiae mole, qua simplex ingens Globus conflatur plures etiam, sed exigui Globuli concorporari possunt. Sic fortasse fieri poterit, ut ex invisibilibus Stellis coentibus latenter innumeris, confletur unum quid compositum, & appareat ingens Stella recentissime a mortalibus visenda"* (Hodierna, 1654, p. 53).

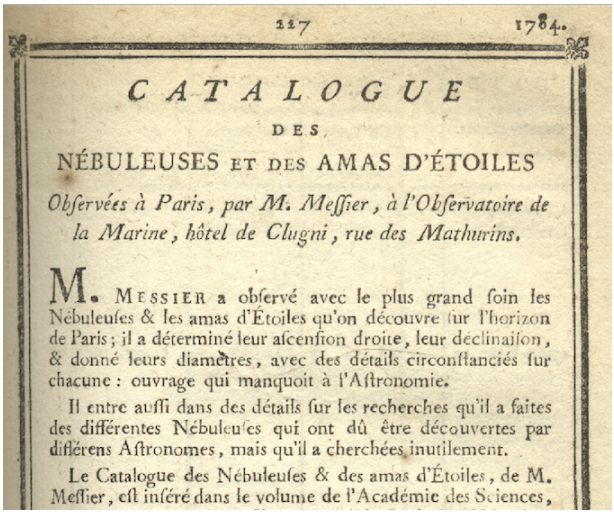

217 1784.

CATALOGUE
DES
NÉBULEUSES ET DES AMAS D'ÉTOILES
Observées à Paris, par M. Messier, à l'Observatoire de la Marine, hôtel de Clugni, rue des Mathurins.

M. MESSIER a observé avec le plus grand soin les Nébuleuses & les amas d'Étoiles qu'on découvre sur l'horizon de Paris; il a déterminé leur ascension droite, leur déclinaison, & donné leurs diamètres, avec des détails circonstanciés sur chacune : ouvrage qui manquoit à l'Astronomie.

Il entre aussi dans des détails sur les recherches qu'il a faites des différentes Nébuleuses qui ont dû être découvertes par différens Astronomes, mais qu'il a cherchées inutilement.

Le Catalogue des Nébuleuses & des amas d'Étoiles, de M. Messier, est inséré dans le volume de l'Académie des Sciences,

Figure 1.4: First page of the *Catalogue of Nebulae and Clusters of Stars* by Charles Messier. From Messier (1781).

of Stars published in 1781 (Messier, 1781). Messier was actually interested in comets, not star clusters and published this catalogue exactly to list objects which observers could wrongly confuse for comets. The final version of the catalogue counts 103 objects (7 more were added later, from some other Messier's studies), half of which are open and globular cluster.

Few years later another catalogue was published by William Herschel, as a result of his "review of the heavens", i.e. survey, with a 20-foot (∼6m) telescope. This milestone work was published in 3 parts (Herschel, 1786, 1789, 1802) and by 1802 listed a total of 2500 objects. The second part of the catalogue (Herschel, 1789) is particularly interesting since we found the first mention to the term "globular cluster"[4].

The description of these objects made by Herschel is extraordinary, communicating at the same time the scientific enthusiasm due to the features of their structure and the aesthetic beauty of the new discovery:

> *"These are certainly the most magnificent objects that can be seen in the heavens. They are totally different from mere groups of stars,*

[4] *"And thus, from the above-mentioned appearances, we come to know that there are globular clusters of stars nearly equal in size, which are scattered evenly at equal distances from the middle, but with an encreasing accumulation towards the center"* (Herschel, 1789, p.218)

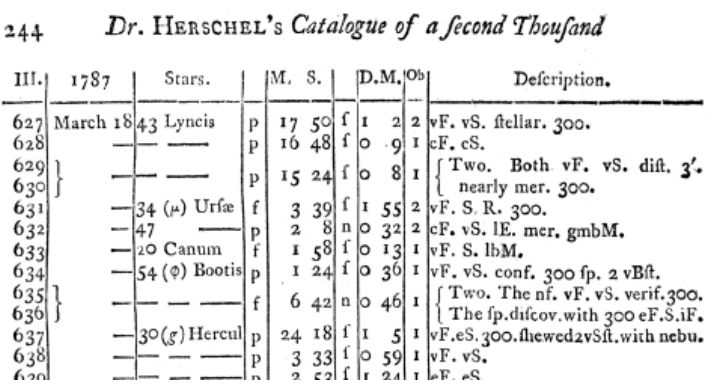

244 *Dr.* HERSCHEL'S *Catalogue of a ſecond Thouſand*

III.	1787	Stars.		M. S.		D.M.	Ob	Deſcription.
627	March 18	43 Lyncis	p	17 50	f	1 2	2	vF. vS. ſtellar. 300.
628	—	—	p	16 48	f	0 9	1	cF. cS.
629	—	—	p	15 24	f	0 8	1	Two. Both vF. vS. diſt. 3′. nearly mer. 300.
630	—	—						
631	—	34 (μ) Urſæ	f	3 39	f	1 55	2	vF. S. R. 300.
632	—	47 —	p	2 8	n	0 32	2	cF. vS. lE. mer. gmbM.
633	—	20 Canum	f	1 58	f	0 13	1	vF. S. lbM.
634	—	54 (φ) Bootis	p	1 24	f	0 36	1	vF. vS. conf. 300 ſp. 2 vBſt.
635	—	— — —	f	6 42	n	0 46	1	Two. The nf. vF. vS. verif. 300. The ſp. diſcov. with 300 eF. S. iF.
636	—	— — —						
637	—	30 (g) Hercul	p	24 18	f	1 5	1	vF. eS. 300. ſhewed 2 vSſt. with nebu.
638	—	— — —	p	3 33	f	0 59	1	vF. vS.
639	—	— — —	p	2 52	f	1 24	1	eF. eS.

Figure 1.5: An extract from the Catalogue of Nebulae and Clusters of Stars by Herschel. From Herschel (1789).

> *in their beautiful and artificial arrangement.: their form is generally round; and the compression of the stars shows a gradual, and pretty sudden accumulation towards the centre, where, aided by the depth of the cluster, which we can have no doubt is of globular form, the condensation is such that the stars are sufficiently compressed to produce mottled lustre, nearly amounting to the semblance of a nucleus. A centre of attraction is so strongly indicated by all the circumstances of the appearance of the cluster, that we cannot doubt a single moment of its existence, either in a state of real solidity, or in that of an empty centre, possessed of an hypothetical force arising from the joint exertion of the numerous stars that enter into the composition of the cluster."* (Herschel, 1802, p.497)

These observations triggered the discussion about the formation and origin of these cluster of stars. In Herschel (1789) the astronomer reports the results of John Michell regarding the probability that these stars clusters were just fortuitous aggregation of stars (Herschel, 1789, p.215). This was obviously the simplest hypothesis, to assume that the stars appeared to be in cluster just by chance. But as Herschel pointed out *"But who, that is acquainted with the doctrine of chances can seriously maintain such improbable conjectures?"*. Indeed, in 1767 John Michell considered the brightest stars of the Pleiades (6 stars) and estimated the number of stars as bright as the faintest of these 6 to be $\sim$1500 in number, scattered random in the whole sky. He then computed the probability that other 6 stars (between these

1500) are at the same distance between each other as the Pleiades are: the probability for this to happen is 0.0002% (Michell, 1767, pp.246-249). With this result Michell concluded that:

> *"We may from hence, therefore, with the highest probability conclude (the odds against the contrary opinion being many million millions to one) that the stars are really collected together in clusters in some places, where they form a kind of systems, whilst in others there are either few or none of them, to whatever cause this may be owning, wheter to their mutual gravitation, or some other law or appointment of the Creator."* (Michell, 1767, p.249),

The author suggested with this that there is a dynamical origin at the base of the star cluster structure, which is the gravitational attraction.

On the same line of thought, Herschel (1785) assumes that in the very early Universe stars were first scattered uniformly and then, due to gravity, were collected into streams, which subsequently fragmented into denser and smaller clusters (Hoskin, 1979).

In the wake of Herschel's work, at the end of XIX century John Dreyer published a novel catalogue, titled *New General Catalogue*, which reached to include (after successive supplements) a total of almost ∼13 000 objects, counting ∼700 open clusters and ∼100 globular clusters (Dreyer, 1888, 1895, 1910).

In the XX century physical quantitative studies on the properties of star clusters started accompanying observations: proper motions studies allowed to identify cluster members more accurately (van Maanen, 1945) and the first colour-magnitude diagrams of the Pleiades and Hyades star clusters were published (Hertzsprung, 1911). After these pioneers, in the last century many researchers dedicated their time to the study of star clusters, allowing huge advancements in our knowledge of these objects and at the same time generating hundreds of unanswered questions about them.

More recently, the technological advancement allowed the construction of gigantic ground telescopes (at least compared to the galileian *perspicillum*) and the launch in orbit of space telescopes, which revolutionised once more astronomy. Some of the greatest observers of star clusters on the Earth are located in very remote and high-altitude areas of Chile and Hawaii, these are indeed the telescopes of Paranal, La Silla and Mauna Kea observatories. These instruments operate mainly in visible and near-infrared light, due to the atmospheric absorption of the remaining wavelengths shorter than radio. The atmosphere is in fact, the main enemy for this kind of instruments, since its turbulence contributes to the distortion of the observed

signals. However, the introduction of adaptive optics techniques massively improved the quality of images.

The king is anyway still the space telescope Hubble, which has been providing photometric and spectrographic data for more than 25 years, in ultraviolet, visible and near-infrared light. Infrared and X-ray complementary information come from Spitzer and Chandra space telescopes. Astrometric data are the goals of research of the Gaia mission, which has already released the precise position on the sky and brightness of 1 billion stars (1% of all stars in the Milky Way) and will in the future register also their positions, parallaxes and proper motions, effectively building the largest catalogue of stars ever. The future, then, is represented by the James Webb Space Telescope, the successor of Hubble, an infrared telescope which promises to investigate the formation of stars, exoplanets and first galaxies.

2

STAR CLUSTERS: A FAMILY PORTRAIT

In this chapter I will give a detailed overview of the main classes of star clusters and their properties from an observational point of view. Indeed, under the broad terminology of "star cluster"' we find different objects which exhibit very specific characteristics. The most basic, general and true definition of "stars cluster" is "a self-gravitating system of stars". And this is substantially the only possible common description one can give, any further qualification would not be generally representative of every category. The classes I will take into consideration are globular clusters, open clusters, young star clusters (articulated into associations, dense and embedded clusters) and finally nuclear star clusters. How exactly these categories are related to each other is a million-dollar-question but some connections can be derived. I will focus on the most peculiar properties of every group, trying to highlight each time what are they interesting for, why should we do research on them and what are the puzzling aspects we still do not understand.

2.1. Globular clusters

If we consider a galaxy to be a city, then globular clusters would be very old people, who lived there since ever. And exactly as old people, everyone thought they were quite simple and boring objects, mainly useful as laboratory for pure stellar dynamics, while they turned out to have quite

Figure 2.1: 47 Tuc from Paranal. The field of view is a bit more than 50 pc across. Credit:ESO/M.-R. Cioni/VISTA Magellanic Cloud survey.

some tales and mysteries to unveil. Moreover since they are the oldest alive beings, who can claim of having met the early Universe, they can provide fundamental information to understand the formation of the frst galaxies and the Universe.

Globular cluster are systems composed of $10^4 - 10^6$ stars (total mass $10^5 M_\odot$), arranged in an almost spherical distribution. They appear deprived of gas and dust, as a typical example as 47 Tuc reveals (Figure 2.1). In the Milky Way we count 157 globular clusters (Harris, 2010), distributed both in the halo and in the disk of the Galaxy.

Until few years ago globular clusters were considered perfect example of isolated spherically symmetric, pure stellar systems, excellent representation of a simple stellar population. More recently these simple assumptions have been relaxed, since some globular clusters exhibit flattening due to rotation, some reveal multiple stellar populations, thus several episodes

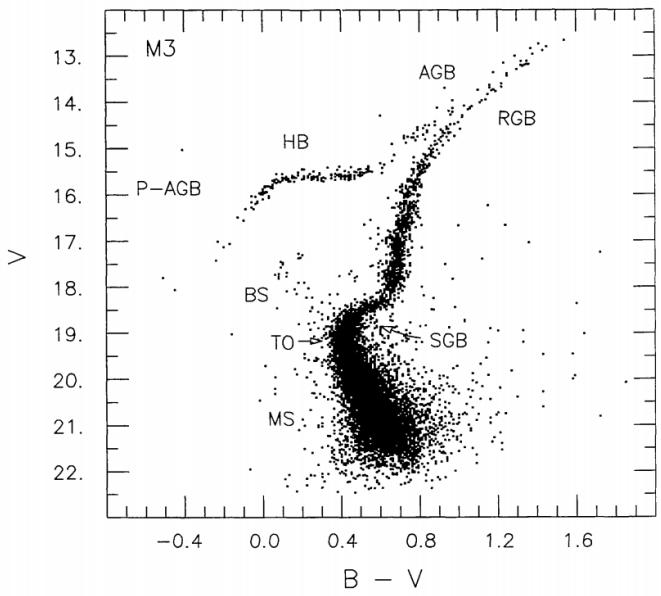

Figure 2.2: Color magnitude diagram of M3 (Renzini & Fusi Pecci, 1988)

of star formation, some are found in the disk of the Galaxy, close to the Galactic Centre, where tidal effects are not negligible.

Figure 2.2 shows the color magnitude diagram (CMD) of the globular cluster M3 (Renzini & Fusi Pecci, 1988). This can be considered a very archetypical CMD, very representative for an average globular cluster and extremely different from the ones of younger clusters (Section 2.2, see for a comparison Figure 2.9). Being the globular clusters old structures, the diagram exhibits most sequences of classic stellar evolution: main sequence (MS), subgiant branch (SGB), red giant branch (RGB), horizontal branch (HB) and asymptotic giant branch (AGB). The presence of RR Lyrae stars on the HB is revealing that globular clusters host Pop II stars.

We notice that the MS is particularly short, the turn-off happening at fainter luminosity than other types of cluster (Ashman & Zepf, 1998), which means that massive stars already moved to subsequent stages of stellar evolution, and hence the cluster is quite old. The average value of turn-off mass for globular clusters is $\sim 0.8\ \mathrm{M}_{\odot}$.

The turn off-mass is a fundamental piece of information to estimate the

age of the cluster. The older the cluster, the lower the turn-off point along the MS, therefore the absolute magnitude at turn-off ($\mathrm{M_V(TO)}$) directly points to the cluster age. The analytic expression which relates magnitude and age is (Binney & Merrifield, 1998)

$$\mathrm{M_V(TO)} = 2.70\log(\mathrm{t/Gyr}) + 0.30[\mathrm{Fe/H}] + 1.41\ . \tag{2.1}$$

Using stellar evolution models it is possible to predict luminosities and effective temperatures as a function of time and chemical content and built complete theoretical isochrones to be compared to observations. By minimising the residuals between the modelled and observed isochrones, it is possible to infer the cluster age.

The main source of error in these estimates is due to the distance calculation (to convert magnitudes from apparent to absolute) which is usually derived through MS fitting or using the RR Lyrae stars as standard candles (for a review on all the main techniques to derive distances see the review by Krauss & Chaboyer (2003)). According to Krauss & Chaboyer (2003) the error on the distances is $\sim$6% which implies an error on the age estimate around 13% (Chaboyer, 2008).

To circumvent this problem other distance-independent magnitude-base age estimates have been developed, such as the ΔV or $\Delta(B-V)$ method (Binney & Merrifield, 1998). They are both based on the difference in the CMD between two values of magnitude or colour, respectively. Specifically the first method uses the difference in the turn-off point and horizontal branch ($\Delta\mathrm{V} = \mathrm{M_V(TO)} - \mathrm{M_V(HB)}$), and the second one the difference between the colour of the turn of the SGB and the colour of the turn-off point ($\Delta(B-V) = (B-V)_{SGB} - (B-V)_{TO}$). Nevertheless, also these methods are not free from problems (Ashman & Zepf, 1998), mainly related with the necessity of having a perfect estimate of the position of the turn-off point or turn of the SGB, which severely affects their accuracy (Jimenez, 1999).

Some of the most recent studies date GCs to be between 11.3 and 14.4 Gyr old (An et al., 2009; Chaboyer, 2008; Gratton et al., 2003; Krauss & Chaboyer, 2003; VandenBerg, 2000), in agreement with ΛCDM estimate of the age of the Universe (Collaboration et al., 2016). GCs are by no doubt among the oldest inhabitants of the Universe.

The fact globular clusters are old does not mean they are all equally old: the relative age of globular clusters has fundamental implications in our Galaxy formation scenario. However, from the study of different HR diagrams different globular clusters appear to have very close turn-off points, therefore the relative age difference is limited.

Using analogue techniques to determine the absolute age, it has been possible to estimate that galactic globular cluster exhibit a mean age range $\sim$2-3 Gyr (Hansen et al., 2013; Sarajedini, 2009). In particular, metal-poor ($[\mathrm{Fe/H}] < -1.7$) are found to be older and mostly coeval, with age dispersion value $\sim$0.6 Gyr (De Angeli et al., 2005; Marín-Franch et al., 2009). Intermediate-metallicity clusters ($-1.7 < [\mathrm{Fe/H}] < -0.8$) are younger than the previous sample and have age dispersion $\sim$1 Gyr and total age interval of $\sim$ 3 Gyr (De Angeli et al., 2005). For metal-rich clusters the age spread goes up to $\sim$ 6 Gyr (Chaboyer et al., 1996; Marín-Franch et al., 2009; Sarajedini, 2009). From the spatial point of view, there is no trace of correlation between galactocentric distance and age (Chaboyer et al., 1996; De Angeli et al., 2005; Marín-Franch et al., 2009), but clusters at $> 20kpc$ are generally older and more uniform in age (De Angeli et al., 2005; Sarajedini, 2009).

The SGB provides useful information on the relative age of stars in the cluster: a sharp SGB (like in M3) and well defined turn-off point have always been interpreted as the proof that the members of the cluster are coeval (e.g. for M92: max age spread between consituents $\sim$2.4% age of the cluster, $\sim$0.4 Gyr (Stetson, 1993)).

The narrowness of stellar evolution sequences puts also an upper limit on the fraction of binaries in the cluster (Ashman & Zepf, 1998). If the cluster hosts a large number of multiple systems, we should see a broadening of the sequence, due to the fact that unresolved binaries would populated the upper edge of the sequence (e.g. MS), appearing more luminous than a single star of the same spectral class. Ji & Bregman (2015) applied this technique to the MS for 35 globular cluster and determined that in all of them the percentage of binaries does not exceed $\sim$12%. Using the data from Milone et al. (2012b) they also determined that above 10 relaxation times[1], no clusters have binary fractions higher than 6% and nearly half have binary fractions below 2%. An exception to this evidence is constituted by the percentage of core binary fraction, indeed some globular clusters (Pal13, E3, NGC 6752, NGC 288) have shown a higher fraction of binaries in the core, up to $\sim 30\%$ (Fregeau, 2008). However, in Sections 2.2 and 2.3.2 we will see that in general the fraction of binaries is much higher in younger systems.

Moreover very narrow sequences (both MS and RGB) reveal the homogeneity in terms of chemical compositions of the global clusters' stars. Most globular clusters, in fact, contain stars with similar metallicity, and this is a unique feature which distinguishes them from dwarf galaxies or galaxies, which exhibit an internal metallicity variation (Ashman & Zepf,

[1] A complete definition of relaxation time is give in Section 4.2.1.

1998).

However, in the recent years, this picture has been revolutionised, when early photometric and spectrographic observations suggested the existence of multiple populations (e.g. Canon & Stobie 1973; Freeman & Rodgers 1975; Geyer 1967; Hesser & Bell 1980). Photometric data analysed by Anderson (1997) indicated a bifurcation of colors in the main sequence (MS) of Omega Cen. Furthermore, Lee et al. (1999) and Pancino et al. (2000) reported the presence of at least four different RGBs in the same GC. *Hubble Space Telescope* (Bedin et al., 2004) clearly showed that Omega Cen has two distinct MS branches, differing in He content (Norris, 2004). Based on a spectroscopic analysis of MS stars in Omega Cen, Piotto et al. (2005) surprisingly found out that the less populous MS branch, the bluer one, is 0.3 dex more metal-rich than the redder one (requiring thus an He enrichment of $\sim 0.35 - 0.40$). This was just the beginning of a long list of detections of multiple populations in globular clusters: 47 Tuc (Anderson et al., 2009), NGC 6752 (Milone et al., 2013, 2010), NGC 6397 (Milone et al., 2012a). Evidence of multiple populations was also found in some intermediate-age globular clusters of the Magellanic Clouds (Milone et al., 2008). Multi-branch features were observed not only in MS stars, but also in the SGB, RGB and HB stars (Gratton et al., 2012).

The first studies on the abundance variations of the four light elements (Na, O, Al, Mg), carried out since the late 90s (Briley et al., 1996; Gratton et al., 2001), revealed star-to-star abundance variations for elements lighter than Si (Carretta et al., 2009a; Cohen, 1978; Gratton et al., 2001; Kraft et al., 1992; Peterson, 1980). Moreover they discovered that these variations are anti-correlated with one another (e.g. O-Na, Mg-Al). Evidence for an anti-correlation of light elements has been found in all observed Milky Way GCs (except for Terzan 7 and Pal 12), suggesting that multiple populations exist in all globular clusters, and not only in the most massive ones (Carretta, 2012; Gratton et al., 2015, 2001, 2012, 2011, 2013; Milone et al., 2016). The main explanation behind this phenomena is connected to internal enrichment by proton-capture H-burning reactions at high temperature (Gratton et al., 2004). Several models have been proposed (for a complete review see Renzini 2008), postulating single ("early disc accretion model" (Bastian et al., 2013)) or multiple star-formation episodes (AGB stars (D'Ercole et al., 2008), fast rotating massive stars (Decressin et al., 2007)).

A particularly intriguing aspect is that a minority of GCs shows also abundance variations in heavy-elements (i.e. Fe). These clusters, denominated "iron-complex" GCs are (Johnson et al., 2015): ωCen, M22, M2, M54, NGC 1851, NGC 5286, NGC 5824, Terzan 5 and M19. These clusters, which

present multiple photometric sequences and both light and heavy elements abundance variations, have different ratios between metal-poor and metal-rich populations (Johnson et al., 2015; Milone et al., 2015), and in some cluster the metal-poor component is more concentrated than the metal-rich one, in some clusters is valid the opposite (Bellini et al., 2009; Carretta et al., 2011). In chapter 6 we will focus specifically on a possible formation scenario for the "iron-complex" globular clusters.

The surface brightness profiles of globular clusters is well described by the 3-parameters empirical King model (King, 1962). The King profile is characterised by a small, high constant density central part ("core"), and a distributed, less dense outer region. This two profile components are identified by two parameters respectively: the core radius, $\mathrm{r_c}$, defined to be the radius at which the surface brightness has fallen to half its central value and a limiting radius, called $\mathrm{r_t}$, also called tidal radius (King, 1962). The underline assumption behind this is that the the cluster has a finite maximum radius ($\mathrm{r_t}$), beyond which the gravitational influence on the stars by the star cluster is negligible respect to the one by the hosting galaxy (Binney & Merrifield, 1998). The third parameter of the model is a number factor (k). The resulting surface density expression is given by (King, 1962)

$$f = k \left\{ \frac{1}{[1 + (r/r_c)^2]^{\frac{1}{2}}} - \frac{1}{[1 + (r_t/r_c)^2]^{\frac{1}{2}}} \right\}. \tag{2.2}$$

The ratio of the tidal radius and the core radius defines the concentration *c* as

$$c = log(r_t/r_0) \; ; \tag{2.3}$$

(King, 1962), this provides an immediate measure of the cluster's morphology. The King models are, therefore, effectively a one-parameter family which can be identified through the concentration c (or equivalently the central dimensionless potential $\mathrm{W_0}$, see chapter 4).

However, even though many globular clusters present central cores and are so well fitted by King profiles, some clusters ($\sim$ 20% (Djorgovski & King, 1986; Trager et al., 1995)) show rather central cusps in the surface brightness profile (Figure 2.3).

This is generally ascribed to the core collapse phase (Hénon, 1961; Lynden-Bell & Wood, 1968; Spitzer, 1975). A full description of this mechanism can be found in Section 4.2.3. However, alternative mechanisms to produce a cusp were also investigated, mainly the presence of a central

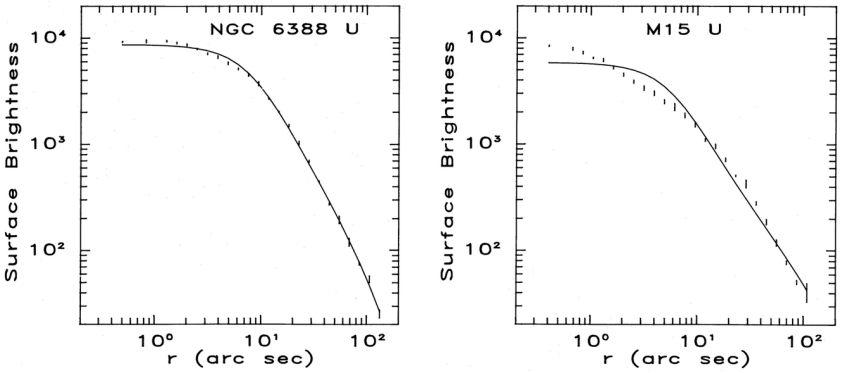

Figure 2.3: Surface brightness profile for NGC 6388 and M15. The solid line indicate the best-fit King model, the dashed line is the observed profile. From Lugger et al. (1987).

massive black hole (Baumgardt et al., 2004; Guhathakurta et al., 1996; Kamann et al., 2016; Noyola & Baumgardt, 2011) Such very high density values (up to $10^4\ \mathrm{M_\odot pc^{-3}}$) reached in the cores (or cusps) of globular clusters make them among the most crowded places in a Galaxy. This fact seems to indicate globular cluster as the main birthplace of many so-called *stellar exotica* (blue stragglers, X-ray binaries, cataclysmic variables), since the formation of these objects is possible only in highly collisional environments (Verbunt, 2007). Blue stragglers, stars on the MS beyond the turn-off point, may be formed via mergers or mass transfer between lower-mass MS stars. X-ray binaries and cataclysmic variables are probably produced via encounters between compact objects (white dwarfs) and either single stars or binaries (Davies, 2005).

An important assumption made by the the King profile is to consider a spherical distribution of stars, which is a good first-order-approximation. However, flattening has been detected in several galactic globular clusters (Chen & Chen, 2010; White & Shawl, 1987) and could be explained by several physical factors, such as pressure anisotropy, external tides (van den Bergh, 2008) or internal rotation (Fabricius et al., 2014). This last is observed in several GCs (Anderson & King, 2003; Bellazzini et al., 2012; Kimmig et al., 2015; Lardo et al., 2015; Pancino et al., 2007; van den Bosch et al., 2006) (solid body within the half-mass radius, differential outside (Bianchini et al., 2013; Fabricius et al., 2014; Meylan & Mayor, 1986)). Rotation can in principle arise from a variety of mechanisms (second-generation disk-

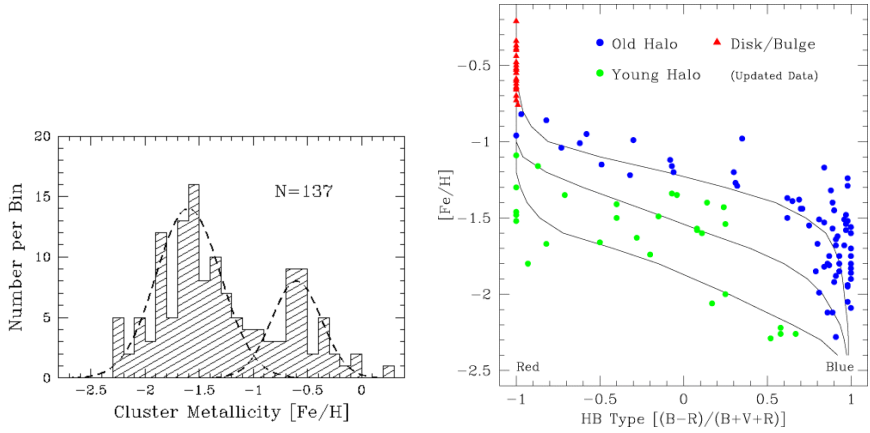

Figure 2.4: *Left:* Metallicity distribution for Galactic globular clusters with available [Fe/H] values (137 objects). From Harris (2001). *Right:* HB-type versus metallicity diagram of 137 Galactic globular clusters. The sample is divided in subclasses following Mackey & Gilmore (2004); Zinn (1993). The overplotted isochrones are 1.1 Gyr and 2.2 Gyr younger than the top isochrone. From Mackey & Gilmore (2004).

like structure, initial violent relaxation, merging)(Bianchini et al., 2015; Mastrobuono-Battisti & Perets, 2013; Vesperini et al., 2014). Chapter 6 of this thesis specifically explores the merging scenario between globular clusters and derives some the kinematics signatures visible in the merger output.

So far, we considered the characteristics of single globular clusters, however much interest towards these objects comes from their properties as a system. As already mentioned, at the moment the Milky Way counts 157 detections of globular clusters (Harris, 2010), the best estimate for the total population being $\sim$ 180 objects (Ashman & Zepf, 1998). The most striking feature and most studied topic of discussion is the bimodality of the cluster metallicity distribution. If we look at Figure 2.4 (left panel) we can clearly distinguish two main peaks in the distribution, well fitted by two gaussian distributions of centroids [Fe/H]$\sim$ -1.6 and [Fe/H]$\sim$ -0.6 (Harris, 2001). The trough between the two distributions is located around [Fe/H]$\sim$-0.8 (Zinn, 1985).

These two distributions have been associated with two distinct cluster populations, *metal rich clusters*, [Fe/H] $>$ -0.8, and *metal poor clusters*,

[Fe/H] $<$ -0.8. By studying the correlation between metallicity and galactocentric distance (R_{GC}) is evident the scatter in metallicity at any radius. The presence of a correlation between metallicity and distance from the Galactic centre is a foggy issue: there is clearly no trace of correlation among clusters located at $R_{GC} > 8$ kpc (Searle & Zinn, 1978), while a very weak negative gradient in metallicity is reported for objects with R_{GC} <7kpc (Zinn, 1993). It is however clear that the metal richer population is confined to R<10 kpc (Grebel, 2016), while the metal poorer one extends from close to the Galactic centre to over 100 kpc (Mackey & Gilmore, 2004). This different spatial dichotomy classifies the two populations even further in a "halo" population, consisting of metal-poor clusters, occupying mainly the galactic halo in an almost symmetrically spheric distribution (Ashman & Zepf, 1998) and a "disk" population, composed by metal-rich clusters, confined mainly to the thick disc (Zinn, 1985) and bulge (Minniti, 1995) of the Galaxy.

A further classification, based on the metallicity and HB morphology (Zinn, 1993), depicted an even more complex situation: the halo clusters exhibit a clear dispersion in their HB morphology at given metallicity (see Figure 2.4, right panel). In fact, most of the inner halo clusters define a tight relationship between [Fe/H] and the HB index (Lee et al., 1994)), while many of the clusters in the remote outer regions of the halo show much redder HB morphologies for a given abundance (Brodie & Strader, 2006). This effect can be justified considering the cluster age as extra parameter and explain the redder HB morphology at constant metallicity as consequence of younger age of the cluster (Brodie & Strader, 2006). Therefore, the two halo subsystems are defined: "young halo" and "old halo" (Zinn, 1993). The age difference between these two groups is $\sim$ 1.5 Gyr (Mackey & Gilmore, 2004).

According to recent results (Mackey & Gilmore, 2004) it is clear that the metal-rich clusters (37 objects) are strongly concentrated towards the Galactic centre (see Figure 2.5), with almost the totality lying very close to or within $R_{GC} = 6$ kpc (specifically 60% of these lies within 3 kpc, consistent with bulge population, the rest with thick disk population). These objects also form a very flattened system, (with 90% of objects having distance above or below the Galactic centre $<$ 2 kpc) and have disc-like kinematics, rotating around the Galactic centre ($V_{rot} \sim 190$ km/s and $\sigma_{los} \sim 60$km/s according to Mackey & Gilmore (2004), Harris (2001) reports $V_{rot} \sim 90$km/s for the bulge population and $V_{rot} \sim 150$ km/s for the disk population).

The majority of old halo members (total: 70 objects) is found within 6 kpc (with some overlapping with the bulge population) and the rest is any-

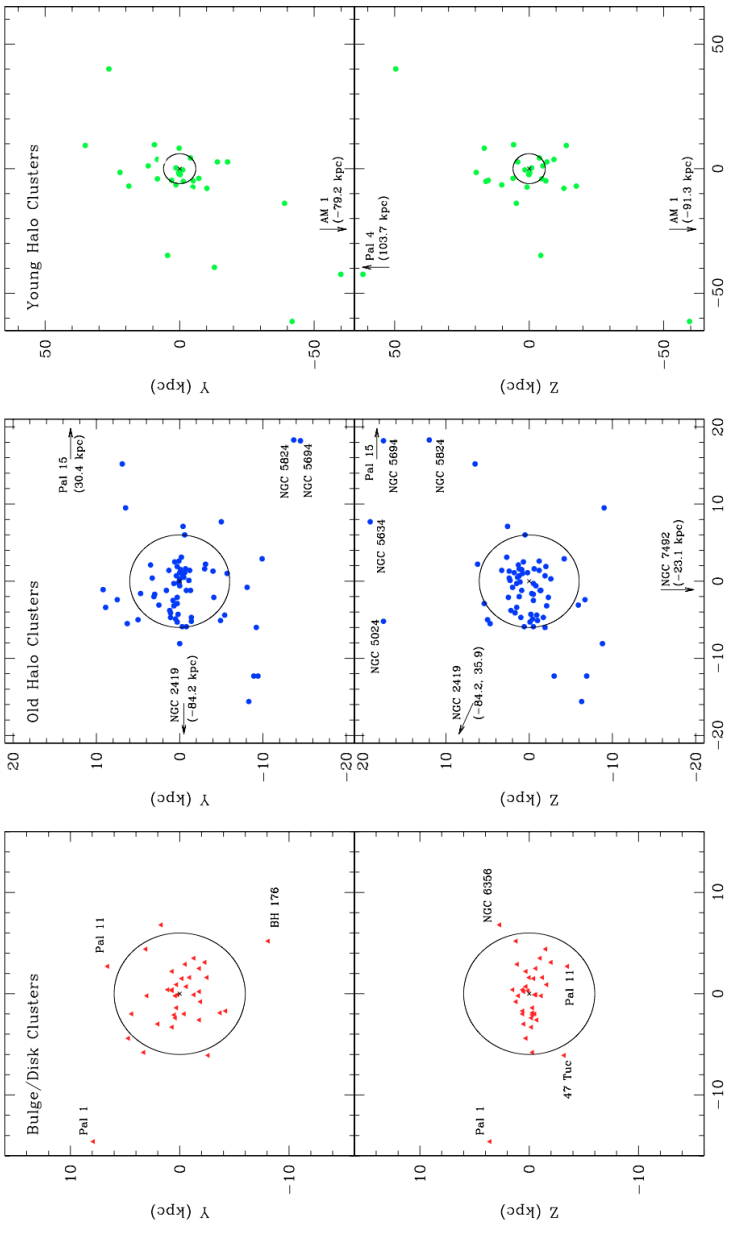

Figure 2.5: Spatial positions of globular clusters in each of the Galactic subsystems (disk, young and old halos) in Galactocentric cartesian coordinates. In each diagram a circle of radius equal 6 kpc is marked. From Mackey & Gilmore (2004).

way within 30 kpc (with only 2 exceptions). They occupy the inner halo of the Galaxy (Mackey & Gilmore, 2004). The young halo clusters (30 objects), according to Zinn (1993), occupies the outer halo, with no cluster within 6 kpc and 5 objects over 40 kpc. However, according to Mackey & Gilmore (2004) the young halo extends from the bulge region (with 5 objects within 6 kpc) to the remote halo (20 objects between 7 and 40 kpc, the rest over 40 kpc) (see Figure 2.5, last panel on the right).

From the kinematical point of view, both the old and young halo display halo-like properties, with a roughly isotropic orbit distribution (as a system). In particular the young halo is charachterized by large energetic orbits of high eccentricity and intermediate inclination (including retrograde motions) (Mackey & Gilmore, 2004). This is in line with Zinn (1993) who describes young halo's rotation as consistent with zero and velocity dispersion to be very large ($\sim$150km/s). Old halo clusters show analogous kinematical feature but have much smaller total energies and eccentricities (Mackey & Gilmore, 2004), as reported by Zinn (1993) $\mathrm{V_{rot}} \sim 70$ km/s and $\sigma_{\mathrm{los}} \sim 90$ km/s.

Outside the Milky Way, globular clusters are found in several galaxies in our Local Group (precisely in 12 over 76 members). The metallicity bimodality seems to be a common property, but the different systems differ substantially in terms of number, specific frequency [2], kinematics and spatial distribution of globular clusters. Figure 2.6 gives a short summary on the main properties of the different globular cluster systems in our Local Group: for a full review see Grebel (2016) (from which the table was taken).

We can see that the variance in number of clusters spans almost 3 orders of magnitude as well as the specific frequency. Not all galaxies in the group exhibit a rotating population of cluster, but many show the duality in the halo subpopulations. In some cases highly eccentric orbits of the outer halo clusters (MW) or association with stellar tidal streams (M31) suggest an accretion origin for the outer halo globular cluster population (Grebel, 2016). In Galactic satellites the core radius size of globular clusters is compatible with the one of the Milky Way young halo population, much larger than the average value for most of Galactic bulge, disk and old halo clusters, hence supporting the hypothesis of a dwarf galaxy origin for young halo globulars (Grebel, 2016).

The study of globular clusters extended to many extragalactic systems beyond the Local Group, ranging from dwarf to giant galaxies, covering

[2]The specific frequency ($\mathrm{S_N}$) of a galaxy is defined as number of clusters ($\mathrm{N_{GC}}$) per unit galaxy luminosity ($\mathrm{M_V}$), $\mathrm{S_N} = \mathrm{N_{GC}} 10^{0.4(\mathrm{M_V}+15)}$ (Harris & van den Bergh, 1981). It quantifies the efficiency of a galaxy to create and/or retain globular clusters.

Galaxy	Type	M_V	N_{GC}	S_N	Remarks
M31	SA(s)b	−21.2	> 700	> 2.3	Rotation, [Fe/H] gradient, on avg. younger; accretion
Milky Way	SBbc	−20.9	∼ 160	∼ 0.7	[Fe/H] gradient, Na–O anticorrelation, accretion
M33	SA(s)cd	−18.9	75–98	2–2.7	Outer halo stripped?
Sgr	dSph(t)	∼ −15.0	5–11	5–9	"Young" & "old halo" GCs; Na–O anticorrelation
For	dSph	−13.1	5	22.8	"Young" & "old halo" GCs; multiple pop.? [Fe/H] grad.
NGC 205	dE5, N	−16.4	∼ 6	1.7	"Young" & "old halo" GCs; [α/Fe] enhanced
NGC 185	dE3	−15.6	∼ 7	∼ 4	"Young" & "old halo" GCs; ∼ solar [α/Fe]
NGC 147	dE5	−15.1	8–10	∼ 7–9	Near-solar [α/Fe]?
LMC	SB(s)m	−18.5	15–16	0.6	Rotation, "young" & "old halo", Na–O, [α/Fe] spread
SMC	SB(s)mp	−17.1	1	0.1	Younger than oldest MW & LMC GCs, high ellipticity
NGC 6822	IB(s)m	−16.0	8	3	Some GCs: high ellipt., one w. solar [α/Fe]. No rotation
WLM	IB(s)m	−14.4	1	1.7	Na–O anticorr.? [α/Fe] enhanced, high ellipticity

Figure 2.6: Summary of the main properties of globular cluster systems in the Local Group. From Grebel (2016).

the full Hubble sequence of morphological types. The presence of dark matter in globular cluster has been excluded due to low values of mass-to-light ratio (< 2.5) observed (Baumgardt et al., 2009; Bradford et al., 2011) and predicted from dynamical modelling (Mashchenko & Sills, 2005; Moore, 1996). Metal-poor and metal rich populations have been found in most galaxies (Brodie et al., 2012), specific features of both populations are linked to the differences among parent galaxies. The discussion of the specific properties of different environments is beyond the goals of this thesis, therefore we refer to the work by Brodie & Strader (2006) for a full review.

The presence of different metallicity subpopulations in such old stellar systems provide some of the strongest constraints on hierarchical galaxy formation theories.

Before this duality was established, the main paradigm for galaxy formation was a simple monolithic-collapse model: a galaxy forms out from the monolithic collapse of a gas cloud which cools and contracts (Ashman & Zepf, 1998). The onset of star formation enriches the gas and yield to a metallicity gradient in the stellar populations. The absence of metallicity gradient in globular clusters (Searle & Zinn, 1978) gave space to alternative models describing the galaxy formation as a chaotic assembling process of gaseous clumps. The observed bimodality made clear that alternative scenarios to the monolithic collapse were necessary.

The major merger scenario (Ashman & Zepf, 1992) predicts that the bimodal cluster population is a result of major mergers of disk galaxies: metal-poor GCs are donated by the progenitor spirals and the metal-rich GCs are formed in the gas-rich merger. Forbes et al. (1997) proposed the multiphase dissipational collapse scenario, in which the metal-poor GCs were formed in gaseous fragments in early epoch and their formation was then truncated (by feedback or reionization) at high redshift. Metal-rich globular clusters formed in a second phase, together with the bulk of the galaxy field stars. An alternative to this is the so called dissipationless accretion scenario (Côté et al., 1998), according to which the metal-rich GCs were formed in situ in a massive seed galaxy, whereas the metal-poor GCs were acquired in the dissipationless accretion of neighboring lower-mass galaxies (Brodie & Strader, 2006).

All these scenarios present at the same time precious insights and observational difficulties, nevertheless they all point in the direction of hierarchical galaxy formation, either through mergers or accretions, which is the only way to account for a bimodal metallicity distribution of globular clusters. The current most accepted scenario proposes that metal-poor global clusters form in high-redshift low-mass dark matter halos (Boley

et al., 2009; Moore et al., 2006; Peebles, 1984),their formation being truncated by reionization (Beasley et al., 2002; Santos, 2003) (but very recent results seems to challenge this picture, see Forbes et al. (2015)), whereas metal-rich globular clusters form in the subsequent dissipational merging responsible for the formation of the parent galaxy as well (Puzia et al., 2005; Strader et al., 2005).

Despite some success of the theory, the formation of globular cluster, and in particular the connection with galaxy formation, is still a very open issue and a global model is far to be presented (Brodie et al., 2014; Forbes et al., 2015; Richtler, 2013). Moreover, a satisfying theoretical formation scenario should also be able to bridge between the formation of globular clusters as a system and as single structures, reproducing some of the internal features previously described (structure, kinematics, stellar populations). Some of the latest results seem promising (Renaud et al., 2017), but the whole puzzle is far for being solved, with the impression that for every piece which fits in, the others get smaller and more numerous.

2.2. Open clusters

If we go back to the image of our Galaxy as representative of the average society, open clusters would definitely be a normal adult person, between 30 and 60 years old, with a normal life, a wife/husband, two kids and a lot of Ikea furniture. As much as any human city is full of this type of person, as well the galaxy is flooded of open clusters. A typical example of open cluster can be seen in Figure 2.7. We are going to present here only the most noticeable characteristics of open clusters, a more detailed review can be found in Moraux (2016).

The Galactic open clusters which have been catalogued are about 2000 (Dias et al., 2012), but, taking as volume density ~ 1000 clusters kpc^{-3} (Clarke et al., 2015), we expect the total population of open clusters in the Milky Way to count about 10^5 members (3×10^4 according to Portegies Zwart et al. (2010)), 3 orders of magnitude more than the expected number of globular clusters in our Galaxy.

Another clear difference from globular clusters is the location: from Figure 2.8 it is clear that, while globular clusters are distributed in a mostly spherical configuration, both in the halo and disk of the Galaxy, open clusters occupy only the disk, with the older clusters extending in the outer parts of it, and the younger ones populating mainly the think disk with scale height 50-300 pc (Röser et al., 2010). Their location close to the plane of the Galaxy represents one of the main difficulty for observers, due to the

Figure 2.7: Open Cluster. Wide field image of the Jewel Box cluster (NGC 4755) taken with the Wide Field Imager (WFI) on the MPG/ESO 2.2-metre telescope at ESO's La Silla Observatory. The field of view is 20 arcminutes across, roughly 12 pc. The picture is based on images obtained through B, V and I filters. Credits: ESO

contamination from unrelated field stars and heavy extinction (Binney & Merrifield, 1998).

According to Piskunov et al. (2008) the majority of open clusters have present-day masses between 100 and 10^4 $M_\odot$, with average around 700 $M_\odot$. The average initial cluster mass is estimated $\sim 4500 M_\odot$ (Zinnecker, 2010). The gap between the two values reveals how much mass loss a cluster experiences; indeed the 50% of field stars in the solar neighbourhood is thought to originate from disintegrating open clusters (Zinnecker, 2010). Of particular relevance is the origin of the field OB stars. Indeed, some of these are the so called *runaway* stars, with this meaning they are high velocity stars (>30 km/s), which are thought to originate because ejected from massive binaries (after the companion exploded as supernova) or ejected

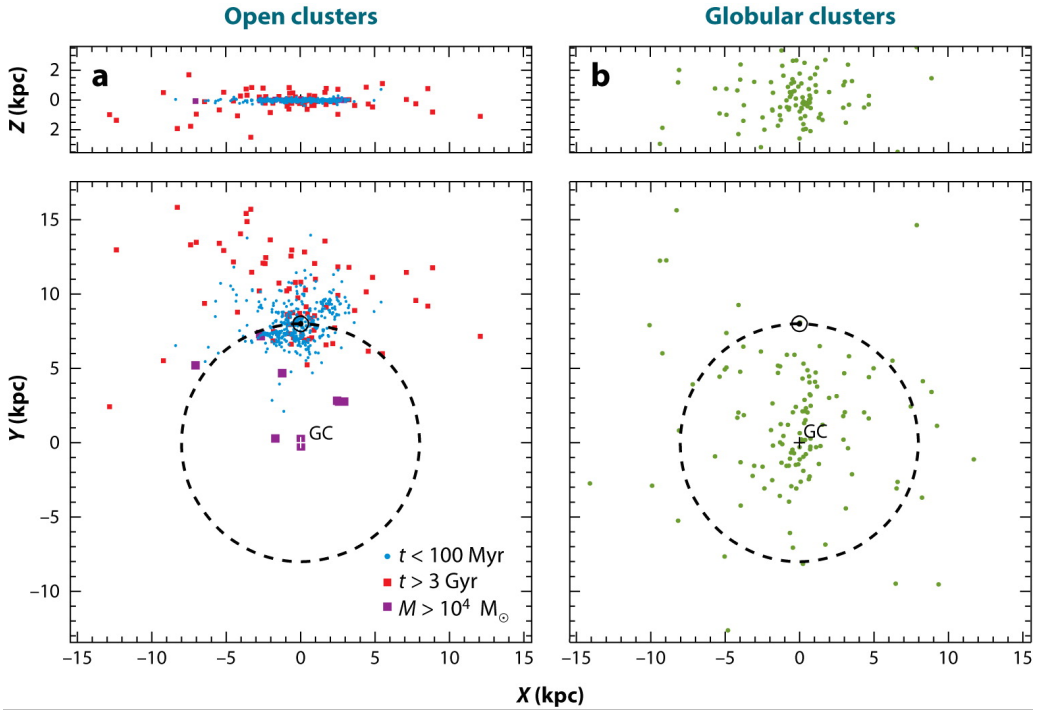

Figure 2.8: Spatial distribution of open (left) and globular (right) clusters in the Milky Way. Top panels are edge-on view, lower panels face-on view. From Portegies Zwart et al. (2010).

from very dense clusters due to internal dynamics. This phenomenon has a direct impact also on galactic scales, since these massive stars on the run constitute a widely effective supernova energy input directly in the interstellar medium (Zinnecker, 2010). Schilbach & Röser (2008) found that the origin of almost 80% of O-field stars can be traced back to some young open cluster. In Section 5 we will come back to this topic, and estimate the number of ejected stars from strong encounters in emerging star clusters.

The difference between open and globular clusters becomes obvious by looking at a typical CMD (Figure 2.9, top). The main feature in the plot is a very extended and clear MS, which stretches up to the bright blue stars at the upper end of the sequence (Binney & Merrifield, 1998). The presence of these massive, short-lived stars is emblematic of the young ages of most open clusters. Moreover, in some diagrams, the bottom end of the MS exhibits broadening due to the presence of very low mass stars still on their Hayashi pre-main sequence tracks: this implies that the age of cluster is less than the time needed for these stars to reach the MS (Binney & Merrifield, 1998).

If we compare the CMD from different open clusters (see Figure 2.9, bottom), the main difference with a group of globular clusters, is the variegate positions of the turn-off points in the diagram. This is revealing of the wide range of ages characterising open clusters. According to Piskunov et al. (2006) the age distribution spans from few Myr[3] to few Gyr, with average age around 300 Myr. The oldest objects are dated $\sim$ 10 Gyr (Salaris et al., 2004). This significant age spread reveals that open clusters are continuously forming in our Galaxy. On the other hand it is know since decades that there is an under-abundance of old open clusters, with age $>$ 1Gyr (Oort, 1958; Wielen, 1971). This fact has been explained as the result of disruptive encounters with massive molecular clouds in the Galactic disk (Gieles et al., 2006b; Spitzer, 1958). The fact that most old open clusters are found in the thick disk, at larger distance from the Galactic plane (see Figure 2.8) represents a valid evidence of this scenario. Despite being the minority, old open clusters represent a fundamental tool to study the early disk evolution (Friel, 1995).

The spatial distribution of a classic relaxed open cluster can generally be described by a multi-mass King radial profile (Clarke et al., 2015), even though many objects cannot be properly described by spherical distribution due to loss of regularity (Binney & Merrifield, 1998).

The younger age of open clusters, compared to globular clusters, con-

[3] $\sim$ 10 Myr, which is larger than the primordial gas dispersal timescale, hence open clusters do not have generally areas of active star formation (Clarke et al., 2015).

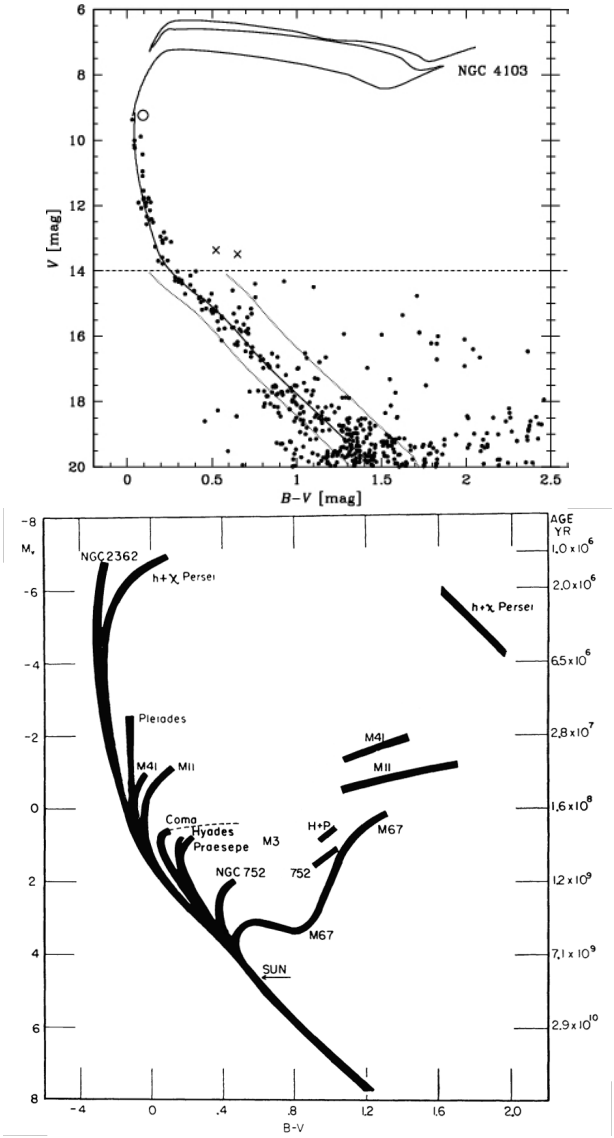

Figure 2.9: *Top:* Colour-magnitude diagram of NGC 4103. The solid line is the best fit isochrone. From Sanner et al. (2001). *Bottom:* Composite colour magnitude diagram for several open clusters. From Sandage (1958).

vert into a rich stellar mass range, which makes them the perfect environment to investigate mass segregation, as result of energy equipartition and dynamical friction (a detailed description of these mechanisms in given in Section 4.2.4). As we will see in Chapter 4, the timescale of energy equipartition is the two-body relaxation time, which is in this case comparable with the age of the system, therefore relaxation effects are expected to be relevant [4]. By analysing cumulative distributions of different mass range groups it is clear that open clusters are mass segregated (Mathieu, 1984), that is massive stars tend to have a greater central concentration. Of course this is especially evident for older open clusters (Binney & Merrifield, 1998).

Another possibility to study the presence of equipartition is analysing proper motions, to investigate whether low-mass stars are characterised by systematic higher velocity than massive stars. This approach is extremely difficult technically due to two main reasons: the typical velocity dispersion of open clusters is quite low, $\sim$ 1-3 km/s and the fraction of stars in binary systems is estimated to be 30-50% (Binney & Merrifield, 1998; Clarke et al., 2015). The low value of velocity dispersion requires highly accurate measurements, but at the same time the high number of unresolved binaries affects negatively the velocity dispersion estimate.

Indeed, it is currently not established whether open clusters show traces of equipartition. Numerical simulations find that simulated clusters become strongly mass segregated but the local velocity dispersion does not change depending on the stellar mass (Spera et al., 2016). Gaia mission and Gaia ESO survey are expected to provide together proper motions and accurate line-of sight velocities for about 100 open clusters. This will help to better clarify this aspect.

In addition, young open clusters provide IMF (initial mass function) studies much valuable information. Effects of stellar and dynamical evolution are relatively small on the younger objects, therefore the observed luminosity function can be considered a proxy for the initial luminosity function, hence the IMF. According to the review of Bastian et al. (2010), by comparing different mass functions from young open clusters, associations and the field, it turns out that the majority shares a similar IMF, characterised by a Salpeter power law for the high-mass part and a log normal or

[4] As we will explain in Chapter 4, for all star cluster categories the relaxation timescale is comparable with the typical age, hence two-body relaxation interactions play a role, therefore we could expect to detect mass-segregation also in globular cluster. Some globular clusters are indeed mass segregated. However the advantage of open clusters respect to globular clusters is that they still have massive stars which did not evolve and lower densities, which allow a better observation of the central part.

shallower power law for lower masses (De Marchi et al., 2010). However, the shape and universality of the IMF is still an open issue.

Open clusters have long been recognised as important tools in the study of the Galactic disk, especially to determine the spiral arm structure and to map the rotation curve of the Galaxy (Bragaglia, 2010; Friel, 1995). Detailed kinematics of ~ 500 open clusters of our Galaxy considered as a system were released by Dias et al. (2002, 2012). Piskunov et al. (2006) calculated the open cluster orbits and identified four open cluster groups, whose members share the same kinetic behaviour and age. Wu et al. (2009) calculated three different axisymmetric Galactic potentials and computed the orbits of over 400 open cluster up to 5 Gyr old. They found that the velocity ellipsoid derived is consistent with a thin-disc population and the velocity dispersion increase with the age of cluster subsamples.

Most recent results point towards an heterogeneous population of open clusters, which seems to be divided into two main groups differing by their mean parameters, properties, and origin (Gozha et al., 2012; Pang & Shu, 2010). The first group includes the clusters formed from interstellar matter of the thin disk with nearly solar metallicity ($[Fe/H] \gtrsim 0.2$) and almost circular orbits (i.e. crown orbit (Vande Putte et al., 2010)), whose short distance from the Galactic plane is consistent with field stars (Gozha et al., 2012) . The second group includes outlier clusters characterised by high eccentricities and/or large distance from the disk plane and/or lower metallicity (Vande Putte et al., 2010).

Theoretical computation of the orbits birthplace proved that the bulk of the clusters from both groups were formed within a Galactocentric radius of 11 kpc and closer than 180 pc from the Galactic plane (Reddy et al., 2016; Vande Putte et al., 2010). Subsequently, due to larger eccentricities and initial velocities, the outlier clusters moved from they birthplaces to the current location beyond 12 kpc, where the survivability rate is higher due to larger excursions from the Galactic midplane.

For the most peculiar clusters, to which the above consideration does not apply, the main hypothesis is that they could have extra-Galactic origin (e.g.Be 20, Be 29, Be 31, Be 33, NGC2158, 2420, 7789, and IC1311), resulting from the interaction of an external high velocity cloud with the interstellar matter. Others may be due to globular cluster impact on the disk (e.g.NGC6791, 1817, and 7044), or could be generated through merger (Gozha et al., 2012; Vande Putte et al., 2010).

There has been evidence of a radial metallicity gradient for the Galactic open cluster system (Bragaglia, 2010; Frinchaboy et al., 2013; Pancino et al., 2010). Reddy et al. (2016) confirms that open clusters present a constant

steep decline of metallicity out to a distance of 12 kpc from the Galaxy centre, followed by a change of slope and further flattening out to the entire radial extent in the outer part. The clusters within 12 kpc lie close to the Galactic mid plane, are younger than 1.5 Gyr and have thin disk kinematics, the cluster beyond 2 kpc have $[Fe/H] < -0.2$ dex, thick disk kinematics and are between 1 and 8 Gyr old. However, as the authors point out, this bimodality suffers definitely of selection effects.

2.3. Young star clusters

Young people are the most unpredictable and surprising. That is why I decided to dedicate an extra section to young star clusters, which in our beyond-the-mirror society would represent inexperienced, youthful, dreamful, under-30-year-old people. Clearly, like all sensible categories, boundaries must be taken "cum grano salis", which means at the edge open and young clusters overlap, and effectively the second one is partially included in the first. But it is not surprising at all that some people are adults already at 20 years old and some probably will never be.

"Young" is however rather generic. During youth the timescale over which events happen is extremely short, time flies terribly fast, every upcoming year will be completely different from the previous one, and being 10 or 18 or 29 years old is *not at all* the same. And of course this is valid for us as much as for our systems of stars. Therefore I articulated this part in three other subsections: stellar associations, young massive clusters and embedded clusters.

2.3.1. Stellar associations

It will be soon clear why I think stellar associations can be considered "immature young adults": they are young-ish, they have still many elements of recent on-going star formation but the bulk of explosive activity is over, and there are no hints which suggest whether they will ever become serious, stable, solid open clusters.

A stellar association is a very low density, $0.2 \mathrm{stars/pc}^3$ (slightly higher than field stars density) (Ambartsumian, 1947; de Zeeuw et al., 1999), and loosely bound (or unbound) system of stars. We refer to Blaauw (1958) for a classic review. Despite exhibiting some similar features, in the past they were considered completely different from open clusters, while the modern community sees a smooth transition (or lack of transition, actually) and common origin between these two groups (Torres et al., 2010).

From a spatial point of view they are generally large and diffuse, with an amorphous shape and undefined boundaries. They typically can extend up to tenth of parsecs, e.g. the virial radii[5] of I Lac1, Lower Cen Crux, Ori Ia, Upper Cen Crux span between 30 and 60 pc (Portegies Zwart et al., 2010). Associations usually counts very few to hundreds members. They are usually distinguished from field stars due to a higher fraction of star belonging to the same spectral type, indeed associations are usually identified as "OB associations" (Ambartsumian, 1947), "T associations" (Ambartsumian, 1947) or "R associations" (van den Bergh, 1966).

OB associations are aggregations of very young, massive O or B stars. They are usually populated by 10-100 detected massive members and hundreds of lower mass stars. The mass of single OB stars ranges between 10 and 70 $\mathrm{M}_{\odot}$, hence the total solar mass can reach $10^3\mathrm{M}_{\odot}$. There are around 70 catalogued OB associations in the Milky Way, the overall expectation is >1000 (Janes, 2000). Their age, ranging between 2-20 Myr (Pfalzner, 2009), is also usually slightly larger than the timescale for natal gas to be dispersed, but in most structures there is still evidence of ongoing star formation (Clarke et al., 2015), which means there is still some gas. A milestone in this field is the work by de Zeeuw et al. (1999), a comprehensive census of the stellar content of the OB associations within 1 kpc from the Sun, based on Hipparcos positions, proper motions, and parallaxes.

T associations, instead, contains T Tauri stars, that are low mass ($< 3\mathrm{M}_{\odot}$) pre-main sequence stars (of subsequent spectral type F,G,K,M), still in the contracting phase. The classic example is represented by the Taurus-Auriga association which is 140 pc far from the Sun, around 1 Myr old, does not show any presence of massive star and presents a clumpy distribution of stars, which seems to follow the gas morphology.

Finally, R associations are agglomerations of young, intermediate-mass stars (3-10 $\mathrm{M}_{\odot}$) embedded in a reflection nebula. The stars in this case are not massive enough to disperse the gas around and their light is actually reflected by dust.

The typical velocity dispersion of associations of young stars is $1-3$ km/s, an order of magnitude lower than the dispersion of field stars. Therefore associations can be detected also kinematically. Through proper motions and radial velocity surveys, stars which share the same bulk motion can be identified as members of the association (de Zeeuw et al., 1999).

Pfalzner (2009), taking into account only massive clusters ($> 10^3\mathrm{M}_{\odot}$) distinguishes two sequences in the size-density diagram, corresponding to dense young clusters (see next section) and associations (or "leaky clus-

[5]See Section 4.1.1 for a definition of virial radius.

ters"). Gieles & Portegies Zwart (2011); Portegies Zwart et al. (2010) found that a more quantitative distinction can be obtained with the ratio $\mathrm{age}/\mathrm{t_{dyn}}$, where t_{dyn} is the dynamical time of the system (see Section 4.2.1). The threshold value between dense clusters and associations was found to be $\mathrm{age}/\mathrm{t_{dyn}} \sim 3$. Associations have on average 0.5 and in general <1 (Portegies Zwart et al., 2010), which is a classic indication of the unbound state of these structures (Gieles & Portegies Zwart, 2011).

All types of associations are characterised by some elements of very young star forming regions: very young massive OB stars, pre-main sequence stars or not expelled gas. They are all still connected with molecular cloud. The historical division between open clusters and associations, representing two different fundamental states 'bound' and ''unbound' has been recently revisited after realising that star formation proceeds throughout the molecular clouds with greater rates in some areas, producing bound structures where young stars are contained in a few pc size area and unbound structure somewhere else (Clarke et al., 2015). Associations are then the natural result of low efficiency star formation going on in molecular clouds without global densities high enough to remain bound (Clarke et al., 2015; Pfalzner, 2009).

2.3.2. Young massive clusters

Young massive clusters (YMCs) are the true face of youth (see Figure 2.11). In our parallel society, they are between 18 and 30 years old, massive, dense, too much self-confident, enthusiastic and full of energy. It is not yet clear what it will be their future, whether they will develop into open clusters, get disrupted in the galactic centre or become globular clusters. In any case, it will be glorious.

Young massive clusters are identified as bound star clusters, younger than 100 Myr and more massive than $10^4\mathrm{M}_\odot$ (see Portegies Zwart et al., 2010, for a review). The mass limit guarantees a survivability of at least 1 Gyr (see Section 4.2.2) and the age constrain limits them by the epoch at which a cluster enters the evolutionary phase dominated by stellar dynamics.

Figure 2.11 (Portegies Zwart et al., 2010) summarises the property of Galactic YMCs (all occupying the spiral arms or centre of the galaxy), in relation to the main other two groups we considered so far. In the Milky Way we can count ~ 10 objects which satisfy the mass/age requirements set. From the figure it is visually clear that they somehow fill the gap between open and globular clusters. Their half-mass relaxation times span

Figure 2.10: Optical and infrared image of the rich star forming region NGC 3603 and its massive compact central young star cluster (indicated in the square). Taken with the Advanced Camera for Surveys (ACS), B-V-I filters, on the NASA/ESA Hubble Space Telescope. The field of view is about 6 pc. Credits: NASA, ESA and the Hubble Heritage (STScI/AURA)-ESA/Hubble Collaboration

between 10Myr and 1 Gyr, and for the majority of them is $\lesssim 100\mathrm{Myr}$. They are the densest objects among the star clusters considered, since they have size-scales similar to the open clusters, but masses on the order of low-mass globular clusters: the resulting half-mass density ranges between 10^2 and $10^4\ \mathrm{M}_\odot/pc^3$.

YMCs are not an uncommon phenomenon but they numerously populate other galaxies in the Local group, i.e. LMC (Baumgardt et al., 2013), SMC (Mackey & Gilmore, 2003a), M31 (Fouesneau et al., 2014), M33 (Maíz-Apellániz, 2001) and in many other nearby spirals (Bastian et al., 2012; Konstantopoulos et al., 2013; Maíz-Apellániz, 2001; Ryon et al., 2015). Extragalactic YMCs can reach higher masses, $\sim 10^5 - 10^6\mathrm{M}_\odot$.

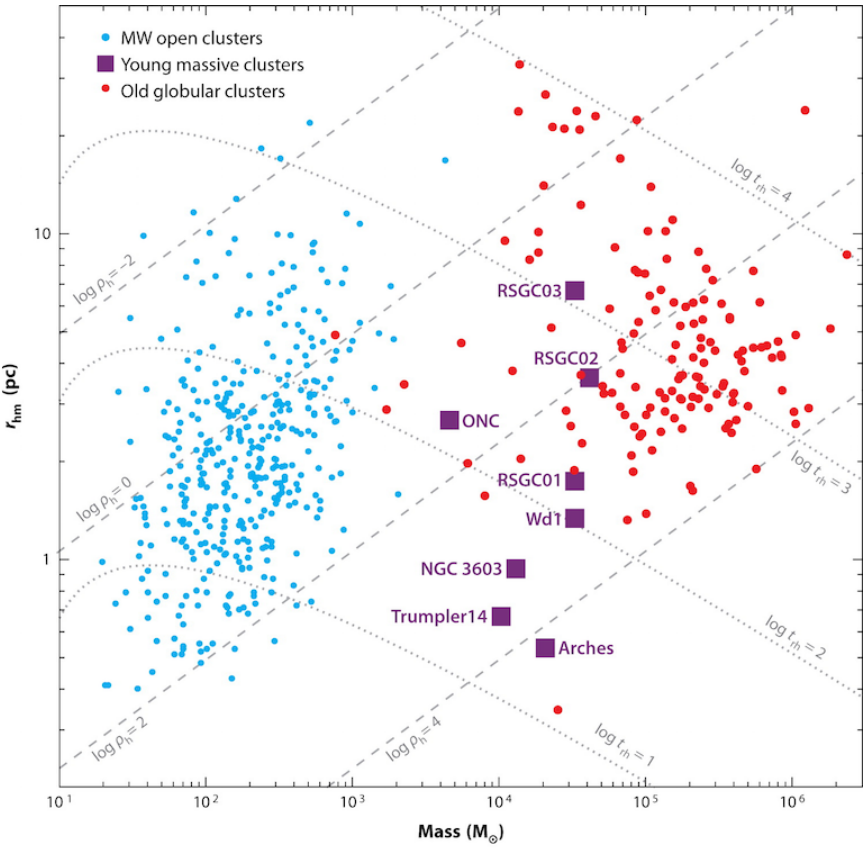

Figure 2.11: Radius - mass diagram of Milky Way open clusters (blue), young massive clusters (purple) and old globular clusters (red). Dashed and dotted lines represent constant half-mass density and half-mass relaxation time (Eq. 17), respectively. From Portegies Zwart et al. (2010)

Galactic YMCs are a particularly young population: indeed the oldest are only $\lesssim 20$ Myr (RSGC 02, 03) and the youngest (Arches, NGC3603 and Trumpler 14) only $\lesssim 2$Myr. This is probably to due to observational difficulty of observing older clusters, hence depleted of luminous stars, in situation of such high extinction and extra-stars contamination as in the Milky Way.

As we already pointed out, two-body relaxation timescale and lifetime are generally comparable in case of star clusters, therefore results of dynamical interactions, such as mass segregation, should be in principle clearly detectable.

If we now turn to YMCs the situation is quite puzzling. If we compare the *half-mass* relaxation timescale to the age of many Galactic and extragalactic YMCs, we find that in most cases the relaxation timescale is greater by at least one order of magnitude. However, at the same time, several observations tell us that most of these clusters are mass segregated (de Grijs et al., 2002; Gennaro et al., 2011; Gouliermis et al., 2004; Hillenbrand & Hartmann, 1998; Sana et al., 2010; Stolte et al., 2006, 2005). In these observations mass segregation is usually inferred through a variation in the slope of the mass function as a function of the distance from the centre of the cluster. Some selection effects in the central crowded regions could affect this analysis, since they tend to give shallower profile than in less crowded regions (Bastian, 2016)

The immediate justification was to explain this in terms of primordial mass segregation (Bonnell & Davies, 1998), i.e. the cluster formed massive stars preferentially closer to the centre, since it can not be of dynamical origin, being the cluster so young. However, numerical simulations showed that, if the star cluster formation process result from from mergers of subclumps, the level of mass segregation in the final merger remnant would be higher and consistent with observations, having the smaller clumps shorter relaxation times (Fujii et al., 2012; McMillan et al., 2007).

Olczak et al. (2011); Spera & Capuzzo-Dolcetta (2015) showed that mass segregation occurs very quickly for spherical systems with subvirial initial condition, even without substructures. It is indeed known that dynamically "cool" systems relax violently in few crossing times (Binney & Tremaine, 2008). For sake of clarity, we stress that mass segregation cannot be a direct outcome of violent relaxation (see Section 4.4 for details), however, in the short interval of time in which violent collapse takes place, a very dense core is created, which can contains half the mass of the stellar system in a radius of about one tenth of its initial size (Allison et al., 2009). In this dense core, the two-body relaxation time is much shorter and, de-

spite the dense core short lifetime, mass segregation can be reached, at least down to some mass M[6].

Following this reasoning, Allison et al. (2009); Pang et al. (2013); Sana et al. (2010), suggested a dynamical origin for mass segregation due to two-body relaxation in a dense phase in the cases of Orion Nebula Cluster, Trumpler 14 and NGC 3603. Using a minimum spanning tree algorithm, they estimated the degree of mass segregation and down to which stellar mass the cluster has segregated ($\sim 5, 10, 30 \mathrm{M}_{\odot}$, respectively), which compared positively with the theoretical expectations.

However, to date, the issue of primordial or dynamical mass segregation remain still highly debated and far from finding general agreement. The implication of a primordial nature of mass segregation would be a clear indication of the non-universality of the IMF, implying that the environment does affect the type of stars that are born in a given volume, at a given time (Bastian, 2016). We will come back to the topic in Chapter 5.

Studies of the structural parameters of YMCs in the LMC (Elson et al., 1987; Mackey & Gilmore, 2003b) showed that surfaces brightness profiles of young clusters are not well fitted by King profile, but rather by a core profile with power-law halos, with no evidence of truncation at large radii (cfr. globular cluster),

$$\Sigma(r) = \Sigma_0 \left(1 + \frac{r^2}{a^2}\right)^{-\frac{\gamma}{2}} , \tag{2.4}$$

known as EFF profile (Elson et al., 1987). The parameter *a* is a characteristic scale radius and γ was found to have values between 2.1. and 3.35 (Elson et al., 1987; Larsen, 2004; Mackey & Gilmore, 2003b).A proposed explanation for this difference between YMC and globular clusters is that the power-law profiles, with which all clusters were born, were then reshaped during cluster evolution, truncated by the tidal field (Bastian, 2016).

Quantitatively, the YMC populations in nearby spiral galaxies were found to have half-light radius distribution peaking near $\sim 3\mathrm{pc}$ and extending until 20 pc (Larsen, 2004; Ryon et al., 2015). The core radius distribution in M83 had a peak around 1.3 pc Ryon et al. (2015)

[6] We will see in Chapter 4 that the *half-mass* relaxation timescale is a cluster-wide estimate of the two body relaxation timescale: it considers the cluster in its totality, assuming virial equilibrium, and it takes into account "average mass" stars (see Section 4.2.1). Using the *local* two-body relaxation timescales can be more appropriate in out-of-equilibitum cases. Moreover, if the cluster is segregated only down to mass M, then the relevant timescale is indeed the dynamical friction timescale, which is lower than the two-body relaxation timescale by a factor depending on the mass M

Several studies argued that clusters do not exhibit a clear mass (or luminosity) - size relation (Larsen, 2004; Ryon et al., 2015; Scheepmaker et al., 2007). However, Portegies Zwart et al. (2010) showed how the very young clusters (< 10 Myr) actually appear to follow lines of constant density, while clusters > 10 Myr do not and have a slight trend of constant radius with mass. The lack or presence of correlation between mass and radius is relevant both in the context of cluster formation theories (since molecular clouds do follow scaling relation between mass and radius) (Portegies Zwart et al., 2010) and for the long-term survivability of clusters (since higher mass clusters will have higher density, hence higher chances to survive encounters with massive molecular clouds) (Bastian, 2016).

Global properties of YMCs can be derived from the numerous populations in the Magellanic Clouds and M31, M33, since they are less affected form extinction and they constitute a more complete group that Galactic YMCs, at least in terms of age, filling the gap between 20 and 100 Myr. Several studies confirmed that the clusters luminosity function, i.e. number of clusters per unit luminosity, follows a power-law relation with index ~ 2 ($\mathrm{dN/dL} \sim \mathrm{L}^{-\mathrm{alpha}}, \mathrm{alpha} \sim 2$) with a steepening at the bright end (Adamo & Bastian, 2015; Larsen, 2002). Inferring the clusters initial mass function from this is not straightforward since the luminosity changes dramatically in the first hundreds Myr of cluster lifetime and the cluster luminosity function is obtained from a non-coeval sample, anyway most studies indicate a power-law relation, truncated at high masses (Adamo & Bastian, 2015; Gieles et al., 2006a). As result, the functional form of the initial cluster mass-function seems to be a Schlechter distribution $\mathrm{dN/dM} = \mathrm{AM}^{-\beta}\exp(-\mathrm{M/M_*})$, with $\beta \sim 2$ and M_* between $10^5 - 10^6 \mathrm{M}_\odot$ (Bastian, 2008; Gieles et al., 2006a). The value of M_* seems to depend on the local galactic environment, meaning that in starburst galaxies (e.g. Antennae) is possible to form more massive cluster (thee truncation of the mass function is at higher masses) that in quiescent ones (e.g. Milky Way) (Portegies Zwart et al., 2010).

A final consideration is dedicated to the possible connection between very young and very old, YMCs and globular clusters. From the selection properties (mass range, hence long term survivability, high density) the first ones are sometimes indicated as possible younger version of the second ones. However, this hypothesis has still many pieces which do not match, starting from the mass function of clusters, which is a truncated power law for YMCs, while is a log-normal shape for globular clusters. A possible explanation for this could be that a large fraction of low mass clusters was disrupted due to interactions with the surrounding gas in this

primordial high density environment (Elmegreen, 2010; Kruijssen, 2015), interactions with clouds (Gieles et al., 2006a) or a combinations of various mechanisms (Fall et al., 2009).

However, recent studies of Fornax GCs indicate that, in the hypothesis that a fraction of metal-poor stars in field comes form early destroyed low-mass clusters, then this should be much higher than what it actually measured, which is fully compatible with evaporation from the 5 GCs already known in the dwarf galaxy (Larsen et al., 2012).

Another critical point is the presence of multiple populations. This has been repeatedly confirmed in globular clusters, while there has not been a direct detection in younger clusters yet (Krause et al., 2016). From the theoretical point of view also, none of the proposed scenarios for the multiple populations in GCs is clearly consistent with observations of YMCs. According to Cabrera-Ziri et al. (2014, 2016), in these young objects there is no trace of multiple bursts of star formation (they rule out age difference > 30 Myr) and in general all gas is expelled within few Myrs, leaving no possible reservoir with which a second generation could be built. However, some other studies report the presence of at least two distinct stars populations, with mean age spread of 10-30 Myr and different spatial configurations, in several YMCs (Beccari et al., 2015; De Marchi et al., 2013) . Anyway such a small age difference does not require an AGB/FRMS self-enrichment scenario to be explained, but could also be consistent with a merging origin or a single star formation scenario ("early disc accretion model"). With regards to the latter, Stolte et al. (2015) claims that there is also not much evidence of many stars with disc in nearby YMCs (Stolte et al., 2015), casting a doubt on the effective survivability of disc structure.

Moreover, the comparison between YMCs and GCs is particularly difficult (when dealing with multiple populations but also with the stellar mass function) because it involves two different mass ranges which don not intersect: generally $> 5\mathrm{M}_{\odot}$ for the first ones (it is challenging to observe $< 1\mathrm{M}_{\odot}$) , $< 0.8\mathrm{M}_{\odot}$ for the second ones. In addition the two groups differ also in terms of binary populations, making once more the comparison not direct. The binary fraction of globular clusters, which involves low-mass stars, is indeed much lower than that what found in YMCs ($\sim 50\%$), which is probably related partially with the higher number of high-mass stars.

In summary, even if YMCs and GCs share some basic similarities, there are not yet enough elements proving they are the same objects separated by 13 Gyr of evolution, nor that they are distinctly two different class of objects.

2.3.3. Embedded star clusters

Figure 2.12: WISE composite infrared image of the embedded cluster AFGL 490. Blue and cyan are infrared light at 3.4 and 4.6 μm, star emission, green and red are infrared light at 12 and 22 μm, emitted by warm dust. The image width scale is about 19 pc. Credit: NASA/JPL-Caltech/WISE Team

Embedded stars clusters are still babies, busy playing with their toys, hidden in the gaseous cloud which still surrounds them. They do not really care of the rest of the galaxy yet and the main expectation from them is that they eat and grow healthy. What they do, what they think, is kind of a mystery, because the gaseous blanket does not let much go through.

With ages lower than a 1 Myr, young clusters are usually still embedded in their parent molecular clouds (see Figure 2.12), and this is pretty much the description of an embedded cluster. The name is actually very "optimistic", meaning that at this stage there is no guarantee that they will necessarily evolve in bound open cluster, they could also become an unbound stellar association and disperse. What an embedded cluster will become, when it will become it and how exactly, are all unanswered thrilling questions so far and objects of much research.

The discovery of this kind of structures is linked to the development of

infrared and X-ray telescopes (Spitzer, WISE, Chandra, ...). These objects are indeed found in the most massive and densest cores of giant molecular clouds (see Section 3.1). Therefore, they suffer of very high extinction produced by the high column density of dust, which limits the detection of their stellar population at optical wavelengths. Dust extinction is significantly lower at longer wavelength, such as near-infrared. Moreover, dust grains absorb part of the UV radiation coming from newborn stars and reemit it in infrared, tracing the nebulous structure.

There is at the moment no comprehensive catalog, but roughly 100 embedded clusters have been described, even if the total number of Galactic embedded clusters is expected to be much higher. Lada & Lada (2003) estimated about 200 embedded clusters within 2.5 kpc from the Sun, implying roughly 10^4 of these in the whole Galaxy.

The most common criterion to identify embedded cluster is the one reported in Lada & Lada (2003), which should considered as reference review. They require these objects to be embedded in natal gas cloud and to be stable against tidal fields of the Galaxy and interstellar clouds, which signifies having about ten $0.5\mathrm{M}_\odot$ stars within a radius of 1 pc. Moreover, they expect a bound cluster to have relaxation time around 100 Myr, value taken as open cluster lifetime. This implies a sample of 35 stars per clusters.

With selection criteria, the typical median age of stars in clusters classified as "embedded" ranges between 1 and 3 Myr (Lada & Lada, 2003). The size scale varies from 0.5 pc to roughly 2 pc. They are generally very compact, although some spans vast regions and count hundreds of stars

The cluster mass distribution derived from the catalogue in Lada & Lada (2003) is interestingly flat in the range $50\mathrm{M}_\odot$ to $10^3\mathrm{M}_\odot$, which means that low-mass and high-mass clusters (in this range) contribute equally to the total mass of clusters. In other words, if a star is born in a cluster, it has the same probability to form in a $50\mathrm{M}_\odot$ as in a $1000\mathrm{M}_\odot$ cluster (Lada, 2010). The correspondent cluster mass spectrum is a negative power law with index ~ 2, in line with the value of the dense cloud cores spectrum and at the same time with the one of young clusters (Piskunov et al., 2008). Moreover, the mass function drops for cluster masses lower than $50\mathrm{M}_\odot$, which does not seem to depend on the selection biases of Lada & Lada (2003). Porras et al. (2003) found, indeed, that 80% of the total number of stars in clusters belong to clusters with 100 or more members, which corresponds to the peak of $50\mathrm{M}_\odot$ in the mass function.

From the structural point of view there appear to be two main types of clusters. In fact, some exhibit extended, irregular surface-density distributions, with multi-peaks density, and others (the majority) are more com-

pact and have centrally-condensed one peak surface-density (Lada, 2010). Embedded cluster shape is usually slightly elongated, reflecting the filamentary structures of molecular clouds where they originated (Gutermuth et al., 2009). The issue of mass segregation in embedded clusters in highly controversial. Indeed, some objects (e.g. Trapezium, NGC 2024) show signs of mass segregation, which seems to point in the direction of a primordial origin, while in others (e.g. IC 5146) massive stars are found both in the inner regions and in the outer ones (Lada & Lada, 2003).

Due to the very young age of embedded clusters, they result particularly interesting within the context of star cluster formation, providing information from a very initial phase of the star formation process.

The study of embedded clusters is particularly relevant for the determination of the birthrate of clusters and the connected issue of *infant mortality*. Lada & Lada (2003) estimated the embedded cluster formation rate to be between 2 and 4 clusters $\mathrm{Myr}^{-1}\mathrm{kpc}^{-2}$, while the one for open clusters is $0.45\mathrm{Myr}^{-1}\mathrm{kpc}^{-2}$ (Battinelli & Capuzzo-Dolcetta, 1991). This large discrepancy is usually refereed to with the expression infant mortality, to indicate that most (90%) of clusters do not survive the embedded phase and disperse within 10 Myr. The mechanisms behind this phenomenon are not yet clear, even if there has been a lot of studies related. The main idea is that the death of the cluster is the result of the disruptive power and inefficiency of the star formation process itself. If the expulsion of gas happens too rapidly or the amount of mass converted into stars is too low, the intuitive expectation is that the cluster will unbind, since the gravitational potential provided by the gas is not strong enough.

The star formation efficiency (SFE), defined as $M_{stars}/(M_{gas} + M_{stars})$, is therefore thought to be the first main parameter, which decides if the cluster will survive the emergence from the gas. Accurate observational SFE measurements are still difficult to obtain in cluster forming regions, however in fully embedded clusters they range between 10% and 30% (Lada & Lada, 2003) (the average value for giant molecular clouds is 1-5%). Analytic considerations (Hills, 1980) set the threshold SFE value, which can guarantee the survival of the cluster, to 50%. Hence, the aforementioned lower observed values would explain such high rate of infant mortality. However, the second fundamental factor playing a role is the time over which the gas is expelled. The 50%-SFE-boundary assumes instantaneous gas removal, but if we consider an adiabatic slow expulsion, the stars have time to resettle to the new potential and a 30% SFE can actually be enough for the cluster to stay bound. The virial status of the cloud has also shown to influence the result Goodwin (2009). In Chapter 5 we will come back to

the topic, numerically studying the process of emergence and survival of a cluster from the its cloud, providing new insights on the matter.

The study on the universality of the IMF also rely on embedded clusters since in this case it is possible to witness the very early build-up of the mass function, despite some major caveats, due to the use of pre-mainsequence stars to determine the luminosity function (and therefore the mass function). Indeed, in the first Myrs of lifetime of a star the luminosity changes significantly. The most studied embedded cluster, i.e. the Trapezium cluster in the Orion Nebula, offers the most reliable IMF profile, which consist of a power-law with index $\Gamma = -1.2$ (slightly fatter than the Salpeter canonical Γ =-1.35) in the range $0.6 - 10\mathrm{M}_{\odot}$, a flattening from 0.1 to $0.6\mathrm{M}_{\odot}$ and a steep decline for masses $< 0.1\mathrm{M}_{\odot}$ (Muench et al., 2002b). Despite the poor statistics, a comparison of the IMF for different embedded clusters seems to point toward the existence of a universal profile (Muench et al., 2002a).

Finally, embedded stars clusters are fundamental in the study of star formation and planetary models, since most stars in the cluster are still in a pre-main sequence phase, often with circumstellar disks, considered the progenitor of planetary systems.

2.4. Nuclear star clusters

Nuclear star clusters are among the most mysterious and weird inhabitants of a galaxy. They live in the very central part (see Figure 2.13), which in case of galaxies is actually the most dangerous and violent zone, not the typical residential area. Since none really has seen them clearly, they are mythical objects, from the huge mass and extraordinary luminosity. The veil of mystery in which they are wrapped (and the difficulty to observed the centre of the galaxy) gave rise to legends, which narrate how these objects are thought to cage and tame terrible beasts, such as supermassive black holes. They are without any doubt sources of great fascination and active research.

Scientifically speaking, nuclear star clusters (also "stellar nuclei") are compact, barely resolved, and massive star clusters found in the nuclei of most galaxies, despite the morphological type. The nuclei of galaxies are very special extreme environments, giving rise to super-massive black holes (SMBHs), active galactic nuclei (AGN), central starbursts, and extreme stellar densities. The recent interest towards nuclear star clusters is motivated exactly in relation with these exotic phenomena. The high stellar density found in this type of clusters make them suitable place for the

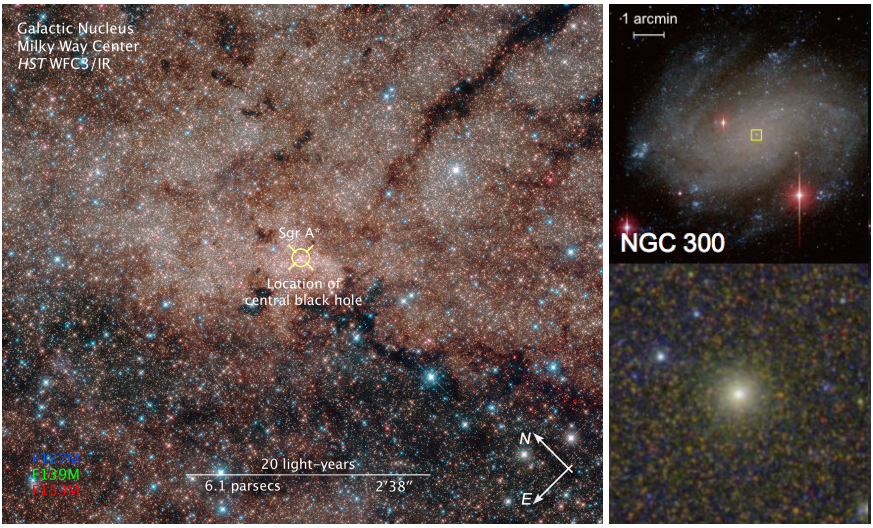

Figure 2.13: Nuclear star clusters. *Left*: Infrared image from Hubble (31st March 2016) of the Galactic centre. Some foreground blue stars don't actually belong to the star cluster. The cross in the middle indicates the position of the supermassive black hole, hosted by the nuclear star cluster. Credits: NASA, ESA, and the Hubble Heritage Team (STScI/AURA). *Right*: Color composite images of NGC 300 and its nuclear star cluster. The size bar in the top panel corresponds to 0.6 kpc. The bottom panel focus on the inner region of the galaxy (12" x 12", hence 100 pc x 100 pc). From Carson et al. (2015)

formation of massive black hole, moreover they could explain the formation of some globular clusters and their very peculiar location establishes a strong connection with the evolution of the host galaxy. We point to the work by Genzel et al. (2010) for a complete review of the topic.

Around 50-70% of galaxies (late/early type spirals, spheroidal) have been observed to host a nuclear star cluster (Böker et al., 2002; Carollo et al., 1997; Carson et al., 2015; Côté et al., 2006; den Brok et al., 2014). Nuclear star clusters are characterised by high luminosity, 40 times higher than average globular clusters (Böker, 2010), compact size, with typical half-light radius is between 2 and 5 pc (Böker et al., 2004) and very high mass, $10^6 - 10^8 \mathrm{M}_\odot$ (Georgiev & Böker, 2014; Walcher et al., 2005). Multiple generations of stars have been observed (mostly $>$ 1Gyr old stars but also $<$ 100 Myr) (Böker,

2010; Walcher et al., 2005),pointing to a complex star formation history, characterised by several star formation episodes. Moreover, nuclear star clusters follow similar scaling relations with host galaxy properties as do SMBHs (Böker, 2010).

The masses of SMBHs are well known to correlate with their host galaxy properties including the bulge velocity dispersion, the bulge mass and the bulge luminosity. Interestingly analogous scaling relations have been found to be valid for nuclear star clusters, in particular the luminosity and mass of these objects have been found to correlate with their host galaxy properties. This similarity made the community think that SMBHs and nuclear star clusters can be grouped under the same definition of "compact massive object" and could share a common formation mechanism. Actually in the recent years it became clear that the scaling relations for collapsed and stellar objects are not the same, which brought to the conclusion that different physical processes regulate star clusters and SMBH growth. Despite all this, the fact that both these objects show tight correlations with the properties of the hosting galaxies suggest at least a coevolution. The coexistence of nuclear star clusters and SMBHs was confirmed in some galaxies (Seth et al., 2008). Graham & Spitler (2009) found that massive bulges only host SMBHs, but no nuclear clusters, while in low-mass, pure disk galaxies the mass of the star cluster is dominant. The observational difficulties to observe such compact objects leave the link between SMBH and nuclear star cluster still not fully understood.

The formation scenario of this type of cluster is still unclear. A first theory hypothesises that the massive cluster did not formed in the center of galaxy but got there by dynamical friction or other mechanisms (Andersen et al., 2008; Capuzzo-Dolcetta & Miocchi, 2008; Tremaine et al., 1975), after having formed somewhere else. This process is potentially followed by dry mergers (i.e. gas free) with other clusters (Andersen et al., 2008; Antonini, 2013a; Mastrobuono-Battisti et al., 2014). A second hypothesis theorises in-situ formation (Milosavljević, 2004), which means that gas falls (episodically) on to the galactic centre, triggering star formation in the central few parsecs and eventually the NC formation (Aharon & Perets, 2015).

Both these scenarios present problematic aspects. The in-situ scenario is not able to retrieve the properties expected from the scaling relations between the nuclear star cluster and the hosting galaxy, while the migration model seems to be more successful in this respect (Antonini, 2013a; Hartmann et al., 2011). Moreover it is not clear how the gas can accumulate in the centre in absence of high central mass concentration (Böker, 2010), some viable solutions seem to be invoke magneto-rotational insta-

bility (Milosavljević, 2004) or compressive tidal fields (Emsellem & van de Ven, 2008). Antonini et al. (2015) found that in situ star formation as well as growth through migrating clusters reproduce the observed star cluster-host galaxy scaling relations. However, the observed correlations between colors and luminosities and the complex star formation histories may be difficult to explain only through merging (Antonini, 2013b), unless there is some mechanism able to transport gas towards the nucleus and support recurrent star formation (Emsellem & van de Ven, 2008; Milosavljević, 2004).

The two scenarios are not auto-excluding and they both probably played a role (den Brok et al., 2014). Very recently a new scenario ("wet migration") has been proposed (Guillard et al., 2016), suggesting that the star cluster forms ex-situ in the galactic disc and it is dense enough to retain a gas reservoir which allows a prolonged star formation activity (100 Myr). Then though dynamical friction and interactions with the rest of the disc the star cluster migrates to the galactic centre. Possible (wet) mergers with other dense clusters produce mass increasing and star formation quenching.

Table 2.1: Summary of main properties of star clusters. Data are taken from all cited sources in the chapter. A dashed line indicates that no data were found in the literature, a question mark is corresponds to a tentative guess. Columns list in order from left to right: globular clusters, open clusters, OB associations, young massive clusters, embedded clusters and nuclear star clusters. Rows list in order from top to bottom: central density, core radius, virial radius, tidal radius, central velocity dispersion, dynamical time, half-mass relaxation time, total mass, stellar mass at the turn-off point, age, number of catalogued objects in the Milky Way, number of expected objects in the Milky Way, metallicity.

	GC	OC	OB ass.	YMC	EC	NSC
ρ_c [$M_\odot\,pc^{-3}$]	$> 10^3$	$10 to \lesssim 10^3$	0.2	$> 10^3$	$10 - 10^3$	10^5
core radius [pc]	1	1	-	0.5	-	-
virial radius [pc]	10	1	-	1	-	$2 - 5$
tidal radius [pc]	35	10	50	10	2	-
σ_c [km/s]	6	0.3	1-3	4	-	-
t_{dyn} [Myr]	0.5	7	$\lesssim$1-3	1	1	-
t_{rh} [Myr]	10^3	100	-	10	-	-
mass [$M_\odot$]	$> 10^5$	$300 - 10^3$	1000	$\gtrsim 10^4$	$10^2 - 10^3$	10^7
mass at turn-off	0.8	$\lesssim 4$	-	$\gtrsim 5$	-	-
Age [Myr]	10^4	300	1-2	< 100	$1 - 2$	$\mathrm{Age_{galaxy}}$?
N_{MW} (catalogue)	157	1629	70	12	100	1?
N_{MW} (expected)	180	10^5	> 1000	50?	10^4	1?
$[Fe/H]$	$-2.3 \mathrm{to} + 0.2$	$-0.7 \mathrm{to} 0.3$	$PopI$	$PopI$	$PopI$	?

3

Star and Star Cluster Formation

Figure 3.1: *Nymphéas*, Claude Monet, 1908, Dallas Museum of Arts. From Wikipedia.

Star formation can be compared to a painting of Monet. One of those representing waterlilies or flowery gardens. The absolute perfect resemblance of the painting to reality makes it appear *easy*, easy to decipher, to understand, to decompose: waterlilies and water, only green, blue, white, some violet. However, the closer the observer looks at the painting (or at star formation), more details appear and one realises that there are tens of brush strokes of other ten different green or blue shades. The risk of virtually drowning in the pond is high and diving so much into this complexity, not to be able anymore to distinguish plants from water, but seeing only traits and colours.

Studying star formation theory is like wanting to reproduce a painting of Monet. The basic image, the basic concept is extremely clean, but it lasts very short before the true complexity of the phenomenon is revealed and one understands that many distinct effects and important details must be taken into account in order to give a realistic representation.

We will start from the naive image, correct but simplified. And then we will introduce more and more brush stokes, of imperceptible different tones, to get a more realistic effect.

Stars originate from molecular clouds. Molecular clouds are very fragmented and clumpy environments, hierarchically organised in clumps and then cores. The whole ensemble contracts under its own gravity and some clumps are compressed at the point they are gravitationally bound, these are the locations where star clusters are expected to form. Clumps have themselves a high degree of internal substructure (cores), characterised by large density contrasts. Being gravitationally unstable, some of these density fluctuations begin to collapse on a short time scale and eventually form a protostar. Protostars are not yet fully developed stars and keep accreting gas from the surrounding. Meanwhile, gravitational instability might cause some cores or clumps to merge, hence creating systems of protostars which could start interacting dynamically, causing ejection of lower-mass objects. Newly born stars affect the environment though stellar evolution feedback effects. In particular the feedback from massive stars is thought to be responsible for the gas dispersion, which terminates the star formation and accretion processes. The final outcome is a gas free, brand new, bound or unbound star cluster[1].

[1]The main comprehensive works on star formation we generally refer to for this Chapter are the reviews by Klessen & Glover (2016); Krumholz (2014) and the textbook Stahler & Palla (2005).

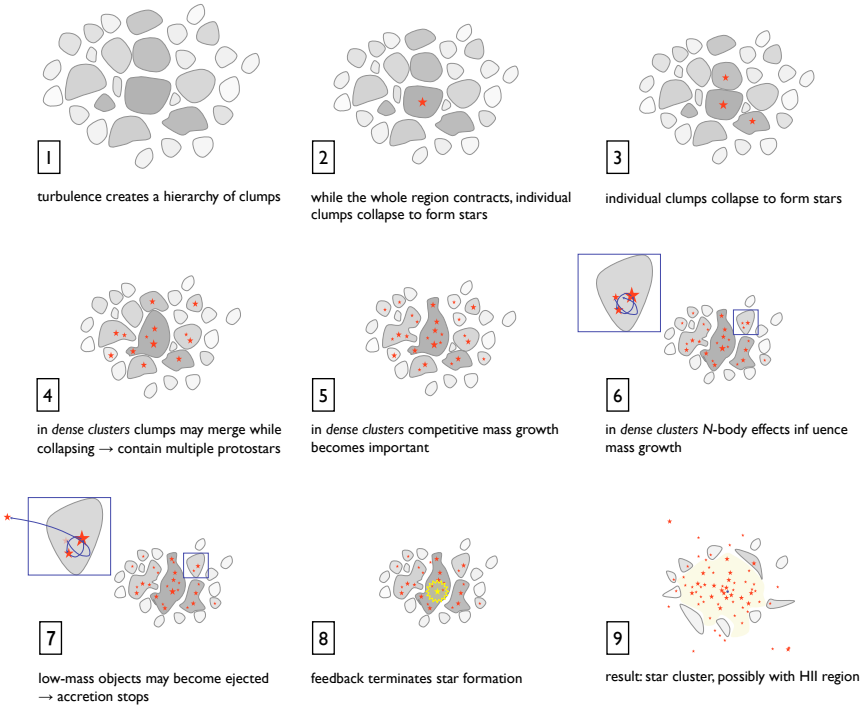

Figure 3.2: Schematic representation of the star cluster formation process. From Klessen & Glover (2016).

3.1. Molecular clouds

Molecular clouds are turbulent, fragmented interstellar clouds, composed mainly by hydrogen in molecular form (but also helium, dust and metals). They are usually embedded in more diffuse regions of atomic hydrogen in interstellar space. A complete review is given by Hennebelle & Falgarone (2012), here we will report the most interesting properties and most recent results not included in the review.

According to Heyer & Dame (2015), the molecular mass in our Galaxy is $(1.0 \pm 0.3) \times 10^9 \mathrm{M}_\odot$, 25% of which has been catalogued as 1064 molecular clouds (Rice et al., 2016), mainly confined in the spiral arms of the galaxy (see Figure 3.3).

When dealing with molecular clouds, average properties varies signif-

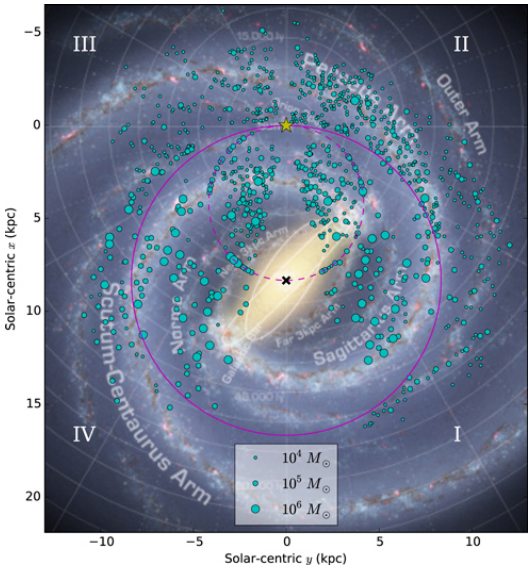

Figure 3.3: Locations of the catalogued molecular clouds (cyan full circles) in the Milky Way (representation). The star indicates the position of the Sun, the areas of the cyan circles are proportional to cloud masses. The purple circles indicate the solar circle (solid line) and the inner tangential circle (dashed line). From Rice et al. (2016).

icantly due to their nested nature and depend on the scale considered. Giant molecular clouds have typical mass around few $10^5 M_\odot$ and upper limit slightly above $10^6 M_\odot$ (Clarke et al., 2015). Clumps and cores are both a couple of orders less massive, respectively $10-10^3 M_\odot$ and $0.1-10 M_\odot$ (Klessen, 2011). The cloud mass spectrum in our Galaxy can be described generally by a power-law ($dN/dm \propto m^\gamma$), whose index and profile depend on the location in the Galaxy (Rice et al., 2016). In the inner part, the behaviour is best described by a truncated power law with index $\gamma = -1.6 \pm 0.1$ and truncation mass $M_0 = (1.0 \pm 0.2) \times 10^7\ M_\odot$. In the outer parts the best fit is represented by a steeper power law with index -2.2 ± 0.1. It should be noticed that in this case the mass spectrum does not exhibit a sharp truncation, but we find no cloud over $(1.5 \pm 0.5) \times 10^6 M_\odot$ (Rice et al., 2016). Similar results are available for other nearby galaxies (Colombo et al., 2014; Rosolowsky, 2005). This seems to suggest that the higher density inner Galactic environment favours the formation and survival of more massive

molecular complexes, while the outer parts is limited to lower mass clouds.

The typical size goes from 2 to 20 pc for molecular clouds, down to 0.1 pc for the substructures, which yields a mean density ranging between $10^2 - 10^3$ $\mathrm{H_2/cm^3}$ on large scale and $> 10^5$ $\mathrm{H_2/cm^3}$ for the dense prestellar cores (Klessen & Glover, 2016).

Kinematics properties of molecular clouds are obtained through the analysis of molecular line emission, mainly CO, which provides an estimated of the internal velocity dispersion via Doppler shift. The outcome values are between 1-10 km/s on large scale and 0.2-0.5 km/s on the small scale (Klessen & Glover, 2016).

The most fundamental result about molecular cloud properties is that these turn out to be correlated with each other. The inter-relationships between mass, linear size and velocity are known as "Larson's Laws". In their original form (Larson, 1981) these are:

- Velocity dispersion (σ) is proportional to the cloud size (L), $\sigma \propto L^{0.38}$ (size-linewidth relation) ,
- Cloud density (n_{H_2}) is inversely proportional to cloud size, $n_{H_2} \propto L^{-1}$,
- Velocity dispersion is proportional to the cloud mass (M), $\sigma \propto M^{0.20}$.

This result is important to understand the origin of molecular cloud systematics. The first law was immediately interpreted in terms of turbulence, due to the similarity with the predictions of the Kolmogorov theory (Kolmogorov, 1941). According to Kolmogorov the velocity field in incompressible turbulent flows turns our to be self-similar across different velocity scales, due to the cascade of energy from large to small scales. The velocity in this case scales as $L^{1/3}$ (Kolmogorov, 1941), extremely close to the Larson's first law. More recent surveys gave a new estimate of the size-linewidth exponent ~ 0.5 (Falgarone et al., 1992; Heyer et al., 2001; Rice et al., 2016; Solomon et al., 1987), which was by some interpreted as confirmation that this law arises from the the cloud being in virial equilibrium (see also next law) (Heyer & Dame, 2015).

However, such a divergence from the Kolmogorov predictions should not be surprising, since molecular clouds can not be treated as incompressible fluids. Moreover, the velocity dispersion predicted by the first Larson's law results much higher than what obtained from linewidth measurements due to thermal motions at typical temperature in a cloud ($\sim 10 - 20$ K), pointing in the direction of a supersonic state. If we consider other categories of turbulence, such as the pure-shocks Burgers' turbulence, we

get a closer agreement for the velocity scaling exponent. In general, a spectral slope which lies in between the Kolmogorov's value (-5/3) and the Burgers' value (-2). turns out to be in better agreement with observations (Boldyrev, 2002; Boldyrev et al., 2002). Recent numerical simulations proved that the size-linewidth $\sigma \propto L^{1/2}$ is consistent with supersonic turbulence (Federrath, 2013; Kritsuk et al., 2013).

The second law states basically that the surface density should be roughly constant, which is what was initially observed (Heyer et al., 2009; Solomon et al., 1987), but that clearly cannot be true down to every scale otherwise there would be no contrast between substructures. Lombardi et al. (2010) showed that the actual average surface mass density is a function of the specific extinction threshold, therefore different clouds have almost identical average surface densities above a given extinction threshold. Moreover the authors show that the second Larson's law does not hold within single clouds, indicating that individual clouds are not objects that can be described by a constant surface density. Nevertheless, they found molecular clouds exhibit, as universal feature, a log-normal surface density distribution.

The third law can be derived from the previous two and accounts for the role of gravity in shaping the properties of the clouds. Indeed, this relation can be rewritten, using the size-linewidth, as $\sigma^2 \propto GM/L$, which tells $E_{kin} \propto E_{grav}$, the proportionality being consistent with virial equilibrium (see Section 3.2.2.1). This lead the conception that molecular clouds should be expected to be mostly bound and in approximate virial equilibrium. Several contrasting studies proved the limitations of such a strong belief (e.g. Dib et al. 2007; Morata et al. 2005)showed that molecular clouds are virialised only for surface densities higher than $100\ \mathrm{M}_{\odot}\ pc^{-2}$, on the other side (Heyer et al., 2009) claims that molecular clouds sampled by this survey are in virial balance. Dobbs et al. (2011) questions this last results using the same set of observations and data from Solomon et al. (1987). The debate concerning which Larson's law is the most fundamental and whether is mainly turbulence or gravity responsible for the properties of molecular clouds, remains open.

A full analysis about the physical mechanisms determining the structure of molecular clouds and the theory of their formation is beyond the aims of this thesis. Probably the wiser position is to admit that both mechanisms must play a role somehow. The fact that supersonic turbulence is in approximate virial balance with self-gravity signifies that turbulent and gravitational energy density are of the same order of magnitude in molecular clouds (both exceeding the thermal energy contribution). This implies

that on large scales turbulence can support clouds against contraction. On smaller scales fluctuations in the turbulent velocity field allow the creation of high density peaks, which can result in localised collapse. However, this density enhancements can be dispersed as fast as they have been created (Klessen, 2011). We will see in the the next section that the timescale over which the collapse takes place is a crucial parameter: to be successful, the collapse timescale must be shorter than the timescale over which density fluctuates, which is set by the frequency of turbulence induced shocks. For supersonic turbulence the density enhancement is strong but highly transient.

Molecular clouds are characterised by Mach numbers ≥ 5, up to 50 (Klessen, 2011). On the scale of clumps turbulence is still supersonic with Mach number values, between 2 and 15, which would in some cases produce density fluctuations exceeding the threshold for gravitational collapse to set in. However the supersonic nature of turbulence at this scale cause the fragmentation of the clumps in smaller cores, instead of the collapse into a one massive object. Finally at the scale of cores turbulence becomes subsonic and this allow gravity to proceed in the collapse of single (or binary) stars. A summary of the turbulent energy spectrum at different scales is represented by Figure 3.4 from Klessen (2011). The scale, at which velocity (therefore energy) transitions from supersonic to subsonic, can be directly computed from the first Larson's law and is called *sonic scale*. In molecular cloud cores this is ~ 0.1 pc. In numerical experiments of star formation (see Chapter 5), it is of crucial importance being able to resolve the sound scale, since it is the scale over which stars form. This process is defined as *gravoturbulent fragmentation*, a detailed study can be found in Mac Low & Klessen (2004).

In the previous considerations we completely neglected the effect of magnetic fields. Measurements of magnetic field strength in molecular clouds are in general problematic, therefore the estimates are still very sparse. The current results, using Zeeman effect and dust polarisation techniques, vary between 0.5 and 50 μG (Chapman et al., 2011; Crutcher et al., 2010). This suggests magnetic energy is non-negligibile in molecular cloud, generally comparable with the turbulent and gravitational contributions. It is therefore in principle important to take the magnetic field into account, since strong magnetic fields can prevent the cloud collapse (subcritical cloud). Most observations indicate that molecular cloud are mainly supercritical (Crutcher, 2012, and references therein), which means magnetic pressure is insufficient to balance gravity, however in most cases we are talking about slightly supercritical clouds. Therefore, due to the high

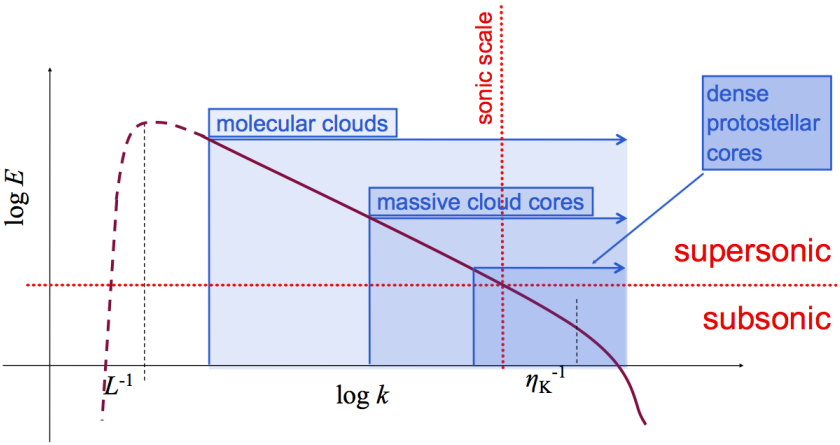

Figure 3.4: Turbulent energy spectrum as a function of the wavenumber k. Small values of k corresponds to large scales (L), large values of k to small scales (η_μ). From Klessen (2011).

variability of field strength from cloud to cloud, the possibility that some structures may be magnetically supported stays open.

One of the main tests for star formation theories is deriving the correct stellar initial mass function (IMF). In the previous chapter we saw most open clusters are characterised by a Salpeter power law ($dN/dm \propto m^\alpha$, with $\alpha = -2.35$) profile for high-masses and a log normal or shallower power law for low masses. The mass function of molecular pre-stellar cores, originated from the gravoturbulent fragmentation process (Chabrier & Hennebelle, 2011; Guszejnov & Hopkins, 2015; Padoan & Nordlund, 2002), has an extremely similar behaviour, with $\alpha = 2.5$ for $M \geq 0.5\mathrm{M}_\odot$ and $\alpha = 1.5$ for $M \leq 0.5\mathrm{M}_\odot$ (e.g. Alves et al. 2007; André et al. 2010; Motte et al. 1996; Olmi et al. 2013; Sandell & Knee 2001). An exact matching of the two mass functions would imply a star formation efficiency around 30% (Alves et al., 2007). However, this direct mapping between core and stellar mass functions should be considered with caution: Clark et al. (2007) warns about the fact that clumps of varying mass are likely to have varying lifetimes. How it will be clear after the next section, the authors explains that, if we assume all cores contains one Jeans mass, low-mass cores will have higher density, therefore shorter free-fall time. This means that cores

of different masses will evolve on different timescales, producing a steeper outcoming stellar mass function. Padoan & Nordlund (2011) argue that in observations there is no trace of such a correlation between mass of the cores and density, hence varying lifetimes are not an issue.

From the thermodynamical point of view the temperature of the molecular clouds is determined by interplay of heating, mainly due to ionisation by cosmic rays, and cooling, mainly due to line radiation from molecules, especially CO (Goldsmith & Langer, 1978). In general, these structures can be considered roughly isothermal, with temperatures around 15-20 K on cloud scales and around 10 K on pre-collapsing core scales (Bergin & Tafalla, 2007). In the next section we will see how the temperature turns out to be a fundamental parameter for the collapse and that during the collapse the thermodynamical state of the cloud will change dramatically.

3.2. Gravitational collapse

Now that we described the properties of molecular clouds, we will focus on the physics of the gravitational collapse from an analytic perspective, to better understand under which conditions the collapse takes place and the timescale involved. The following derivation is mostly based on the classic reference textbooks Binney & Tremaine (2008) and Shu (1991).

The basic equations of hydrodynamics are derived by taking the moments of the Vlaslov-Boltzmann equation, which describes the evolution of the phase-space particle distribution function of an infinitesimal fluid element. The result is the Euler equations.

$$\frac{\partial \rho}{\partial t} + \nabla \cdot (\rho \boldsymbol{v}) = 0 \tag{3.1}$$

$$\frac{\partial (\rho \boldsymbol{v})}{\partial t} + \nabla \cdot (\rho (\boldsymbol{v} \otimes \boldsymbol{v}) + \overline{\boldsymbol{P}}) = \rho \boldsymbol{a} \tag{3.2}$$

$$\frac{\partial E}{\partial t} + \nabla \cdot (E + P)\boldsymbol{v} = \rho \boldsymbol{a} \cdot \boldsymbol{v}, \tag{3.3}$$

where (all quantities refer to the fluid) ρ is the density, $\boldsymbol{v}$ the velocity, $\boldsymbol{a}$ the acceleration, $\overline{\boldsymbol{P}}$ the pressure tensor, E total fluid energy density and P is the scalar pressure[2]. These equations govern the gas dynamics and encapsulate three main conservation laws (mass, momentum and energy). In case of self-gravitating fluids and under the assumption of spherical

[2]Using the Lagrangian derivative operator ($\frac{D}{Dt} = \frac{\partial}{\partial t} + \boldsymbol{v} \cdot \nabla$), it is possible to have an

symmetry, $\rho = \rho(r)$, $\overline{\boldsymbol{P}} = P(r)\mathbb{1}$ and $\boldsymbol{a} = -\nabla\phi$. The gravitational potential is given by the Poisson equation

$$\nabla^2\phi = 4\pi G\rho. \tag{3.7}$$

An important starting point to study the collapse of a system is actually determining its condition of equilibrium. The equilibrium solution is obtained by requiring a stationary status ($\partial/\partial t \equiv 0$) and zero velocity. With the assumption of spherical symmetry and self-gravity, equation 3.2 then becomes

$$\frac{1}{\rho}\frac{\partial P}{\partial r} = -\nabla\phi\,, \tag{3.8}$$

which is known as *hydrostatic equilibrium equation*. This says that at equilibrium the pressure gradient oppose the gravitational force, preventing the collapse or the dispersion of the cloud. If the inward force prevails, the system collapses ($\frac{1}{\rho}\frac{\partial P}{\partial r} < -\nabla\phi$), and we can at least qualitatively estimate the timescale of this process. If we assume the difference between the opposing effects to be of the same order of magnitude as the gravitational acceleration itself (meaning the outward pressure gradient is negligible),

$$|\nabla\phi - \frac{1}{\rho}\frac{\partial P}{\partial r}| \sim |\nabla\phi| \tag{3.9}$$

we can estimate the timescale over which density changes. Let's consider equation 3.5. Reorganising a bit the terms, we obtain an approximation for the fractional change of density

$$\frac{\Delta\rho}{\rho} \sim -(\nabla\cdot\boldsymbol{v})\Delta t \sim (\nabla\cdot(\nabla\phi\Delta t))\Delta t. \tag{3.10}$$

Recalling now the Poisson equation (3.7),

$$\nabla\cdot\nabla\phi = \nabla^2\phi = 4\pi G\rho, \text{ so} \tag{3.11}$$

$$\frac{\Delta\rho}{\rho} \sim 4\pi G\rho(\Delta t)^2 \tag{3.12}$$

---

alternative formulation of the same equations

$$\frac{1}{\rho}\frac{D\rho}{Dt} = -\nabla\cdot\boldsymbol{v} \tag{3.4}$$

$$\rho\frac{D\boldsymbol{v}}{Dt} = -\nabla\cdot\overline{\boldsymbol{P}} + \rho\boldsymbol{a} \tag{3.5}$$

$$\rho\frac{D\epsilon}{Dt} = -P\nabla\cdot\boldsymbol{v} \tag{3.6}$$

also called *Lagrangian formulation*.

The timescale over which density changes happen is of order

$$\Delta t \sim (G\rho)^{-1/2} \,. \tag{3.13}$$

This is indeed the *free-fall timescale*. The exact expression will be derived in the next section.

3.2.0.1. Free-fall timescale

Thanks to Gauss' flux law, we know that the gravitational field of an homogeneous sphere of density ρ_0 and initial radius r_0 computed in a point outside the sphere is equivalent to the one generated by a point particle with $M = \frac{4}{3}\pi\rho_0 r_0^3$ located at the centre of the sphere. We can therefore tackle the problem of the collapse of a gravitating sphere, simply as the free-fall of a test particle towards a point mass (M) at the centre.

The easiest way now is to impose the energy conservation law. We assume that initially the particle mass is at rest at an initial distance r_0 and it will be at location $r < r_0$ with velocity v at time t. Therefore,

$$E_{pot}^{in} = E_{kin}^{fin} + E_{pot}^{fin} \tag{3.14}$$

$$-\frac{GM}{r_0} = \frac{1}{2}v^2 - \frac{GM}{r} \,. \tag{3.15}$$

Reorganising the terms and substituting, $v = dr/dt$, we get

$$\frac{1}{2}\left(\frac{dr}{dt}\right)^2 = \frac{GM}{r} - \frac{GM}{r_0} \,. \tag{3.16}$$

We now take the negative solution of the square root of the right-hand side, since we want the test particle to move towards the massive particle, to get to $r < r_0$,

$$\frac{dr}{dt} = -\sqrt{\frac{2GM}{r} - \frac{2GM}{r_0}} \,. \tag{3.17}$$

By inserting $M = \frac{4}{3}\pi\rho_0 r_0^3$ in the previous expression, we have

$$\frac{dr}{dt} = -r_0\sqrt{\frac{8\pi G\rho_0}{3}\left(\frac{r_0}{r} - 1\right)} \,. \tag{3.18}$$

To solve this differential equation, it is convenient perform the following change of variable,

$$r = r_0 \cos^2\phi \,, \tag{3.19}$$

which implies

$$\frac{dr}{dt} = r_0 \frac{d}{dt} \cos^2 \phi = -2 r_0 \cos\phi \sin\phi \frac{d\phi}{dt} \,. \tag{3.20}$$

It follows that

$$\frac{d\phi}{dt} = \frac{1}{2\cos\phi \sin\phi} \sqrt{\frac{8\pi G \rho_0}{3} \left(\frac{1}{\cos^2\phi} - 1 \right)} \tag{3.21}$$

$$= \frac{1}{2\cos^2\phi \sin\phi} \sqrt{\frac{8\pi G \rho_0}{3} (1 - \cos^2\phi)} \tag{3.22}$$

$$= \frac{1}{2\cos^2\phi} \sqrt{\frac{8\pi G \rho_0}{3}} \tag{3.23}$$

We then integrate on both sides,

$$\int_{\phi_0}^{\phi} \cos^2\phi' d\phi' = \frac{1}{2} \sqrt{\frac{8\pi G \rho_0}{3}} \int_0^{t_{ff}} dt' \,, \tag{3.24}$$

where $\phi_0 = 0$ and $\phi = \pi/2$ (corresponding respectively to $r = r_0$ and $r = 0$), which brings to the result

$$\int_{\phi_0}^{\phi} \cos^2\phi' d\phi' = \left[\frac{\phi}{2} + \frac{\sin 2\phi}{4} \right]_0^{\pi/2} = \frac{\pi}{4} = \frac{t_{ff}}{2} \sqrt{\frac{8\pi G \rho_0}{3}} \,. \tag{3.25}$$

We finally obtained the expression for the free-fall timescale, which, as anticipated is proportional to $(G\rho)^{-1/2}$:

$$t_{ff} = \sqrt{\frac{3\pi}{32 G \rho_0}} \,. \tag{3.26}$$

It is important to stress how there is no dependence on the size of the cloud, but exclusively on the density. If we consider the characteristic molecular cloud densities quoted in the previous section, the typical collapsing times go from 2 Myr (for the large structure) to 0.1 Myr for the densest cores.

In the derivation we assumed that the collapse proceeds spherically, without any preferential direction, however under real conditions (angular momentum, magnetic fields..) a molecular cloud usually flattens first along one direction, creating almost a disk whose collapse proceeds slower due to the presence of rotation, hence this is just an approximation. We will

see in Chapter 4 how the free-fall timescale effectively represents the dynamical timescale of gravitational interactions of a system of particles.

To characterise even further the process of collapse we need to determine the spatial scale over which it occurs, therefore we need to analytically introduce perturbations to the equilibrium.

3.2.1. Jeans' Mass and Length

Here I present the classic argument of the Jeans instability criterion (Jeans, 1902), which derives a critical mass and length for which the collapse can take place. The idea is to study the small fluctuations in an infinitely extended, homogeneous, self -gravitating gas using linear perturbation analysis.

The basic equations to be used are the first two Euler's equations, Poisson's equation and an equation of state. The most simple choice is to assume an isothermal equation of state, $P = c_s^2 \rho$ (with c_s being the sound speed), which is in line with observed properties of molecular clouds.

$$\frac{\partial \rho}{\partial t} + \nabla \cdot (\rho \boldsymbol{v}) = 0 \tag{3.27}$$

$$\frac{\partial \boldsymbol{v}}{\partial t} + (\boldsymbol{v} \cdot \nabla)\boldsymbol{v} = -\frac{c_s^2}{\rho}\nabla\rho - \nabla\phi \tag{3.28}$$

$$\nabla^2 \phi = 4\pi G \rho. \tag{3.29}$$

The initial condition is a static background configuration, characterised by

$$\rho_0 = const \tag{3.30}$$

$$\boldsymbol{v}_0 = 0. \tag{3.31}$$

If we plug these values in equation 3.28 we face a first inconsistency. Indeed, we get

$$\nabla\phi_0 = 0, \text{ which implies } \nabla^2\phi_0 = 4\pi G\rho_0 = 0 \tag{3.32}$$

which means that the background state is not a solution. The problem arises from the fact that imposing constant density and zero mean velocity both to the Euler and Poisson equations is incompatible, unless the value of density is also zero. From a physical point of view, the second Euler's equation requires the balance between pressure gradient and gravitational

attraction to have a static system, hence the absence of the first one forces also the second one to be null. On the other hand, Poisson's equation does not "detect" the pressure gradient and just compute a gravitational potential from the background density. This problem can be avoided with an expedient, the so called "Jeans swindle", which consists in *ad hoc* requiring the Poisson's equation to be valid only for the perturbed quantities, and not for the background initial values. The initial unperturbed potential is assumed to be zero.

Let's now assume small perturbations around the initial state

$$\rho = \rho_0 + \rho_1, \ \rho_1 \ll \rho_0 \tag{3.33}$$

$$\boldsymbol{v} = \boldsymbol{v}_1, \ |\boldsymbol{v}_1| \ll c_s \tag{3.34}$$

If we insert them in equations 3.27-3.29 and linearise the outcome, we get

$$\frac{\partial \rho_1}{\partial t} + \rho_0 \nabla \cdot \boldsymbol{v}_1 = 0, \tag{3.35}$$

$$\frac{\partial \boldsymbol{v}_1}{\partial t} = -\frac{c_s^2}{\rho_0} \nabla \rho_1 - \nabla \phi_1, \tag{3.36}$$

$$\nabla^2 \phi_1 = 4\pi G \rho_1. \tag{3.37}$$

This system can be rearranged in only one equation, by taking the divergence of 3.36 and using Poisson's equation to eliminate the Laplacian of the potential

$$\nabla \cdot \frac{\partial \boldsymbol{v}_1}{\partial t} = -\frac{c_s^2}{\rho_0} \nabla^2 \rho_1 - 4\pi G \rho_1, \tag{3.38}$$

then switching divergence and temporal derivative in the first term, and eliminating $\nabla \cdot \boldsymbol{v}_1$ using equations 3.35, yields to

$$\frac{\partial^2 \rho_1}{\partial t^2} - c_s^2 \nabla^2 \rho_1 = -4\pi G \rho_0 \rho_1 \, . \tag{3.39}$$

The similarity of this last expression to the general formula for wave equations, with the addition of an extra term, justifies the assumption of a planar wave as ansatz solution,

$$\rho_1(\boldsymbol{x}, t) = a e^{i(\boldsymbol{k}\boldsymbol{x} - \omega t)} \, . \tag{3.40}$$

The dispersion relation is obtained once the ansatz is substituted in equation 3.39

$$\omega^2 = |\boldsymbol{k}|^2 c_s^2 - 4\pi G \rho_0. \tag{3.41}$$

We face now two different cases. A first possibility is that ω is real, that is $\boldsymbol{k}$ is large enough to have $|\boldsymbol{k}|^2 c_s^2 - 4\pi G\rho_0 > 0$, and this mens that the perturbation is stable and varies periodically in time, but the amplitude does not increase progressively. On the other hand, for large values of density, $|\boldsymbol{k}|^2 c_s^2 - 4\pi G\rho_0 < 0$, which means ω would be imaginary and therefore perturbations would grow exponentially with time. This second is a case of unstable equilibrium, which gives rise to gravitational collapse. If we rewrite the wave number as $|\boldsymbol{k}| = 2\pi/\lambda$, the previous expression becomes

$$\omega^2 = \frac{4\pi^2 c_s^2}{\lambda^2} - 4\pi G\rho_0. \tag{3.42}$$

The right hand side of the equation gets more negative the larger λ is. This means perturbations with larger wavelengths have higher growth rate and collapse faster. The border value between stable and unstable perturbation corresponds to the critical wavelength,

$$\lambda_J = \sqrt{\frac{\pi c_s^2}{G\rho_0}}, \tag{3.43}$$

called *Jeans length*. This condition define the scale of the collapse: perturbations with wavelength larger than λ_J are unstable. It follows, that a molecular core whose size is larger than the Jeans length can not be supported by thermal pressure and inevitably undergoes gravitational collapse. It is sometimes more convenient to use the Jeans mass to determine the condition for the collapse. This is defined simply as:

$$M_{\mathrm{J}} = \rho_0 \frac{4\pi}{3}\left(\frac{\lambda_{\mathrm{Jeans}}}{2}\right)^3 \tag{3.44}$$

in this case the collapse proceeds for $M > M_J$. If we assume for simplicity the ideal gas equation of state,

$$c_s = \left(\frac{P}{\rho_0}\right)^{1/2} = \left(\frac{k_B T_0}{\mu m_u}\right)^{1/2}, \tag{3.45}$$

with k_B being the Boltzmann constant, μ the mean molecular weight and m_u the atomic mass unit, the Jeans mass can be rewritten in a very instructive form,

$$M_J = \frac{\pi\rho_0}{6}\left(\frac{\pi c_s^2}{G\rho_0}\right)^{3/2} = \frac{\pi\rho_0}{6}\left(\frac{\pi k T_0}{4\mu m_u G\rho_0}\right)^{3/2} \propto T_0^{3/2}\rho_0^{-1/2}. \tag{3.46}$$

The Jeans mass has a direct dependence from temperature and inverse from density. It is now clear that a fundamental reason why stars form in molecular cloud is because here the Jeans mass is low, being these clouds cold and dense. Equations 3.43 and 3.46 can be expressed using normalisation values typical of dense regions in molecular clouds

$$\lambda_J = 0.06pc\sqrt{\frac{T}{10K}\frac{10^5 cm^{-3}}{n}}\,, \tag{3.47}$$

$$M_J = 0.2\mathrm{M}_\odot\sqrt{\left(\frac{T}{10K}\right)^3\frac{10^5 cm^{-3}}{n}}\,, \tag{3.48}$$

where in this case T is the temperature and n is the number density of hydrogen (Clarke et al., 2015).

The influence of temperature on the Jeans mass, and therefore the collapse, translates into the so called *fragmentation* process. During the initial phases of collapse, still at low density, molecular gas contracts but remains almost isothermal, because emitted radiation from fine structure transition in CO molecules act as a cooling and the medium is still optically thin to this photons. During this phase the Jeans mass decreases since, the temperature is constant and the density raises. This means smaller and smaller clumps of the original cloud may be unstable, a process known as fragmentation of the cloud, which implies less massive stars are formed. As the collapse proceeds and the density increases ($\rho_{\mathrm{crit}} \sim 10^{-13}\mathrm{gcm}^{-3}$), the cloud becomes optically thick to its own infrared radiation, which has now a mean free path comparable with the cloud size. In this way the heat generated from the compression can not be radiated away and determines an increase of temperature. The gas has transitioned to an adiabatic phase (also called *first hydrostatic core* or *first Larson core* (Larson, 1968)), with $P \propto \rho^{5/3}$ initially, and $P \propto \rho^{7/5}$ when the H_2 rotational degrees of freedom get excited. The higher temperature causes the Jeans mass to increase again, putting an end to further fragmentation. The opacity limit sets the minimum Jeans mass around $10^{-2}\,\mathrm{M}_\odot$ for density $\sim \rho_{crit}$ (Goodwin et al., 2007). This mechanism is repeated when the core reaches $\sim$2000 K, gravitational energy is employed to dissociates molecular hydrogen, the thermal support is lost and a second isothermal collapse begins. This ends once more with the creation of an another Larson core, the second one, also called *stellar* core. This happens for densities $\sim 10^{-3} g/cm^3$, for which all hydrogen molecules have been dissociated. During the second collapse, a new fragmentation can take place, probably at the origin of the formation of primordial close binary stars (Goodwin et al., 2007).

3.2.2. Virial theorem

The virial theorem is a fundamental result of classic statistical mechanics, which finds numerous applications in the astrophysical context. It ca be seen as a consequence of hydrostatic equilibrium, representing a volume-average expression of it We will derive here the general formulation, which can lead to the very (ab-)used concept of virial equilibrium. As for simplicity, we will neglect magnetic support, but we will discuss at the end the consequence of an eventual inclusion of it. In comparison with the previous stability analysis, this theorem provides a more general discussion. We will show at the end how we can a posteriori retrieve the Jeans's mass and length from it.

We start considering the symmetric tensor of inertia $\overline{\boldsymbol{I}}$,

$$I_{ij} = \int_{\Omega(t)} \rho r_i r_j \, \mathrm{d}V. \tag{3.49}$$

Assuming Lagrangian coordinates, which means that our system of reference is moving with the fluid, we compute the first time-derivative of the tensor of inertia, using *Reynolds transport theorem* in case of *specific variables*[3]. Indeed, $\rho r_i r_j$ is a specific quantity and so the time derivative of its

[3] *Reynolds transport theorem*: If $C = \int_{V(t)} \alpha(x,t) d^3x$, then

$$\frac{dC}{dt} = \int_{V(t)} \left[\frac{\partial \alpha}{\partial t} + \nabla \cdot (\alpha \boldsymbol{v}) \right] d^3x. \tag{3.50}$$

In the special case where α is a *specific quantity*, which means can be expressed in the form $\alpha = \rho A$ (with ρ indicating the usual density), it is trivial to show that the Reynolds transport theorem reduces to compute the Lagrangian derivative of the A. This can be demonstrated using the continuity equation (Equation 3.1):

$$\frac{dC}{dt} = \int_{V(t)} \left[\frac{\partial(\rho A)}{\partial t} + \nabla \cdot (\rho A \boldsymbol{v}) \right] d^3x = \int_{V(t)} \left[A \frac{\partial \rho}{\partial t} + \rho \frac{\partial A}{\partial t} + A \nabla \cdot (\rho \boldsymbol{v}) + \rho (\boldsymbol{v} \cdot \nabla A) \right] d^3x \,. \tag{3.51}$$

The first and third term of the integral cancel each other thanks to the continuity equation and the second and fourth term constitute the lagrangian derivative $\frac{D}{Dt} = \frac{\partial}{\partial t} + \boldsymbol{v} \cdot \nabla$ (see previous footnote). In cases where $\alpha = \rho A$, we can therefore rewrite the time derivative of the integral simply as

$$\frac{dC}{dt} = \int_{V(t)} \rho \frac{DA}{Dt} d^3x. \tag{3.52}$$

integral is performed through a lagrangian derivative $\frac{D}{Dt} = \frac{\partial}{\partial t} + \boldsymbol{v} \cdot \nabla$

$$\frac{\mathrm{d}}{\mathrm{d}t} I_{ij} = \int_{\Omega(t)} \rho \frac{D}{Dt}(r_i r_j)\,\mathrm{d}V \tag{3.53}$$

$$= \int_{\Omega(t)} \rho \boldsymbol{v} \cdot \nabla(r_i r_j)\,\mathrm{d}V \tag{3.54}$$

$$= \int_{\Omega(t)} \rho(r_i v_j + r_j v_i)\mathrm{d}V\,. \tag{3.55}$$

To calculate the second derivative in time of I_{ij} we apply once more the Reynolds transport theorem at equation 3.55, noticing that also $\rho(r_i v_j + r_j v_i)$ is a specific quantity. Thus,

$$\frac{1}{2}\frac{\mathrm{d}^2}{\mathrm{d}t^2} I_{ij} = \frac{1}{2}\int_{\Omega(t)} \rho \frac{D}{Dt}(r_i v_j + r_j v_i)\,\mathrm{d}V \tag{3.56}$$

$$= \frac{1}{2}\int_{\Omega(t)} \rho(r_j \frac{\partial v_i}{\partial t} + r_i \frac{\partial v_j}{\partial t}) + \boldsymbol{v} \cdot \nabla(r_i v_j + r_j v_i)\mathrm{d}V \tag{3.57}$$

$$= \int_{\Omega(t)} \rho v_i v_j + \frac{1}{2}\left(r_i \frac{\mathrm{D}v_j}{\mathrm{D}t} + r_j \frac{\mathrm{D}v_i}{\mathrm{D}t}\right)\mathrm{d}V\,. \tag{3.58}$$

The first term in equation 3.58 can be identified as twice the kinetic energy tensor K_{ij} of the gas and the second one is the left hand side of the momentum conservation equation in lagrangian form. Until here the derivation was very general, but now we need to make some assumptions on the physical properties of our fluid, which will determine the terms appearing in the momentum equation. In principle we could now include forces of various nature at this point (magnetic, radiation...), but for sake of simplicity we will assuming a basic inviscid fluid subject to gravity and thermal pressure.

Keeping in mind that in our case the acceleration is given by the gravitational field $\boldsymbol{g}$, we proceed by substituting equation 3.5,

$$\rho \frac{\mathrm{D}v_i}{\mathrm{D}t} = \rho g_i - \partial_k P_{ki}, \tag{3.59}$$

in the second term of the integral 3.58, assuming for simplicity that $\overline{\boldsymbol{P}} = P\mathbb{1}$, which means $P_{kj} = P\delta_{kj}$.

$$\frac{1}{2}\frac{\mathrm{d}^2}{\mathrm{d}t^2} I_{ij} = 2T_{ij} + \frac{1}{2}\int_{\Omega(t)} \rho r_i a_j + \rho r_j a_i - r_i \partial_k P \delta_{kj} - r_j \partial_k P \delta_{ki}\,\mathrm{d}V. \tag{3.60}$$

We compute now the trace of the previous expression to retrieve the scalar moment of inertia, $I = Tr(I_{ij})$:

$$\frac{1}{2}\frac{\mathrm{d}^2 I}{\mathrm{d}t^2} = 2T + \int_{\Omega(t)} \rho\, \boldsymbol{r}\cdot\boldsymbol{g}\,\mathrm{d}V - \int_{\Omega(t)} \boldsymbol{r}\cdot\nabla P\,\mathrm{d}V. \tag{3.61}$$

We can now rewrite the second integral in the right hand side using the relation $\nabla\cdot(P\boldsymbol{r}) = P\nabla\cdot\boldsymbol{r} + \boldsymbol{r}\cdot\nabla P$ and split it into a volume and surface term with Gauss' divergence theorem. We then get the final expression for the scalar virial theorem

$$\frac{1}{2}\frac{\mathrm{d}^2 I}{\mathrm{d}t^2} = \underbrace{\int_{\Omega(t)} \rho\,|\boldsymbol{v}|^2\,\mathrm{d}V}_{\text{kinetic}} + \underbrace{\int_{\Omega(t)} \rho\,\boldsymbol{r}\cdot\boldsymbol{g}\,\mathrm{d}V}_{\text{virial}} + \underbrace{3\int_{\Omega(t)} P\,\mathrm{d}V}_{\text{pressure volume}} - \underbrace{\int_{\partial\Omega(t)} P\boldsymbol{r}\cdot\boldsymbol{n}\,\mathrm{d}A}_{\text{pressure surface}}. \tag{3.62}$$

Let's now focus on each term. The first one, as already said, is exactly double the kinetic energy. The second one is the one which actually gives the name to the theorem, indeed is called the *virial* term. Etymologically, *virial* is connected with the latin word (*vis*) which means force (also energy in some sense) and in fact this term includes the acceleration. It is probably the most misunderstood term of the equation, since it is very often considered to be simply the gravitational energy. However, this is true only under the specific assumption of isolation, that is if the gravitational potential is entirely due to the matter inside $\Omega(t)$ exclusively. If the volume is within a bigger structure, this assumption is not strictly valid anymore and one should consider second order corrections connected with the tidal tensor. The third term is related to the internal pressure of the fluid and can be interpreted as twice the thermal energy for some specific equation of state (e.g. ideal gas). In this cases kinetic and thermal energy are considered as one thermal+non-thermal kinetic energy term. The last one is a surface term related with the external pressure. It can be neglected if the pressure is constant, since the two pressure terms cancel out or if the external pressure is anyway much lower than the internal one. As we said at the beginning of this section, there can be more sources of energy which enter the stability analysis and more terms get added in the equation. We can predict this contribution. In case of inclusion of radiative forces, we have to account for a new term analogous to the virial one where the acceleration will be due to the radiation. With presence of magnetic fields we will add a magnetic volume term and surface stress terms. In general, all stress terms (magnetic, tidal..) will contribute to the equation through a generic stress tensor, which will replace $\overline{\boldsymbol{P}}$ in the derivation.

3.2.2.1. Virial equilibria

The main application of the virial theorem is in conjunction with the so called *virial equilibrium*. This apply when $\frac{\mathrm{d}^2 I}{\mathrm{d}t^2} = 0$, therefore, in the assumption of no surface terms, no magnetic fields, isolated system and monoatomic gas, the virial theorem reads

$$2E_{kin} + E_{grav} = 0\,, \tag{3.63}$$

where E_{kin} accounts for kinetic and thermal energies and E_{grav} is the gravitational potential energy. This could be the case of a cloud gas or a star, supported by pressure only against the collapse. We can therefore also from here recover a Jeans-like criterion. Assuming an ideal gas equation of state and spherical symmetry

$$E_{kin} = \frac{3}{2}\frac{Mk_BT}{\mu m_u} \tag{3.64}$$

$$E_{grav} = -\frac{3}{5}\frac{GM^2}{R}\,, \tag{3.65}$$

where M is the total mass in the system, k_B being the Boltzmann constant, μ the mean molecular weight,m_u the atomic mass unit, T is the temperature and R the size of the system. By equating the two terms and considering $M = (4\pi/3)\rho R^3$ we can recover once more the minimum scale and mass for the collapse

$$R = \left(\frac{15k_BT}{4\pi\mu m_u \rho G}\right)^{1/2} \tag{3.66}$$

$$M = \left(\frac{5k_BT}{\mu m_u G}\right)^{3/2}\left(\frac{3}{4\pi\rho}\right)^{1/2}. \tag{3.67}$$

Of course, this is note the only possible equation of virial equilibrium. Indeed, if we consider different terms entering the virial theorem, for example we assume to have a self-gravitating cloud of gas threaded by a constant uniform magnetic field B, we can derive the critical condition for the magnetic field to prevent the collapse. For simplicity, we assume the magnetic energy is larger than kinetic and thermal, so the virial equilibrium equation reads:

$$E_{mag} + E_{grav} = 0\,. \tag{3.68}$$

Neglecting the surface terms, the magnetic energy in the cloud is given by

$$E_{mag} \sim \frac{B^2 R^3}{6} \sim \frac{\Psi^2}{6\pi^2 R}, \tag{3.69}$$

where in the last expression we replaced the flux of the magnetic field $\Psi = B\pi R^2$. Using the previous expression for the gravitational term, the virial equilibrium equation is

$$\frac{\Psi^2}{6\pi^2 R} - \frac{3}{5}\frac{GM^2}{R} = 0\,, \tag{3.70}$$

from which one can derive a new threshold condition for the magnetic flux in order to have a collapse. In fact, only if

$$\Psi \lesssim \sqrt{\frac{18}{5} G\pi^2 M^2}\,, \tag{3.71}$$

the collapse can proceed. We finally notice that, from this approximated argument, since the term $\sqrt{\frac{18}{5}G\pi^2}$ is a constant, also the ratio Ψ/M is fixed, which means that the condition on the collapse is blocked. If the magnetic flux is strong enough to halt the collapse, the cloud will never collapse. On the other hand, if the the flux is too weak, it will never manage during the contraction, to halt the collapse of the cloud.

3.3. Feedback mechanisms

If what presented so far was the full story about star formation, it would impossible to reproduce observational results. Indeed, the gravitational collapse theory is a correct theory but incomplete, it is like if we repainted the waterlilies by Monet drawing the leaves as round green circles and the water as homogeneous light blue expanse. For example, the gravitational collapse theory predicts all the gas mass to be eventually transformed into stars, however observations contradicts this scenario with only few percent of gas effectively transformed into stellar objects (see Section 2.3.3). Moreover, a pure free-fall collapse is unable to recover the observed IMF, since there is an overproduction of massive stars. The fraction of bounded stars still in cluster is also usually another critical point for simulations, because they tend to produce mainly bound clusters. If we have a look to observations of star forming regions, we found presence of warm ISM, X ray emissions and Hα lines of ionised gas within the molecular gas nebula. All this need an explanation.

The quite reasonable assumption behind this is that stars, once formed and during the formation itself, have deep impact on the surrounding gaseous environment through their stellar evolution mechanisms and as a consequence on the star formation process itself. This influence translates into an injection of energy and momentum into the gas, which is what is normally referred to as *stellar feedback*.

Feedback is a general term which includes a list of possible mechanisms which can shape the medium. The first big distinction within feedback is made by the timescale over which energy is injected/radiated away, which is what discriminates between momentum feedback and explosive feedback. If the gas is very efficient in radiative cooling the energy injected from stars, the dominant feedback will come actually from the momentum injection. Protostellar outflows and radiation pressure are examples of this.

On the other hand, if stars heat up quickly the gas, this latter is unable to cool down in less than a cloud dynamical time, therefore this hot, higher pressure gas violently expands and affects the cloud structure. The kinetic energy difference between explosive and momentum feedback can be up to a factor of 400. Examples of explosive feedback are winds from massive stars, phoionisation and supernovae. On top of this, also the non-ionising radiation emitted from stars contribute to heat the gas, constituting a form of thermal feedback. However, this last effect does not affect the large-structure of the cloud, even if it inevitably influences the fragmentation process (see section 3.2.1).

We will now describe the main types of stellar feedback. The main reference for this section are the reviews by Krumholz et al. (2014) and Dale (2015), which provide an exhaustive treatment to the topic. We will focus on feedback mechanisms which potentially affect large scales and dispersal of the collapsing cloud, hence we will neglect the thermal effect of radiation on the direct surroundings of stars. We will also not discuss the mutual interaction between distinct feedback processes or the combined effect of magnetic fields and stellar feedback, because in Chapter 5 the numerical simulations conducted will focus exclusively on photoionisation in a non-magnetised cloud. We will discuss in that context whether the contributions of other effects is necessary and what are the expected outcomes.

3.3.1. Stellar winds

3.3.1.1. Protostellar outflows

Protostellar objects have been observed ejecting significant amount of their mass via outflows and jets (Bjerkeli et al. 2016, see Bally 2016 for a review).

Even if the exact mechanism is not yet know, outflows are though to be the way the protostellar system can lower the angular moment gained from the inspiraling material and therefore keep accreting from the circumstellar disk.

The average velocity V_{out} of these outflows (estimated as the total momentum carried by outflows divided by the total mass in outflows) is around 20-40 km/s (Matzner, 2007). Despite the lower escape velocities, the main contributors to the outflow average velocity estimate are low-mass stars, because most of the mass of the cluster is found in them (Krumholz et al., 2014). This type of feedback is considered important when stars are generated close in space and time. The main ways outflows are considered to have an impact on the cloud is trough rapid cloud dispersal (Elmegreen, 2007) and/or as sustain for turbulence (Nakamura & Li, 2014; Tan et al., 2006).

From a theoretical point of view, the momentum injection could give the cloud a total velocity equal to $SFE \times V_{out}$, which, taking SFE = 20% and $V_{out} = 25km/s$, means about 5 km/s. For small clouds, this value is higher than the typical velocity dispersion, hence it could in principle unbind most of the cloud (Matzner, 2007; Matzner & Jumper, 2015). However, one should consider that this works in the assumption that all the outflow would kick in together at the same time. Among the caveats, we point out that according to some observations (Arce et al., 2010; Narayanan et al., 2012), the total kinetic energy of outflows is only 20% the cloud binding energy, hence outflows alone cannot disperse the cloud, only eventually in combination with other feedback mechanisms.On the other hand, (Dunham et al., 2014) claims that actual observations underestimate the outflows masses and momenta and they are expected to be more energetic than reported. For small clouds (e.g. L1551) the situation is a bit different and outflows can produce a significant gas cavity (Stojimirović et al., 2006)

Aside from the unbinding power of outflows, if the momentum injection happens gradually, then they could maintain turbulence against dissipation and produce as a result an extended star formation and aeduction of the star formation rate (Li & Nakamura, 2006; Matzner, 2007; Nakamura & Li, 2014). In this case observations confirm that outflows appear capable of driving turbulence, with a total energy up to $\sim 30\%$ the turbulent energy of the cloud (Arce et al., 2010; Bally et al., 2014; Curtis et al., 2010; Narayanan et al., 2012). The total outflow power results comparable with the turbulent energy dissipation rate, which means outflows are not only able to drive turbulence but also to sustain it (Nakamura et al., 2011). Despite all this, a full description of how outflow motions are converted into

turbulence is still an open issue. Moreover, it is still unclear why the outflow injection scale is much smaller than the scale at which outflows are detected. This seems to indicate that outflows can not be the source of turbulence on scales larger than 10 pc and and alternative possibilities should be considered.

Protostellar outflows directly affect also massive stars formation in the same clump. In fact, Wang et al. (2010) found that simulated outflows are responsible for breaking up the dense filaments feeding massive stars at early times, therefore mass accretion rates of these latter are reduced.

3.3.1.2. Massive hot stars

Massive ($> 40M_{\odot}$) hot ($> 2.5 \times 10^3 K$) stars produce strong stellar winds, which can reach very high terminal velocities ($\sim 1000 km/s$) (Vink, 2011). However, overall the total momentum per star mass is less than the radiation field one, around 20-30 km/s (Krumholz et al., 2014). Wind mass fluxes are typically $10^{-5} - 10^{-4} M_{\odot} yr^{-1}$ (Dale, 2015). These estimates are based on stellar models without rotation: the inclusion of this latter is expected to increase the values for the winds momentum. A certain level of uncertainty in inevitable, because the process of evolution from massive stars to luminous blue variable is mostly unknown. The power of stellar winds as a source for violent feedback resides in the shocks between terminal high velocities winds, which can heat the ISM up to $10^7 K$. At such high temperature, radiative losses can not cool rapidly, therefore the gas stays warm and an energy-driven, adiabatic flow can be generated. This, however, assume no leaks, while winds could escape from their expanding shells, hence diminish the effective pressure. The real contribution of winds to the general dynamical budget is still not clear.

Measurements of X-ray luminosities from the hot post-shock wind gas in HII regions (M17, Rosette Nebula, Carina Nebula, 30 Doradus) seems to rule out a determinant role of winds in large-scale dynamics (Lopez et al., 2011; Pellegrini et al., 2011; Townsley et al., 2011, 2006, 2003). From theoretical modelling of massive star winds it emerges the crucial effect of leakage. Indeed in models where this was not taken into account the wind feedback resulted dominant Arthur (2012); Castor et al. (1975); Silich & Tenorio-Tagle (2013); Weaver et al. (1977). In principle indeed, the integrated kinetic energy of winds is comparable with the one injected by supernovae. However, according to Clarke et al. (2015), the minor effect of winds can be ascribed to the highly inhomogeneous front seen by massive stars, which typically form at the intersection of massive filaments and hence are sur-

rounded by a highly anisotropic distribution of gas. The winds produces can therefore escape through low-density channel.

Examining different mechanism through which clusters can lose the wind energy (radiative cooling, mechanical work on the gas, thermal conduction, collisional dust heating, and physical leakage of hot gas), Rosen et al. (2014) found that large fractions of the it is lost via leakage of hot wind gas through holes in the bubble shell, created by stellar feedback itself or due to the expansion of the shell in a non-uniform ISM. As alternative they also found that hot gas could lose a significant amount of energy by mixing with the cold gas, followed by thermal conduction at the turbulent interface.

The first scenario found confirmation in the numerical simulations by Rogers & Pittard (2013), which claims that the hot gas due to shock heated stellar winds from O stars flows out from the cloud via low-density channel. Other recent simulations (Fierlinger et al., 2016) found that the radiative losses peak during the pressure-driven phase of the stellar wind generated bubble are located near the contact discontinuity. The scales of mixing processes across the discontinuity set the amount of retained energy. When combining the effect of winds with other sources of feedback (supernovae, photoionisation), Dale et al. (2014); Peters et al. (2016) found that the impact of winds is minimal.

3.3.2. Radiation-gas interaction

3.3.2.1. Radiation pressure

Radiation pressure is strictly speaking a force, which in some specific cases can be written as pressure-gradient force, and in this cases the term "radiation pressure" is appropriated. In general, radiation generated by stars transfers momentum to the surrounding cloud, this is what is defined as radiation force (Krumholz et al., 2014). The radiation we are talking about is both the direct optical and ultraviolet (UV) emission from (mainly) massive stars and the infrared (IR) radiation coming from dust. In the first cases we are dealing with anisotropic photons which interact with the gas once, deposit their momentum and free-stream away. In the case of dust, if the cloud density is enough to be opaque to IR radiation, the emitted infrared photons are trapped and they can effectively be considered isotropic radiation. In this specific, case photons effects can be described in terms of pressure, which drives the expansion much more efficiently than single kicks momentum transfer. UV photons are trapped only in the interior of stars, otherwise their effect is of direct radiation force. Rosdahl &

Teyssier (2015) found that the effects of radiation force becomes comparable to photoionisation heating only for ultra-compact region with density higher than $10^{-15} g/cm^3$ and size smaller than $10^{-3} pc$.

Theoretically (Krumholz & Matzner, 2009; Murray et al., 2010), the effect of pressure from infrared radiation has been usually modelled parametrising the fraction of photons trapped in an opaque cloud. This parameter f measures how effective the radiation force is. If $f >> 1$, then photons have many interactions with the medium and radiation pressure would have large effect on the cloud, while, if f =1, photons deposit their momentum at the first absorption and escape. This technique was used in larger scale simulations (galaxy formation) as radiation pressure subgrid recipe (Agertz et al., 2013; Hopkins et al., 2011), in which single scattering ionising radiation is boosted with a photon trapping factor, dependent on the optical depth of the cloud to infrared radiation. Clearly, the choice of value assumed by this parameter has huge impact on the outcome of the simulation, resulting in contrasting conclusions from different studies. More recent radiation hydrodynamics simulations (Raskutti et al., 2016; Skinner & Ostriker, 2015) found that in these subgrid models the true reprocessed radiation could be overestimated by a factor of 5. They found also that reprocessed radiation could be able to eject considerable amount of mass from a cloud and affect star formation, only for opacity values and dust abundances higher than what expected for Solar metallicity. Krumholz & Thompson (2013) also found that the trapped photons parameter is close to one, due to the contrasting effect on Rayleigh-Taylor instability on the gas configuration which allows photons to escape trough optically thin bubbles and therefore causes the reduction of momentum transfer rate. The overall picture seems to suggest that, even if on small scales radiation forces can be stronger than gravity, radiation pressure eventually fails to stop accretion (Krumholz et al., 2014). Kuiper et al. (2010) reached the same conclusion, without invoking Rayleigh-Taylor instability, but taking into account frequency-dependent radiative feedback and dust sublimation front.

From an observational point of view, it is not yet established the importance of observed radiative pressure, due to contrasting conclusions for the HII region 30 Doradus (Lopez et al., 2011, 2014; Pellegrini et al., 2011). Despite disagreement on the importance of radiation pressure on small scale, a general conclusion seems to be than the effect of these type of feedback are anyway secondary respect to the dominant effects of warm ionised gas pressure in this region.

3.3.2.2. Photoionisation

A large part of very hot and massive stars' spectrum is represented by ionising radiation. The interaction of photons of energy > 13.6 eV with neutral hydrogen gas gives rise to what is called *HII region*, which is basically a bubble of ionised gas. The basics properties of this region can be derived analytically (Strömgren, 1939). The number of ionising photons per second emitted is represented by Q_H. These photons once emitted constitute an *ionisation front* which expands progressively. Photons deposit the energy onto neutral atoms, ionising them, and then stream away. The new photons emitted will therefore ionise more and more distant atoms. If the cloud has a number density n_0, the assumption of neutrality requires that when the cloud gets fully ionised than the number density of ions and electrons is equal to n_0, i.e. $n_0 = n_{ions} = n_e$. However, while the ionisation front advances, some ions recombine with electrons. Some photons will therefore do not contribute to expansion of the front but they will re-ionise recombined atoms. When the recombination rate equals the ionisation rate, a stationary situation is reached and the HII region will have reached a constant volume of radius R_S. The volumetric recombination rate is given by $\alpha n_e n_i = \alpha n_0^2$, where α is the recombination coefficient (considering only recombinations to states above the ground one).The volumetric ionisation rate quantifies the number of atoms ionised per second per unit volume and it is calculated as $n_0 \int_{\nu_0}^{\infty} \frac{L_\nu}{4\pi r^2 h\nu} \alpha_\nu d\nu$, where L_ν is the luminosity of the star and α_ν is the photoionisation cross section. It can be demonstrated that the ionisation rate is equivalent to $\frac{3Q_0}{4\pi R^3}$, where Q_0 is the emission rate and R is the extent of the HII region. Equating recombination rate and emission rate of the source in case of a fully ionised cloud,we get

$$\alpha n_0^2 = \frac{3Q_0}{4\pi R_S^3}\,, \tag{3.72}$$

which immediately leads to the final size of the HII region (Strömgren Sphere)

$$R_S = \left(\frac{3Q_0}{4\pi\alpha n_0^2}\right)^{1/3}\,. \tag{3.73}$$

Due to highly energetic photons absorption, the ionised gas inside the Strömgren sphere heats up to temperature $\sim 10^4 K$. At this temperature metal cooling is not particularly efficient. Therefore the temperature difference between ionised and neutral gas outside the nebula (10-100K), will

determine the onset of an overpressure inside the HII region, which will drive the expansion even further. The radial evolution of this second phase of expansion of the HII region was first derived by Spitzer (1978) and it is given by

$$R(t) = R_S \left(1 + \frac{7}{4}\frac{c_i t}{R_S}\right)^{4/7}, \tag{3.74}$$

where R_S is the initial radius, equal to the Strömgren sphere radius and c_i is the sound speed of the ionised gas.

From an observational point of view, HII regions are very well studied at radio and infrared wavelength and can be found in diffuse (1-30 pc) or more compact (0.01-0.5 pc) configurations. In ultra-compact HII regions the density can be higher than 10^5 particles pc^{-3}. They are usually not characterised by a regular spherical shape, but, depending on the surrounding mass distribution variations, can have cometary, elongated or irregular morphologies (Fuente et al., 2010; Hampton et al., 2016).

Theoretically, photoionisation is expected to stop the growth of massive stars, however results from observations and simulations indicate the opposite (Klaassen & Wilson, 2007; Peters et al., 2010). On larger scale, photoionisation is expected to drive turbulence (Dale et al., 2012b; Walch et al., 2012) and destroy the parent molecular clouds. However, on this last point there is some disagreement when dealing with turbulent, structured clouds. Some simulations suggest photoionisation is very effective in destroying $10^4\mathrm{M}_\odot$ clouds within 1 Myr (Walch et al., 2012), others found that the success of photoionisation depends on the cloud's escape velocity, reaching a maximum for clouds with escape velocities $<$10 km/s (Dale et al., 2012b). We will come back on this extensively in Chapter 5, when describing the outcome of our simulations of star cluster formation.

3.3.3. Supernovae

The last stage of massive stars ($> 8\mathrm{M}_\odot$) is represented by the explosion as supernova. This can significantly affect the cluster evolution in principle, since the energy injected is of order 10^{51} erg. However, the real contribution of supernovae explosions to the disruption of the gas is minimal. The main reason for this is the timescale of the phenomenon: the first supernovae starts exploding around 3-4 Myr, which, depending on the mass of the protocluster, can be much larger than the free-fall time. This means that almost all the gas has been already converted into stellar objects, before the first supernovae could explode. This is typically the case for clusters with

masses $\sim 10^4$, for which there must be another mechanism effective earlier in dispersing the gas. This finds confirmation in observations of Westerlund I, (Muno et al., 2006a,b), where traces of supernova explosion have been detected, but no correspondent shock-remnant has been found, probably because the gas already got ejected. A totally different case is when dealing with much more massive initial clouds (10^6 $M_\odot$), where the dynamical time is larger and the previous feedback mechanisms are probably not strong enough to destroy the gaseous structure. In this case, the contribution from supernovae explosions is definitely needed and should be taken into account (Geen et al., 2016). Supernovae can also play an important role connecting the scale of star clusters to that of galaxies. Massive stars are often found in binary systems, characterised by very high orbital velocities. The evolution to supernova of one of the binary members, or a three body interaction, can cause the ejection of the second massive star. Many escaping massive stars (runaways) constitute a source of energy which can be released at much larger distance from their star cluster of birth and can change the structure of the interstellar medium (Gatto et al., 2015).

4

Dynamical Evolution of Stellar Systems

If star formation is art, then stellar dynamics is solid technical craftwork. Dynamics is a fortress, a castle made of simple but solid bricks, whose theory consists in steadily posing one stone next to each other and then build over this a second layer, and a third and so on. At any step, one can stop and the castle is there, maybe incomplete, but clearly in the shape of a castle, as solid as the gravitational force.

In this chapter, indeed, we focus on the description of classic internal dynamical theory of star clusters. For this scope, we define a star cluster as a system of N point masses, affected only by gravitational interactions. The textbooks and reference material for this chapter are Spitzer (1987), Binney & Tremaine (2008) and Bertin (2014).

The first crucial distinction to be made is between *collisional* and *collisionless* systems. The criterion for this distinction is based on the age of the system and its two-body relaxation timescale, which is a concept we will derive properly in the next sections. To give a first definition, the two-body relaxation timescale is defined as the timescale over which the stars in the system lose memory of the original initial kinematics of the system and this happens because of repeated long-distance two-body interactions, during which particles slowly exchange energy. This is just the natural consequence of gravity being a long-range force, which means that the influ-

ence from distant bodies is not (always) negligible. The cumulative effect of all these weak, mutual interactions changes the state of the system toward equilibrium, which is the most general definition of relaxation process.

Collisionless systems are those, whose lifetime is shorter that the relaxation timescale, which means that for those systems interactions between particles are negligible. In this case particles are effectively only subjected to the influence of a collective gravitational potential, generated by an approximately uniform mass distribution. Collisional systems are instead systems, for which the lifetime is comparable with the relaxation time. Therefore two-body relaxation is, in this case, an efficient process to redistribute energy between particles.

Emblematic examples of collisionless systems are galaxies, for which the two-body relaxation timescale is $\sim 10^5 - 10^8$ Gyr, even larger than the Hubble time. Star clusters, instead, belong to the category of collisional systems, with two-body relaxation timescales which span from $10^2 - 10^3$ Myr for globular clusters to < 100 Myr for open clusters and 10 Myr for dense star clusters. From what we reported in Chapter 2, it is clear that for all categories of star clusters the relaxation time is comparable or lower than the age, so stellar interactions play a crucial in driving dynamical evolution for these objects.

4.1. Star cluster equilibrium models

In Chapter 2 we saw how star clusters' surface brightness profiles can be empirically fitted by some analytic expressions (e.g. King and EFF profiles). We will try now to theoretically develop models which describe the structure of star clusters, explaining the empirical fit. The easiest approach is usually to describe the stellar system statistically, in terms of its distribution function $f(\boldsymbol{x}, \boldsymbol{v}, t)$ (also called phase-space density) which is defined such that

$$f(\boldsymbol{x}, \boldsymbol{v}, t) d^3\boldsymbol{x} d^3\boldsymbol{v} \tag{4.1}$$

represents the probability of finding a star a time t in the six-dimensional phase-space $d^3\boldsymbol{x} d^3\boldsymbol{v}$ around the position $(\boldsymbol{x}, \boldsymbol{v})$.

However, we point out that strictly speaking distribution functions are well defined only in case of collisionless systems, where stellar mass is assumed to be distributed smoothly. Therefore we assume that, for a short time, also a collisional systems can be described by continuos functions. The models we will derive constitute a "zero-order" approximation for the

structure of star clusters, in which interactions between particles and other time dependent effects are neglected. The collisional nature of star clusters will be taken into account as perturbation to these equilibria in Section 4.2.

If we assume (for the moment) that a star cluster is a collisionless system, the evolution of f with time is described by the *collisionless Boltzmann equation*

$$\frac{\partial f}{\partial t} + \boldsymbol{v} \cdot \frac{\partial f}{\partial \boldsymbol{x}} - \frac{\partial \phi}{\partial \boldsymbol{x}} \cdot \frac{\partial f}{\partial \boldsymbol{v}} = 0 \tag{4.2}$$

where ϕ is defined by the Poisson's equation,

$$\nabla^2 \phi(\boldsymbol{x}, t) = 4\pi G \rho(\boldsymbol{x}, t)\,, \tag{4.3}$$

with G being the gravitational constant and ρ the density of the system. If the system we want to describe is in equilibrium, this requires that the gravitational potential does not change with time, i.e. $\phi(\boldsymbol{x}, t) = \phi(\boldsymbol{x})$ and the distribution function is steady-state i.e. $f(\boldsymbol{x}, \boldsymbol{v}, t) = f(\boldsymbol{x}, \boldsymbol{v})$.

The next necessary step is establishing the connection between ρ and f. In general, by integrating f with respect to the velocity all over the phase space, $\int f(\boldsymbol{x}, \boldsymbol{v}) d^3\boldsymbol{v}$, we get the probability of finding a star at $\boldsymbol{x}$, regardless of its velocity. For convenience, we can redefine $f d^3\boldsymbol{x} d^3\boldsymbol{v}$ as the the expected total mass of stars in $d^3\boldsymbol{x} d^3\boldsymbol{v}$, by multiplying f for the total mass M of the system. In this way, the density ρ is related to f as

$$\rho(\boldsymbol{x}) = \int f(\boldsymbol{x}, \boldsymbol{v}) d^3\boldsymbol{v}\,. \tag{4.4}$$

Similarly, the probability distribution of stellar velocities at $\boldsymbol{x}$, $P_x(\boldsymbol{v})$, can be obtained dividing $f(\boldsymbol{x}, \boldsymbol{v})$ by $\rho(\boldsymbol{x})$. From this is possible to derive then the mean velocity at $\boldsymbol{x}$ and the associated velocity dispersion, by taking the second (i.e. $\int \boldsymbol{v} P_x(\boldsymbol{v}) d^3\boldsymbol{v}$) and third moment (i.e. $\int \frac{\boldsymbol{v}^2}{2} P_x(\boldsymbol{v}) d^3\boldsymbol{v}$) of the velocity distribution function $P_x(\boldsymbol{v})$.

We now have to choose an expression for f in phase space and from this derive the consequent expression for the density in real space. The Jeans theorem says that any steady-state solution of the collisionless Boltzmann equation depends on the phase-space coordinates only through integrals of motion in the given potential, and any function of the integrals yields a steady-state solution of the collisionless Boltzmann equation (Binney & Tremaine, 2008). Therefore, if we suppose that the system we aim to model is spherical and with isotropic velocity distribution, f depends only on the energy $E = \frac{1}{2}v^2 - \phi$ (a bound system has the extra requirement of E <0).

Combining now equations 4.3 and 4.4, using the Laplacian in spherical coordinates, we obtain

$$\frac{1}{r^2}\frac{d}{dr}\left(r^2\frac{d\phi}{dr}\right) = -4\pi G\int f(\frac{1}{2}v^2-\phi)d^3\boldsymbol{v}\,. \tag{4.5}$$

Once defined $f(E)$, the integro-dfferential equation for $\phi(\boldsymbol{r})$ can be solved. From that it is immediate to derive the correspondant density profile. The main simple expressions for f used in the description of star clusters are the followings.

- Polytropes and the Plummer model
  The distribution function in this case has the form

$$f(E) = \begin{cases} FE^{n-3/2} & (E<0) \\ 0 & (E\geq 0). \end{cases} \tag{4.6}$$

  It can be demonstrated that in this case $\rho = c_n\phi^n$, from which it comes the analogy with the polytropic equation of state of gas $P\propto\rho^\gamma$ (P is the pressure and $\gamma = 1+\frac{1}{n}$). In order for c_n to be finite, the condition on n is $n > 1/2$. A general simple analytic solution for equation 4.5 can not be found for every n. The interesting case for us is $n = 5$, for which the solution for the potential has the following expression

$$\phi(r) = -\frac{GM}{\sqrt{r^2+b^2}}\,, \tag{4.7}$$

  with M being the mass of the system and b defining a characteristic scale length, which guarantees the central potential and density to be finite. This is called the *Plummer model*. The correspondent density profile is given by

$$\rho(r) = \frac{3M}{4\pi b^3}\left(1+\frac{r^2}{b^2}\right)^{-5/2}. \tag{4.8}$$

- Isothermal sphere
  The asymptotic limit of the polytropic model is the isothermal sphere. Indeed, by taking $n\to\infty$, $\gamma = 1$ and $P\propto\rho$., which is the equation of state of an isothermal gas. Isothermal gases have a Maxwell-Boltzmann velocity distribution, with velocity dispersion σ. In analogy with this, the isothermal sphere is represented by the following distribution function

$$f(E) = \rho_1(2\pi\sigma^2)^{3/2}e^{-E/\sigma^2} \tag{4.9}$$

which, integrated over the velocity, gives the relation $\rho = \rho_1 e^{\phi/\sigma^2}$. Inserting the latter in the Poisson's equation yields

$$\frac{1}{r^2}\frac{d}{dr}\left(r^2\frac{d\phi}{dr}\right) = -\frac{4\pi G}{\sigma^2}r^2\rho\,. \tag{4.10}$$

Note that a similar result would have been obtained starting from the hydrostatic equilibrium equation (see Equation 3.8),

$$\frac{1}{r^2}\frac{d}{dr}\left(r^2\frac{d\phi}{dr}\right) = -\frac{4\pi G m}{k_B T}r^2\rho\,. \tag{4.11}$$

We notice that equations 4.10 and 4.11 coincide if $\sigma^2 = \frac{k_B T}{m}$, which proves that a collisions system of stars represented by equation 4.9 has the same structure of an isothermal sphere of gas with temperature T. The resulting density-potential couple is

$$\rho(r) = \frac{\sigma^2}{2\pi G r^2} \tag{4.12}$$

$$\phi = 2\sigma^2\ln(r) + constant. \tag{4.13}$$

From the previous expression, it is clear that the density goes to infinity for r=0, indeed the isothermal sphere model is also addressed as *singular* isothermal sphere. Moreover, by further integration of the density profile, $M \propto r$, thus we also retrieve that the mass is another infinite quantity, this time for $r \to +\infty$

- King models or non-singular lowered isothermal sphere The King model is basically an isothermal sphere without singularities. To eliminate the density divergence in the origin the radial coordinate is rescaled, introducing a new scale radius

$$r_0 = \sqrt{\frac{3\sigma^2}{4\pi G\rho}}\,, \tag{4.14}$$

called *King radius*. In Section 2.1 we already saw that the surface brightness profile can be fitted by what we called an empirical King model, whose characteristic scale is set by r_c, the core radius, which sets the radius at which the surface brightness dropped by a factor of 0.5. It is very common to consider the King radius, r_0, simply a synonym of the core radius r_c, however it is important to stress that

$r_0 \simeq r_c$ only for concentrated King models (large values of r_t/r_0, see later for a definition of r_t).

To eliminate the problem of infinite mass, the distribution function of the isothermal gets modified and for $E \geq 0$ is set to zero,

$$f(E) = \begin{cases} \rho_1 (2\pi\sigma^2)^{3/2} (e^{-E/\sigma^2} - 1) & E < 0 \\ 0 & E \geq 0, \end{cases} \tag{4.15}$$

in this way the system has an escape velocity, unlike the isothermal sphere. This means that the mass of the system is truncated at a certain radius, r_t, and therefore is finite. This radius is called the *tidal (or truncation) radius* and it is defined as the the radius where ϕ tends to a constant $\phi(r_t) = \frac{-GM(r_t)}{r_t}$. Integrating f over all velocities, one derives the expression for the density as a function of the relative potential ($\Psi = -\phi + \phi_0$) :

$$\rho(\Psi) = \rho_1 \left[e^{\Psi/\sigma^2} erf\left(\frac{\sqrt{\Psi}}{\sigma}\right) - \sqrt{\frac{4\Psi}{\pi\sigma^2}} \left(1 + \frac{2\Psi}{3\sigma^2}\right) \right]. \tag{4.16}$$

Once inserted in the Poisson's equation, it is possible to solve for Ψ and from here derive the density profile, which mirrors the surface brightness profiles showed in Section 2.1. The King radius r_c and the tidal radius r_t define two area of the system, i.e. the core ($r < r_c$) and the halo ($r_c < r < r_t$), which exhibit distinct properties. Indeed, the core is effectively almost isothermal, hence the velocity dispersion does not change with radius and the density is roughly constant. In the halo the density is lower and the velocity distribution is no longer Maxwellian, but instead a truncated Maxwellian, with the velocity dispersion decreasing monotonically with radius and becoming null at the tidal radius. As already stated in Section 2.1 the key parameter which describes the parameter of a King model is the concentration c, defined as $c = \log_{10}(r_t/r_c)$. Alternatively, it is also common to use the dimensionless central potential $W_0 = \frac{\phi(r_t) - \phi(0)}{\sigma^2}$, which indicates the depth of the potential well of the system. The two parameters c and W_0 are linearly dependent from each other. The higher the value of c or W_0, the more concentrated the star cluster is. Asymptotically, for $c \to +\infty$, the King model tends to the isothermal sphere.

4.1.1. Size scales

We give here a summary of the main radial scales used, when describing the structure of star clusters.

In the previous section we described the King radius r_0, which identifies the core of the cluster. The observational correspondent of this is the core radius r_c, which is the scale at which the surface brightness dropped of a half. Even if these two definitions do not always fully overlap, they both circumscribe the densest part of the core, where there is higher concentration of bright stars.

In N-body simulations, the core radius is defined exactly considering this last property: the core radius is indeed calculated as a the ρ_i^2-weighted rms stellar distance from the density centre ($r_{core} = \sqrt{\frac{\sum_i \rho_i^2 r_i^2}{\sum_i \rho_i^2}}$), where ρ_i is the local density of the ith-star computed considering the star's k nearest neighbours (Portegies Zwart et al., 2010).

The tidal (or truncation) radius was defined as the radius at which the density of stars drops to zero (or to field value). It is considered the ultimate boundary of the star cluster, where in principle the tidal forces of the host galaxy becomes comparable with the gravitational force of the star cluster.

Another important length-scale quantity is the so-called *virial radius*. This has a pure theoretical definition, which is

$$r_{vir} = \frac{GM^2}{2|U|}, \tag{4.17}$$

where M is the total mass and U is the potential energy of the system (Portegies Zwart et al., 2010).

As last, we recall the half-light (or effective) radius which observationally indicated as the radius which contains half of the projected luminosity of the star cluster. The theoretical analogue is represented by the *half-mass radius*, which simply includes half of the mass of the system and it is $\sim r_{vir}$ most of the times.

4.2. The granularity of the gravitational field: Two-body relaxation

As already anticipated at the beginning of the previous section, the analytical models presented constitute only a first approximation description of the structure of a star cluster. They were derived assuming, for simplicity, that the star clusters could be considered collisionless systems, hence the

gravitational potential was assumed to be a smooth function of the position.

However, since star clusters are actually collisional systems, to give a proper description of these systems, we have to drop the simplified assumption for the potential and consider that the gravitational potential is composed of individual particles, therefore it will slightly fluctuates from point to point in the cluster. Stars orbiting in the cluster will experience these small fluctuations generated by other stars in the field (from here the name *two-body*), or larger fluctuations when passing closer to each other, which will modify locally their velocities. The cumulative effect of small changes in the velocity is the dominant one and can be compared to a random walk process. The net effect of this relaxation process is to lead the velocity distribution towards an equilibrium state, represented by a Maxwellian distribution. Therefore this specific type of relaxation is also defined as "thermalisation".

The timescale for this to happen is the two-body relaxation timescale, which quantifies the time needed to significantly alter the velocity of a particle through two-body gravitational interactions by other stars. If the outcome of two-body relaxation is the Maxwellian distribution function[1], it means that the probability of finding a star in a particular state of energy E_i is $P_i = Cg_i e^{-E_i}$, where C is a normalisation constant and g_i is the phase space volume available. Therefore, the probability maximises either if E_i becomes more negative, hence particles get bounder, and/or if the phase-space volume gets larger, hence if the particle distribution extends spatially. However since there is no upper limit on the spatial extent, there is no maximum entropy for a gravitational system with finite mass and energy. Hence the equilibrium can not be reached in this way and the system keeps evolving (Spitzer, 1987). Moreover, to maximise the aforementioned probability and conserve the total energy, both the contraction of the central part of the cluster and the expansion of the outer "halo" must take place at the same time[2]. Specifically, there are three processes which are direct consequence of this thermal relaxation and drive the cluster evolution, i.e. evaporation, core-collapse and equipartition. We will see their effect on the cluster in the next sections, now we first quantitatively derive the expression for the two-body relaxation timescale.

[1] The outcome is actually a near-Maxwellian, due to the fact that mass is finite, hence there is an escape velocity threshold.

[2] And this is a very general consideration, which apply to every gravitational system.

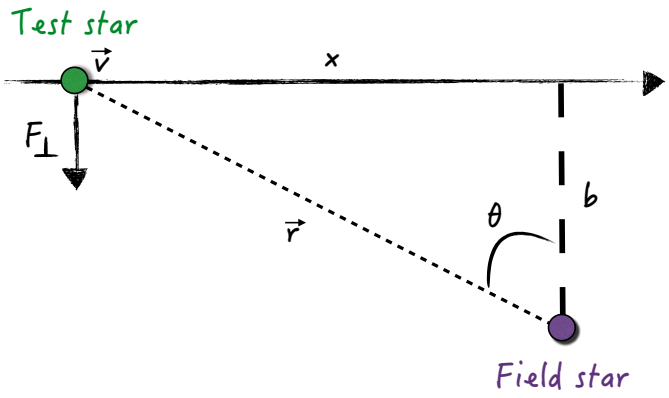

Figure 4.1: Schematic representation of the interaction between a moving test star (green) and a field star (purple).

4.2.1. Timescales

The scale over which thermalisation takes place can be computed from an-order-of-magnitude point of view quite easily, considering the interaction between an individual particle and field stars encountered across its orbit, we will then estimate how much the initial velocity of the individual particle is affected by the interaction (Binney & Tremaine, 2008).

Let's suppose that the star cluster is composed of N identical particles, of mass m and is characterised by size R and uniform density. Let's picture a situation in which a test star is travelling with relative velocity $\boldsymbol{v}$ and impact parameter b nearby a field star, like it is sketched in Figure 4.1. Since we are interested in studying long range encounters, we assume that after the interaction the change in velocity $\delta\boldsymbol{v}$ of the test star is small, that is $|\delta\boldsymbol{v}|/|\boldsymbol{v}| << 1$. In this way, we can also assume that the test star proceeds on a straight line trajectory and the field star is effectively stationary. With these simplifications the variation of velocity is directed perpendicular to the trajectory. To compute the magnitude of $\delta\boldsymbol{v}$, i.e. δv, (similarly, $v = |\boldsymbol{v}|$) we integrate the perpendicular component of the gravitational force be-

tween the two particles ($F_\perp$), which is

$$F_\perp = \frac{Gm^2}{r^3} r_\perp = \frac{Gm^2}{r^2}\cos\theta = \frac{Gm^2 b}{(b^2+x^2)^{3/2}} = \frac{Gm^2}{b}\left[1+\left(\frac{vt}{b}\right)^2\right]^{-\frac{3}{2}}. \tag{4.18}$$

Integration along the trajectory leads to

$$\delta v = \frac{1}{m}\int_{-\infty}^{\infty} F_\perp \mathrm{d}t = \frac{Gm}{b^2}\int_{-\infty}^{\infty} \frac{\mathrm{d}t}{[1+(vt/b)^2]^{3/2}}, \tag{4.19}$$

where we change the variable of integration as $s = \frac{vt}{b}$ and $\mathrm{d}s = \frac{v}{b}\mathrm{d}t$, and we get

$$\delta v = \frac{Gm}{vb}\int_{-\infty}^{\infty} \frac{\mathrm{d}s}{(1+s^2)^{3/2}} = \frac{2Gm}{bv}. \tag{4.20}$$

From this, it results that δv to first-order approximation can be interpreted as the acceleration at closest approach, $\frac{Gm}{b^2}$, multiplied for the duration of this acceleration, $\frac{2b}{v}$. So far we accounted for only one two-body encounter, the next step is then to generalise this result considering all two-body interactions that the test star experiences. If the star cluster contains in total N stars and has a radius R, the surface density of particles is $\frac{N}{\pi R^2}$, so the test star suffers a number δn of encounters

$$\delta n = \frac{N}{\pi R^2} 2\pi b \mathrm{d}b \tag{4.21}$$

with impact parameter b between b and $b + \mathrm{d}b$. Since the distribution of particle is isotropic, every encounter produces a randomly-oriented perturbation δv, whose sum averages out to zero, when considering the mean velocity change. However, the mean-square change in velocity is not zero

$$\sum \delta v^2 \sim \delta v \delta n = \left(\frac{2Gm}{vb}\right)^2 \frac{2N}{R^2} b\mathrm{d}b = 8N\left(\frac{Gm}{vR}\right)^2 \frac{\mathrm{d}b}{b}. \tag{4.22}$$

Integrating over all impact parameters from b_{min} to b_{max} yields

$$\Delta v^2 = 8N\left(\frac{Gm}{vR}\right)^2 \int_{b_{min}}^{b_{max}} \frac{\mathrm{d}b}{b} = 8N\left(\frac{Gm}{vR}\right)^2 \ln\Lambda, \tag{4.23}$$

where $\ln\Lambda = \ln\left(\frac{b_{max}}{b_{min}}\right)$ is called *Coulomb logarithm*. The minimum impact parameter b_{min} is automatically set by the initial requirement that

$\delta v/v << 1$. In fact, the straight line trajectory approximation is not valid anymore for $\delta v \sim v$, which corresponds to a strong encounter, yielding a 90^o deflection. From Equation 4.20, we then get $b_{min} = \frac{2Gm}{v^2}$. The maximum impact parameter, instead, is fixed by the size of the system, R. The Coulomb then reads

$$\ln \Lambda = \ln \frac{v^2 R}{2Gm}. \tag{4.24}$$

By assuming now that the system is in virial equilibrium, the mean square of the velocity distribution v^2 is $\sim \frac{GNm}{R}$. This allows us to eliminate R from Equations 4.23 and 4.24 and gives

$$\frac{\Delta v^2}{v^2} \sim \frac{8 \ln N}{N}, \tag{4.25}$$

which represents the change in in velocity of the test particle considering the interactions from all other particles, after having crossed the system once. At every system crossing of the test particle, the variation on the velocity will be Δv^2. To have a significant change in the velocity (which is what is expected by the relaxation process), i.e. comparable with the velocity itself $\Delta v^2 \sim v^2$, the number of crossings needed is

$$n_{relax} \sim \frac{N}{8 \ln N}. \tag{4.26}$$

Therefore, the relaxation timescale t_{relax} can be defined as the number of crossings needed for the cumulative gravitational perturbations from all stars in the cluster to change the energy of the test star by roughly its orbital energy, n_{relax}, multiplied by the timescale of a system crossing, t_{cross}, i.e. $t_{relax} = n_{relax} \times t_{cross}$. The crossing time, t_{cross} is also defined *dynamical time* (t_d) of the system. A straightforward definition is $t_{cross} = \frac{R}{v}$, where R is the size of the cluster and v is the typical velocity of a star. It is immediate to notice how the dynamical time is directly connected with the free-fall time (see Section 3.2.0.1)

$$t_{cross} = \frac{R}{v} \sim \sqrt{\frac{R^3}{GNm}} \sim \frac{1}{\sqrt{G\rho}}. \tag{4.27}$$

Fundamentally, the dynamical time is the timescale in which a particle responds to the global gravitational potential. If the system is in equilibrium this is basically the orbital time. If this is not the case, the dynamical time is

the timescale over which a system stars to lose non-equilibrium structures, trying to (re-)establishing dynamical equilibrium.

Going back to the relaxation timescale, the final expression derived is

$$t_{relax} = n_{cross} t_{cross} \sim \frac{N}{8 \ln N} \frac{R}{v}. \tag{4.28}$$

With this formulation, we can derive which systems are collisional and which are collisionless. As already anticipated, galaxies, having $N \sim 10^{11}$, R $\sim$ 10 kpc and v $\sim$ 100 km/s, are definitely collisionless system, since their $\mathrm{t_{relax}} \sim 10^6 \mathrm{Gyr}$. The redistribution of energy between particles due to two-body interactions is in this case not yet effective. For globular clusters, $N \sim 10^5$, R $\sim$ 10 pc and v $\sim$ 10 km/s, which leads to $t_{relax} \sim 0.1 - 1 Gyr$, which is less than a typical age of 10 Gyr, therefore we conclude in this case two-body perturbations have significantly affected affected the original orbits of the stars these systems. Same conclusion for open cluster and even more dense young clusters, which can reach relaxation timescale of 10 Myr, which means that these younger systems are more affected by two-body relaxation and evolve faster.

The derived formula for the relaxation timescale is an approximated version of the more accurate one derived by Spitzer (1987) using diffusion coefficients, the main difference being the use of global quantities instead of local, how it should be. A more accurate expression for the *local* relaxation timescale t_{rl} is

$$t_{rl} = \frac{\langle v^2 \rangle^{3/2}}{15.3 G^2 \langle m \rangle \rho \ln \Lambda}, \tag{4.29}$$

where $\langle m \rangle$ is the local mean stellar mass, $\langle v^2 \rangle$ the local velocity dispersion and ρ the local density. This expression can then be applied at various radial different radial scales, the most used of which is the half-mass radius (r_{hm}). By assuming $r_{vir} \sim r_{hm}$ and substituting the local quantities with the global cluster averages in the previous expression, $\langle v^2 \rangle = GM/2r_{vir}$ and $\rho \sim 3M/8\pi r_{vir}^3$, we obtain the *half-mass relaxation timescale*, t_{rh}, which is

$$t_{rh} = 0.14 \frac{N^{1/2} r_{vir}^{3/2}}{G^{1/2} \langle m \rangle^{1/2} \ln \Lambda}. \tag{4.30}$$

The value of Λ is a crucial parameter which depends strongly on the system. The Coulomb logarithm is usually expressed as $\ln \Lambda = \ln(\gamma N)$, with γ being determined numerically. For equal mass systems $\gamma \sim 0.11$

(Giersz & Heggie, 1994), while for systems with an initial mass spectrum ($N(m) \propto m^{-2.5}$) and maximum mass ratio between stars ~ 40, $\gamma \sim 0.021$ (Giersz & Heggie, 1996). In general, $\ln \Lambda$ is assumed to be of order $O(10)$ (Portegies Zwart et al., 2010), but in the results shown in Chapter 6 we used a smaller reference value.

A handy version of t_{rh} with the normalisation constants relevant for young massive star clusters, is given by Portegies Zwart et al. (2010)

$$t_{rh} = 200 Myr \left(\frac{r_{vir}}{1pc}\right)^{3/2} \left(\frac{M}{10^6\,\mathrm{M}_\odot}\right)^{1/2} \left(\frac{\langle m \rangle}{1\,\mathrm{M}_\odot}\right)^{-1} \left(\frac{\ln \Lambda}{10}\right)^{-1}. \quad (4.31)$$

Similarly, we reported a convenient expression for our simulated globular clusters in Section 6.2.

4.2.2. Evaporation

On a two-body relaxation timescale, the system tends to establish a Maxwellian velocity distribution. However, since the system as finite mass (let's assume a King model for example), it necessary has an escape velocity v_{esc}. The stars occupying the tail of the Maxwellian, will have at some point velocity higher than v_{esc} and will therefore escape. If we suppose that the fraction of escaping stars is ξ_e and this gets continuously replenished by the relaxation process every t_{rh}, the time over which the cluster dissolve by evaporation is

$$t_{dis} = \frac{t_{rh}}{\xi_e}. \quad (4.32)$$

It can be easily demonstrated that for an isolated cluster, it holds

$$\langle v_{esc}^2 \rangle = 4 \langle v^2 \rangle, \quad (4.33)$$

which, in case of a Maxwellian distribution, it translates into a fraction of escaping stars equal to 0.74%. With these values, the evaporation time t_{dis} is $\sim 140 t_{rh}$. For a typical density profile, Spitzer (1987) report 3% of stars escaping, therefore $t_{dis} \sim 30 t_{rh}$.

The process of evaporation of the cluster causes the contraction of the core. Indeed, if we assume a constant rate of mass loss per relaxation time and assume that escaping stars carry away a fixed fraction of kinetic energy per unit mass (ζE_m), it is possible to demonstrate that the King radius r_0 goes as

$$\frac{r_0(t)}{r_0(0)} = \left(1 - \frac{t}{t_{dis}(\zeta, \xi_e)}\right)^{2(2-\zeta)/(7-3\zeta)}, \quad (4.34)$$

which means that for reasonable values of ξ_e and ζ, the core shrinks.

However, the assumption of constant ξ_e is an approximation. In fact, the escape fraction depends on the radius (r_{hm}) through $\langle v^2 \rangle$ and, in non isolated clusters, on the external tidal field, which affects v_{esc}. Baumgardt (2001) found that the evaporation time depends on both the relaxation and dynamical timescale, as $t_{dis} \propto t_{rh}^{3/4} t_{cross}^{1/4}$.

4.2.3. Gravothermal instability

The gravothermal instability is the physical process which is at the basis of the phenomenon of core collapse. As we discussed in general terms when introducing the granular aspect of the gravitational field, and just before, dealing with evaporation of stars, the expansion of the cluster effectively transfers energy from the inner to the outer regions and inevitably produces a collapse of the core. The deep motivation behind this is the negative heat capacity of every gravitational system. Indeed, we can define the kinetic energy (K) of an N-body system in terms of mean temperature (T), in analogy with a gaseous system

$$\sum_i \frac{1}{2} m_i v_i^2 = K = \frac{3}{2} N k_b T, \tag{4.35}$$

where k_b is the Boltzmann constant and m_i, v_i are the masses and velocities of particles in the system. Assuming the system is in equilibrium, the virial theorem states that $2K + W = 0$ (W is the potential energy of the system), therefore the total energy E of the system is

$$E = -K = -\frac{3}{2} N k_b T. \tag{4.36}$$

The heat capacity C of a system is defined in general as $C = dE/dT$, which in case of a gravitational system is

$$C = \frac{\mathrm{d}E}{\mathrm{d}T} = -\frac{3}{2} N k_b, \tag{4.37}$$

which is always negative. Having negative heat capacity means that when the system loses energy, it becomes hotter. In a gravitational system the temperature is represented by the velocity dispersion, so "becoming hotter" means increasing its velocity dispersion, and to do this the system has to contract. By contracting and increasing the velocity dispersion, more particles will escape, "cooling" the system and carrying away energy, therefore the core contracts again and so on.

If we now suppose that our gravitational system is composed of a contracting core and rarefied halo, a key condition for this process to continue, is that the halo is larger than the core, such that the kinetic energy injected does not make it become hotter. If this condition is satisfied, the core-collapse becomes (in principle) a runaway process. For an initial Plummer sphere of identical masses, the system reaches a core of zero size and infinite density on a timescale of $\sim 15t_{rh}$ (Portegies Zwart et al., 2010). However, starting with a more concentrated system or assuming a mass-spectrum, can reduce this timescale significantly, up to $0.2t_{rh}$ in case of small clusters (Gürkan et al., 2004; Portegies Zwart & McMillan, 2002).

4.2.4. Equipartition and mass segregation

As result of two-body relaxation the system tend to equipartition, which is a classic theorem of statistical mechanics, stating that particles in a system tend to have the same average kinetic energy. In systems with a mass spectrum, this results in mass segregation. Let's suppose to have two populations of stars in the system with masses m_i and m_j. Equipartition leads to

$$\frac{1}{2}m_i\langle v_i^2\rangle = \frac{1}{2}m_j\langle v_j^2\rangle. \tag{4.38}$$

However, if $m_i < m_j$, the last expression implies

$$\langle v_i^2\rangle > \langle v_j^2\rangle, \tag{4.39}$$

which means that the more massive stars will have on average a lower velocity and the less massive stars will get faster. This has two main consequences. The first is, as we already said, that multi-mass systems collapse faster, because the faster stars, the one removing kinetic energy from the core, are also the lighter, so they remove from the system more kinetic than potential energy.

The second consequence is that the heaviest stars slow down and drift toward the centre. A higher concentration of massive stars at the centre of the star cluster is what is usually defined as *mass segregation*. This process proceeds as consequence of dynamical friction. The basic idea is that a massive star which moves in a field of lighter stars produces by gravitational attraction an overdensity of lighter stars behind him, which will attract the massive body reciprocally, slowing it down. The dynamical friction timescale (t_{df}) is related to the half-mass relaxation timescale by (Spitzer,

1969)

$$t_{df} = \frac{\langle m \rangle}{m_{max}} t_{rh}, \tag{4.40}$$

where $\langle m \rangle$ is the average mass of light stars and m_{max} is the mass of the heavy star. The more massive is the star, the shorter it takes to get to the centre. The timescale for general mass segregation to take place is once more the half-mass relaxation timescale, while the dynamical friction timescale is effectively the timescale over which a cluster segregated up to a mass m_{max}.

If the relative number of heavy stars is too high, equipartition can not be reached and the outcome is a runaway process, called *mass stratification (or Spitzer) instability*. This happens, for example, if the total mass of heavy stars (M_2) is too large compared to the total mass in light stars (M_1). In this case the massive population segregates at the centre, effectively forming a sub-system within the cluster, and keeps transferring kinetic energy to the lighter stars, without ever reaching equipartition. This is possible also in the case in which $M_2 < M_1$, but the density of massive stars exceeds the density of light stars. In the simple case of only two stellar populations, the general analytic condition for equipartition to be reached was found by Spitzer (1969)

$$0.16 < \frac{M_2}{M_1} \left(\frac{m_2}{m_1} \right)^{3/2}, \tag{4.41}$$

where m_1 and m_2 are the single masses of a light and heavy star, respectively.

4.3. Post collapse: Binaries &Co.

The core collapse is a runaway process, which can be stopped only with the addition of an extra source of energy. This energy comes mainly from binaries and multiple systems, which formed in the high density environment of the collapsing core. The binding energy of a binary can be expressed as

$$E_b = \frac{-G m_1 m_2}{2a}, \tag{4.42}$$

where m_1 and m_2 are the masses of the binary constituents and a is the semi-major axis of the reduced particle elliptical orbit.

When a binary interact with another star of the cluster, either by kinetic "kick" or via particle substitution, there are two possible outcomes: either its binding energy increases or diminishes. In the first case, it means that the star transfers energy to the binary, which gets less bound, hence the separation between the constituents (a) increases. The limit case is the ionisation of the binary, which results in three single bodies. In this case, the binary absorbs energy from the cluster.

Alternatively, the binary can release energy to the single star and become more bound. In this case, the kinetic energy of the system gets increased. Binaries are usually divided into "hard" binaries and "soft" binaries, whether their binding energy is greater or lower than the mean stellar kinetic energy in the cluster (Heggie, 1975). The dynamical meaning of this is that after an interaction with another star of the cluster a hard binary on average will become harder and a soft binary will become looser. Hard binaries are responsible for the reversing of the core collapse.

The mean energy gain in a hard binary encounter is $\langle \delta E_b \rangle \sim \gamma E_b$, where, for equal-mass systems, γ is $0.25 - 0.4$ (Heggie, 1975; Spitzer, 1987). As a result of these strong interactions, the binary or the single star can also be ejected from the core by recoil, which constitutes an additional source of indirect heating, especially in the case of massive stars. Intuitively, when the energy generated by three body encounters exceed the potential energy of the core, the collapse is reversed and the core re-expand.

4.4. Additional perturbations

Two-body interactions between stars in the cluster are not the only perturbation to equilibrium that can be considered. There are more sources of corrections one can think of, of which we will only give a brief mention without entering in details.

For instance, star clusters are actually not isolated, but are in fact immersed in the potential of their host galaxy, which clearly exerts an influence on them. The tidal field of the galaxy is particularly important for the evaporation rate of the cluster, because it contributes to reduce the energy required to escape from the cluster. Recent numerical studies investigated the effects of tidal fields and found that they strongly affect the evolution, kinematics and ultimately survivability of the cluster (Renaud et al., 2011; Vesperini et al., 2014).

Furthermore, one could include stellar evolution effects on the cluster. The most important contribution in this case probably comes from the stellar mass loss from winds and supernovae. The dynamical importance of

this lies in the contribution to reverse the core collapse. Numerical simulations have shown that the expansion due to stellar mass loss can be considerable in some cases and even result in the disruption of the cluster, when this latter was already mass segregated before the onset of stellar evolution (Vesperini et al., 2009).

As last thought, we point out that two-body relaxation is not the only form relaxation which might play a role. If a star moves in a potential which is not stationary, a collective relaxation process takes place, connected with the change of the potential with time, called *violent relaxation* (Lynden-Bell, 1967). In this case the energy of stars changes according to $dE/dt = \partial\Phi/\partial t|_{\boldsymbol{x}}$. We stress that, since in the previous equation the mass does not appear, this type of relaxation changes the position and velocity of a star regardless of its mass. This constitute a strong difference with the two-body relaxation mechanism. While the violent relaxation is the only possible relaxation in collisionless systems, in collisional systems it precedes the two-body relaxation, playing a role in the very early dynamical phase (on a dynamical timescale), when the cluster is out of equilibrium.

A full consideration of the complexity of stellar dynamics, however, goes beyond the aim of this thesis and the scope of the applications presented, leaving open interesting possibilities for further investigation.

5

STAR CLUSTER FORMATION & PHOTO-IONISATION: A LOVE STORY

In the previous chapters we presented the most important observational facts and theoretical tools, needed to understand the formation and evolution of star clusters. At the same time we tried also to present some of the most crucial problematic and unanswered questions. We have described how star clusters have different properties and mysteries depending on the category they belong, we explained what are the necessary ingredients of a good star formation theory and the rules which govern star cluster dynamical evolution. Now, we put all together. And with this heritage, we present an original and novel contribution to our knowledge of star clusters, which hopefully constitutes an infinitesimal step forward. In this chapter[1], we focus on the formation of star clusters and the role of photoionisation in freeing the newborn star cluster from its parent cloud. Specifically we performed radiation-hydrodynamical simulations of the collapse of a turbulent molecular cloud using the `RAMSES-RT` code. Stars were modelled using sink particles, from which we self-consistently follow the propagation of the ionising radiation. We study then how different feedback models affect

[1]The work presented in this chapter has been published in the Monthly Notices of the Royal Astronomical Society, Volume 472, Issue 4 under the title "Star Cluster Formation in a Turbulent Molecular Cloud Self-Regulated by Photo-Ionisation Feedback", following peer-review (Gavagnin et al., 2017).

the gas expulsion from the cloud and how they shape the final properties of the emerging star cluster. As main results, we find that the star formation efficiency is lower for stronger feedback models. Feedback also changes the high mass end of the stellar mass function. Stronger feedback also allows the establishment of a lower density star cluster, which can maintain a virial or sub-virial state. In the absence of feedback, the star formation efficiency is very high, as well as the final stellar density. As a result, high energy close encounters make the cluster evaporate quickly. Other indicators, such as mass segregation, statistics of multiple systems and escaping stars confirm this picture. Observations of young star clusters are in best agreement with our strong feedback simulation.

5.1. Introduction

From the previous chapters it should be clear that establishing a full and consistent theory of star cluster formation remains an open task for the scientific community. As we presented, the most widely adopted view is that star clusters form from the collapse of giant molecular clouds. On a timescale of a few millions years, a cloud undergoes gravitational collapse and converts part of its gas into many dense molecular cores, each core leading to the formation of one or a few proto-stellar objects (see Klessen, 2011; Krumholz, 2014, for a review). These protostars can continue accreting material from their surroundings, and eventually become proper stellar, main sequence objects, whose stellar luminosity is high enough to inject considerable amounts of energy into their parent cloud. This stellar feedback modifies the properties of the cloud and the star formation process itself and as a result regulates the properties of the emerging star cluster, such as its dynamical state, the mass distribution and the fate of its stellar population.

Understanding the impact of stellar feedback on the star cluster properties, and the transition from the initial turbulent GMC to the final gas-free association of stars (such as observed open clusters, embedded clusters or even globular clusters) is at the moment one of the most intriguing fields of research in astrophysics, mainly because of the numerous and complex physical processes at play during the entire history of the star cluster formation.

We already referenced to the work of Lada & Lada (2003), which states that 90% of stars are likely to form in star clusters. In Lada & Lada (2003), star clusters are defined as groups of at least 35 stars and with a stellar mass density of at least 1 $\mathrm{M}_{\odot}\ \mathrm{pc}^{-3}$. These numbers can be derived by requiring

that the evaporation timescale of the star cluster is longer than 100 Myr. A more recent study by Bressert et al. (2010) revealed how the fraction of stars in the solar neighbourhood forming in clusters is strongly dependent on the adopted definition for star clusters , with values ranging between 45 and 90%. They concluded that stars form within a broad and smooth distribution of surface densities, which is consistent with star formation proceeding hierarchically, within the turbulent, hierarchical structure of the parent molecular cloud, where denser regions are systematically embedded in less dense regions (Bastian et al., 2007; Elmegreen, 2006).

Defining what is a truly bound cluster or an unbound stellar association is indeed not straightforward, especially when the system is young. It is only after these stellar structures have dynamically evolved, that they are easier to distinguish from their environment. The identification of the fraction of stars residing within these older stellar systems is more reliable, and is observed to be around 10-30% (Adamo et al., 2011; Miller & Scalo, 1978).

It is also very important to establish what is the fraction of stars which formed in star clusters but do not reside there anymore today. This is usually referred as star clusters *infant mortality*, outlining the fact that, when we compare the fraction of stars in young, embedded star clusters with the fraction of stars in older, open clusters, most of the clusters seems to have been disrupted during this transition from embedded to exposed (Lada & Lada, 2003). Note that this interpretation assumes that the fraction of stars in star clusters is the rather old one presented in (Lada & Lada, 2003).

The commonly adopted picture for the cause of this infant mortality is the fast expulsion of the initial gas, leading to the rapid expansion and disruption of the star cluster. Only clusters with a star formation efficiency (SFE, i.e. the fraction of gas converted into stars) higher than 30% are believed to survive the gas removal and stay bound (Bastian & Goodwin, 2006; Hills, 1980; Lada et al., 1984). Yet, the star formation efficiency is not the only parameter that can decide whether a star cluster will survive gas expulsion. Two other important factors are: 1-the timescale of gas removal and 2-the actual dynamical state of the star cluster right before expulsion. Regarding the first point, it has been shown for example that systems with star formation efficiency as low as 10% can remain bound, as long as the gas is removed slowly and adiabatically (Baumgardt & Kroupa, 2007). The second factor has been pointed out by Goodwin (2009), showing a strong dependence of the star cluster mass loss (hence survival) on the virial ratio of the emerging star cluster. Indeed, if the system is sub-virial before gas is expelled, it can survive even with SFE lower than 30%. Conversely, an ini-

tially super-virial system, even with a SFE as high as 50%, will be at edge of survivability (Goodwin, 2009).

The SFE within star forming molecular clouds is poorly understood from theoretical grounds. Simple models based only on self-gravitating turbulence predict a very high SFE, higher than 90%, meaning that star formation occurs during one free-fall time of the parent cloud, in contradiction with observational constraints (Padoan et al., 2014).

Stellar feedback has been invoked to reduce the SFE by terminating star formation in giant molecular clouds (see the review by Dale, 2015, and references therein). Stellar feedback is a broad term that refers to the injection of mass, momentum and energy by stars and protostars into the star forming gas itself. The different mechanisms of stellar feedback are photoionisation from massive main sequence stars, infrared and optical radiation from accreting protostars, radiation pressure associated with these various types of radiation, proto-stellar jets, stellar winds from main sequence or post-main sequence stars, supernovae explosions. Although all these ingredients are likely to play an important role in regulating the star formation efficiency and in setting the properties of the emerging star clusters, they act on different spatial and temporal scales, and are associated with stars of different masses.

On the observational side, several surveys can be used to cast light on the star cluster formation process. The MYSTiX survey (Feigelson et al., 2013), for example, is targeting massive star forming regions and has revealed that star clusters are frequently divided into sub-clusters (Kuhn et al., 2015). We now have evidence that these sub-clusters are expanding or merging, with clear signs of ongoing dynamical relaxation. For example, we observe mass segregation (see Section 5.3.3 for a definition) down to 1.5 $\mathrm{M}_{\odot}$ (Kuhn et al., 2015). Similarly, Da Rio et al. (2014) have studied the morphology and the dynamical state of the Orion Nebula Cluster. They concluded that the core appears rounder and smoother than the outskirts, which is consistent with ongoing dynamical processing.

The Gaia-ESO Survey (Gilmore et al., 2012) has recently discovered several kinematically distinct populations in the young star cluster Gamma Velorum, surrounding the γ^2 Velorum binary in the Vela OB2 association. According to Jeffries et al. (2014), the first component of Gamma Velorum is a bound remnant of an initially larger cluster, formed in a dense region of the Vela OB2 association, that has been partially disrupted by gas expulsion. The second component consists of a scattered population of unbound stars born later (as indicated by lithium depletion) in less dense regions. The gas surrounding this second population was probably evap-

orated by the radiation coming from the first one, quenching the star formation episode quite abruptly.

In general, very young star clusters, sometimes still embedded in their parent gas cloud, are ideal laboratories to study the effect and phenomenology of stellar feedback and gas expulsion. In the Milky way, the so-called "starburst star clusters" (e.g. NGC 3603 YC, Quintuplet, Arches, Westerlund 1 and 2) represent the youngest (< 5 Myr) and more actively star forming clusters (Brandner, 2008). NGC 3603 YC, for example, is only $\sim$ 1 Myr old, and is surrounded by glowing interstellar gas and obscuring dust (Röllig et al., 2011). Arches, the second youngest with an age of $\sim$ 2.5 Myr, is already free of any gas in its centre (Stolte et al., 2003) with a clear X-ray signature of hot outflowing gas (Yusef-Zadeh et al., 2002). These newborn star clusters are characterised by the presence of strongly UV-radiation from O and B stars that ionises the nebula and disperses the gas (Crowther et al., 2010; McLeod et al., 2016).

On the theoretical side, the challenge of modelling star clusters is due to the lack of a complete theory of star formation. This is an inherently multi-scale, multi-physics problem, with a central role played by feedback mechanisms. We point to the reviews by Dale (2015) and Krumholz et al. (2014) for a detailed presentation of the problem. Here we present only a few selected earlier studies, relevant for our work which focuses specifically on the star cluster formation process.

Fujii & Portegies Zwart (2015), Fujii (2015) and Fujii & Portegies Zwart (2016) used direct N-body simulations, starting from initial conditions drawn from the results of previous smoothed particle hydrodynamics (SPH) simulations of turbulent molecular clouds. Because the adopted SPH resolution was relatively low ($\sim$ 0.1 pc), the authors could not resolve the formation of individual stars, but could still capture the clumpy structure of the gas. After one free-fall time of the initial gas cloud, they stopped the hydro simulation and replaced dense enough gas particles with stellar particles, assuming a star formation efficiency (or gas to star conversion factor) depending on the local gas density. The remaining gas particles were removed instantaneously and the stellar particles dynamics was integrated further in time using a direct N-body code. They derived that the initial properties of the parent cloud (mass, density) determine the characteristics of the emerging cluster, whether it will become an association, an open cluster or a dense massive one. Moreover, to form massive clusters, they claimed that a local star formation efficiency $>$50% is needed.

Using a more elaborate methodology, Dale & Bonnell (2011), Dale & Bonnell (2012), Dale et al. (2012a), Dale et al. (2012b), Dale et al. (2013a)

and Dale et al. (2013b) studied in a series of papers the effects of photo-ionisation feedback on embedded clusters and its disruptive impact on clouds of different masses (from 10^4 to 10^6 $M_\odot$) and sizes (from 2 to 220 pc), either initially bound or unbound. In Dale et al. (2014), the authors added stellar winds to photoionisation feedback and studied how the overall star formation efficiency, the average star formation rate (SFR) and the fraction of unbound gas varied with the initial cloud properties. Their methodology was based on SPH simulations of turbulent molecular clouds, with an initial shallow Gaussian density profile. The velocity field was initialised as a turbulent, divergence-free Gaussian random field, with a power spectrum to $P(k) \propto k^{-4}$ consistent with isothermal supersonic turbulence. The cloud was evolved using self-gravity and cooling, and star formation was modelled using sink particles. The mass and spatial resolution was also relatively low, with only 10^4 particles per cloud. Radiative transfer of the photo-ionising photons was performed using a Strömgren sphere filling technique (see Dale et al., 2007, for details). Using the same set of simulations, Dale et al. (2015) focused on the properties of the stellar populations of the star clusters formed. They found that the star formation efficiency is lowered by the presence of feedback, however they stressed how the disruptive effect of feedback depends on the cloud properties, especially the escape velocity. Natal gas from massive clouds with elevated escape velocities is expelled only in minimal part. Winds are found to have little impact on the dynamics of gas compared to ionising feedback. Moreover, in these simulations the number of stars unbound by feedback is very modest and is not related to the fraction of gas expelled.

Along the same lines as in Fujii & Portegies Zwart (2015), the longer term evolution of these star clusters was finally investigated in another series of paper by Parker & Dale (2013, 2015); Parker et al. (2015). They concluded that clusters formed in simulations with feedback tend to remain sub-structured longer than in the non-feedback cases. Moreover, at the end of the pure N-body evolution, the authors found that simulations with feedback contain fewer bound stars than in the control run. In terms of mass segregation, they do not provide a unique conclusion, because different analysis return contrasting evidence.

More recently, several papers have addressed the problem of star cluster formation from a realistic, gaseous, turbulent environment using grid-based simulation techniques. Using the `RAMSES` code, Lee & Hennebelle (2016) studied the conditions required in the parent cloud to obtain a bound star cluster. The authors aimed to examine the properties of the gaseous proto-cluster born from the collapse of a 10^4 $M_\odot$ molecular cloud.

To achieve this they performed magnetohydrodynamics simulations, without stellar feedback and varying the initial level of turbulent support. Prestellar cores were followed using the same sink particle algorithm adopted in our work. The typical mass of a sink was $10\ \mathrm{M}_{\odot}$. The proto-cluster turned out to be in virial equilibrium, with turbulence and rotation supporting the collapse. The virial status and size of the proto-cluster were considered to be directly imprinted by the parent cloud, therefore they concluded that the study of the gaseous proto-cluster phase is a fundamental step in the context of stellar cluster formation.

Using the FLASH code, coupled to a ray tracing code, Howard et al. (2016) studied the effect of various cloud initial conditions, then subjected to the ionising radiation of massive stars, on the final properties of the star cluster system. This study focused on giant $10^6 M_{\odot}$ molecular clouds, with different initial virial parameters (α), ranging from bound ($\alpha = 0.5$) to unbound ($\alpha = 5$). The main goal was to study how feedback and the virial status affect the formation of star clusters and subsequent evolution of the cloud. In this case sink particles represented single star clusters and star formation within each cluster is implemented with a subgrid model, by randomly sampling the IMF. Their conclusion was that the initial virial parameter strongly influences the SFE, with more bound clouds having higher efficiency, while radiative feedback did not play a major role, lowering the previous values only by few percent. They also found that the number of star clusters formed depends on the boundedness of the cloud: the more bound the cloud, the fewer the star clusters. Moreover, the clusters from unbound clouds were gas poorer and star richer than the ones formed from bound clouds.

In this work, we model the collapse of a $\sim 2.5 \times 10^4\ \mathrm{M}_{\odot}$ turbulent cloud with photo-ionisation feedback from massive stars at extremely high resolution (smallest cell size $\sim$ 500 AU), and study how the star cluster forms and emerges from its parent cloud. Our radiative transfer technique is based on the moment method with the M1 closure (Rosdahl et al., 2013) and allows to model an arbitrary number of photon sources, much faster than traditional ray tracing schemes. We consider two different feedback scenarios (strong and weak) and a reference simulation without any feedback. We subsequently analyse how the different feedback scenarios affect the properties of our new born star clusters, using various observables related to the stellar mass function, its spatial distribution, the mass segregation, the distribution of escaping stars and the stellar multiplicity function.

5.2. Numerical Methods

We now describe in details the numerical techniques we use to model the collapse of a turbulent molecular cloud and the formation of massive stars, following the effects of ionising radiation on the cloud itself.

5.2.1. Initial Conditions

We first perform a decaying turbulence simulation in a periodic box sampled with 1024^3 cells. This simulation is initialised with a uniform gas density $\rho_0 = 1$ (in arbitrary units) and a Gaussian random velocity field with a power spectrum $P(k) \propto k^{-4}$, where k is the wavenumber. $P(k)$ is normalised so that the 3D velocity dispersion in the full box was set to $\sigma_{3\mathrm{D}} = \mathcal{M}c_s$, where the sound speed is $c_s = 1$ in arbitrary units and the initial Mach number is set to $\mathcal{M} = 20$. After one turbulence crossing time, $t_{\mathrm{turb}} = L/\sigma_{3\mathrm{D}}$ (where the box size was also set to 1 in arbitrary units), the kinetic energy has decayed by a factor of two, and the actual Mach number by a factor of $\sqrt{2}$. At that time, the turbulence is fully developed, with density fluctuations following a clear log-normal distribution function and the variance in $\log \rho$ reaching its peak value.

We then use this final snapshot as a template for the initial turbulent cloud. We first set up the physical scales of our problem. The cloud is considered to be composed of fully molecular Hydrogen with temperature $T_0 = 10$ K and isothermal sound speed $c_s = 0.2$ km/s. The mean density in the box is set to $n_H = 10^3$ H/cc and the periodic box length to 20 pc. We carve out of the periodic box a sphere of radius 5 pc, centred on a large filament resulting from a large compressive mode. As a result, the mean density in the spherical cloud is larger than the mean density in the original box, and the Mach number in the cloud is smaller than in the original box (by another factor of $\sqrt{2}$) with $\mathcal{M} \simeq 10$. The final cloud properties are the following: radius $R = 5$ pc, mass $M \simeq 2.5 \times 10^4$ $\mathrm{M}_\odot$ and velocity dispersion $\sigma_{3\mathrm{D}} \simeq 2$ km/s. Note that, because we have adopted a velocity dispersion at the low end of values found in observations of clouds of a similar size, our cloud virial parameter

$$\alpha_{\mathrm{vir}} = \frac{5\sigma_{3\mathrm{D}}^2 R}{3GM} \simeq 0.3, \tag{5.1}$$

is small enough to ensure a fast collapse, i.e. the free-fall time is ~ 1 Myr. The simulations are then run to t=2Myr.

5.2.2. Refinement strategy

Our initial coarse grid corresponds to a minimum refinement level $\ell_{\rm min} = 10$ with cell size $\Delta x_{\rm max} \simeq 0.02$ pc, which allows us to resolve our sonic scale $l_s \simeq 0.08$ pc, i.e. the scale at which our scale-dependent 3D velocity dispersion is equal to the sound speed. During the course of the simulation, we refine this initial grid level using a quasi-Lagrangian refinement criterion. Our maximum resolution is fixed to our maximum refinement level $\ell_{\rm max} = 13$, which corresponds to a minimum cell size of $\Delta x_{\rm min} \simeq 500$ AU. Assuming for the isothermal sound speed $c_s = 0.2$ km/s, and requiring for the Jeans length

$$\lambda_{\rm J} = c_s \sqrt{\frac{\pi}{G\rho}} > 4\Delta x_{\rm min}, \tag{5.2}$$

this gives us the constraint that $\rho < \rho_{\rm J} \simeq 2 \times 10^{-17}$ g/cc. This maximum density corresponds also to a Jeans mass

$$m_{\rm J} = \frac{4\pi}{3}\rho_{\rm J}\left(\frac{\lambda_{\rm J}}{2}\right)^3 \simeq 0.14\ M_\odot. \tag{5.3}$$

We require to resolve this Jeans mass with at least 64 resolution elements, which gives us a mass resolution of $m_{\rm res} \simeq 2 \times 10^{-3}\ M_\odot$. Our refinement strategy is thus the following: if a cell has accumulated a gas mass larger than $m_{\rm res}$, then it is refined individually into 8 new children cells, up to the maximum refinement level. Note that with our adopted initial coarse level and our quasi-Lagrangian strategy, we also automatically satisfy the additional criterion that the Jeans length is always refined by at least 4 cells for any gas density smaller than $\rho_{\rm J}$.

5.2.3. Sink Particles

When the gas density exceeds $\rho_{\rm J}$, we violate our requirement to always resolve the Jeans length with 4 cells and the Jeans mass with 64 resolution elements. Therefore we adopt this criterion to form sink particles, using the technique developed in Bleuler & Teyssier (2014). We first detect density peaks in our 3D density field using the PHEW clump finder (Bleuler et al., 2015). The density threshold is set to $\rho_{\rm threshold} = 2 \times 10^{-18}$ g/cc, or 10% of the Jeans density. After we have identified a discrete set of peak patches delimited by either the isosurface at the density threshold or the saddle surface with a neighbouring peak patch, we draw a sphere, 4 cell size in radius, around the density maximum. If the density at the maximum

exceeds the Jeans density, if the sphere is contracting and if its virial parameter is less than 1, we form a sink with a seed mass equal to $m_{\rm J} \simeq 0.14\ M_{\odot}$ (see Bleuler & Teyssier, 2014, for details). In our simulations one sink corresponds to a single star.

The sink particle is then treated like a point mass. We follow the sink particles dynamics by a leap-frog, direct N-body integrator, using a softened $1/r^2$ acceleration (with softening length $0.5\Delta x_{\rm min}$) between sinks, and also between the sinks and the gas. Only the self-gravity of the gas is based on the grid-based Poisson solver in `RAMSES`. Gas accretion onto the sink particles is modelled through what is described as "flux accretion" in Bleuler & Teyssier (2014).

5.2.4. Radiative Processes

In this paper, we model the emission and the propagation of ionising, ultra-violet (UV) radiation, together with associated heating and cooling processes. We used the `RAMSES-RT` radiative transfer module developed by Rosdahl et al. (2013), using one photon group, with energies between 13.6 eV and 24.6 eV.We do not account for photon energies below 13.6 eV, namely optical and infrared radiation, as the scope of the paper is to study the effect of photo-ionisation heating on the molecular cloud. We will study these other sources of radiation in a follow-up paper. Details in the adopted photo-absorption cross section, chemistry and cooling processes are available in Rosdahl et al. (2013). Metal cooling prescriptions are based on Sutherland & Dopita (1993) for temperatures above 10^4 K and on Rosen & Bregman (1995) for metal fine-structure cooling below 10^4 K. Following Geen et al. (2015, 2016), the photon group energy and cross-section are derived sampling the blackbody spectral energy distribution of a 20 $\rm M_{\odot}$ star. The frequency-dependent ionisation cross sections are taken from Verner et al. (1996) and Hui & Gnedin (1997). A reduced speed of light of $10^{-4}c$ is used. This is done to improve the efficiency of our simulations, since the speed of light affects the tilmestep calculation, through the Courant factor.

The UV radiation emitted by the sink particles is modelled using the following simple strategy. We implemented two feedback regimes, namely *strong* and *weak*. For the strong feedback case, we basically consider all the energy emitted from the sink/star (even optical and infrared) as ionising radiation. To derive the energy associated with every sink we assume a power-law luminosity-mass relation, $\rm L = L_{\odot}(M/M_{\odot})^{3.5}$, where $L_{\odot}$ and $M_{\odot}$ are the solar luminosity and solar mass, respectively . For the weak feedback case, we computed an analytical fit of photon emission rates pre-

sented in Sternberg et al. (2003), obtained through radiation-driven wind atmosphere models of OB stars. We derived the following analytic expression of the number of emitted ionising photons per second, Q_{HI}, as a function of the stellar mass:

$$\log[Q_{HI}(M)] = 48.65 + \log(M/M_{\odot}) - \frac{2.4}{\log(M/M_{\odot} - 8)^{1.9}} . \quad (5.4)$$

This formula was applied to calculate emission rates for all sinks with $M > 10M_{\odot}$. For stars with lower mass we assume there are no ionising photons.

5.3. Analysis

In this section we focus on the analysis of the simulations. In particular, we study the structural characteristics of the star cluster (such as mass function, virial status, mass segregation, escapers, binaries) in the three different runs, to understand the role of feedback (FB) in shaping the star cluster itself.

Figure 5.1 shows ratios of kinetic to potential energies of sinks (upper panel) and the SFE (lower panel) as a function of time. Focusing first on the SFE, the ionising radiation clearly has a major effect in suppressing star formation. In Figures 5.2 and 5.3 we demonstrate the effects of the radiation qualitatively, plotting time-sequences of gas density and temperature maps, to compare the strong, weak and no feedback cases. The initial phase of the cloud collapse proceeds identically in the three cases. The cloud gravitationally contracts and starts forming filaments, where local overdensities allow the creation of stars, here represented by sinks (in yellow or turquoise, depending on the map).

In the no-feedback case this contraction proceeds without resistance until, eventually all the gas is converted into stellar objects; from Figure 5.2 we can see how even in the latest snapshot the amount of dense gas is still high and by the end of the simulation time (2 Myr) the fraction of total mass still available in gas is $\sim 10\%$. In general, we can notice how the final shape of the star cluster becomes more and more spherical with the simulation progressing. The gas temperature in the no-feedback case does not show huge changes throughout the collapse.

In the weak-feedback case, stars emit ionising radiation and we now follow the photo-chemistry of Hydrogen. Differences with the no-feedback case start being visible around already 0.4 Myr in the temperature map, when the most massive stars in the lower part of the filament start emitting UV photons and cause the gas temperature to increase locally. This bubble

of hot gas becomes more and more extended since more stars are formed, accreting more gas. The neutral HI gets dissipated, due to the quick expansion of the HII region. At the end of the simulation, the star cluster is completely free of dense and neutral gas. The strong-feedback case is analogous to the weak-feedback case but the process of photoionisation and gas expulsion is much more rapid and violent, so as a result the star cluster is devoid of gas already at 1.2 Myr.

5.3.1. Virial properties

In the top panel of Figure 5.1 we show the evolution over time of the virial ratio of the star cluster, $\mathrm{E_k/E_p}$ (where E_k and E_p are respectively the total kinetic and potential energy of the sinks) for the three simulations. We do not consider snapshots before 0.5 Myr because the rate of sink formation is still to high and strongly influences the virial analysis. As seen in the figure, the two cases with feedback result in virial or even sub-virial state. The case without feedback is clearly super-virial, hence expanding. This can be explained as a result of feedback, which halted the collapse of the cloud, ionising and dispersing the neutral gas. This determined the formation of a much less dense aggregation of stars than in the control simulation. In the run without feedback, the collapse proceeds unhindered and the new-born stars are immersed in a dense, highly-collisional environment, experiencing very strong close interactions. This inevitably leads to the ejections of many sinks and expansion of the cluster. On the other hand, the feedback opposes this runaway collapse and allows the onset of a lower density regime, where the stellar distribution finds a stable configuration.

It is interesting to notice how this result goes against traditional predictions (see the Introduction), which argue for a complete disintegration of the star cluster after a violent expulsion of gas. However, these often assume a fully formed star cluster still embedded in gas, which at some point gets ejected. In our case, stars are created while the gas is expelled in a self-regulating fashion. Therefore the virial status of the emerging star cluster changes along with the collapse. In our simulations, the two main agents determining the internal dynamics and survival of the cluster are the virial ratio of the molecular cloud (highly subvirial) and the strength of the feedback: a very subvirial cloud produces a cluster too dense to survive, unless feedback slows down the collapse. We also conclude that the star formation efficiency alone is not a good indicator of the survivability, as it is usually believed.

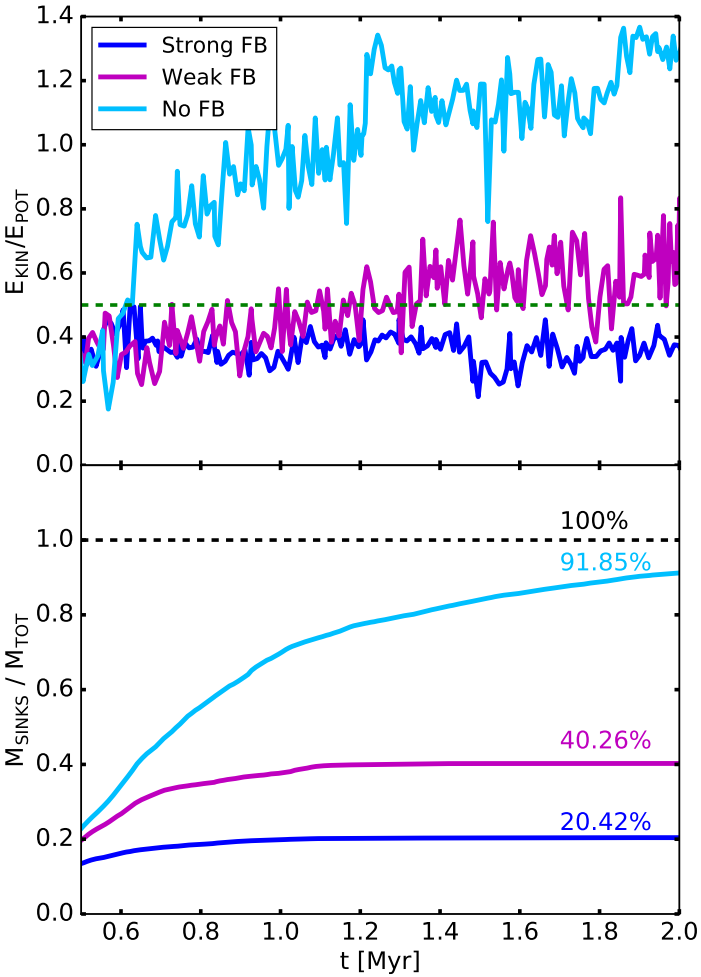

Figure 5.1: Top panel: ratio of total kinetic to potential energy of the sinks (virial ratio, E_k/E_p), the dashed green line indicates the virial equilibrium. Bottom panel: star formation efficiency evolution with time computed as the mass fraction in sinks (M_{SINKS} indicates the total mass in sinks, M_{TOT}, the total initial mass of the gas cloud). The ionising radiation suppresses the formation of stars by clearing gas out of the cloud, and it increases the virial stability of the emerging star cluster.

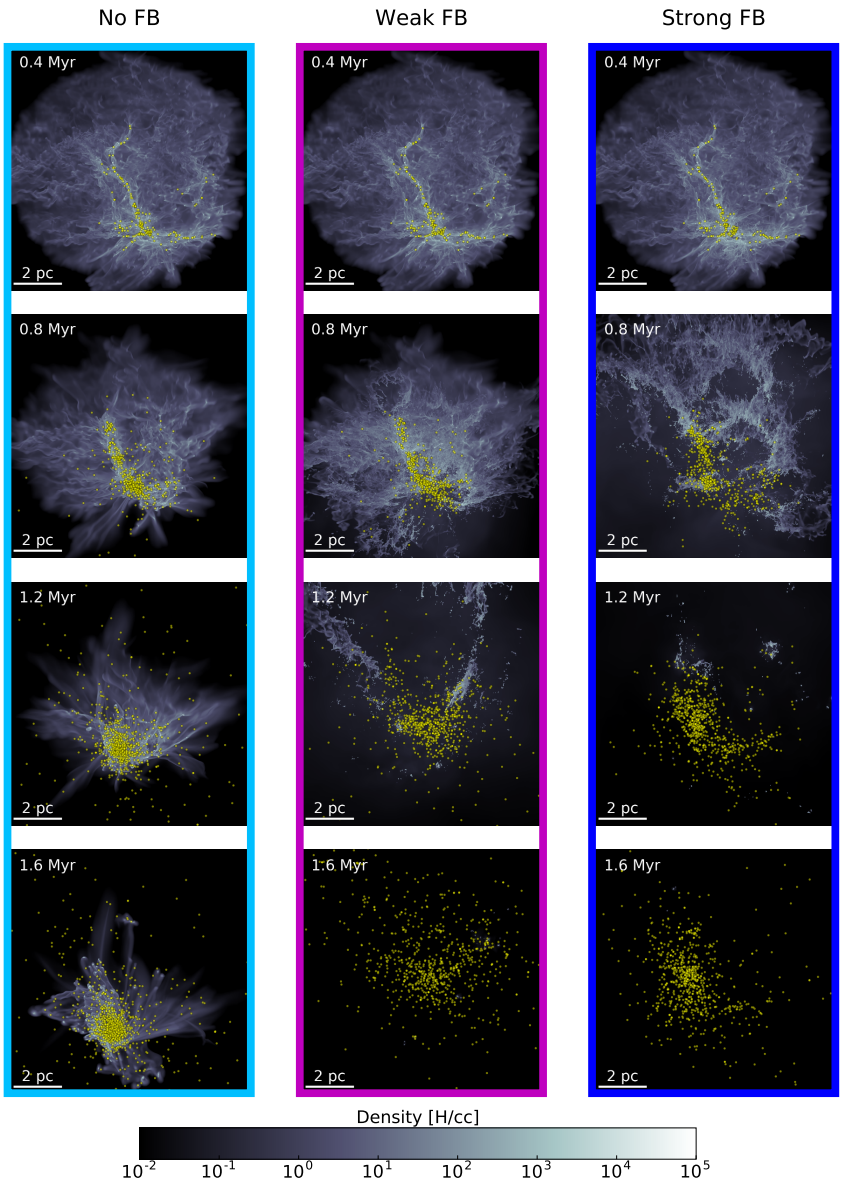

Figure 5.2: Mass weighted line-of-sight projections of gas density for all three runs at different times. The strong feedback case in always denoted with dark blue colour, weak feedback case with magenta and the run without feedback with azure). Sink particles are indicated in yellow.

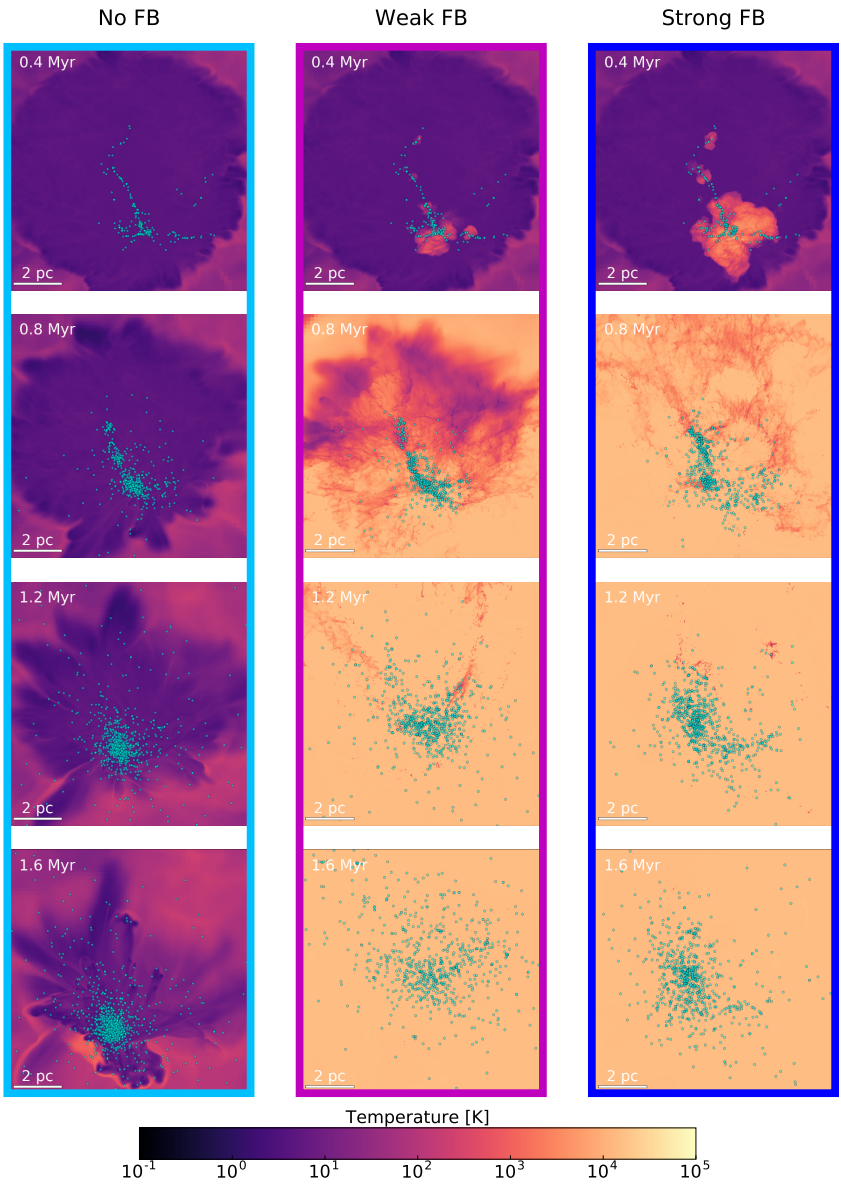

Figure 5.3: Mass weighted line-of-sight projections of gas temperature for all three runs (strong, weak and no feedback) at different times. Sink particles are indicated in turquoise.

In the lower part of Figure 5.1 we show the fraction of gas transformed into stars. Stellar feedback is very efficient in stopping the collapse and lowering the SFE. In fact in the case with the strongest feedback the SFE halts at $\sim$20% (while virtually unity for the control simulation). For a weaker feedback, we get a higher fraction. Despite the fact that in the simulation without feedback all gas is eventually transformed into stars, we stress that the outcome of the simulation is the dispersal of the emerging star cluster, while for the strong feedback case, which results in a very low star formation efficiency, the outcome is a stable (or even subvirial) star cluster.

5.3.2. Mass function

In Figure 5.4, we plot the stellar mass function for all the feedback cases we have considered and at different times. In the run without feedback, our mass function peaks at a relatively large mass of $\sim$10 $\mathrm{M}_{\odot}$ and shows a strong accumulation of very massive stars at the high mass end, with the mean sink mass being around 15 $\mathrm{M}_{\odot}$ and the most massive sink reaching 460 $\mathrm{M}_{\odot}$. This is due partly to our limited resolution (see later) and to the lack of feedback to limit the maximum stellar mass. In the weak feedback scenario, the maximum mass is lower, around 250 $\mathrm{M}_{\odot}$ and the mass function flattens, with a slight increase of very low mass stars (close to our resolution limit of 0.1 $\mathrm{M}_{\odot}$). The trend gets even clearer if we look at the case with strong feedback, where there is a significant peak of stars with mass around 0.1 $\mathrm{M}_{\odot}$ (corresponding to the sink seed mass) and the most massive star is now around 120 $\mathrm{M}_{\odot}$. We observe in the simulation that this excess of low mass stars close to the resolution limit is caused by the fragmentation of the outer dense shells of HII regions.

Looking at the mass function at earlier times (specifically, t=0.25 Myr and t=0.5 Myr, paler lines in figure 3), it is clear that the onset of the sink mass function proceeds similarly in the three cases. It is mainly the final mass distribution that shows visible differences between the feedback and no-feedback cases. To summarise, these are 1) the high-mass cut-off due to feedback effects that stop accretion onto massive sinks, 2) a peak at the low-mass end, due to fragmentation of dense gas around HII regions.

5.3.2.1. Comparison to observations

It is very instructive to compare the results of our simulations to available observations. We choose to consider NGC 3603 and the Arches cluster,

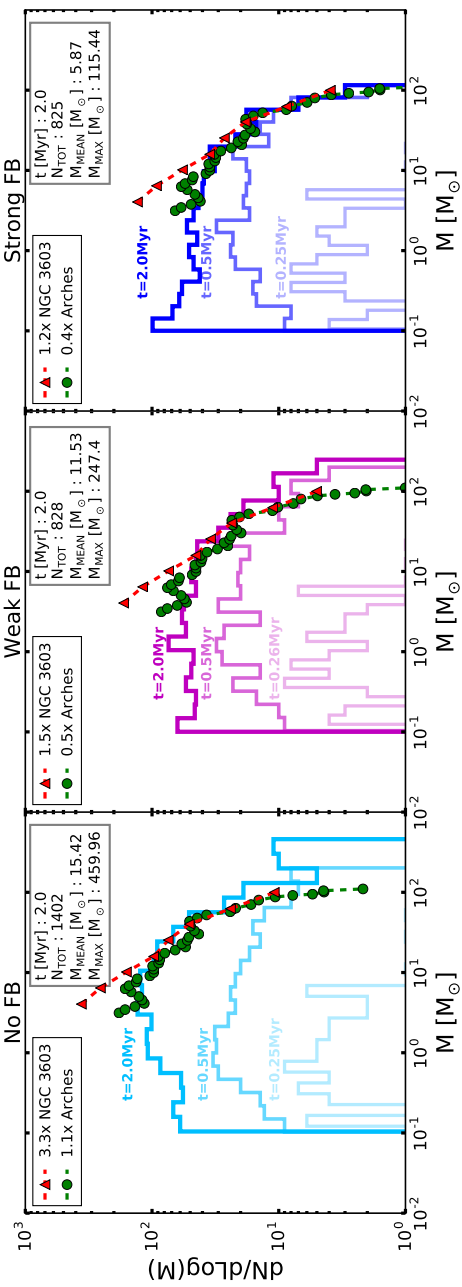

Figure 5.4: Mass function profile for all 3 feedback regimes. The thicker and darker lines indicate for every run the mass function profile at t=2 Myr. In the top right box of every subplot the we indicated the total number of sinks, the average and maximum sink masses at t=2 Myr. In every subplot we plot also the mass functions at t=0.5 Myr and t=0.25 Myr in paler colours. The green dots correspond to the normalised observational data for the Arches cluster (Stolte et al., 2005), the red triangles the same for NGC 3603 (Pang et al., 2013). The normalisation factors are reported in the top left box. Our strong feedback case compares best with the normalised observations, although all models fail to reproduce the steep curve towards lower masses in NGC 3603.

since they are among the youngest ($<$ 2 Myr) well-studied star clusters and are still very actively star forming.

NGC 3603 YC (also known as HD 97950) is a very compact and massive young star cluster at the centre of the vast homonym HII region. It is composed of three Wolf-Rayet stars and around 40 O-type stars, a dozen of which resides in the very central part of the core, within less than 1 ly from the centre (Drissen et al., 1995). Harayama et al. (2008) estimated the total mass to be between 1 and $2\times\ 10^4\ \mathrm{M}_\odot$. The H-R diagram in Melena et al. (2008) reveals the presence of at least 15 stars with masses greater than 60 $\mathrm{M}_\odot$. The most massive stars in the cluster seem to be coeval with ages between 1 and 2 Myr (Kudryavtseva et al., 2012; Melena et al., 2008; Stolte et al., 2004). However, the age spread between the pre-main-sequence stars (Beccari et al., 2010) and the slightly older stars in the cluster outskirts (Sung & Bessell, 2004) suggests a possible extended star formation scenario.

The Arches cluster is considered to be the densest cluster in our Galaxy. It also falls in the category of so-called starburst star clusters. It is located near the Galactic centre and its age is estimated to be around 2 Myr. Its total mass is estimated to be around $2\ \times\ 10^4\ \mathrm{M}_\odot$ (Espinoza et al., 2009) and it contains 160 O-stars and 13 Wolf-Rayet[2] (Figer, 2004; Martins et al., 2008).

For NGC 3603 YC, we considered the mass function results published by Pang et al. (2013) and for Arches the one published by Stolte et al. (2005). To derive the mass function of NGC 3603 YC, the authors considered stars in absolute V-magnitude bins and then derived the correspondent masses using the isochrone models from Lejeune & Schaerer (2001) for high mass stars and Siess et al. (2000) for low mass stars. Their mass bins have a logarithmic size of 0.2. The data were corrected both for incompleteness and foreground stars contamination and include all stars within 60" ($\sim$ 2 pc).

Stolte et al. (2005) derived the present day mass function of the Arches cluster by converting the K-band magnitudes from the corrected color-magnitude diagram into masses using a 2 Myr Geneva main-sequence solar metallicity isochrone from Lejeune & Schaerer (2001). They also binned their data using logarithmic intervals of size 0.2 and they computed the mass function 10 times, each time shifting the bins by 0.02. The final present-day mass function was created by averaging all the points from these 10 mass functions and takes into account all stars within 0.4 pc.

Comparing these observational data to our simulations is not trivial, since we do not know the SFE of the parent clouds of both NGC 3603 YC and the Arches. The targeted clusters have about twice the mass of our

[2]This is about 5% of all known Wolf-Rayet stars in the Milky Way (Figer et al., 2002).

simulated ones from the feedback runs, but roughly equal to the one in our no-feedback simulation. If the true SFEs of the observed star clusters were very low, say 10%, this would imply that the original clouds would be as massive as $10^5 M_\odot$, which is computationally too expensive to simulate at the current resolution and with our radiation solver. Therefore, we decided to re-normalise the observations. The normalisation factors are computed requiring that the mass bin at $15\ M_\odot$ in the two observational datasets have the same value, equal to that of our simulated data set. The normalisation coefficients for the Arches dataset are 0.4, 0.5 and 1.1 with respect to the strong, weak and no feedback cases, respectively, while the normalisation coefficients for the NGC 3603 dataset are 1.2, 1.5 and 3.3 with respect to the strong, weak and no feedback cases, respectively

In Figure 5.4 we compare these renormalised observed mass functions to our simulated ones. Renormalised observational data are showed with red triangles (NGC 3603) and green circles (Arches). The best agreement, especially at the high-mass end, is obtained with the strong feedback (after renormalisation). The weak and no-feedback runs clearly produce too many very high-mass stars. The agreement is worse at lower masses, especially below $10\ M_\odot$. As we explain below, we believe this is due to our limited resolution.

5.3.2.2. Slope of the mass function

The previous analysis was carried out considering all the sinks in the simulation box. We now study the mass function dependency with radius. In Fig. 5.5, we show the mass function taking into account only sinks within specific radii[3], namely 1, 3 and 5 pc, and for all three feedback regimes. The last radial bin contains 92%, 74% and 88% of the simulated sinks respectively for strong, weak, no feedback. The solid curve corresponds to the whole box, or a radius of 10 pc. Although the mass function appears to be independent of radius for the no feedback case, it looks clearly flatter in the inner parts and steeper in the outer parts for the two feedback cases. Pang et al. (2013) showed that a similar effect is present in NGC 3603: the slope of the mass function steepens with radius, indicating that the most massive stars are mostly concentrated in the centre. This feature is generally explained by mass segregation. We will develop this topic in the next section.

If we now quantify the slope of the mass function, we found that all our

[3]Unless otherwise stated, the radius is always considered respect to the centre of density of the system defined as in Portegies Zwart et al. (2001).

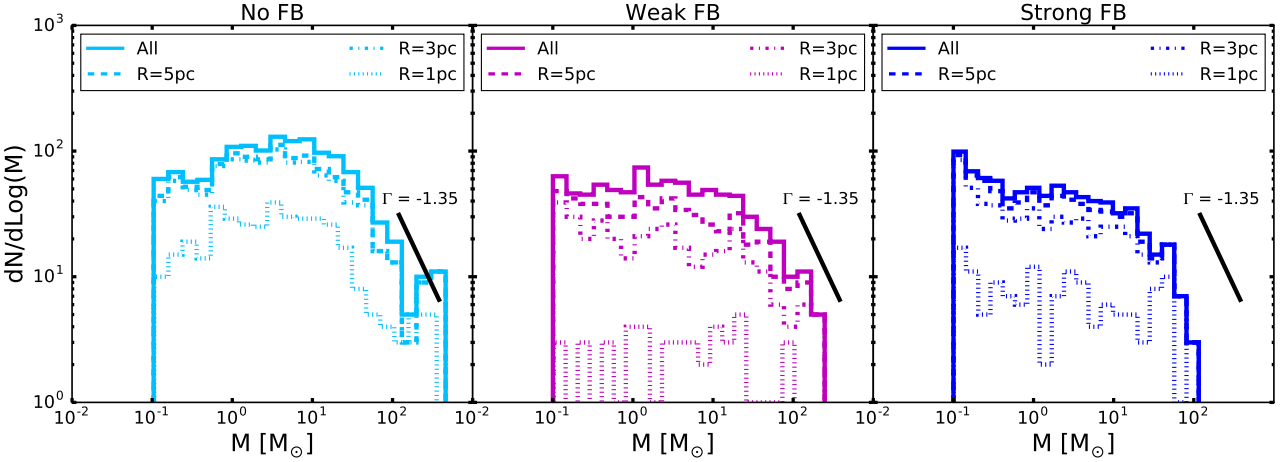

Figure 5.5: Mass functions at different radii, R=1, 3, and 5 pc. The solid thick line refers to the total mass function (all sinks included). In black the Salpeter slope (Γ = -1.35) is indicated as a reference. In all cases the slope of the simulated mass functions is flatter than the Salpeter one. Moreover, the slope steepens with radius, especially in the feedback cases, indicating a higher concentration of massive stars in the centre.

simulations show a slope (Γ) much flatter than that of the Salpeter IMF (i.e. Γ=-1.35), depending sensitively on the range of masses used to compute it (see Fig. 5.5). This is also the case for observed young and embedded star clusters. NGC 3603, for example, has $\Gamma = -0.88 \pm 0.15$, considering only $\log(\mathrm{M}/\,\mathrm{M}_\odot) > 0.6$ for completeness reason. For the Arches, Stolte et al. (2005) detected a change in the slope of the mass function at about 6 $M_\odot$, hence they fitted the mass function in the range $\log(\mathrm{M}/\,\mathrm{M}_\odot) > 0.8$. The resulting value was measured to be $\Gamma = -0.86 \pm 0.15$. Both these clusters have slopes flatter than the Salpeter slope, which seems to be in general a distinguishing feature of young starburst clusters.

The origin of this discrepancy from the Salpeter slope is probably due to many reasons. On the simulation side, Bertelli Motta et al. (2016) showed that the simulated IMF can be affected by resolution, with the peak or turn-over mass depending directly on it. The higher the resolution, the lower the turn-over mass, which implies a progressive steepening of the mass function with increasing resolution. These authors estimated that the peak mass is roughly ~ 30 times the minimum Jeans mass, which is our case corresponds to about 4.5 $M_\odot$, and agrees quite well with our no-feedback case.

So, resolution effects are likely a cause of the low value for Γ in our simulations in the intermediate mass range $\log(\mathrm{M}/\,\mathrm{M}_\odot) < 1$. Moreover, feedback inevitably plays a role in all this, lowering the number of stars in the intermediate-high mass range, therefore contributing to an even shallower slope. At larger masses, on the other hand, recent theories of turbulent cloud collapse argue for an asymptotic Salpeter slope (Hennebelle & Chabrier, 2008; Hopkins, 2012). This could be consistent with our simulated star clusters, but also with the observed ones, without being very conclusive, reminding us that the story is probably not so simple.

It is quite possible that the mass function of these observed objects is not yet the final one, due to their very young age. The final IMF could evolve into a steeper function by dynamical and stellar evolution. Another theory for the IMF is based on the self-similar fragmentation of molecular clouds into clumps and clumps into stars, leading to a power law mass distribution with $\Gamma = 1$ (Oey, 2012). Yet another explanation has been designed using competitive Bondi accretion on random seeds, leading also to a $\Gamma = 1$ mass function (Zinnecker, 1982). In these two theories, the Salpeter slope was obtained by identifying massive stars as rare events that cannot form in the low-mass available gas clumps of the cluster (Oey, 2012).

5.3.3. Mass segregation

We have already introduced mass segregation in the previous section to explain a steepening of the slope of the mass function as a function of radius. We now analyse our simulations with more traditional tools to quantify mass segregation in star clusters. A star cluster is considered to be mass segregated when the massive stars are more centrally concentrated than the lower mass stars. The main question related with mass segregation is whether it has a primordial or a dynamical origin. Mass segregation can indeed be the result of two or three body interactions between stars (dynamical) or the direct outcome of the star formation process within the gas cloud itself (primordial). Our simulations are ideal experiments to try and answer this question.

The problem of comparing the mass function for different radii to characterise mass segregation is that we need to define unambiguously the centre of the star cluster, which is a difficult task. Allison et al. (2009) introduced the Minimum Spanning Tree (MST) to quantify the degree of mass segregation in a star cluster. The MST is defined as the shortest path connecting all points, which does not contain any closed loop. We used the routine included in the `csgraph` module of `scipy`, which implements the MST according to Kruskal's algorithm (Kruskal, 1956).

We followed Allison et al. (2009) prescription to quantify mass segregation using the MST. We computed the length, $\mathrm{L_{massive}}$, of the MST of the N most massive stars and compared this to the average length of the MST of N random stars in the cluster, or $\mathrm{L_{random}}$. $\mathrm{L_{random}}$ was calculated by picking 1000 random sets of N stars, in order to have a small error on the dispersion σ. Mass segregation is quantified using the *Minimum Spanning Tree Ratio* Λ_{MSTR} defined by Allison et al. (2009) as

$$\Lambda_{\mathrm{MSTR}} = \frac{\mathrm{L_{random}}}{\mathrm{L_{massive}}} \pm \frac{\sigma}{\mathrm{L_{massive}}}.$$

For $\Lambda_{\mathrm{MSTR}} \sim 1$, the distribution of massive stars is comparable to that of all stars. For $\Lambda_{\mathrm{MSTR}} > 1$, massive stars are more concentrated, a clear sign of mass segregation. The larger Λ_{MSTR}, the more pronounced is the mass segregation.

This method was already adopted by Parker et al. (2015, 2014) to analyse the dynamical evolution of star forming regions, starting from the final states of the SPH simulations by Dale et al. (2012a,b). Using Λ_{MSTR} for their $N = 10$ most massive stars, they found in their no-feedback simulation a strong primordial mass segregation with $\Lambda_{\mathrm{MSTR}} \simeq 5$, which disappears

after 3 Myr due to stellar evolution and reappears at the same level after 8 Myr due to dynamical interactions between the cluster members. However, in their feedback simulations that include winds and photoionisation, they did not detect any mass segregation, with $\Lambda_{\rm MSTR} \simeq 1$ at all times.

In Figure 5.6, we plot $\Lambda_{\rm MSTR}$ as a function of N_{MST}, the number of stars we use for the spanning tree, at t = 2Myr. We include in our analysis all stars up to an outer radius of 7.7 pc, 9.3 pc and 9.8 pc, corresponding to the distance from the centre of the cluster of the most external bound star, in the strong, weak, and no feedback cases respectively. This is done to prevent extreme outlier stars to dominate the calculation of the random spanning tree. Our data point with $N = 10$ corresponds to the estimator used in Parker et al. (2015).

All three cases show some degree of mass segregation. Our no-feedback case is strongly mass segregated for N=10 with $\Lambda_{\rm MSTR} \simeq 10$, and is still significantly segregated for N=20 with $\Lambda_{\rm MSTR} \simeq 5$. The signal however disappears for $N \geq 30$. The strong feedback case shows the weakest mass segregation for $N = 10$ with $\Lambda_{\rm MSTR} \simeq 2$, but the segregation signal is still detectable up to $N = 60$. The weak feedback case lies in between the two other cases.

The two crucial pieces of information Figure 5.6 provides are 1) the degree of mass segregation of the cluster, namely the value of $\Lambda_{\rm MSTR}$ and 2) the extent of mass segregation, namely the maximum number of stars that are mass segregated. From our results, two different situations emerge. In the no feedback case (and to some extent in the weak feedback case), only a handful of super-massive stars are tightly concentrated at the centre. Only those most massive stars are mass segregated. The high stellar density is supported by the high measured values of $\Lambda_{\rm MSTR}$. This population of massive stars forms effectively a sub-cluster at the centre of the main cluster, that keeps contracting and decouples dynamically from the rest, transferring its kinetic energy to less massive stars that are ejected (see next Section).

On the contrary, in the strong feedback case, photo-ionisation feedback is efficient enough to halt the collapse of the gas, limiting the number density of massive stars. This prevents the formation of an independent self-gravitating system within the cluster itself. This translates into a lower degree of mass segregation and at the same time a higher number of stars being mass segregated.

In order to compare with observations, we plot $\Lambda_{\rm MSTR}$ as a function of the stellar mass (Fig. 5.7). Following Pang et al. (2013), we sort the stars by their mass and then consider blocks of 20 stars moving in steps of 10

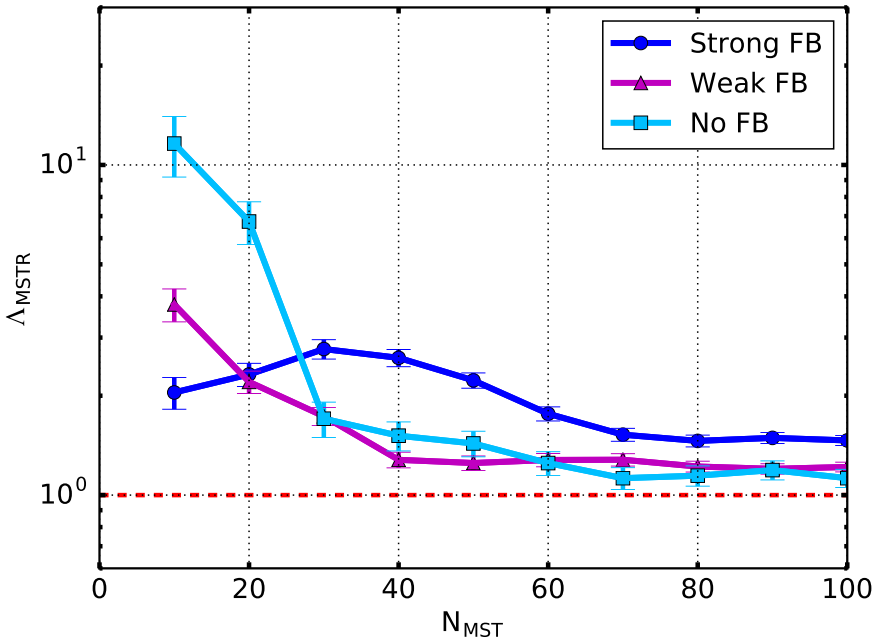

Figure 5.6: Minimum spanning tree ratio $\Lambda_{\rm MSTR}$ against number of stars used to calculate the length of the tree. The red dashed horizontal line indicate the value $\Lambda_{\rm MSTR}$=1, meaning no mass segregation. The vertical bars correspond to 1 σ error of $\Lambda_{\rm MSTR}$. All three cases show some degree of mass segregation.

stars, such that the data partially overlap. For example, the first 20 stars in the weak feedback case (magenta line in Figure 5.7) cover the range 200 to $80\,\mathrm{M}_\odot$ in mass, the second mass group goes from 130 to $60\,\mathrm{M}_\odot$, etc. The mass interval considered is indicated by horizontal bars in the plot. For every bar a marker denotes the mean mass of the interval.

The three profiles of Λ_{MSTR} versus mass in Figure 5.7 look qualitatively similar, but they are shifted to higher and higher masses with increasing feedback strength. The no feedback case shows mass segregation only in the first bin ($\mathrm{M}>200\,\mathrm{M}_\odot$) with an amplitude much larger than unity. For the weak feedback case, only stars down to a mass of 60 $\mathrm{M}_\odot$ are weakly segregated, with an amplitude of 2, and for the strong feedback case, the transition goes down to 30 $\mathrm{M}_\odot$.

In Figure 5.7, we compare our simulations to the data of Pang et al. (2013) on NGC 3603 (yellow points). A very good agreement is obtained with the strong feedback case. In Figure 5.8, we plot only the strong feedback case and the observations using a linear scale in mass to allow a better comparison and to outline the very good quantitative match between our model and the observed segregation, both in terms of amplitude and of transition mass.

Despite being young, NGC 3603 shows already a clear signal of mass segregation. This is not an isolated case. There is also strong evidence of mass segregation in the Orion Nebula clusters, but also in the Arches, NGC 6611, NGC 2244 and NGC 6530, to name a few (Bonatto et al., 2006; Chen et al., 2007; Hillenbrand & Hartmann, 1998; Schilbach et al., 2006; Stolte et al., 2002). The origin of the mass segregation in these clusters is still an open question (primordial or dynamical).

Pang et al. (2013) proposes for NGC 3603 a dynamical origin. Using analytical arguments, they show that the cluster dense core could dynamically segregate in one crossing time down to a mass of 30 $\mathrm{M}_\odot$. To test this hypothesis, we have performed our clustering analysis at earlier times and find no indication of mass segregation for massive stars. We have estimated the local two-body relaxation timescale of the densest part of the cluster ($r < 2$ pc) and find it to be less than 0.5 Myr for all 3 cases, supporting our claim that dynamical friction can cause mass segregation after 1 Myr.

To quantify further the structure and morphology of our star clusters , we have used another statistical indicator called the Q parameter (Cartwright & Whitworth, 2004). Q is defined as the ratio between the normalised mean edge length $\overline{\mathrm{m}}$ of the MST of all stars in the cluster and

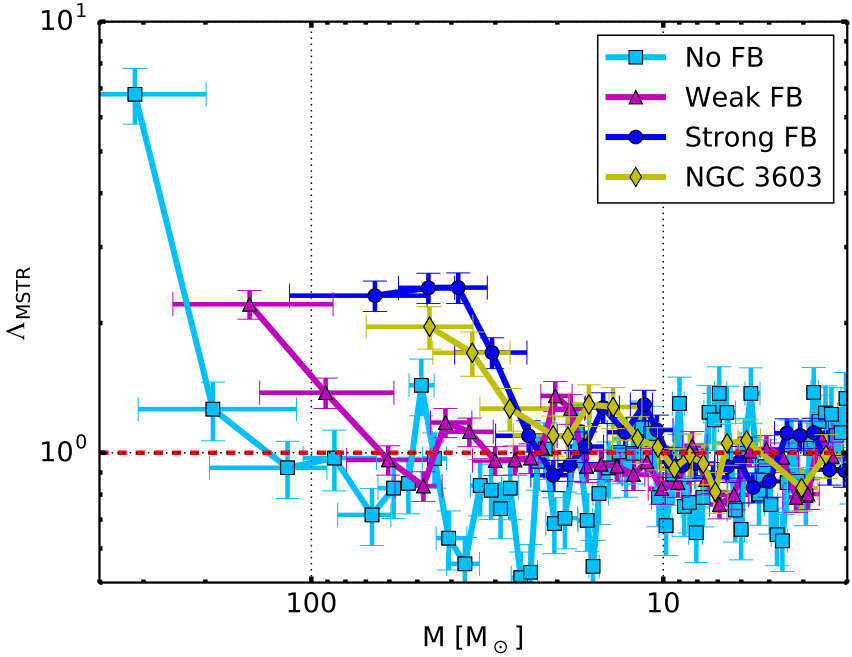

Figure 5.7: Minimum spanning tree ratio $\Lambda_{\rm MSTR}$ versus stellar mass. The red dashed horizontal line indicate the value $\Lambda_{\rm MSTR}$=1, meaning no mass segregation. The vertical bar corresponds to 1 σ error of $\Lambda_{\rm MSTR}$. Horizontal bars show the mass interval covered by every group of 20 stars. Note that the horizontal line associated with the first data point for the non-feedback case extends to the left until ~ 400 $M_\odot$. Observations are indicated in yellow. All curves show a similar behaviour, even if shifted towards higher masses. The best agreement with observations is provided by the strong feedback simulation.

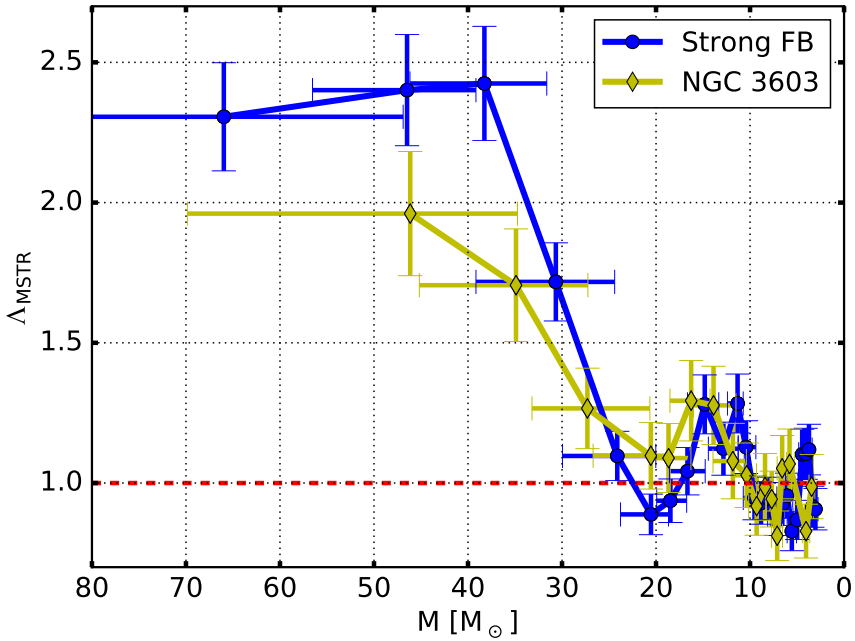

Figure 5.8: Zoom-in plot of Figure 5.7. The comparison here is only between strong feedback case and NGC 3603 YC.

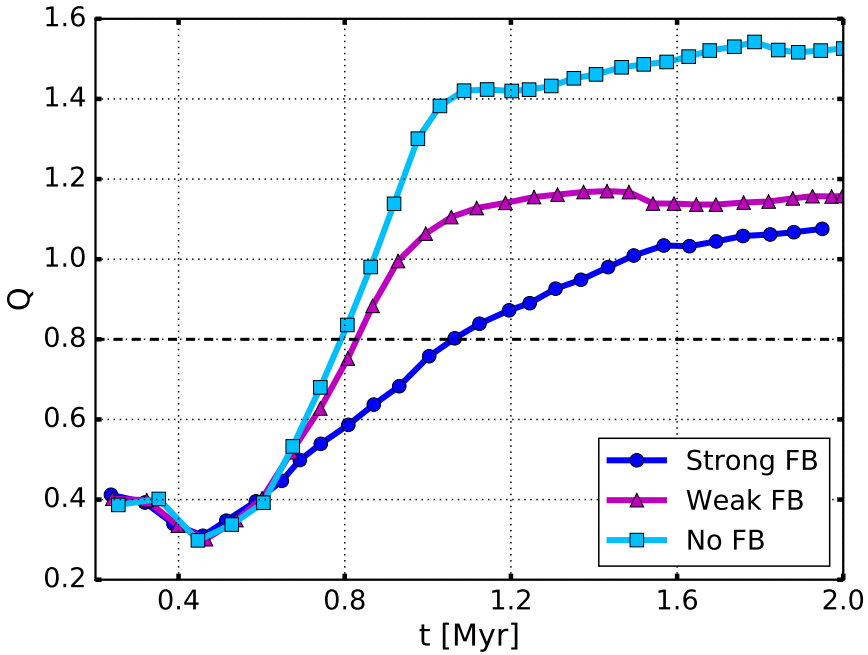

Figure 5.9: Evolution with time of the Q parameter. The dashed horizontal line correspond to Q=0.8. This value discriminates between centrally concentrated (> 0.8) and fractal (< 0.8) spatial configuration. The simulations with feedback preserve substructures longer than the control run.

the normalised correlation length $\bar{s}$ of the same stars[4]. These parameters taken separately cannot distinguish between a smooth, radially concentrated distribution and an extended, fractal distribution, but their ratio can (Cartwright & Whitworth, 2004). A cluster with $Q > 0.8$ is smooth and centrally concentrated, while if $Q < 0.8$, it is extended with a fractal distribution.

In Figure 5.9, we show the evolution of the Q parameter with time. In all our simulations, the star cluster is initially fragmented and extended. The no feedback case rapidly evolves towards a more spherical and centrally concentrated distribution with $Q \simeq 1.5$, while in the two other cases, the transition is slightly slower, supporting a longer survival of substructures, and reaches a smaller maximum value with $Q \simeq 1.1$ and 1.2. This supports

[4]The correlation length is defined as the mean separation between stars in the cluster.

a scenario in which gravitational collapse together with stellar dynamical interactions progressively erase the initial conditions in the gas cloud and build up a dense and spherical star cluster. In this context, feedback acts as a delay mechanism, favouring lower stellar densities with a longer relaxation timescale, allowing the longer survival of the initial substructure and a more extended final distribution.

5.3.4. Stellar dynamics

In this section, we focus on the dynamics of individual stars and study the influence of the star cluster formation scenario. Our interest is on escaping stars, due to various dynamical interactions in the densest regions of the star cluster. We then study binary stars, as they are the most likely source of escaping stars during the early phase of the life of the star cluster.

5.3.4.1. Escaping stars

Escaping stars are particularly interesting when they are massive: they can travel long distances in the galaxy and eventually explode as supernova (SN) in a location far from their original birthplace, typically in the diffuse ISM. In the kiloparsec scale simulations of Hennebelle & Iffrig (2014) and Iffrig & Hennebelle (2015), the global star formation rate in the Galaxy was reproduced if supernovae were allowed to explode up to 20 pc from their natal cloud, while "homebred" supernova explosions were much weaker in suppressing star formation . Similarly, Gatto et al. (2015) showed that allowing SN to explode at random positions, rather than at density peaks significantly changes the properties of the ISM, resulting in a hot gas filled volume ISM in the first case and a filamentary, hot gas deprived ISM in the second one. Thus, being able to predict the correct number of escaping massive stars to be used as input in galactic scale simulations is of vital importance.

Escaping stars (or for short "escapers") are usually categorised into "walkaway stars" and "runaway stars"[5]. Runaway stars (RS) are defined as stars with velocities larger than 30 km/s (Blaauw, 1961), produced either by supernova explosion in a tight binary system, during which the

[5]Hypervelocity stars are here considered an extra category, which is not treated in this work. These stars are thought to have a Galactic centre origin (Brown et al., 2005), probably resulting from close encounters between binary systems and the central supermassive black hole. They reach velocities of $\sim$1000 km/s, and hence they are actually unbound from the Galaxy. The current fraction of known hypervelocity stars is $\sim 10^{-8}\%$ of all stars in our Galaxy (Brown et al., 2007).

Table 5.1: Statistics about escapers and multiple systems for all simulations (Strong FB, Weak FB, No FB). In brackets are indicated the percentages, when relevant.

	Strong	Weak	No FB
2-body systems	51	39	40
3-body systems	9	9	5
>3 body systems	6	5	5
Tot multi-body syst	66	53	50
Stars in multi-body syst	155(19%)	126(15%)	150(11%)
with M>1 $M_\odot$	128(31%)	109(20%)	129(12%)
with M>10 $M_\odot$	70(55%)	78(39%)	94(24%)
Bound stars	510 (62%)	473 (57%)	900 (64%)
Unbound stars	315 (38%)	355 (43%)	502 (36%)
Runaway	1 (1‰)	3 (4‰)	31 (2%)
of which in multi syst	1	0	2
Walkaway	230(28%)	297 (36%)	476 (34%)
of which in multisyst	60(7%)	50 (6%)	39(3%)

companion star of the supernova gets expelled (Eldridge et al., 2011; Portegies Zwart, 2000) or through dynamical ejection due to very close, three body encounters with massive stars (Banerjee et al., 2012; Oh & Kroupa, 2016; Perets & Šubr, 2012). In this section, we focus only on the latter mechanism, while the former can be thought of as a direct consequence of the multiplicity function which we will discuss in the next section. Walkaway stars (WS , velocities lower than 30 km/s) are normally defined as "slow escapers", since these are slowly moving stars ejected though normal relaxation processes, such as evaporating stars though distant two-body encounters with other single stars or soft binaries (Spitzer, 1987).

In Figure 5.10, we plot the modulus of velocity versus position of all stars in the cluster. The size of the symbols is proportional to the mass of the star. Filled symbols indicate single stars, while open circles denote stars which are part of a multiple system (binary, triple or more). The escape velocity is computed as a function of radius (green solid line in Fig. 5.10), assuming spherical symmetry, which is a good approximation at t=2Myr (see Fig. 5.9), by averaging over the individual escape velocities at different positions within the same spherical shell.

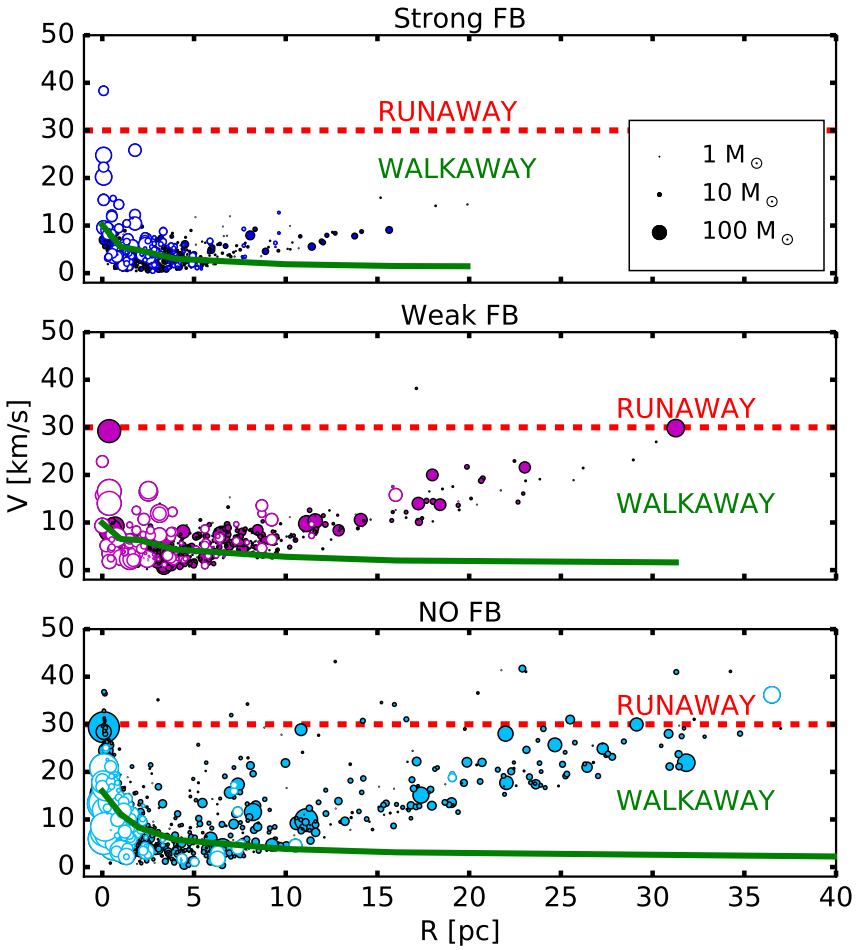

Figure 5.10: Velocity-position diagram of all stars in the cluster for all 3 simulations at t= 2Myr. The symbol size is proportional to the stellar mass. Filled circles: single stars. Open circles: stars which are part of multiple systems (binaries, triple systems etc). The dashed red horizontal line indicates the conventional velocity above which stars are classified as "runaway". The solid green line indicates the escape velocity.

The no feedback case exhibits the highest number of RS candidates[6], namely 31, or about 2 % of the total number of stars in the cluster. In the cases with feedback, the number of RS is lower, only 1 and 3 in the strong and weak feedback respectively, accounting only for 0.1% and 0.4% of the total number of stars. The RSs in our simulations are generally only massive stars ($38\,M_\odot$, $229\,M_\odot$, $132\,M_\odot$, $2\,M_\odot$) in the feedback cases, while in the no feedback they cover the whole mass spectrum, going from 0.15 $M_\odot$ to 417 $M_\odot$.

Regarding WS, the fraction changes slightly depending on the exact definition used. A first possibility is to take all stars with velocity higher than the escape velocity at a given radius and lower than 30 km/s. This gives us a percentage of WS similar in all simulations, around 30%. If we remove stars in multiple systems that are still bound (see Footnote 2), then the fraction is reduced to 20%. The final option is to consider WS only in the outskirts of the star cluster, in order to avoid counting stars that are only momentarily unbound. If we call R_{esc} the radius at which the escape velocity becomes comparable to the average stellar velocity at that radius, we can impose the extra-requirement to be at a distance greater than $R_{esc} \simeq 5$ pc from the centre of the star cluster. In this case, we get a very conservative estimate of the fraction around 15% of the total number of members of the cluster.

Table 5.1 gives an overview of the statistics for escaping stars and multiple systems. We also report the fractions of bound and unbound stars, derived by calculating the kinetic and potential energy for every star, and then verifying whether the sum of the two energies is negative and positive, respectively. In all simulations the fraction of bound stars is about the same, around 60%.

Comparing the populations of RS and WS in the three simulations, we find that the run without feedback produces much more fast escaping stars than the two feedback cases. This is consistent with our conclusions in the previous sections, of a very dense star cluster hosting a central clump of tight multiple systems of fast massive stars. Three-body interactions can cause the violent ejection of a member of a binary, of the perturber or of the entire binary system (see Fig. 5.10). In the feedback cases the central densities are lower, and therefore RS stars are rare events.

[6]It is important to clarify that in Figure 5.10 for binaries, triple systems and more, we plot the true velocity, not the velocity of the centre of mass of the multiple system. Thus, some very high velocity binary members are actually still bound. In the computation of the number of RS we did not correct for this, hence we prefer to talk about RS "candidates", meaning that some are probably not unbound yet, but very likely to be, due to frequent interactions with other particles.

The number of WS follow the same trend, with the strong feedback case having slightly less WS stars than the weak and no feedback cases. Strong feedback leads to the less frequent interactions, owing to the lower stellar density, which slows down the evaporation of the stars. We also notice that the different conditions in the three runs have an effect on the typical velocity and mass of WS. In the strong feedback case, they don't reach velocities higher than 10 km/s and are mostly low mass stars, probably escaping due to several repeated low energy kicks, typical of evaporation, while in the no feedback case both low- and high-mass stars can reach velocities close to the RS limit of 30 km/s, as a result of direct ejection.

5.3.4.2. Multiple systems

We focus now on the analysis of multiple stellar systems. We identify candidate multiple systems by analysing all possible pairs of stars from the cluster. For each pair we calculate the internal energy, as the total energy of the system in the frame of their centre of mass (Binney & Tremaine, 2008),

$$\widetilde{E} = \frac{1}{2}\mu v_{12}^2 - \frac{Gm_1 m_2}{r_{12}}, \tag{5.5}$$

where m_1 and m_2 are the masses of the two stars, $\mu = \mathrm{m}_1\mathrm{m}_2/(\mathrm{m}_1 + \mathrm{m}_2)$ is the reduced mass, v_{12} is the relative velocity, r_{12} the relative distance between the two stars, and G is the gravitational constant.

We define the two stars as a binary when $\widetilde{\mathrm{E}} < 0$. We consider all the binary connections as edges in a graph, whose nodes are all the stars involved in multiple systems. We use graph reduction algorithms to extract which edges share the same nodes, and we group the nodes together, defining triple, quadruple or quintuple systems in this way. For example, two binary systems, (i, j) and (j, k), which share one node, are considered a triple system.

A slightly different technique was used by Bate (2009) to identify multiple systems. They replaced the binary systems by a virtual star sitting at the centre of mass and with mass equal to the sum of the two masses. They then searched for isolated stars with a negative binding energy with these virtual stars. The same procedure was iterated only up to quadruple systems.

An advantage of our graph-based method is that we can easily identify systems with multiplicity larger than 4. However, in most cases the two algorithms will produce the same catalogue of multiple systems, since, in

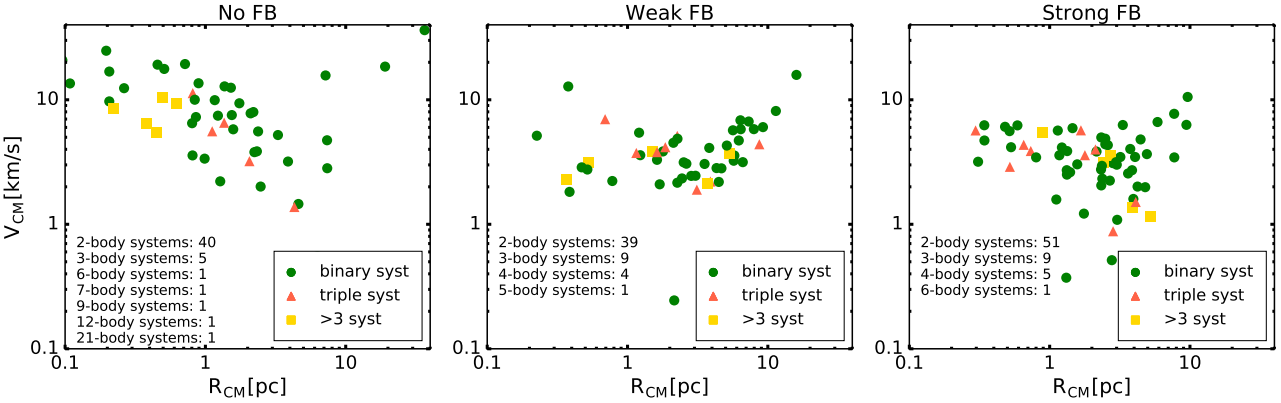

Figure 5.11: Velocity-position diagram of multiple systems (binary, triple, > 3) in the cluster for all 3 simulations. We consider velocities (V_{CM}) and positions (R_{CM}) of the centres of masses of the multi-systems of stars. In text we give details about the statistics of the systems.

our case, most multiple systems include a massive star, which dominates the gravitational potential of the system (see Fig. 5.13).

In Table 5.1, we report on the statistics of binary, triple and more than 3-body systems for all three simulations. We note that the fractions of stars in multiple systems, also known as the multiplicity fraction, correlates with the strength of feedback, with overall percentages spanning from 11% (no feedback) to 19% (strong feedback). If we exclude stars with mass lower than 1 $M_\odot$, the multiplicity fraction differentiates even more between the three feedback regimes and rises to 12%, 20% and 31% for no, weak and strong feedback respectively. For stars, with mass greater than 10 $M_\odot$, the fraction goes up to 24%, 39% and 55%.

The observed multiplicity fraction is around 20%, when one considers field stars and low mass stars, but reaches 60% for OB and massive stars (Goodwin, 2010; Kraus & Hillenbrand, 2007; Lafrenière et al., 2008). These values are well reproduced by our strong feedback case, while our no feedback run underestimates the number of stars in multiple system, when compared to observations, especially for massive stars. Observations also reveal that the binary fraction is higher in lower density star forming regions, like in our strong feedback case, while denser clusters exhibit multiplicity fractions comparable to the field or low mass stars, like in our no feedback case (Lafrenière et al., 2008; Reipurth et al., 2007).

In Figure 5.11, we plot the distribution of multiple systems in terms of position versus velocity. Here, we consider the positions and the velocities of the centres of masses, explaining why velocities are lower than in Figure 5.10. In general, we observe that in the feedback simulations binary, triple and more than 3-body systems are uniformly distributed throughout the cluster, while the no feedback case shows many systems with very high multiplicity in the very inner part of the cluster, while binaries and triple systems occupy the outskirts. In all cases, we see many ejections of binary systems.

In the same plot, we also indicate the exact count of multiple systems, in particular for groups with more than 3 bodies. We notice that the maximum multiplicity reaches a much higher value in absence of feedback, due to the very high stellar density. With feedback, the most crowded multiple systems have 5 or 6 members, while in the no feedback run we have systems with as many as 9, 12 and 21 members. All these high multiplicity systems are highly unstable and they will be destroyed during the subsequent dynamical evolution of the cluster. As a matter of fact, we do not observe such systems in real star clusters .

In the strong feedback case, the lower stellar density will also guarantee

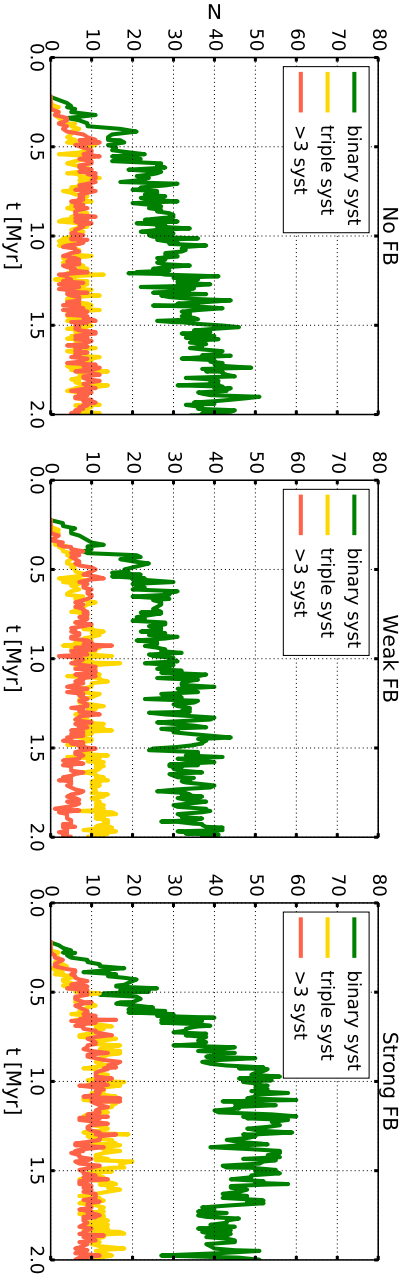

Figure 5.12: Evolution with time of the number of multiple systems (binary, triple, > 3).

the survival of the binary systems, which otherwise, like in the no feedback case, aggregate in bigger associations or are destroyed in three-body interactions. In that context, it is useful to divide binaries into two categories, *soft* binaries and *hard* binaries. Soft binaries are systems for which $|\widetilde{E}| < \overline{K}$, while hard binaries have $|\widetilde{E}| > \overline{K}$, where $\overline{K}$ is the typical kinetic energy of the stars in the cluster (Binney & Tremaine, 2008). We use here the median kinetic energy. According to this definition, for the two feedback cases, we have 50% hard and 50% soft binaries, while the no feedback case shows only 30% hard and 70% soft binaries, which support even more our conclusion that binaries will survive longer in the strong feedback case.

In Figure 5.12, we plot the time evolution of the number of binary, triple and more than 3-body systems. In all three models, the number of triple (or more) systems is almost constant. This is not the case for the number of binaries. In the strong feedback case, it increases sharply during cloud collapse and after the gas has been dispersed around 1 Myr, it slowly decreases. No additional stars are created and the soft binaries get destroyed through ejection or evaporation. In the no feedback case, the number of binaries keeps increasing since star formation continues until the end of the simulation. The weak feedback case shows an intermediate behaviour, with a mild initial increase, followed by a almost constant evolution.

5.4. Summary and Discussion

In this work, we have performed radiation hydrodynamics simulations of a collapsing turbulent molecular cloud with the adaptive mesh refinement code `RAMSES`. We have studied in detail the emergence of the star cluster from the parent gas cloud with and without the influence of photoionisation feedback. Stars are modelled using a sink particle algorithm. Photoionising radiation is included with two different regimes: weak and strong feedback. We also perform a reference simulation without any feedback. Our main focus is the emerging properties of the star cluster, both from a structural and a dynamical point of view.

The main effect of photo-ionisation feedback is to reduce considerably the stellar density of the star cluster and to limit the accretion on very massive stars. This has a large impact on the dynamical properties of the final star cluster. As a result of the reduced stellar density, the star cluster can settle in virial (or even sub-virial) state, while in the absence of feedback, strong and frequent close interactions in a highly collisional environment lead to the disruption of the cluster. For this reason we conclude that the

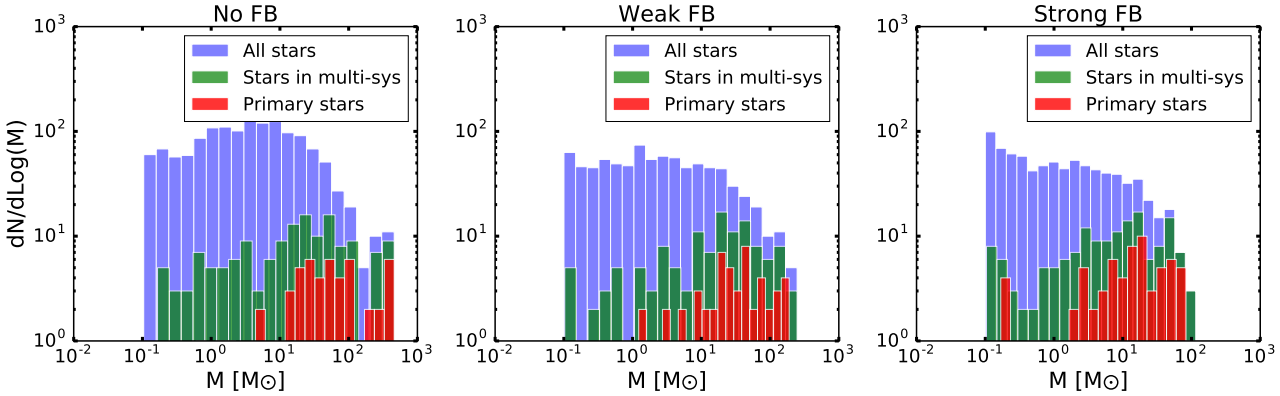

Figure 5.13: Mass diagrams of stars in multiple systems . The blue histogram reports the total mass function of the cluster. In green we show only stars which are member of multiple systems (binaries, triple, >3) and in red we plot the mass of the primary star, intended as the most massive star in the multi-body system. Most multiple systems contain at least one star with $M > 10 M_{\odot}$. In the case with feedback we have also some systems composed only from low-mass stars.

one between photo-ionisation and star cluster formation is a "love story", with the feedback effectively "saving" the cluster from being destroyed. This is in contrast with the traditional view that strong feedback is responsible for the star cluster early mortality, by rapidly removing gas from the emerging cluster (Hills, 1980). The star formation efficiency can be reduced down to 20%, without affecting the virial equilibrium of the star cluster.

The stellar mass function is also affected at the high mass end, with a clear self-regulating role played by feedback, limiting the mass of the most massive stars by a factor of 4 compared to the no feedback case. As a result, our mass function with strong feedback compares favourably with observations of two starburst clusters (NGC 3603 and the Arches) but only after re-normalising the data and for masses larger than $10 M_{\odot}$.

We also use mass segregation statistics to test our model. In absence of feedback, the higher stellar density causes an unrealistically too high degree of mass segregation for a few very massive stars. When including strong feedback, we obtain a more extended star cluster with a degree of mass segregation consistent with the one observed in NGC 3603.

We have also computed the number of ejected stars, which anti-correlates with the feedback strength: for weaker feedback, we get a higher stellar density and more stars are escaping, both as runaway and walk-away stars. This result has profound implications for galactic evolution, when supernovae will start exploding at later time in a large variety of galactic environments.

Our statistics of multiple systems of stars supports the same conclusion: in a denser environment, the fraction of stable binary systems is lower, and most stars tend to either cluster into unstable many-body systems, or are ejected. On the other hand, in the strong feedback case, the lower stellar density guarantees the survival of a higher fraction of binaries, in better agreement with observations.

Our results are in line with the findings of Dale et al. (2012a, 2013a, 2015), which showed that photo-ionisation feedback effectively lowers the star formation efficiency, and, for low-mass clouds like ours, can expel most of the gas within 3 Myr, before the first supernova can explode. Parker & Dale (2013, 2015); Parker et al. (2015) also observed that photo-ionisation feedback reduces the stellar density in the emerging cluster, which allows substructures to survive longer than in a scenario without feedback. However, in contrast with Parker et al. (2015) who did not find any mass segregation in the feedback case, we do see a weak mass segregation signature, which is well in agreement with observations. Interestingly, although Fujii (2015) found that a local star formation efficiency of at least 50% is neces-

sary for the formation of young massive clusters, we could reach a value as low as 20% and still form a bound star cluster.

Our goal in this work is to better understand the transition from a gas cloud to a stellar cluster, or in other words, from gas dynamics to stellar dynamics. In that context, our direct N-body integrator, a second order leap frog scheme is probably accurate enough for our relatively short time integration, but its accuracy is far below the required standards in stellar dynamics for longer time scales. This sets the limit on the runtime of our simulations to a couple of Myr. This explains why, in comparison to Parker et al. (2015), who were able to investigate the long term evolution of the star cluster, we are forced to limit our study to the first 2 Myr.

We have also decided in this work to focus exclusively on photo-ionisation radiation. We have therefore neglected magnetic fields and other radiation processes, but also other important physical processes that could be relevant. Supernovae explosions, for example, are ignored, but, given the cloud mass we have adopted, all the gas is removed from the star cluster after only 2 Myr and they are therefore irrelevant. For larger cloud masses, however, this would not be the case. We have also ignored the possible role of stellar winds, but these have been shown to be negligible compared to photo-ionisation feedback (Dale et al., 2015).

We have also ignored the effect of the UV radiation force (or UV radiation pressure) on the gas dynamics. It has been shown that momentum transfer from photo-absorptions is only relevant for ultra compact HII regions, with densities larger than 10^{-15} g/cc and sizes smaller than 10^{-3} pc, completely unresolved in our simulations (see e.g. Rosdahl & Teyssier, 2015). More relevant would be the inclusion of lower energy photons, in the optical and infrared range. These propagate from accreting stars through dust grains, and are scattered into new infrared photons. Inside the HII regions we can probably ignore these effects as dust is quickly sublimated at 10^4 K, however, infrared and optical radiation can play a role before massive stars form. Skinner & Ostriker (2015) have shown that infrared radiation has very little impact on the gas removal and on the cloud destruction for realistic values of the dust opacity. Infrared radiation is likely to play a more important role on the fragmentation of molecular cores, but at scales we also do not resolve in our simulations.

In summary, we are able to simulate the collapse of a molecular cloud and the emergence of a star cluster, whose properties are tightly connected to the gas dispersal process. Comparing our results to two observed, very young and still active star cluster, NGC 3603 and the Arches, we conclude that an initially sub-virial molecular cloud with a star formation efficiency

lower than 30% can reproduce observations fairly well. Our analysis provides useful insights also for simulations on galactic scales. Star clusters are indeed the building blocks of galaxy formation and evolution. Understanding in details their properties, such as mass segregation, mass and multiplicity functions and escaping stars statistics, just after they emerged from their parent cloud, is of primary importance for their longer term dynamical evolution, but also for the evolution of their host galaxies.

6

Can Merging Explain Iron-Complex Globular Clusters?

After the gas has been dispersed, the resulting star cluster evolve into as a gas-free stellar system, of which globular clusters represent a perfect example. In this case the system can be treated as a pure N-body system. In this chapter[1] we explore this second phase of life of a cluster, focusing on a very specific problem. As we mentioned in the introduction, globular clusters exhibit a series of puzzling features, among which we listed multiple populations. While almost all globular cluster present multiple photometric and spectroscopic sequences, in a small group of them it was observed also a spread in iron abundance. These are the so-called iron-complex globular clusters. By means of N-body simulations, we investigate if merging is consistent with the observations of sub-populations and rotation in these clusters. The key parameters are the initial mass and density ratios of the progenitors. We find that when densities are similar, the more massive progenitor dominates the central part of the merger remnant and the less massive progenitor forms an extended rotating population. The low-mass progenitor can become the majority population in the central regions of the

[1]The work presented in this chapter has been published in the Monthly Notices of the Royal Astronomical Society, Volume 461, Issue 2 under the title "A critical look at the merger scenario to explain multiple populations and rotation in iron-complex globular clusters", following peer-review (Gavagnin et al., 2016).

merger remnant only if its initial density is higher by roughly the mass ratio. To match the radial distribution of multiple populations in two iron-complex GCs (ω Cen and NGC 1851), the less massive progenitor needs to be four times as dense as the larger one. Our merger remnants show solid-body rotation in the inner parts, becoming differential in the outer parts. Rotation velocity V and ellipticity ϵ are in agreement with models for oblate rotators with isotropic dispersion. We will discuss several kinematic signatures of a merger with a denser lower mass progenitor that can be tested with future observations.

6.1. Introduction

As we mentioned in the introductory chapter, for many decades GCs were described as stellar systems with homogeneous chemical composition and no age spread, despite early data showing multiple populations in M22 and ω Cen (Canon & Stobie 1973; Freeman & Rodgers 1975; Geyer 1967; Harris 1974; Hesser & Bell 1980).

Hubble Space Telescope data show a clear bifurcation of colour in the main sequence (MS) of ω Cen (Anderson, 1997), with more recent data showing at least four distinct red giant branches (RGBs, Lee et al. 1999; Pancino et al. 2000). Currently, most observed GCs show signatures of multiple populations, both in the Milky Way (Anderson et al., 2009; Carretta, 2015; Carretta et al., 2009a, 2007, 2010b; Gratton et al., 2004; Kayser et al., 2008; Milone et al., 2013, 2012a, 2010; Pancino et al., 2010) and in the Magellanic Clouds (Milone et al., 2008).

Most GCs contain stars with similar heavy-element abundances (especially [Fe/H]), but large (> 0.5 dex) star-to-star abundance variations for elements lighter than Si (e.g. Carretta et al. 2009a; Cohen 1978; Gratton et al. 2001; Johnson et al. 2015; Kraft et al. 1992; Peterson 1980; Sneden et al. 1991). Moreover, the variations of light-element abundances are anti-correlated with one another (e.g. the O$-$Na anti-correlation, Gratton et al. 2001). This phenomenology is generally considered to be due to internal enrichment by proton capture H-burning reactions at high temperature (e.g. Gratton et al. 2004).

A minority of GCs also show significant Fe abundance variations. In particular, ω Cen (Bellini et al., 2010; D'Orazi et al., 2011; Lee et al., 1999; Norris & Da Costa, 1995; Pancino et al., 2011), M22 (Hesser et al., 1977; Lee, 2015; Marino et al., 2009), M2 (Lardo et al., 2013; Milone et al., 2015; Piotto et al., 2012), M54 (Bellazzini et al., 2008; Carretta et al., 2010a; Sarajedini & Layden, 1995), NGC 1851 (Carretta et al., 2010c, 2011; Milone et al., 2009;

Yong & Grundahl, 2008), NGC 5286 (Marino et al., 2015; Nataf et al., 2013), NGC 5824 (Da Costa et al., 2014; Saviane et al., 2012), Terzan 5 (Ferraro et al., 2009; Massari et al., 2014) and M19 (Johnson et al., 2015) are labelled as 'iron-complex' GCs, because they have (i) a spread[2] in [Fe/H] exceeding ~ 0.10 dex, (ii) multiple photometric sequences, and (iii) a significant abundance spread for both light and heavy elements (Johnson et al., 2015). Iron-complex GCs differ from other GCs in several ways. In most GCs, the stellar population showing no enrichment by proton capture accounts for about one third of the total GC mass, with little spread among GCs (Carretta et al., 2009b). In contrast, in the iron-complex GCs, the ratio between the metal-poor and the metal-rich population changes from cluster to cluster. For example, in M19 the metal-poor component is ~ 50 % of the entire population (Johnson et al., 2015), whereas ~ 96 % of spectroscopically studied stars in M2 belong to the metal-poor component (Milone et al., 2015). Moreover, in the vast majority of GCs, the proton-capture enriched population is more radially concentrated than the most numerous one. In the iron-complex GCs the metal-poor population can be either more concentrated (NGC 1851, Carretta et al. 2011) or less concentrated (ω Cen, Bellini et al. 2009) than the metal-rich one.

Several theoretical models have been proposed to explain the multiple populations (Bastian et al. 2013; see Renzini 2008 for a review). A first class of models appeals to multiple star-formation events. After first population stars form out of pristine, metal-poor gas, the second population of stars might form from either the ejecta of asymptotic giant branch (AGB) stars (D'Ercole et al., 2008) or fast rotating massive stars (FRMS, Decressin et al. 2007). In the 'AGB scenario', winds and supernovae (SNe) of the first population evacuate the residual gas. After $\sim 30\,\mathrm{Myr}$, low-velocity winds from AGBs enriched in He and s-process elements start accumulating at the centre and form the second population. However, the predicted mass of the second population is an order of magnitude lower than what is observed, requiring a top-heavy first population initial mass function and an unusually efficient second population star formation.

A second model, called the 'early disc accretion model' (Bastian et al., 2013), proposes that the two populations formed during the same star formation episode, but underwent different chemical enrichment. This model requires very fast mass segregation and gas evaporation. With rapid mass segregation, the most massive stars sink to the centre where high-mass

[2]Recent studies highlight the possibility that the [Fe/H] spread is spurious, at least in some GCs (e.g. M22, Mucciarelli et al. 2015), because spectroscopically derived Fe abundances might be inaccurate due to non-local thermodynamical equilibrium effects.

stars in interacting binaries eject the primary's He-enriched envelope. This material pollutes the circumstellar discs of low mass stars that are still accreting, so they will grow in mass thanks to these ejecta from more massive (but still same-generation) stars. The main drawbacks of this model are disc lifetime and uniformity of enrichment. Even if circumstellar discs survive for the required $5 - 10\,\mathrm{Myr}$ (De Marchi et al., 2013), the "rainfall" of enriched material onto them is unlikely to be uniform (Kruijssen, 2014).

All the aforementioned scenarios are aimed to explain multiple populations with no or negligible iron spread, while they fail to reproduce the [Fe/H] variations observed in the iron-complex GCs. So far, the only proposed scenario that can naturally account for a metallicity spread is the merger between GCs (Amaro-Seoane et al., 2013; Makino et al., 1991; Pasquato & Chung, 2016; Sugimoto & Makino, 1989; van den Bergh, 1996). In this scenario, the different metallicities are signatures of the progenitors and can be used as a tag to make predictions about the distribution and dynamics within the final merger remnant. Iron abundance is, in this respect, a good tag to identify uniquely the different populations.

The merger scenario might be consistent with the oldest metal-rich stars in ω Cen being a few Gyrs older than the oldest metal-poor stars (Villanova et al., 2014), a circumstance that is against the predictions of self-enrichment scenarios. Furthermore, a merger can explain the kinematical differences in the velocity dispersion of the calcium-weak and calcium-strong RGB stars in M22 (Lee, 2015). The merger scenario has been proposed also for NGC 1851, where the most metal-rich population is less concentrated than the metal-poor one (Bekki & Yong, 2012; Carretta et al., 2010c, 2011; van den Bergh, 1996).

Another advantage of the merger scenario is that it can account for signatures of rotation in GCs, which have been observed in several GCs with multiple populations, both with (e.g. ω Cen, M2, M22, M54, NGC1851, Bellazzini et al. 2012; Kimmig et al. 2015; Lardo et al. 2015; Lee 2015; Pancino et al. 2007; Pryor et al. 1986) and without (e.g. Fabricius et al. 2014) a metallicity spread. If the two progenitors have non-zero relative orbital angular momentum, the merger remnant will likely preserve a signature of rotation in the merger plane. However, there is no evidence that GCs with a metallicity spread (the best-candidate merger remnants) have systematically higher rotation than the other GCs. Moreover, other physical mechanisms can account for rotation in GCs (e.g. Bianchini et al. 2015; Mastrobuono-Battisti & Perets 2013; Vesperini et al. 2014).

The main problem for the merger scenario is that two GCs are expected to merge only if their relative velocity is smaller than (or of the same order

of magnitude as) their velocity dispersion. The largest GC in the galaxy, ω Cen, has a dispersion of ~ 8 km s^{-1}, with typical values being $\sim 4-6$ km s^{-1}. The relative velocities of current GCs in the Milky Way halo are at least one order of magnitude larger than these values. This means that a merger between two GCs that are in the halo of our galaxy is extremely unlikely. Two GCs will have a sufficiently low relative velocity to merge only if they formed in a small dwarf galaxy or in the same molecular cloud. However, if the two progenitor clusters formed in the same molecular cloud and merged slightly after their formation, it is difficult to explain why the two populations have a different proton-capture enrichment and even a different metallicity. Therefore, GCs in small dwarf galaxies represent the most likely scenario where GC mergers will produce clusters that have a spread in metallicity.

We take a critical approach to the merging scenario by examining how the initial mass and density ratios of the progenitors affect the distribution and concentration of the sub-populations in the remnant (Section 6.3.1). Moreover, we also examine the rotation signature of the merger product and we show that the profile of rotation is related to the initial density ratio of the progenitors (Section 6.3.2). In the event of equal-mass mergers, we expect that the denser initial progenitor will be more centrally concentrated in the remnant. In the case of unequal-mass mergers, the more massive progenitor will be closer to the centre than the less massive progenitor and hence be more concentrated. We examine how the density ratio can counter the mass ratio.

6.2. Methods and simulations

We used the STARLAB public software environment (Portegies Zwart et al., 2001) ported to GPUs (Gaburov et al., 2009) to run the simulations. To investigate the role of the relative masses and densities of the progenitors, we performed a grid of simulations varying the mass ratio, i.e. M_1/M_2 (where M_1 is the mass of GC1 and M_2 is the mass of GC2) and the density ratio, i.e. ρ_1/ρ_2 (where ρ_1 and ρ_2 are the densities measured at the virial radius of GC1 and GC2, respectively).

We consider mass ratios of 1, 2, 4, with density ratios of 0.25, 0.5, 1, 2, 4. The range is motivated by the ratio of the populations in GCs (Johnson et al., 2015; Milone et al., 2015) and the absence of strong correlations between luminosity and density in present-day GCs (Harris, 1996). The GCs are modelled as non-rotating spherical King profiles (King, 1966) with central dimensionless potential $W_0 = 5$ (this sets the core radius

Table 6.1: Initial conditions of the simulations. Run (column 1): identifying name of the run, 'M' stands for mass ratio ($M1/M2$), 'ρ' for density ratio (ρ_1/ρ_2), both followed by the values assumed, e.g. M4ρ0.25, means mass ratio = 4, density ratio = 0.25; column 2: progenitor identifier; N (column 3): number of particles; M (column 4): total mass of the progenitor; $R_{\rm V}$ (column 6): virial radius; D (column 7): initial distance between the progenitors' centres of mass; $r_{\rm peri}$ (column 9): orbital pericentre; V (column 10): initial relative velocity.

Run		N	M [$\mathrm{M}_\odot$]	$R_{\rm V}$ [pc]	D [pc]	$r_{\rm peri}$ [pc]	V [km s^{-1}]
	GC2	20k	10^5	4			
M1ρ0.25	GC1	20k	10^5	6.34	111.58	5.17	5.59
M1ρ0.50	GC1	20k	10^5	5.03	88.5	4.51	6.27
M1ρ1	GC1	20k	10^5	4	70.4	4	7.03
M1ρ2	GC1	20k	10^5	3.17	70.4	3.59	7.03
M1ρ4	GC1	20k	10^5	2.52	70.4	3.26	7.03
M2ρ0.25	GC1	40k	$2 \cdot 10^5$	8	140.8	6	6.09
M2ρ0.50	GC1	40k	$2 \cdot 10^5$	6.34	111.58	5.17	6.84
M2ρ1	GC1	40k	$2 \cdot 10^5$	5.03	88.5	4.51	7.68
M2ρ2	GC1	40k	$2 \cdot 10^5$	4	70.4	4	8.61
M2ρ4	GC1	40k	$2 \cdot 10^5$	3.17	70.4	3.59	8.61
M4ρ0.25	GC1	80k	$4 \cdot 10^5$	10	176	7	7.03
M4ρ0.50	GC1	80k	$4 \cdot 10^5$	8	140.8	6	7.86
M4ρ1	GC1	80k	$4 \cdot 10^5$	6.34	111.58	5.17	8.83
M4ρ2	GC1	80k	$4 \cdot 10^5$	5.03	88.5	4.51	9.92
M4ρ4	GC1	80k	$4 \cdot 10^5$	4	70.4	4	11.12

$R_{\rm c} = 0.41\,R_{\rm V}$). The second GC (GC2) is always composed of 20 000 particles of equal mass $m_* = 5\ {\rm M}_\odot$ for a total mass of $10^5\ {\rm M}_\odot$. Its virial radius $R_{\rm V} = 4$ pc. The first GC (GC1) is varied to set the mass ratio and density ratio. To double (or quadruple the mass) of GC1, we double (or quadruple) the number of particles.

The density ratio is set by adjusting the virial radius of GC1, e.g. in the run $M2\rho1$ the GC1 has twice the mass as GC2 and R_V of GC1 is $\sim 1.26\times$ larger than the one of GC2, so that the density ratio between the two clusters is 1. We note that, assuming a fixed value for W_0, the density ratio is the same at every fiducial radius, i.e. the core radius ($R_{\rm c}$), the tidal radius ($R_{\rm t}$) and the virial radius ($R_{\rm V}$).

To prevent strong encounters and binary formation, we adopt a gravitational softening $\epsilon = 0.1 R_{\rm V}$ of the progenitor with the smallest radius. The initial binary fraction is zero and binaries do not form with this softening. We omit stellar and binary evolution to minimise the amount of free parameters in these models. Stellar and binary evolution might affect the structural properties of GCs (Chernoff & Weinberg, 1990; Gieles, 2013; Mapelli & Bressan, 2013; Mapelli et al., 2013; Sippel et al., 2012; Trani et al., 2014) and will be considered in a follow up study. Stars initially belonging to each of the two progenitors are "tagged" with a different metallicity flag. Initial conditions (ICs) are summarised in Table 6.1.

The two GCs are initially set on a parabolic orbit. To define the parabolic orbit we fixed the minimum encounter distance (in the point-mass assumption), i.e. the pericentre $r_{\rm peri}$, to be half the sum of the virial radii of the two progenitors GC1, GC2 [$r_{\rm peri} = 0.5\,(R_{V1} + R_{V2})$]. The initial distance D between the progenitors is four times the maximum value between $R_{\rm t,1}$ and $R_{\rm t,2}$, where $R_{\rm t,1}$ and $R_{\rm t,2}$ indicate the tidal radius of GC1 and GC2, respectively. The initial relative velocity is then calculated as the escape velocity at the initial position.

We choose a parabolic orbit because it is a representative case for mergers (Alladin, 1965; White, 1978). Hyperbolic encounters (with relative velocity much larger than the GC velocity dispersion) are the most common, as the phase space for encounters increases with the cube of the velocity of encounter and the cube of the impact parameter. However, the probability of merging encounters is sharply truncated (by failure to merge) when the orbits become very weakly hyperbolic. In contrast, the two GCs will merge on a shorter timescale if they are on a bound orbit, but bound orbits are associated with smaller values of the velocity. As we mentioned in the introduction, the main drawback of the merger scenario is that the observed relative velocities between GCs are generally larger than the value

needed for a merger to be successful. Thus, we consider bound orbits very unlikely. In summary, a parabolic orbit is representative of the most likely orbits leading to a merger.

The half-mass relaxation time is (Spitzer, 1987)

$$t_{\rm rlx} \sim 3 \times 10^8 {\rm yr} \left(\frac{M}{10^5\,{\rm M}_\odot} \right)^{1/2} \left(\frac{R_{\rm hm}}{3\,{\rm pc}} \right)^{3/2} \left(\frac{m}{5\,{\rm M}_\odot} \right)^{-1} \left(\frac{\ln \Lambda}{3} \right)^{-1}, \quad (6.1)$$

where $R_{\rm hm}$ is the initial half-mass radius, M the total mass, m is the particle mass and $\ln \Lambda$ is the Coulomb logarithm (set here by the system size and gravitational softening). For our progenitors, the relaxation timescales are between $400\,{\rm Myr}$ and $1.7\,{\rm Gyr}$. The initial crossing time at the virial radius in the equal mass, equal density progenitors is ~ 0.4 Myr and scales as $\rho^{-1/2}$. We run our simulations for 550 Myr. This is less than one half-mass relaxation timescale characteristic of the merger product in all cases, but two-body encounters have likely contributed to isotropising the velocities in the remnant.

6.3. Results

We examine the relative concentration and rotation of the two different populations in the merger remnant.

6.3.1. Relative Concentration

We plot the relative concentration using normalised density profiles of the sub-populations (i.e. each density profile is divided by its progenitor's mass). Figure 6.1 shows the density profile of GC1 and GC2 in green and in magenta respectively (where $M_{GC1} \geqslant M_{GC2}$).

We plot the profiles of nine selected runs. The profiles are at time ~ 550 Myr since the beginning of the simulation. We see that the final density profiles of the merger remnants are consistent with a single King model profile, although the two populations have different densities in the central regions. Depending on the run, we note that at small radii the normalised density of GC1 members can be higher than that of GC2 members or *vice-versa*. This suggests that the initial mass and density ratios affect the *relative* central density of the two populations in the final merger remnant (Figure 6.1). Despite the normalisation to the progenitor's mass, at large radii one curve is below the other in several panels. For example, in several plots of Figure 6.1 the magenta curve is below the green one (see especially the

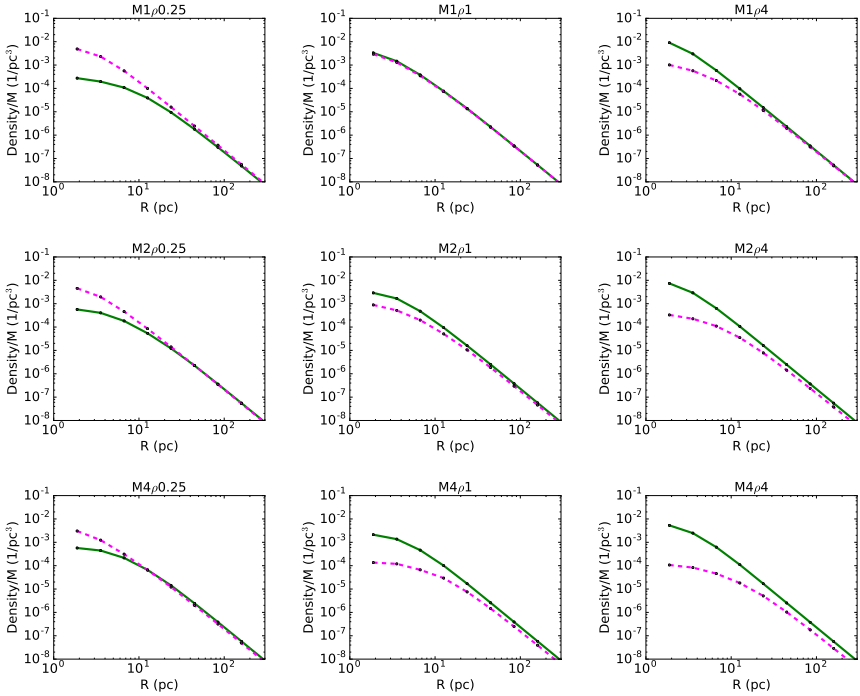

Figure 6.1: Normalised density profiles of the two populations in the final merger remnant. Note that the profiles all look like smooth King models. Solid green line refers to GC1, dashed magenta line to GC2. Each profile has been normalised by the mass of the associated progenitor. The code-name on the top of each plot refers to the run considered: 'M' stands for mass ratio M_1/M_2 followed by its value, 'ρ' for density ratio ρ_1/ρ_2 followed by its value. From top to bottom the mass ratio increases by a factor of 2 every row and from left to right the density ratio increases by a factor of 4 every column.

bottom right panel: since the profiles are normalised to the mass of the progenitors, this is a clear signature of mass loss during the merging process).

Figure 6.2 is a colour map of the relative concentration of the two progenitors, defined as '$\log(R_{\rm hm2}/R_{\rm hm1})$', i.e. the logarithm of the ratio between the half-mass radius of GC2 and GC1, in the initial conditions and at the end of the simulations, for the whole grid of runs. The plot on the left-hand side in Figure 6.2 shows the ratio between the half-mass radius of GC2 and GC1 in the ICs, the plot on the right-hand side shows the same quantity after the merger. From the right panel in Figure 6.2, we see that when the initial densities are equal, the more massive progenitor dominates the central part of the merger remnant and the less massive progenitor is more extended in the merger remnant. If the progenitors have equal masses, the denser progenitor is more concentrated in the remnant. To compensate for an unequal mass ratio, the less massive progenitor must have a density larger by roughly the factor by which its mass is lower. If the smaller mass progenitor is $1/A$ as massive, its initial density must be A times greater or alternatively, its radius must be $A^{-2/3}$ as large as the more massive one.

In Figure 6.3 we compare the number ratio of sub-populations (N_2/N_1) in our simulated GCs with the observations. Specifically, we plot the ratio of the minority (N_2) to the majority (N_1) population against the radial distance from the centre, normalised to the half-mass (or half-light) radius. Observational data of three GCs are compared with our simulations: in ω Cen the metal-rich population is the most centrally concentrated and is the minority population (Bellini et al., 2009), in NGC 1851 (Carretta et al., 2011) and M22 (Carretta et al., 2011) the metal-poor population is the more centrally concentrated (note that crowding prevents observing the very central regions of NGC 1851). In M22 the metal-rich population is the minority, while in NGC 1851 the metal-poor population is the minority.

The two runs shown in Figure 6.3 (M2ρ0.25 and M2ρ1) were not tuned to reproduce the observations, but follow the same trend as the data. In our simulations, the metallicity is only a tag: in the top panel of Figure 6.3 we use the same model (with a denser minority population) to match cases where the minority population is more concentrated, but the minority population is metal rich in ω Cen and metal poor in NGC 1851. We adopt a different progenitors model (with equal density) for M 22, where the minority population (metal-rich) is less concentrated.

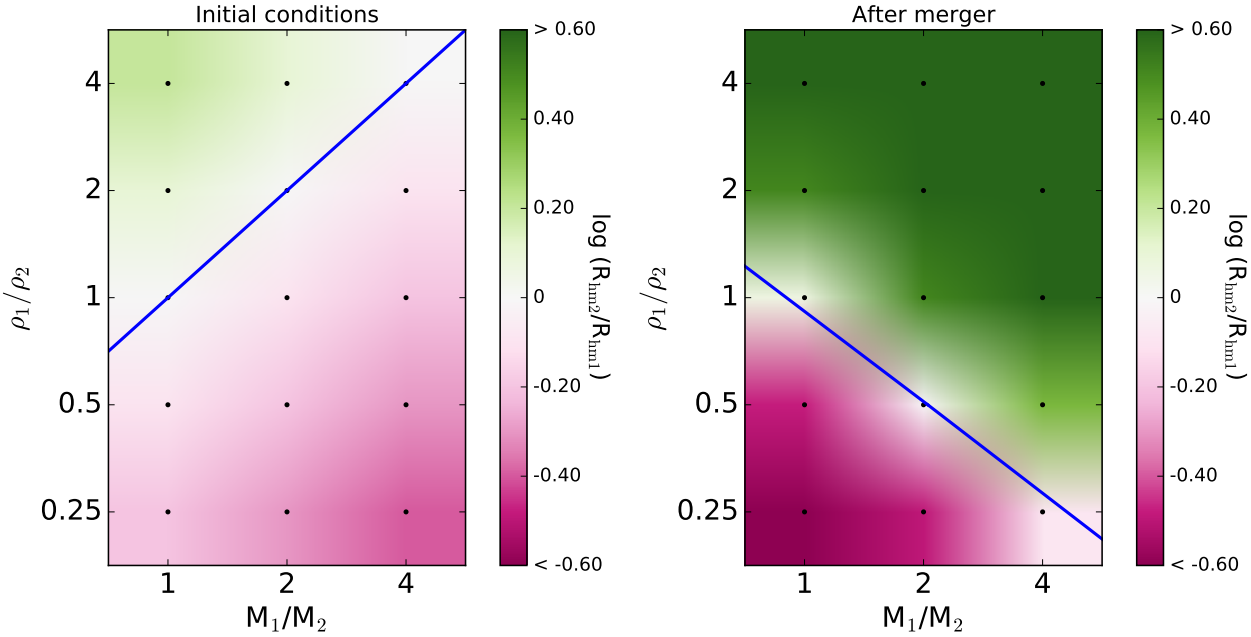

Figure 6.2: Colour map of initial (left) and final (right) ratio between the half-mass radius of GC2 and GC1 ($\log(R_{\rm hm2}/R_{\rm hm1})$). The $x-$ and $y-$axis are the initial mass ratio and the initial density ratio of the two progenitors. The colour map quantifies the relative concentration of the two populations (in logarithmic scale), meaning the ratio of the two half-mass radii i.e. $R_{\rm hm2}/R_{\rm hm1}$. If the logarithm of this value is negative (magenta) GC2 is more centrally concentrated in the merger product; if it is positive (green), GC1 is more centrally concentrated. The blue line marks the boundary between where GC1 is more centrally concentrated (green) and the situations where GC2 is more centrally concentrated (magenta). In both plots, the actual data grid at which $R_{\rm hm2}/R_{\rm hm1}$ is evaluated is marked with black dots, the colour map is then smoothed via interpolation in order to highlight the general trend. Note that the $x-$ and $y-$axis are effectively logarithmic.

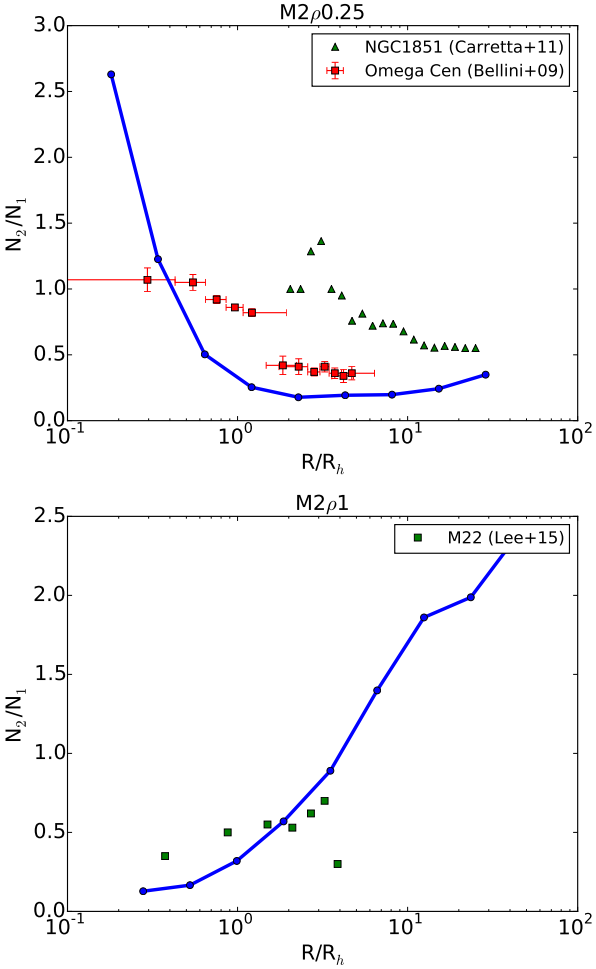

Figure 6.3: Ratio of the minority (N_2) to the majority (N_1) population versus the radial distance from the centre. The blue solid line indicates our simulated models M2ρ0.25 (top panel) and M2ρ1 (bottom panel). The data points refer to observations (Bellini et al. 2009 for ω Cen, Carretta et al. 2011 for NGC 1851, and Lee 2015 for M 22). N_2/N_1 is normalised to the half-mass radius and to the half-light radius for the simulations and for the observations, respectively.

6.3.2. Rotation

Rotation is observed in nearby GCs (Anderson & King, 2003; Bellazzini et al., 2012; Fabricius et al., 2014; Lardo et al., 2015; van den Bosch et al., 2006), which can arise from a variety of mechanisms (Bertin & Varri, 2008; Bianchini et al., 2013; Varri & Bertin, 2012; Vesperini et al., 2014). While there is no connection demonstrated between rotation and multiple populations, Amaro-Seoane et al. (2013) pointed out that ω Cen, M 22, and NGC 2419 are among the most flattened clusters.

Flattening has been detected in several galactic GCs (Chen & Chen, 2010; White & Shawl, 1987) and could be explained by several physical factors, such as pressure anisotropy or external tides (van den Bergh, 2008). Another possible justification for the flattening is the internal rotation of GCs (Fabricius et al., 2014). A correlation between flattening and iron-complex multiple populations would favour the merger scenario.

In this section, we look at the detailed kinematics of our merger remnants, as a function of mass and density ratios. We want to quantify their amount of rotation and see whether their degree of flattening correlates with rotation.

All of our merger remnants have rotation, as a consequence of the parabolic orbits of their progenitors. In Figs. 6.4, 6.5 and 6.6, we show velocity maps for the complete range of initial mass ratios and the limiting cases of density ratios $\rho_1/\rho_2 = 0.25, 4$. In all cases, we plot line-of-sight velocities for an observer sitting on the mid-plane perpendicular to the rotation axis. For comparison with the observations (Fabricius et al., 2014), we used a Gaussian filter to create the velocity map, progressively zoomed from left to right. Even the largest spatial scales of the final merger state (left-hand columns) show a clear flattening and the two populations have similar properties in configuration and velocity space.

These maps illustrate some important trends: the rotation within 5 pc is generally solid body, it becomes differential at $5-10$ pc, and the rotation is cylindrical everywhere. The similarity of the maps shows that these features are common to all our simulations. Solid-body rotation is the most probable distribution function (maximal entropy) for the relaxed core of a rotating N-body system (Lightman & Shapiro, 1978; Lynden-Bell, 1967). Observations of clusters also show solid body rotation over most of the half-mass radius and differential rotation outside (Bianchini et al., 2013; Fabricius et al., 2014; Meylan & Mayor, 1986).

Figure 6.7 shows the line-of-sight rotation profiles of all the simulations for an observer sitting on the rotation plane. As in the velocity maps, we

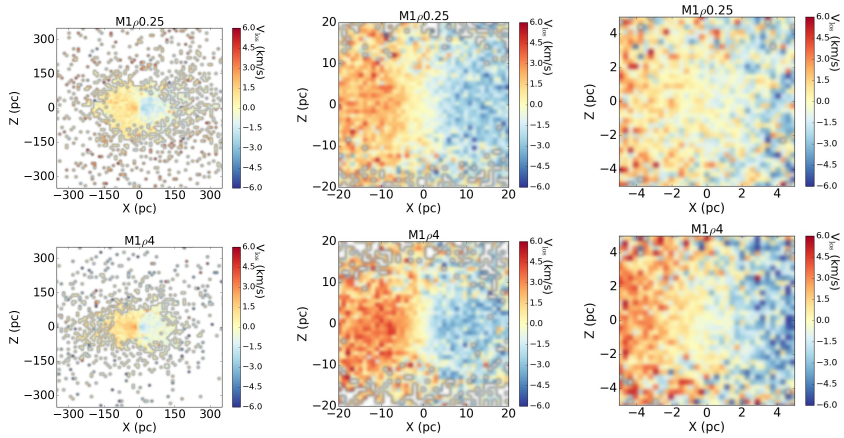

Figure 6.4: Line-of-sight velocity maps at different scales at t= 550 Myr for the case with equal mass ratio between the progenitors and ρ_1/ρ_2=0.25 (top row), ρ_1/ρ_2=4 (bottom row). From left to right, we zoom in the central parts of the remnant. The largest scales (left-hand columns) show a clear flattening. Examining these colour maps, the rotation within 5 pc is generally solid body (colour is changing), it becomes differential at 5-10 pc (the colour stays constant outside this radius in the rotation plane) and it is cylindrical everywhere (weak or no colour trend vertically). The similarity of all the maps reveals that these are common features of mergers.

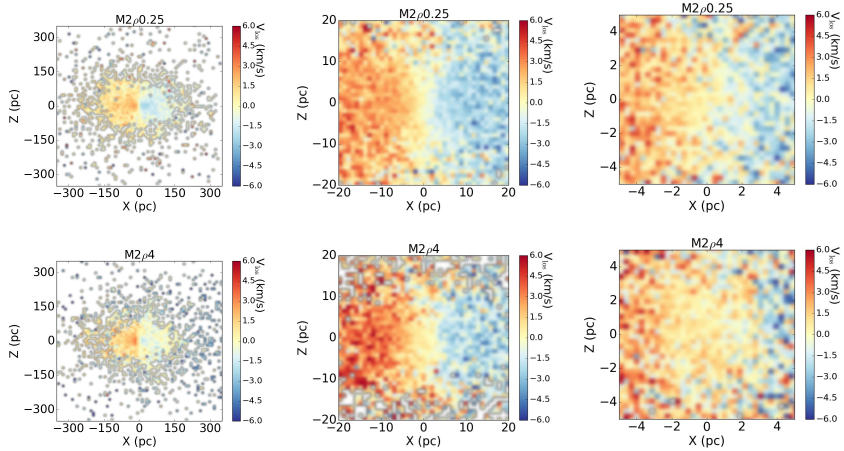

Figure 6.5: The same as Figure 6.4, but for the case with 2:1 mass ratio between the progenitors and ρ_1/ρ_2=0.25 (top row), ρ_1/ρ_2=4 (bottom row).

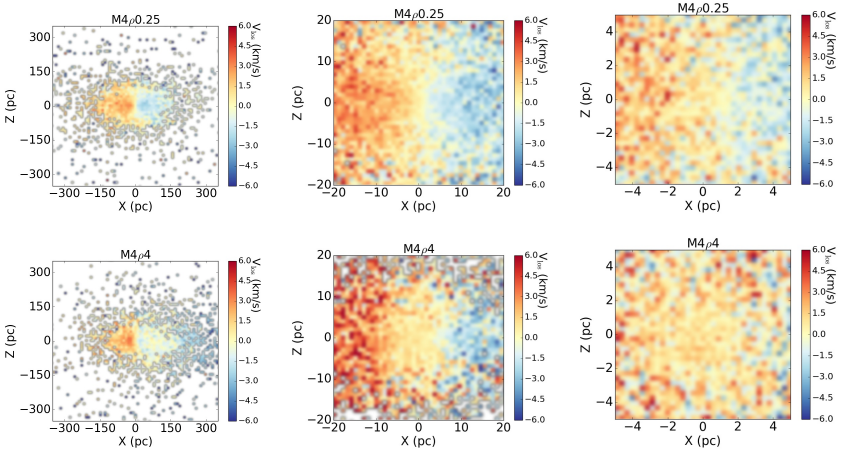

Figure 6.6: The same as Figure 6.4, but for the case with 4:1 mass ratio between the progenitors and ρ_1/ρ_2=0.25 (top row), ρ_1/ρ_2=4 (bottom row).

see that the inner rotation is solid-body, then it becomes differential at 5-10 pc. The solid-body rotation region is more extended in the runs with higher mass ratio; the angular momentum of the less massive object is preferentially deposited in the outskirts of the remnant.

At the half mass radius, the merger remnant exhibits solid-body or differential rotation depending on the initial density ratio between the progenitors. In Figure 6.8, we examine the ratio of the rotation velocity at the half-mass radius to the maximum rotation velocity $V_{\rm Rhm}/V_{\rm max}$, as a function of density ratio. For equal-mass ratios the quantity $V_{\rm Rhm}/V_{\rm max}$ is almost constant with respect to the density ratio (top panel of Figure 6.8). Therefore each of these model clusters have transitioned from solid-body to differential rotation by the half mass radius. In contrast, the trend for unequal mass ratios provides an interesting test of the model. When the less massive progenitor is less dense, it deposits its angular momentum in the outer parts. In contrast, small-mass progenitors with larger density burrow into the centre. When the minority population is more concentrated, the rotation curve will peak at roughly the half-mass radius, whereas when the minority population is less concentrated, the peak occurs outside the half-mass radius. Therefore, for unequal-mass ratios, $V_{\rm Rhm}/V_{\rm max}$ decreases for increasing values of the density ratio.

In order to compare the outcomes of our simulations with observations,

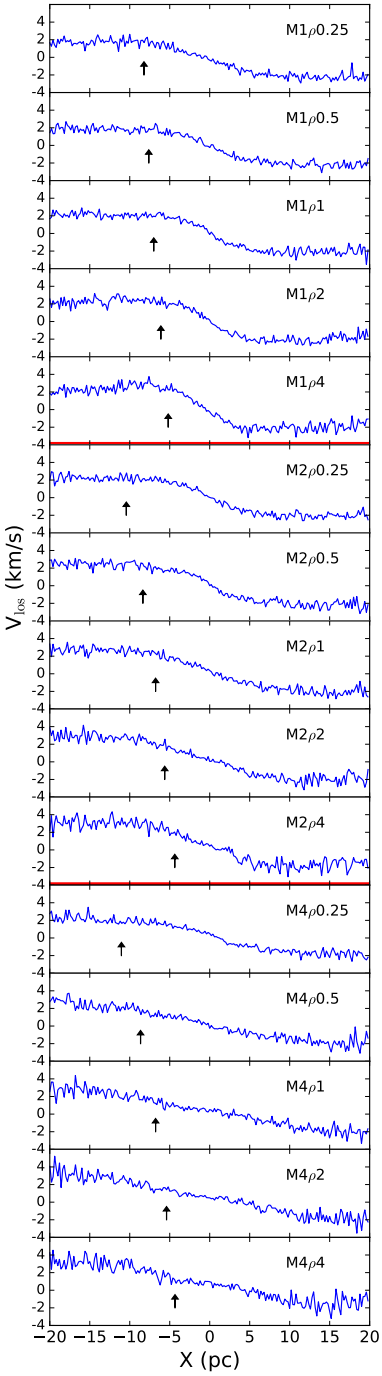

Figure 6.7: Line-of-sight velocity profile for all the simulations for an observer in the mid plane ($V_{\rm los}$). The half-mass radius is denoted by an arrow in each plot. The thicker red horizontal lines divide the panels by mass-ratio (the top group has $M_1/M_2 = 1$, the central $M_1/M_2 = 2$, the bottom one $M_1/M_2 = 4$). Every group has plots for the 5 density ratios considered.

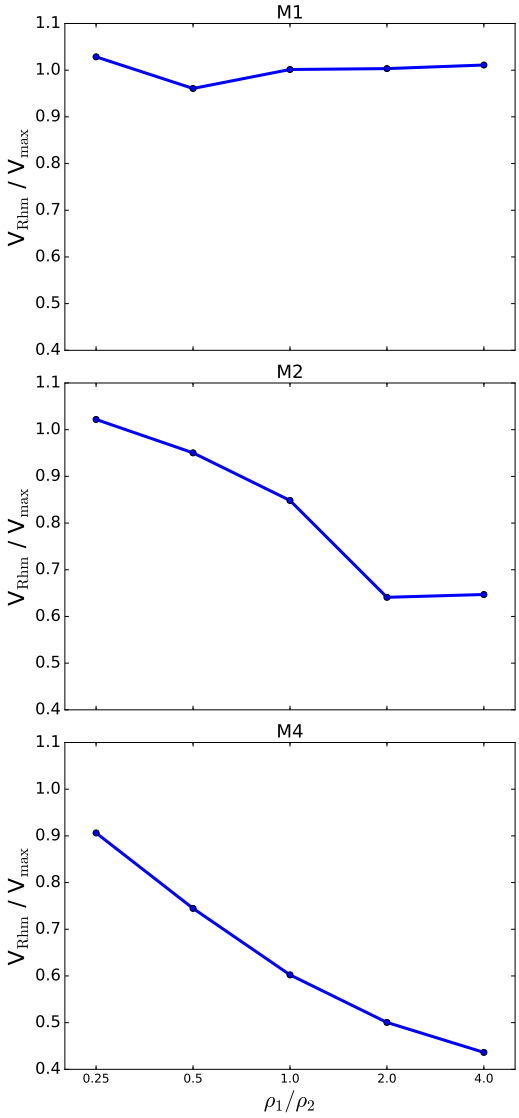

Figure 6.8: Ratio of the rotation velocity at the half-mass radius to the maximum rotation velocity, $V_{\rm Rhm}/V_{\rm max}$, as a function of density ratio. From top to bottom: each panel refers to GCs with mass ratio $M_1/M_2 = 1, 2$ and 4. Note that the $x-$axis is effectively logarithmic.

we study now the (V/σ, ϵ) diagram, which relates the ratio of the rotation velocity V and random motion σ to the ellipticity ϵ, which measures the flattening.

The expectation for isotropic rotators are derived from the tensor virial theorem (Chandrasekhar, 1969). The rotation velocity is the square root of the mass weighted streaming velocity squared. The velocity dispersion is the unordered kinetic energy. If the mass is stratified on concentric similar ellipsoids, the density profile drops out (Chandrasekhar & Lebovitz, 1962; Roberts, 1962) and the ratio of the ordered kinetic energy to the unordered one (or its square root V/σ) is a function only of the ellipticity ϵ (Binney, 1978). The application to elliptical galaxies is straightforward since V, σ and ϵ are all nearly constant with radius (Emsellem et al., 2007).

For GCs, ϵ has a greater variation with radius and V is rising with an asymptote at a radius beyond the observations. Hence, we look at how well 'proxy' and 'measured' rotations relate to one another in the simulated merger remnants. As always with proxies and dimensionless parameters that vary with radius, the results will be mixed.

In Figure 6.9 we plot the (V/σ, ϵ) diagram, following the prescription of Fabricius et al. (2014) as proxies for V and ϵ, including both data from our simulations and observed GCs. Fabricius et al. (2014) fit a plane $V(x, y) = ax + by + V_{\rm sys}$ (where $V_{\rm sys}$ is the systemic velocity) to the velocity fields to determine the central velocity gradient, $||\nabla V|| = \sqrt{a^2 + b^2}$. They take velocity dispersions σ and half-light radii R_{hl} from Harris (1996) to create a proxy for rotational velocity $\nabla V \cdot R_{hl}$, and find V/σ increasing with ellipticity. In our case, we define V in similar way ($\nabla V \cdot R$) leaving though R as free parameter, with the intent to explore how this proxy for V depends on the radius used to define it. ∇V is also calculated within the radius considered each time. Specifically, in Figure 6.9 we considered three different values of radius R, that are $R_{\rm hm}$, $R_{\rm hm}/2$, and $R_{\rm hm}/4$. Our choice is justified by Figure 6.7, where the solid-body rotation shifts to differential rotation at radii varying from $\sim 0.5\, R_{\rm hm}$ to $\sim 1.5\, R_{\rm hm}$.

σ in our case is just the line-of-sight velocity dispersion. As for the ellipticity, we follow the prescriptions found in Fabricius et al. (2014) and calculate ellipticity values (ϵ) from the eigenvalues (λ_1, λ_2) of the covariance matrix of stellar positions (within the relevant radial dimension), i.e. $\epsilon = \sqrt{1 - \lambda_2/\lambda_1}$.

Figure 6.9 shows that the result strongly depends on the choice of radius. The V/σ ratio increases with ellipticity, but ellipticities and V/σ both increase with radius. If we looked at Figure 6.7, we might guess that something close to $\nabla V \cdot R_{\rm hm}$ would be the best proxy and certainly would not

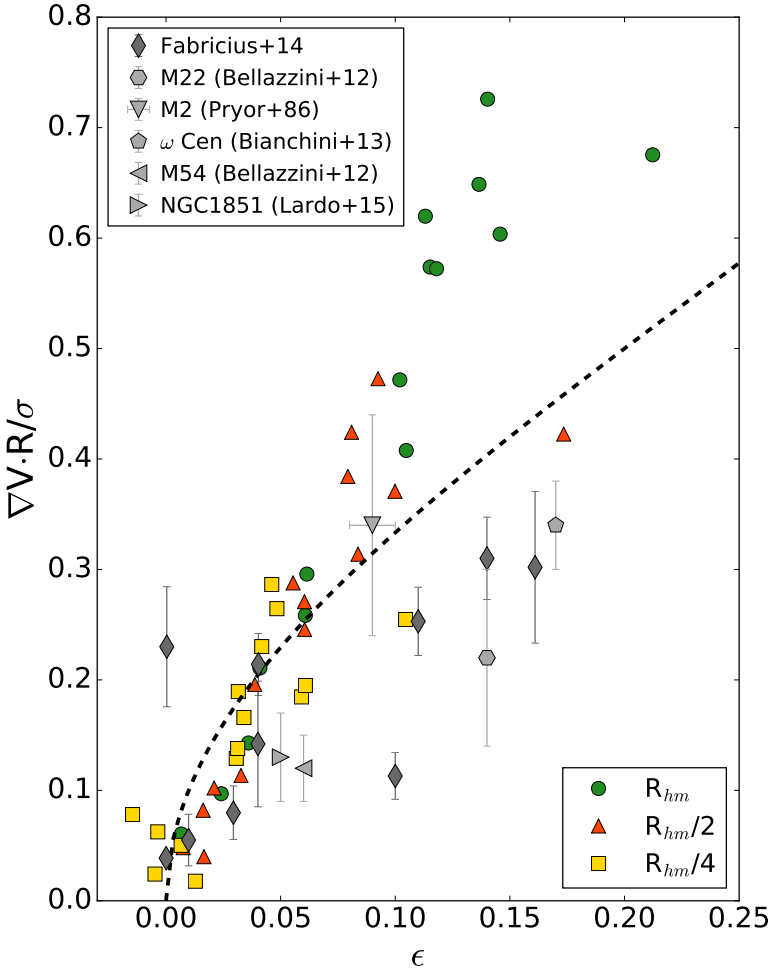

Figure 6.9: $(\nabla V \cdot R/\sigma, \epsilon)$ for each model at different values of R. The observational points (grey) are indicated in legend in the top-left corner. The black dashed line indicates the behaviour of an isotropic oblate rotator.

have guessed that the plot using $\nabla V \cdot R_{\rm hm}/4$ would look most like the oblate rotator (dashed line in the plot) and would be most in agreement with the data from Fabricius et al. (2014) . Thus, the choice of rotational velocity in a $(V/\sigma, \epsilon)$ diagram is not unique[3].

Another possibility is to take as the rotation velocity the maximum rotational velocity. In Figure 6.10, we plot the ellipticity ϵ of our simulated merger remnants versus $V_{\rm max}/\sigma$, where $V_{\rm max}$ is the maximum rotational velocity (see Figure 6.7). The result (shown as star symbols in Figure 6.10) compares favourably with the oblate rotator curve and observations. Having set the initial orbits to parabolic, the values of $(V_{\rm max}/\sigma, \epsilon)$ for the simulated GCs are all in the same portion of the oblate rotators curve. With time, the merger remnants will radiate away angular momentum through two-body encounters (Fall & Frenk, 1985). This will make them slide down on the curve to lower ellipticity and V/σ values, closer to the observational data, because rotation and ellipticity will decrease significantly as soon as the system relaxes and the two populations mix completely (velocities will isotropise and angular momentum will diminish).

In Figure 6.9 and Figure 6.10, we plot not only the observational sample of Fabricius et al. (2014), whose 11 GCs do not show any significant spread in Fe abundance, but also data of some iron-complex GCs (M 22 and M 54 from Bellazzini et al. 2012, M 2 from Pryor et al. 1986, ω Cen from Bianchini et al. 2013, NGC 1851 from Lardo et al. 2015). To derive the value of $V_{\rm max}/\sigma$ for the iron-complex GCs, we use the double mean velocity amplitude (i.e. $A_{\rm rot}$) which is considered a good representation of $V_{\rm max}$ (Pancino et al., 2007). From the kinematical point of view, the iron-complex GCs for which V/σ and ϵ are available do not stand out in comparison with the sample of Fabricius et al. (2014).

6.4. Discussion and Conclusions

In this section, we discuss the results of our simulations in light of the observational properties of iron-complex GCs. We focus on GCs with multimodal iron-complex abundances because they have unique tags that can be mapped to possible progenitors.

In the merger scenario, we find that the minority population is less centrally concentrated unless the initial density of the less massive progenitor

[3]The proxy for ∇V adopted by Fabricius et al. (2014) would always be higher than the true rotation velocity at the radius R, because it comes from the best linear fit to the velocities within R and the second derivative of V with respect to R is negative (the rotation curve is flattening).

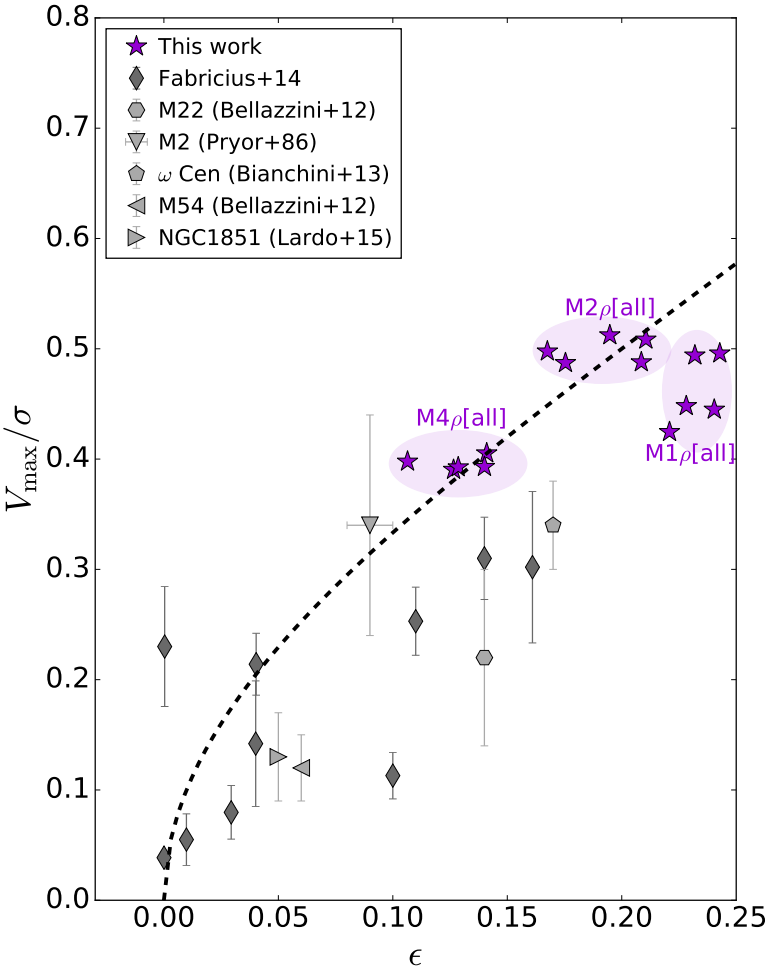

Figure 6.10: $(V/\sigma, \epsilon)$ diagram. The purple stars refer to this work, using the maximum rotation velocity ($V_{\max}$) for V. The observational points (grey) are indicated in the legend. The dashed black line shows the behaviour of isotropic oblate rotators.

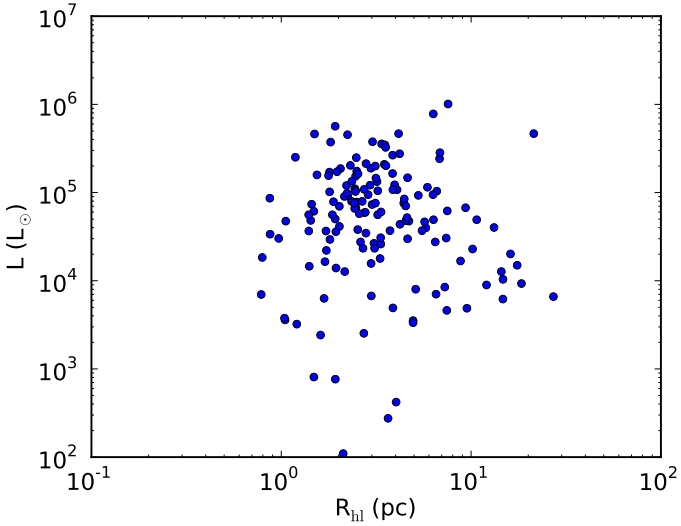

Figure 6.11: Total luminosity versus half-light radius of Milky Way GCs from Harris (1996)

.

is greater by more than the mass ratio. In M22, the minority is metal poor and extended. The distribution compares well to equal density progenitors with a mass ratio of 2:1. In ω Cen and NGC1851 the less massive population is more centrally concentrated than the majority population (Bellini et al., 2009). Merging only cares about metallicity if there is a correlation between metallicity and mass or density. The minority is metal rich in ω Cen, while it is metal poor in NGC 1851. In light of our results, this means these GCs can be the result of a merger only if the less massive progenitor was the denser one. These trends are best fit when the mass ratio is 2:1 and the less massive progenitor is four times as dense as the more massive one.

It would be instructive to check with observations whether the less massive progenitors are denser than more massive ones. Figure 6.11 shows the relation between luminosity (as a proxy for mass) and half-light radius in present-day GCs, from the catalogue of Harris (1996). This figure shows that there is no correlation between luminosity (hence, mass) and size in present-day Milky Way GCs. From this fact, we cannot conclude very dense but small mass progenitors would be common, if merger progenitors were like present-day GCs. However, we also warn that consid-

ering present-day GCs as representative of merger progenitors is rather hazardous.

The kinematical signatures of the merger remnant are similar to those observed in GCs. In our simulated remnants: 1) the velocity dispersion is isotropic, 2) the merger product rotates close to solid body in the inner parts, then becomes differential, 3) rotation is cylindrical, 4) at the half mass radius, the merger remnant exhibits solid-body or differential rotation depending on the initial density ratio between the progenitors, 5) the flattening of the remnant is consistent with rotation. Both ϵ and V vary over radius, so defining appropriate values for a (V/σ,ϵ) plot is difficult. Different choices move points around in that plot, but the correlation between flattening and rotation in the remnants is similar to the expectations from the tensor virial theorem (Binney, 1978).

As we already anticipated in the introduction, the most severe drawback of the merger scenario is that the relative velocity between two clusters must be sufficiently low to merge. Here 'sufficiently low' means that their relative velocity cannot be much larger than their velocity dispersion. The velocity dispersion of GCs is ≈ 3 per cent of the velocity dispersion of stars in the field of our Galaxy. This means that GCs move too fast to merge in our present-day Galaxy.

Several studies propose that a sub-population of GCs were the nuclei of dwarf galaxies, with ω Cen as prototype (Carraro & Lia, 2000; Majewski et al., 2000). If one GC were a nucleus, the inspiral of a second GC would create conditions similar to an unequal mass merger.

GCs can sink toward the centre of the host galaxy by dynamical friction. The dynamical friction timescale scales as the inverse of the mass of the GC. Thus, the smaller the GC, the longer it takes for it to sink to the centre by dynamical friction. For example, an object that has a mass of ~ 5 per cent of the total mass of the host galaxy will spiral into the centre by dynamical friction in roughly a dynamical time (Binney & Tremaine, 2008).

The smallest dwarf galaxy in the Local Group with GCs is Fornax, with five clusters (Larsen et al., 2012). The most massive among these GCs has not yet sunk into the centre by dynamical friction (Read et al., 2006). Thus, even Fornax failed to promote mergers or create a nucleus from its most massive GC.

The Sagittarius dwarf galaxy is more promising (Gratton et al., 2012). At least five Milky Way GCs are thought to have been part of Sagittarius (Law & Majewski, 2010). The velocity dispersion of Sagittarius is ~ 20 km s^{-1}. Thus, parabolic encounters between GCs would be rare, but not impossible. Sagittarius does have a nuclear cluster. With a velocity dispersion

of $\sim$ 20 km s^{-1}, Sagittarius has a mass of $2 \times 10^8\,\mathrm{M}_\odot$ within one kpc, so another cluster could inspiral. Most dwarf galaxies have likely dissolved in the old stellar halo of our Galaxy. At $z = 1$, there were roughly three times as many dwarf satellites as today (Kazantzidis et al., 2008). So, there is some chance that several GCs merged within dwarf galaxies in the past. Quantifying the rate of such mergers is beyond the aims of this paper.

Finally, it is possible that two GCs merge slightly after their formation, when they are still part of the same progenitor molecular cloud. In this case, their relative velocity should be of the same order of magnitude as the turbulent motions inside the cloud (approximately few km s^{-1}), enabling a successful merger. There are clusters younger than 100 Myr that are believed to be "caught in the act" of merging while they are still within the parent cloud (Sabbi et al., 2012).

In summary, we confirm that the merger scenario may provide a viable explanation for multiple populations in iron-complex GCs. Our simulations show that the relative concentration in the merger remnant betrays the initial density ratio of the progenitors. Moreover, the density ratio of the progenitors leaves a signature in the rotation curves that should be object of further observations.

7

Conclusions and Outlook

In this thesis, I focused on the study of various aspects related to star clusters, from the formation to the dynamical evolution. I presented the general context in which this work is inserted, describing the main observed properties of these objects and highlighting the interesting problematics related with every specific category of star clusters, from embedded to globular. Then, I summarised the main concepts behind the classic star and star cluster formation theories, going from the gravitational collapse of an instability to the expulsion of gas from by newborn star. Once stars are formed, they interact gravitationally and I reviewed the basic equilibrium models for star clusters and the fundamental two-body relaxation process.

All this found a scientific application in the first original contribution presented, where I specifically addressed the study of photo-ionisation feedback and its influence on the emerging star cluster. Feedback allows the survival of the cluster, guaranteeing a lower density environment, and shapes its structural and dynamical properties. Once gas is ejected, the stage is left only to dynamics. In this context, I showed a possible formation scenario of globular clusters with metallicity spread, based on the merger of two clusters. This would justified both the presence of multi-metallicity populations and the rotational features observed in many globular clusters.

The end is always the perfect moment not only to look back, but also ahead, and think about possible extensions of the current work.

The main general limitation in the study of star cluster formation is the separation, in terms of numerical methods, between the gas-dominated phase and gas-free phase. We saw in Chapter 5 that the simulation time and the binary dynamics was limited by the accuracy achievable with a softened second-order N-body integrator. Indeed, to perform simulations of dynamical evolution of star clusters, dedicated N-body codes are used. The next inevitable and necessary step should be to fill the gap and have a hydrodynamical and a high-precision direct N-body code coupled together. This would allow to have a better understanding of the transition from gas-rich to gas-poor objects.

On top of this, there many other directions in which the current study could be extended. The first one is related with the mass and dimensions of the simulated cloud and star clusters. Scaling to higher masse (e.g 10^6 $\mathrm{M}_\odot$) is not trivial and the conclusions could be different than for smaller clouds. The efficiency of photo-ionisation feedback is definitely one of the big question marks in this context and very likely the inclusion of other sources of feedback (supernovae?) would be necessary.

Furthermore, an improvement to the current work could be the adoption of a more precise feedback model. An optimal description of the stars/sinks spectrum should include also non-ionising radiation, such as infrared and optical, and therefore radiation pressure feedback from it. Of course, the main problem to overcome in this case is resolution, meaning that the density scales on which infrared and optical radiation effects become relevant are higher than what considered so far, and this requires being able to resolve much smaller spatial scales.

The big absent one in all this are magnetic fields. Their presence potentially plays a central role in the collapse of the molecular cloud and then in combination with feedback. The inclusion of this aspect is definitely on the to-do list.

In terms of stellar dynamics and interactions between clusters, the next step should be to go over the isolation model and set the clusters in a galactic environment. We considered the possibility that mergers of globular clusters could take place inside high redshift dwarf galaxies. Being able to simulate this more realistic situation would on one hand represent a good test for the model and on the other hand offer new insights on more realistic initial conditions for the merging.

A

NUMERICAL METHODS

In astrophysics numerical simulations should be considered as the laboratory tools to perform otherwise impossible experiments. Having one, unique, code able to do *everything* is not only difficult to realise, but even inefficient, due to the variety of physical processes and scales involved in the real Universe. In the previous chapter I dealt with systems in which different physical agents acquired with time more or less importance, we transitioned from fully gaseous structures, like molecular clouds, to a mix of collapsed structures and ionised gas, to a dense, highly collisional, gas free cluster of stars. To simulate such different environments I made use of two different codes, STARLAB and RAMSES, which serve different purposes and adopt distinct numerical techniques.

A.1. Starlab

STARLAB (Portegies Zwart et al., 2001) is a direct N-body code coupled with a binary and stellar evolution model, designed to simulate the evolution of dense stellar systems.

The N-body solver (named *Kira*) is a direct N-body integrator, which means it integrates motions of stars by directly computing the force on each stars without any approximation. Indeed, star clusters are collisional systems, which means that two-body interactions are important in driving the dynamical evolution, hence these cannot be neglected like in galaxies, where particles are mainly affected by the central potential.

Kira uses a fourth-order Hermite predictor-corrector scheme, based on

the "jerk" *j*, the time derivative of the acceleration *a*,

$$\mathbf{a}_i = G \sum_{j \neq i} \frac{m_j}{r_{ji}^3} \mathbf{r}_{ji} \tag{A.1}$$

$$\mathbf{j}_i = \frac{d\mathbf{a}_i}{dt} = G \sum_{j \neq i} \left[m_j \frac{\mathbf{v}_{ji}}{r_{ji}^3} - 3 \frac{(\mathbf{r}_{ji} \cdot \mathbf{v}_{ji}) \mathbf{r}_{ji}}{r_{ji}^5} \right] , \tag{A.2}$$

where $\mathbf{r}_{ji} = \mathbf{r}_j - \mathbf{r}_i$, $r_{ji} = |\mathbf{r}_{ji}|$, $\mathbf{v}_{ji} = \mathbf{v}_j - \mathbf{v}_i$ and m_j is the mass of the j-th star.

Let's suppose at $t = t_0$ to know $\mathbf{r}_0$, $\mathbf{v}_0$, $\mathbf{a}_0$, $\mathbf{j}_0$. From Taylor expanding up to the 3rd order, the predicted position and velocity for a generic star *i* (we omit the index for simplicity) at $t_1 = t_0 + \Delta t$ are given by

$$\mathbf{r}_{1p} = \mathbf{r}_0 + \mathbf{v}_0 \Delta t + \frac{1}{2} \mathbf{a}_0 \Delta t^2 + \frac{1}{6} \mathbf{j}_0 \Delta t^3 \tag{A.3}$$

$$\mathbf{v}_{1p} = \mathbf{v}_0 + \mathbf{a}_0 \Delta t + \frac{1}{2} \mathbf{j}_0 \Delta t^2 . \tag{A.4}$$

The predicted values for acceleration and jerk ($\mathbf{a}_{1p}$, $\mathbf{j}_{1p}$) can be obtained by inserting $\mathbf{r}_{1p}$, $\mathbf{v}_{1p}$ in Eqs. A.1, A.2 . The correction is based on the estimated higher-order derivatives of $\mathbf{j}_0$. Using Taylor polynomials once more, we can express the known quantities $\mathbf{a}_{1p}$, $\mathbf{j}_{1p}$ as function of the higher-order derivatives of $\mathbf{j}_0$:

$$\mathbf{a}_{1p} = \mathbf{a}_0 + \mathbf{j}_0 \Delta t + \frac{1}{2} \dot{\mathbf{j}}_0 \Delta t^2 + \frac{1}{6} \ddot{\mathbf{j}}_0 \Delta t^3 \tag{A.5}$$

$$\mathbf{j}_{1p} = \mathbf{j}_0 + \dot{\mathbf{j}}_0 \Delta t + \frac{1}{2} \ddot{\mathbf{j}}_0 \Delta t^2 ; \tag{A.6}$$

reorganising the terms, it is possible to extract $\dot{\mathbf{j}}_0$ and $\ddot{\mathbf{j}}_0$

$$\dot{\mathbf{j}}_0 = \frac{-6(\mathbf{a}_0 - \mathbf{a}_{1p})}{\Delta t^2} - \frac{(4\mathbf{j}_0 + 2\mathbf{j}_{1p})}{\Delta t} \tag{A.7}$$

$$\ddot{\mathbf{j}}_0 = \frac{12(\mathbf{a}_0 - \mathbf{a}_{1p})}{\Delta t^3} + \frac{6(\mathbf{j}_0 + \mathbf{j}_{1p})}{\Delta t^2}. \tag{A.8}$$

The computed values for $\dot{\mathbf{j}}_0$ and $\ddot{\mathbf{j}}_0$ can be now used to further expand the first predictions for position and velocity (Eqs. A.3, A.4) and correct the final estimate of these quantities.

$$\mathbf{r}_1 = \mathbf{r}_{1p} + \frac{1}{24} \dot{\mathbf{j}}_0 \Delta t^4 + \frac{1}{120} \ddot{\mathbf{j}}_0 \Delta t^5 \tag{A.9}$$

$$\mathbf{v}_1 = \mathbf{v}_{1p} + \frac{1}{6} \dot{\mathbf{j}}_0 \Delta t^3 + \frac{1}{24} \ddot{\mathbf{j}}_0 \Delta t^4 . \tag{A.10}$$

Finally $\mathbf{a}_1$ and $\mathbf{r}_1$ can be computed through Eqs. A.1, A.2

This method of integration is non-symplectic, meaning it doesn't conserve phase-space volume or invariant quantities, like the total energy of the system, however is much more accurate on single timesteps than a leapfrog symplectic algorithm.

In this type of direct integration, Newton's equations are solved for all N stars, each time considering the influence of all the rest N-1 stars, therefore time complexity in this case scales as N^3 [1], not as $\mathrm{N}\log\mathrm{N}$ like in classic tree codes. To speed-up the simulation, STARLAB has been adapted to run on GPUs through the Sapporo library (Gaburov et al., 2009).

The use of individual time steps is fundamental to improve the accuracy and speed of N-body integrators. Particles in high density regions and/or undergoing very close encounters (i.e binaries, multiple systems) require shorter integration time steps since forces change more rapidly than for other stars. The first time step of a generic star i is calculated as $\Delta t_i = \nu|\mathbf{a}_{0i}|/|\mathbf{j}_{0i}|$, successively, after at least one iteration of the Hermite scheme, the new individual time steps are computed according to (Aarseth, 1985)

$$\Delta \mathrm{t_i} = \left(\nu \frac{|\mathbf{a_i}||\ddot{\mathbf{a}}_\mathbf{i}| + \mathbf{j_i}^2}{|\mathbf{j_i}||\dddot{\mathbf{j}}_\mathbf{i}| + \ddot{\mathbf{a}}_\mathbf{i}^{\,2}} \right)^{1/2} , \tag{A.11}$$

where ν is an accuracy parameter ($\mathrm{sim}0.1$), $\mathbf{j_i}$ and $\mathbf{a_i}$ are the last evaluation of the jerk and acceleration.

A general strategy to advance groups of particles at the same time and guarantee synchronised integration, is to quantise time steps (Aarseth, 2003). STARLAB and many other codes in stellar dynamics make use of the a block time-step approach (Hut et al., 1995), where the only allowed values for the time step length are powers of two (Aarseth, 2003). The main advantages are that many particles will share the same step size, thus the orbit integration can be parallelised and that position predictions need to be done only once per block time step and not separately for every particle which need to be updated. The block time step $\Delta \mathrm{t_n}$ is defined as $\frac{\Delta \mathrm{t_1}}{2^{\mathrm{n}-1}}$, where $\Delta \mathrm{t_1}$ is the maximum time step length and n is an appropriate integer. Particles are grouped by replacing their individual time steps $\Delta \mathrm{t_i}$ with

[1] Directly solving the equation of motions for N stars, requires $\mathrm{N}(\mathrm{N}-1)/2$ calculations, which scales as $\sim \mathrm{N}^2$. Moreover, the relaxation timescale goes as N, hence overall complexity is N^3

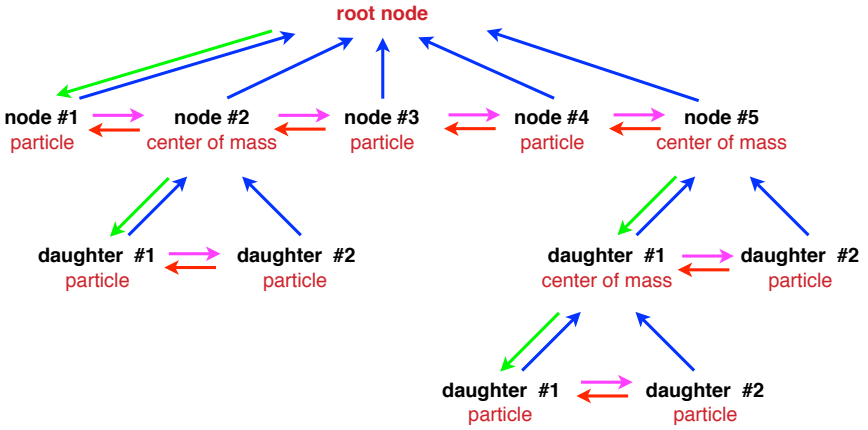

Figure A.1: Schematic representation of hierarchical structure in Starlab. Reproduced from http://www.sns.ias.edu/starlab/

the nearest block time step, $\Delta t_i = \Delta t_n$ for n satisfying (Makino et al., 2006)

$$\mathrm{n} = \min_{\mathrm{k}\geq 1}\left\{\mathrm{k}|\frac{\Delta \mathrm{t}_1}{2^{\mathrm{k}-1}} \lesssim \Delta \mathrm{t}_\mathrm{i}\right\} \tag{A.12}$$

Particles can be refereed to as *active* or *inactive* depending on the time-step. Every particle carries two time parameters: t_i, the last time at which it was last advanced and Δt_i, the individual block time step. Particles with the smallest value of $t_i + \Delta t_i$ are considered active. These are the only one updated according to the full predictor-corrector scheme described before. Practically this means that new positions and velocities are predicted for all particles, but the correction from the computation of acceleration and jerk is performed only for the active ones.

In STARLAB an N-body system is organised according to a tree structure (see Figure A.1), whose leaves are represented by individual stars. Single stars (i.e. stars not members of any multiple system) are all top-level nodes, whose parent node is constituted by the centre of mass of the whole system (root node).This is set as coordinate centre at each time step. In case of binary, triple, multi-body systems the top-level node is the centre of mass of the multiple system itself, then the members of the system are arranged hierarchically in binary sub-trees originating from the top node.

Every top-level node (single star or centre of mass) contain information about dynamics, while stellar properties are stored in leaves. Mass,

position and velocity of every node are relative to the parent node. In fact, the use of relative coordinates at every level ensures that high numerical precision is maintained at all times, even during very close encounters, despite the absence of any regularisation algorithm. It is important to stress that this tree structure is not used to approximate dynamics calculation: forces are computed using direct summation over all other particles in the system, there is no use of any tree or neighbour-list construct.

The tree can transform due to dynamical interaction and a new multiple system is created or an existing one dissolves. If two stars of (masses m_1 and m_2) are closer than $\mathrm{R}_{\mathrm{close}} \sim \mathrm{r}_{\mathrm{vir}} \frac{\mathrm{m}_1+\mathrm{m}_2}{2\mathrm{M}}$ (where M and $\mathrm{r}_{\mathrm{vir}}$ are respectively mass and virial radius of the whole system), they become a binary. Otherwise, if they are more distant than $2.5R_{close}$, they split into single stars. These criteria are valid at every level of the tree, even for two nodes being too close or too distant.

Binaries can be distinguished between perturbed and unperturbed. The perturbation threshold to discriminate between the two cases is set by default as $\mathrm{F}_{\mathrm{p}} = 10^{-7} < |\mathrm{F}| >$, where F is the force within the binary. Stars which exert on the binary a force $\gtrsim F_p$ are listed as perturbers of the system. These are calculated recursively at all levels for multiple systems and are recomputed when the centre of mass is integrated.

Perturbed binaries are resolved into their components, both for purposes of determining their centre-of-mass motion and for determining their effect on other stars. To integrate the motion of the first member of the binary, the solver takes into account both the influence of the companion star and the perturbers.

On the other side, binaries whose perturbation falls below the specific value are treated as unperturbed, meaning their motion is followed analytically as strictly two-body. In relation to other stars, their influence is treated as of point masses.

The presence of the parent galaxy can be simulated by including an external potential. The resulting tidal and Coriolis force terms are added to the equation of motions of all top-level nodes, neglecting the influence on multiple systems. The addition of an external potential automatically defines a scale beyond which particles are treated as escapers, which is usually taken to be the Jacobi radius.

As anticipated before, STARLAB is equipped with a stellar and binary evolution package, *SeBa* (Portegies Zwart & Verbunt, 1996), which computes stellar and binary evolution analytically, following the prescriptions by Eggleton et al. (1989, 1990) and Tout et al. (1997). Depending on the initial mass of the star, *SeBa* derives mass-loss rates, lifetimes, evolution

of the stellar radius and luminosity as a function of time and, therefore, the core mass as a function of luminosity. With these information, particles are assigned to categories which which identify main stellar phases (protostar, browndwarf, main sequence, subgiant, ...). Recently, the recipes for stellar evolution were upgraded as described in Mapelli et al. (2013), to include the metallicity dependence of stellar radius, temperature and luminosity using the polynomial fitting formulae of Hurley et al. (2000). Metallicity dependent-mass loss due to stellar winds were also updated to the ones in Vink et al. (2001). The binary evolution module treats detached, semi-detached and contact binaries, accounting for several effects, such as mass transfer, tidal circularisation, loss of angular momentum by stellar winds/supernova, magnetic braking and gravitational radiation.

A.2. Ramses

RAMSES (Teyssier, 2002) is a massively parallel adaptive mesh refinement code, originally developed to study the co-evolution of dark matter and gas in a cosmological context, is now a complete tool for simulations of self-gravitating flows, equipped with a hydrodynamical as well as magnetohydrodynamical solver and several modules which implement star formation recipes, interstellar medium cooling function, stellar and supernovae feedbacks, AGN feedback and sink formation.

In modern computational astrophysics two main techniques are employed to solve hydrodynamical equations: smoothed-particle hydrodynamics (SPH) and grid-based methods. The difference at the base is how the fluid is discretised. SPH divides it into mass elements (particles), which are then followed, in line with the Lagrangian approach, while grid methods subdivide the computational domain into volume elements (cells), fixed in space, according to the Eulerian formulation of hydrodynamics. The natural outcome of SPH codes is to automatically adapt the numerical resolution in dense regions, with more particles concentrated in those areas, which makes it a valid tool in situations with large density contrasts, such as self-gravitating fluids. Grid-based methods can increase their spatial resolution adopting the adaptive mesh refinement (AMR) technique, which consists in the introduction of new grid elements, from the partition of a cell into smaller cells, triggered by some specified refinement criteria. An exhaustive comparison between SPH and AMR codes was given by Agertz et al. (2007).

The AMR data structure implemented in RAMSES is tree-based. Every cell (or *oct*) can be refined in 2^{ndim} son cells (where $ndim$ is the number of

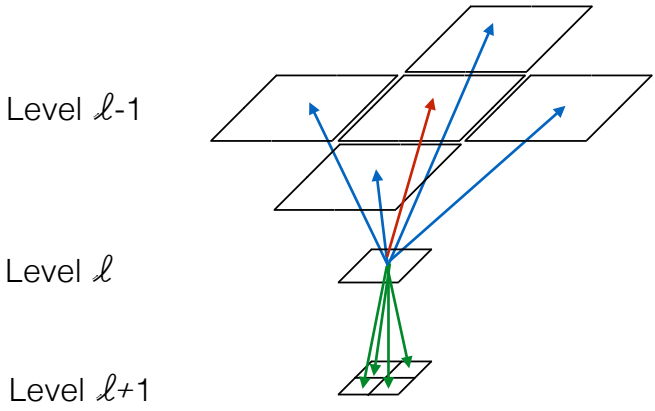

Figure A.2: Schematic representation of the octree system across refinement levels.

dimensions). Every cell at refinement level l points to all the son cells in the next higher refinement level $(l+1)$, to its father cell in $l-1$ and all the 2^{ndim} neighbour cells of the father cell in $(l-1)$ (see Figure A.2).

A cell can be refined according to several criteria (e.g. pressure gradients, density, Jeans length), which can trigger the cell refinement to a higher level. The refinement criteria used in this work are a quasi-lagrangian method, where if the mass contained in a cell is higher than a threshold value, the cell gets refined, and a Jeans-length method, where the Jeans-length is required to be resolved with at least 4 cells.

The spatial finite resolution set by the cell size Δx converts into a maximum time interval necessary to have convergence, which is controlled by the Courant-Friedrich-Lewy condition (Courant et al., 1967),

$$\Delta t < C\frac{\Delta x}{v}, \tag{A.13}$$

where v is the fastest velocity of the system and C is the Courant number, which is typically ≤ 1. Clearly, the highest level of refinement sets the most stringent condition on Δt. Adopting this as general timestep is very expensive computationally, therefore RAMSES adopt the so-called *level subcycling*, to update every level grid according to the correspondent level timestep. Then, every other fine timestep, the l^{th} and $(l-1)^{th}$ grids are synchronised.

In RAMSES, hydrodynamics equations are solved using a method based on the Godunov scheme (Godunov, 1959). Euler equations (see Section 3.2), together with a convenient equation of state can be rewritten for convenience in a more compact form, neglecting the acceleration term, in terms of the state vector $\boldsymbol{U} = (\rho, \rho\boldsymbol{v}, E)^T$ and corresponding fluxes $\boldsymbol{F} = (\rho\boldsymbol{v}, \rho\boldsymbol{v} \otimes +P, (E+P)\boldsymbol{v})^T$,

$$\frac{\partial \boldsymbol{U}}{\partial t} + \nabla \cdot \boldsymbol{F} = 0. \tag{A.14}$$

In this form the Euler equations are expressed in terms of a general conservation law. If for, simplicity we restrict to one dimension, $\nabla \cdot \boldsymbol{F} = \frac{\partial \boldsymbol{F}}{\partial x}$. Evaluating Equation A.14 on a grid, means that the quantities entering the expression are actually spatially averaged over the cell dimension $\Delta x = x_{i+1/2} - x_{i-1/2}$, yielding

$$\frac{\mathrm{d}\boldsymbol{U}}{\mathrm{d}t} + \frac{\boldsymbol{F}_{i+1/2} - \boldsymbol{F}_{1-1/2}}{\Delta x} = 0, \tag{A.15}$$

where $F_{i\pm1/2}$ indicates the flux in positive x-direction across the interface between cell i and cell $i \pm 1$ and U_i is assumed to be constant in the cell. Therefore, with this approach, the resolution of hydrodynamics equations is reduced to the computation of fluxes at cell interfaces. This is known as classic example of *Riemann problem*. in which the task is to solve a conservation law with piecewise constant values, separated by a discontinuity. If the time step $\Delta t = t^{n+1} - t^n$ is small enough, the flux through the interface is constant in time, therefore the time integration of Equation A.15 can be discretised as

$$\frac{\boldsymbol{U}_i^{n+1} - \boldsymbol{U}_i^n}{\Delta t} + \frac{\mathcal{RP}[U_i^n, U_{i+1}^n] - \mathcal{RP}[U_{i-1}^n, U_i^n]}{\Delta x} = 0 \tag{A.16}$$

where $\mathcal{RP}[U_i^n, U_{i+1}^n]$ is the resulting flux from the Riemann problem. Exact Riemann solvers are extremely costly, therefore approximated numerical solutions of the Riemann problem are usually adopted. In RAMSES, several numerical Riemann solvers are implemented, such as HLL (Harten-Lax-von Leer), HLLC (HLL Contact)[2], LLF (Lax-Friederich Solver). For a full description of the Godunov scheme and numerical solutions to the Riemann problem we refer to (Toro, 2009). This basic implementation of the Godunov scheme is stable but has the main drawback to be very diffusive and not very good in resolving shocks. Van Leer (1979) introduced

[2]For the results presented in this thesis we used the HLLC solver

then the MUSCL (Monotonic Upstream-centered Scheme for Conservation Laws) scheme, which is less diffusive and guarantees second order spatial accuracy. The main difference with the basic Godunov scheme resides in the linear interpolation of the cell interface states from the cell-averaged quantities. In order to assure stability against unphysical oscillations, this higher-order scheme need to be coupled with slope limiters. Effectively then RAMSES employs a second-order Godunov scheme, adopting the MUSCL scheme.

As for gravity, the Poisson solver implemented in RAMSES combines an iterative relaxation method (Gauss-Seidel) and multi-resolution approach, according to the multigrid technique (Guillet & Teyssier, 2011; Teyssier, 2002). The residual $r_l = \nabla_l^2 \phi_l - \rho_l$ and the associated error are estimated at the fine grid level l and then used as a guess to solve the coarse grid system. The error on the coarse gird system is then used to correct the solution on the fine grid. In the results presented here, considering only a collapsing cloud of gas, the total density term in the Poisson equation is automatically derived from the gas density[3]. Once the Poisson equation is solved, the gravitational accelerations are computed as the five point finite-difference approximation of the gradient (Teyssier, 2002).

The formation of stars is modelled with sink particles, according to the implementation of Bleuler & Teyssier (2014). Once the density is higher than a specified threshold value, the Jeans length refinement criterion is violated and the high density peak is substituted with a sink particle. Density peaks are identified with the clump finder PHEW (Bleuler et al., 2015) and then a sphere of 4 cells in radius is centred on the peak. To create a sink, the sphere must be subvirial, hence contracting. The initial mass of the sink is set to the minimal Jeans mass, which is the Jeans mass computed at the highest refinement level. Sinks particles are allowed to merge and accrete gas, according to different accretion schemes (threshold, Bondi, flux, no-L). From a dynamical point of view, sink-sink and sink-gas forces can be computed using direct summation or the same technique used for other particles (particle-mesh method).

Recently, radiation hydrodynamics has been integrated in RAMSES (Rosdahl et al., 2013). This was implemented by closing the radiative transfer equations using the M1-approximation of the Eddington tensor and then solving the resulting differential equations using the first-order Go-

[3]In galaxy simulations including stellar particles and dark matter, the discrete particle distribution is transformed into a continuous function, by projecting the particle density onto the grid using a cloud-in-cell (CIC) or triangular shaped cloud (TSC) scheme (Hockney & Eastwood, 1981).

dunov scheme. This moment-based approach has the advantage, over ray-tracing techniques, of being independent from the number of radiative sources. With these module, it is possible to follow non-equilibrium thermochemistry of hydrogen and helium in the gas.

Combining all of these techniques presented above, RAMSES has become a highly sophisticated and powerful tool in the field of numerical astrophysics, not only for cosmological purposes, as originally designed, but also for small scale star cluster formation.

Bibliography

Aarseth S. J., 1985, in Multiple time scales, p. 377 - 418, Brackbill J. U., Cohen B. I., eds., pp. 377–418

Aarseth S. J., 2003, Gravitational N-Body Simulations. p. 430

Adamo A., Bastian N., 2015, ArXiv e-prints

Adamo A., Östlin G., Zackrisson E., 2011, MNRAS, 417, 1904

Agertz O., Kravtsov A. V., Leitner S. N., Gnedin N. Y., 2013, ApJ, 770, 25

Agertz O. et al., 2007, MNRAS, 380, 963

Aharon D., Perets H. B., 2015, ApJ, 799, 185

Alladin S. M., 1965, ApJ, 141, 768

Allison R. J., Goodwin S. P., Parker R. J., de Grijs R., Portegies Zwart S. F., Kouwenhoven M. B. N., 2009, ApJ, 700, L99

Allison R. J., Goodwin S. P., Parker R. J., Portegies Zwart S. F., de Grijs R., Kouwenhoven M. B. N., 2009, MNRAS, 395, 1449

Alves J., Lombardi M., Lada C. J., 2007, A&A, 462, L17

Amaro-Seoane P., Konstantinidis S., Brem P., Catelan M., 2013, MNRAS, 435, 809

Ambartsumian V., 1947, Armenian Acad. of Sci

An D. et al., 2009, ApJ, 700, 523

Andersen D. R., Walcher C. J., Böker T., Ho L. C., van der Marel R. P., Rix H.-W., Shields J. C., 2008, ApJ, 688, 990

Anderson A. J., 1997, PhD thesis, UNIVERSITY OF CALIFORNIA, BERKELEY

Anderson J., King I. R., 2003, AJ, 126, 772

Anderson J., Piotto G., King I. R., Bedin L. R., Guhathakurta P., 2009, ApJ, 697, L58

André P. et al., 2010, A&A, 518, L102

Antonini F., 2013a, ApJ, 763, 62

Antonini F., 2013b, ApJ, 763, 62

Antonini F., Barausse E., Silk J., 2015, ApJ, 812, 72

Arce H. G., Borkin M. A., Goodman A. A., Pineda J. E., Halle M. W., 2010, ApJ, 715, 1170

Arthur S. J., 2012, MNRAS, 421, 1283

Ashman K. M., Zepf S. E., 1992, ApJ, 384, 50

Ashman K. M., Zepf S. E., 1998, Globular Cluster Systems

Bally J., 2016, ARA&A, 54, 491

Bally J., Ginsburg A., Probst R., Reipurth B., Shirley Y. L., Stringfellow G. S., 2014, AJ, 148, 120

Banerjee S., Kroupa P., Oh S., 2012, ApJ, 746, 15

Bastian N., 2008, MNRAS, 390, 759

Bastian N., 2016, in EAS Publications Series, Vol. 80, EAS Publications Series, Moraux E., Lebreton Y., Charbonnel C., eds., pp. 5–37

Bastian N. et al., 2012, MNRAS, 419, 2606

Bastian N., Covey K. R., Meyer M. R., 2010, ARA&A, 48, 339

Bastian N., Ercolano B., Gieles M., Rosolowsky E., Scheepmaker R. A., Gutermuth R., Efremov Y., 2007, MNRAS, 379, 1302

Bastian N., Goodwin S. P., 2006, MNRAS, 369, L9

Bastian N., Lamers H. J. G. L. M., de Mink S. E., Longmore S. N., Goodwin S. P., Gieles M., 2013, MNRAS, 436, 2398

Bate M. R., 2009, MNRAS, 392, 590

Battinelli P., Capuzzo-Dolcetta R., 1991, MNRAS, 249, 76

Baumgardt H., 2001, MNRAS, 325, 1323

Baumgardt H., Côté P., Hilker M., Rejkuba M., Mieske S., Djorgovski S. G., Stetson P., 2009, MNRAS, 396, 2051

Baumgardt H., Kroupa P., 2007, MNRAS, 380, 1589

Baumgardt H., Makino J., Ebisuzaki T., 2004, ApJ, 613, 1143

Baumgardt H., Parmentier G., Anders P., Grebel E. K., 2013, MNRAS, 430, 676

Beasley M. A., Baugh C. M., Forbes D. A., Sharples R. M., Frenk C. S., 2002, MNRAS, 333, 383

Beccari G., De Marchi G., Panagia N., Valenti E., Carraro G., Romaniello M., Zoccali M., Weidner C., 2015, A&A, 574, A44

Beccari G. et al., 2010, ApJ, 720, 1108

Bedin L. R., Piotto G., Anderson J., Cassisi S., King I. R., Momany Y., Carraro G., 2004, ApJ, 605, L125

Bekki K., Yong D., 2012, MNRAS, 419, 2063

Bellazzini M., Bragaglia A., Carretta E., Gratton R. G., Lucatello S., Catanzaro G., Leone F., 2012, A&A, 538, A18

Bellazzini M. et al., 2008, AJ, 136, 1147

Bellini A., Bedin L. R., Piotto G., Milone A. P., Marino A. F., Villanova S., 2010, AJ, 140, 631

Bellini A., Piotto G., Bedin L. R., King I. R., Anderson J., Milone A. P., Momany Y., 2009, A&A, 507, 1393

Bergin E. A., Tafalla M., 2007, ARA&A, 45, 339

Bertelli Motta C., Clark P. C., Glover S. C. O., Klessen R. S., Pasquali A., 2016, MNRAS, 462, 4171

Bertin G., 2014, Dynamics of Galaxies

Bertin G., Varri A. L., 2008, ApJ, 689, 1005

Bianchini P., Renaud F., Gieles M., Varri A. L., 2015, MNRAS, 447, L40

Bianchini P., Varri A. L., Bertin G., Zocchi A., 2013, ApJ, 772, 67

Binney J., 1978, MNRAS, 183, 501

Binney J., Merrifield M., 1998, Galactic Astronomy

Binney J., Tremaine S., 2008, Galactic Dynamics: Second Edition. Princeton University Press

Bjerkeli P., van der Wiel M. H. D., Harsono D., Ramsey J. P., Jørgensen J. K., 2016, Nature, 540, 406

Blaauw A., 1958, Ricerche Astronomiche, 5, 105

Blaauw A., 1961, Bull. Astron. Inst. Netherlands, 15, 265

Bleuler A., Teyssier R., 2014, MNRAS, 445, 4015

Bleuler A., Teyssier R., Carassou S., Martizzi D., 2015, Computational Astrophysics and Cosmology, 2, 5

Böker T., 2010, in IAU Symposium, Vol. 266, Star Clusters: Basic Galactic Building Blocks Throughout Time and Space, de Grijs R., Lépine J. R. D., eds., pp. 58–63

Böker T., Laine S., van der Marel R. P., Sarzi M., Rix H.-W., Ho L. C., Shields J. C., 2002, AJ, 123, 1389

Böker T., Sarzi M., McLaughlin D. E., van der Marel R. P., Rix H.-W., Ho L. C., Shields J. C., 2004, AJ, 127, 105

Boldyrev S., 2002, ApJ, 569, 841

Boldyrev S., Nordlund Å., Padoan P., 2002, ApJ, 573, 678

Boley A. C., Lake G., Read J., Teyssier R., 2009, ApJ, 706, L192

Bonatto C., Santos, Jr. J. F. C., Bica E., 2006, A&A, 445, 567

Bonnell I. A., Davies M. B., 1998, MNRAS, 295, 691

Bradford J. D. et al., 2011, ApJ, 743, 167

Bragaglia A., 2010, in SF2A-2010: Proceedings of the Annual meeting of the French Society of Astronomy and Astrophysics, Boissier S., Heydari-Malayeri M., Samadi R., Valls-Gabaud D., eds., p. 335

Brandner W., 2008, in Astronomical Society of the Pacific Conference Series, Vol. 387, Massive Star Formation: Observations Confront Theory, Beuther H., Linz H., Henning T., eds., p. 369

Bressert E. et al., 2010, MNRAS, 409, L54

Briley M. M., Smith V. V., Suntzeff N. B., Lambert D. L., Bell R. A., Hesser J. E., 1996, Nature, 383, 604

Brodie J. P. et al., 2014, ApJ, 796, 52

Brodie J. P., Strader J., 2006, ARA&A, 44, 193

Brodie J. P., Usher C., Conroy C., Strader J., Arnold J. A., Forbes D. A., Romanowsky A. J., 2012, ApJ, 759, L33

Brown W. R., Geller M. J., Kenyon S. J., Kurtz M. J., 2005, ApJ, 622, L33

Brown W. R., Geller M. J., Kenyon S. J., Kurtz M. J., Bromley B. C., 2007, ApJ, 671, 1708

Cabrera-Ziri I., Bastian N., Davies B., Magris G., Bruzual G., Schweizer F., 2014, MNRAS, 441, 2754

Cabrera-Ziri I. et al., 2016, MNRAS, 459, 4218

Canon R.-D., Stobie R.-S., 1973, MNRAS, 162, 207

Capuzzo-Dolcetta R., Miocchi P., 2008, ApJ, 681, 1136

Carollo C. M., Stiavelli M., de Zeeuw P. T., Mack J., 1997, AJ, 114, 2366

Carraro G., Lia C., 2000, A&A, 357, 977

Carretta E., 2012, in American Astronomical Society Meeting Abstracts, Vol. 220, American Astronomical Society Meeting Abstracts #220, p. 115.04

Carretta E., 2015, ArXiv e-prints

Carretta E., Bragaglia A., Gratton R., Lucatello S., 2009a, A&A, 505, 139

Carretta E. et al., 2010a, A&A, 520, A95

Carretta E. et al., 2009b, A&A, 505, 117

Carretta E. et al., 2007, A&A, 464, 967

Carretta E., Bragaglia A., Gratton R. G., Recio-Blanco A., Lucatello S., D'Orazi V., Cassisi S., 2010b, A&A, 516, A55

Carretta E. et al., 2010c, ApJ, 722, L1

Carretta E., Lucatello S., Gratton R. G., Bragaglia A., D'Orazi V., 2011, A&A, 533, A69

Carson D. J., Barth A. J., Seth A. C., den Brok M., Cappellari M., Greene J. E., Ho L. C., Neumayer N., 2015, AJ, 149, 170

Cartwright A., Whitworth A. P., 2004, MNRAS, 348, 589

Castor J., McCray R., Weaver R., 1975, ApJ, 200, L107

Chaboyer B., 2008, in IAU Symposium, Vol. 248, A Giant Step: from Milli- to Micro-arcsecond Astrometry, Jin W. J., Platais I., Perryman M. A. C., eds., pp. 440–442

Chaboyer B., Demarque P., Sarajedini A., 1996, ApJ, 459, 558

Chabrier G., Hennebelle P., 2011, A&A, 534, A106

Chandrasekhar S., 1969, Ellipsoidal figures of equilibrium

Chandrasekhar S., Lebovitz N. R., 1962, ApJ, 136, 1037

Chapman N. L., Goldsmith P. F., Pineda J. L., Clemens D. P., Li D., Krčo M., 2011, ApJ, 741, 21

Chen C. W., Chen W. P., 2010, ApJ, 721, 1790

Chen L., de Grijs R., Zhao J. L., 2007, AJ, 134, 1368

Chernoff D. F., Weinberg M. D., 1990, ApJ, 351, 121

Clark P. C., Klessen R. S., Bonnell I. A., 2007, MNRAS, 379, 57

Clarke C., Mathieu R., Reid I., Bell C., Eyer L., Meyer M., 2015, Dynamics of Young Star Clusters and Associations: Saas-Fee Advanced Course 42. Swiss Society for Astrophysics and Astronomy, Saas-Fee Advanced Course. Springer Berlin Heidelberg

Cohen J. G., 1978, ApJ, 223, 487

Collaboration P. et al., 2016, A&A, 594, A13

Colombo D. et al., 2014, ApJ, 784, 3

Côté P., Marzke R. O., West M. J., 1998, ApJ, 501, 554

Côté P. et al., 2006, ApJS, 165, 57

Courant R., Friedrichs K., Lewy H., 1967, IBM journal, 11, 215

Crowther P. A., Schnurr O., Hirschi R., Yusof N., Parker R. J., Goodwin S. P., Kassim H. A., 2010, MNRAS, 408, 731

Crutcher R. M., 2012, ARA&A, 50, 29

Crutcher R. M., Wandelt B., Heiles C., Falgarone E., Troland T. H., 2010, ApJ, 725, 466

Curtis E. I., Richer J. S., Swift J. J., Williams J. P., 2010, MNRAS, 408, 1516

Da Costa G. S., Held E. V., Saviane I., 2014, MNRAS, 438, 3507

Da Rio N., Tan J. C., Jaehnig K., 2014, ApJ, 795, 55

Dale J. E., 2015, New A Rev., 68, 1

Dale J. E., Bonnell I., 2011, MNRAS, 414, 321

Dale J. E., Bonnell I. A., 2012, MNRAS, 422, 1352

Dale J. E., Ercolano B., Bonnell I. A., 2012a, MNRAS, 427, 2852

Dale J. E., Ercolano B., Bonnell I. A., 2012b, MNRAS, 424, 377

Dale J. E., Ercolano B., Bonnell I. A., 2013a, MNRAS, 431, 1062

Dale J. E., Ercolano B., Bonnell I. A., 2013b, MNRAS, 430, 234

Dale J. E., Ercolano B., Bonnell I. A., 2015, MNRAS, 451, 987

Dale J. E., Ercolano B., Clarke C. J., 2007, MNRAS, 382, 1759

Dale J. E., Ngoumou J., Ercolano B., Bonnell I. A., 2014, MNRAS, 442, 694

Davies M., 2005, The Astrophysics of Crowded Places, Thompson J. M. T., ed., pp. 245–262

De Angeli F., Piotto G., Cassisi S., Busso G., Recio-Blanco A., Salaris M., Aparicio A., Rosenberg A., 2005, AJ, 130, 116

de Grijs R., Gilmore G. F., Mackey A. D., Wilkinson M. I., Beaulieu S. F., Johnson R. A., Santiago B. X., 2002, MNRAS, 337, 597

De Marchi G., Beccari G., Panagia N., 2013, ApJ, 775, 68

De Marchi G., Panagia N., Guarcello M. G., Bonito R., 2013, MNRAS, 435, 3058

De Marchi G., Paresce F., Portegies Zwart S., 2010, ApJ, 718, 105

de Zeeuw P. T., Hoogerwerf R., de Bruijne J. H. J., Brown A. G. A., Blaauw A., 1999, AJ, 117, 354

Decressin T., Meynet G., Charbonnel C., Prantzos N., Ekström S., 2007, A&A, 464, 1029

den Brok M. et al., 2014, MNRAS, 445, 2385

D'Ercole A., Vesperini E., D'Antona F., McMillan S. L. W., Recchi S., 2008, MNRAS, 391, 825

Dias W. S., Alessi B. S., Moitinho A., Lepine J. R. D., 2002, VizieR Online Data Catalog, 7229

Dias W. S., Alessi B. S., Moitinho A., Lepine J. R. D., 2012, VizieR Online Data Catalog, 1

Dib S., Kim J., Vázquez-Semadeni E., Burkert A., Shadmehri M., 2007, ApJ, 661, 262

Djorgovski S., King I. R., 1986, ApJ, 305, L61

Dobbs C. L., Burkert A., Pringle J. E., 2011, MNRAS, 413, 2935

D'Orazi V., Gratton R. G., Pancino E., Bragaglia A., Carretta E., Lucatello S., Sneden C., 2011, A&A, 534, A29

Dreyer J. L. E., 1888, MmRAS, 49, 1

Dreyer J. L. E., 1895, MmRAS, 51, 185

Dreyer J. L. E., 1910, MmRAS, 59, 105

Drissen L., Moffat A. F. J., Walborn N. R., Shara M. M., 1995, AJ, 110, 2235

Dunham M. M., Arce H. G., Mardones D., Lee J.-E., Matthews B. C., Stutz A. M., Williams J. P., 2014, ApJ, 783, 29

Eggleton P. P., Fitchett M. J., Tout C. A., 1989, ApJ, 347, 998

Eggleton P. P., Fitchett M. J., Tout C. A., 1990, ApJ, 354, 387

Eldridge J. J., Langer N., Tout C. A., 2011, MNRAS, 414, 3501

Elmegreen B. G., 2006, ArXiv Astrophysics e-prints

Elmegreen B. G., 2007, ApJ, 668, 1064

Elmegreen B. G., 2010, ApJ, 712, L184

Elson R. A. W., Fall S. M., Freeman K. C., 1987, ApJ, 323, 54

Emsellem E. et al., 2007, MNRAS, 379, 401

Emsellem E., van de Ven G., 2008, ApJ, 674, 653

Espinoza P., Selman F. J., Melnick J., 2009, A&A, 501, 563

Fabricius M. H. et al., 2014, ApJ, 787, L26

Falgarone E., Puget J.-L., Perault M., 1992, A&A, 257, 715

Fall S. M., Chandar R., Whitmore B. C., 2009, ApJ, 704, 453

Fall S. M., Frenk C. S., 1985, in IAU Symposium, Vol. 113, Dynamics of Star Clusters, Goodman J., Hut P., eds., pp. 285–296

Federrath C., 2013, MNRAS, 436, 1245

Feigelson E. D. et al., 2013, ApJS, 209, 26

Ferraro F. R. et al., 2009, Nature, 462, 483

Fierlinger K. M., Burkert A., Ntormousi E., Fierlinger P., Schartmann M., Ballone A., Krause M. G. H., Diehl R., 2016, MNRAS, 456, 710

Figer D. F., 2004, in Astronomical Society of the Pacific Conference Series, Vol. 322, The Formation and Evolution of Massive Young Star Clusters, Lamers H. J. G. L. M., Smith L. J., Nota A., eds., p. 49

Figer D. F. et al., 2002, ApJ, 581, 258

Fodera-Serio G., Indorato L., Nastasi P., 1985, Journal for the History of Astronomy, 16, 1

Forbes D. A., Brodie J. P., Grillmair C. J., 1997, AJ, 113, 1652

Forbes D. A., Pastorello N., Romanowsky A. J., Usher C., Brodie J. P., Strader J., 2015, MNRAS, 452, 1045

Fouesneau M. et al., 2014, ApJ, 786, 117

Freeman K.-C., Rodgers A.-W., 1975, ApJ, 201, L71

Fregeau J. M., 2008, in IAU Symposium, Vol. 246, Dynamical Evolution of Dense Stellar Systems, Vesperini E., Giersz M., Sills A., eds., pp. 239–245

Friel E. D., 1995, ARA&A, 33, 381

Frinchaboy P. M. et al., 2013, ApJ, 777, L1

Fuente A. et al., 2010, A&A, 521, L23

Fujii M., Portegies Zwart S., 2015, IAU General Assembly, 22, 2254970

Fujii M. S., 2015, PASJ, 67, 59

Fujii M. S., Portegies Zwart S., 2016, ApJ, 817, 4

Fujii M. S., Saitoh T. R., Portegies Zwart S. F., 2012, ApJ, 753, 85

Gaburov E., Harfst S., Portegies Zwart S., 2009, New A, 14, 630

Galilei G., 1610, Sidereus nuncius magna, longeque admirabilia spectacula pandens lunae facie, fixis innumeris, lacteo circulo, stellis nebulosis, ... Galileo Galileo : nuper a se reperti beneficio sunt observata in apprime vero in quatuor planetis circa Iovis stellam disparibus intervallis, atque periodis, celeritate mirabili circumvolutis ... atque Medicea sidera nuncupandos decrevit. Venetiis: apud Thomam Baglionum

Gatto A. et al., 2015, MNRAS, 449, 1057

Gavagnin E., Bleuler A., Rosdahl J., Teyssier R., 2017, MNRAS, 472, 4155

Gavagnin E., Mapelli M., Lake G., 2016, MNRAS, 461, 1276

Geen S., Hennebelle P., Tremblin P., Rosdahl J., 2015, MNRAS, 454, 4484

Geen S., Hennebelle P., Tremblin P., Rosdahl J., 2016, MNRAS, 463, 3129

Gennaro M., Brandner W., Stolte A., Henning T., 2011, MNRAS, 412, 2469

Genzel R., Eisenhauer F., Gillessen S., 2010, Reviews of Modern Physics, 82, 3121

Georgiev I. Y., Böker T., 2014, MNRAS, 441, 3570

Geyer E. H., 1967, ZAp, 66, 16

Gieles M., 2013, in Astronomical Society of the Pacific Conference Series, Vol. 470, 370 Years of Astronomy in Utrecht, Pugliese G., de Koter A., Wijburg M., eds., p. 339

Gieles M., Larsen S. S., Scheepmaker R. A., Bastian N., Haas M. R., Lamers H. J. G. L. M., 2006a, A&A, 446, L9

Gieles M., Portegies Zwart S. F., 2011, MNRAS, 410, L6

Gieles M., Portegies Zwart S. F., Baumgardt H., Athanassoula E., Lamers H. J. G. L. M., Sipior M., Leenaarts J., 2006b, MNRAS, 371, 793

Giersz M., Heggie D. C., 1994, MNRAS, 268, 257

Giersz M., Heggie D. C., 1996, MNRAS, 279, 1037

Gilmore G. et al., 2012, The Messenger, 147, 25

Godunov S. K., 1959, Matematicheskii Sbornik, 89, 271

Goldsmith P. F., Langer W. D., 1978, ApJ, 222, 881

Goodwin S. P., 2009, Ap&SS, 324, 259

Goodwin S. P., 2010, Philosophical Transactions of the Royal Society of London A: Mathematical, Physical and Engineering Sciences, 368, 851

Goodwin S. P., Kroupa P., Goodman A., Burkert A., 2007, Protostars and Planets V, 133

Gouliermis D., Keller S. C., Kontizas M., Kontizas E., Bellas-Velidis I., 2004, A&A, 416, 137

Gozha M. L., Koval' V. V., Marsakov V. A., 2012, Astronomy Letters, 38, 519

Graham A. W., Spitler L. R., 2009, MNRAS, 397, 2148

Gratton R., Lucatello S., Carretta E., Bragaglia A., 2015, Highlights of Astronomy, 16, 230

Gratton R., Sneden C., Carretta E., 2004, ARA&A, 42, 385

Gratton R. G. et al., 2001, A&A, 369, 87

Gratton R. G., Bragaglia A., Carretta E., Clementini G., Desidera S., Grundahl F., Lucatello S., 2003, A&A, 408, 529

Gratton R. G., Carretta E., Bragaglia A., 2012, A&A Rev., 20, 50

Gratton R. G., Johnson C. I., Lucatello S., D'Orazi V., Pilachowski C., 2011, A&A, 534, A72

Gratton R. G. et al., 2013, A&A, 549, A41

Grebel E. K., 2016, in IAU Symposium, Vol. 312, Star Clusters and Black Holes in Galaxies across Cosmic Time, Meiron Y., Li S., Liu F.-K., Spurzem R., eds., pp. 157–170

Guhathakurta P., Yanny B., Schneider D. P., Bahcall J. N., 1996, AJ, 111, 267

Guillard N., Emsellem E., Renaud F., 2016, MNRAS, 461, 3620

Guillet T., Teyssier R., 2011, Journal of Computational Physics, 230, 4756

Gürkan M. A., Freitag M., Rasio F. A., 2004, ApJ, 604, 632

Guszejnov D., Hopkins P. F., 2015, MNRAS, 450, 4137

Gutermuth R. A., Megeath S. T., Myers P. C., Allen L. E., Pipher J. L., Fazio G. G., 2009, ApJS, 184, 18

Hampton E. J., Rowell G., Hofmann W., Horns D., Uchiyama Y., Wagner S., 2016, Journal of High Energy Astrophysics, 11, 1

Hansen B. M. S. et al., 2013, Nature, 500, 51

Harayama Y., Eisenhauer F., Martins F., 2008, ApJ, 675, 1319

Harris W. E., 1974, ApJ, 192, L161

Harris W. E., 1996, AJ, 112, 1487

Harris W. E., 2001, in Saas-Fee Advanced Course 28: Star Clusters, Labhardt L., Binggeli B., eds., p. 223

Harris W. E., 2010, ArXiv e-prints

Harris W. E., van den Bergh S., 1981, AJ, 86, 1627

Hartmann M., Debattista V. P., Seth A., Cappellari M., Quinn T. R., 2011, MNRAS, 418, 2697

Heggie D. C., 1975, MNRAS, 173, 729

Hennebelle P., Chabrier G., 2008, ApJ, 684, 395

Hennebelle P., Falgarone E., 2012, A&A Rev., 20, 55

Hennebelle P., Iffrig O., 2014, A&A, 570, A81

Hénon M., 1961, Annales d'Astrophysique, 24, 369

Herschel W., 1785, Philosophical Transactions of the Royal Society of London Series I, 75, 213

Herschel W., 1786, Philosophical Transactions of the Royal Society of London Series I, 76, 457

Herschel W., 1789, Philosophical Transactions of the Royal Society of London Series I, 79, 212

Herschel W., 1802, Philosophical Transactions of the Royal Society of London Series I, 92, 477

Hertzsprung E., 1911, Publikationen des Astrophysikalischen Observatoriums zu Potsdam, 22, A1

Hesser J. E., Bell R. A., 1980, ApJ, 238, L149

Hesser J. E., Hartwick F. D. A., McClure R. D., 1977, ApJS, 33, 471

Heyer M., Dame T. M., 2015, ARA&A, 53, 583

Heyer M., Krawczyk C., Duval J., Jackson J. M., 2009, ApJ, 699, 1092

Heyer M. H., Carpenter J. M., Snell R. L., 2001, ApJ, 551, 852

Hillenbrand L. A., Hartmann L. W., 1998, ApJ, 492, 540

Hills J. G., 1980, ApJ, 235, 986

Hockney R. W., Eastwood J. W., 1981, Computer Simulation Using Particles

Hodierna G. B., 1654, De systemate orbis cometici deque admirandis coeli characteribus explicantur, necnon vie Com etarum, per orbem cometicum multiplices opuscula duo, in quorum primo cometarum causae disquiruntur, & indicantur. In secundo vero quid, quales, quotue sint stellae luminosae, nebulae, necnon, & occultae, manifestantur & rerum caelestium studiosis commendantur

Homer, 1919, The Odyssey with an English Translation by A.T. Murray, PH.D. in two volumes. Cambridge, MA., Harvard University Press; London, William Heinemann, Ltd.

Hopkins P. F., 2012, MNRAS, 423, 2016

Hopkins P. F., Quataert E., Murray N., 2011, MNRAS, 417, 950

Hoskin M., 1979, Journal for the History of Astronomy, 10, 165

Howard C. S., Pudritz R. E., Harris W. E., 2016, MNRAS, 461, 2953

Hui L., Gnedin N. Y., 1997, MNRAS, 292, 27

Hurley J. R., Pols O. R., Tout C. A., 2000, MNRAS, 315, 543

Hut P., Makino J., McMillan S., 1995, ApJ, 443, L93

Iffrig O., Hennebelle P., 2015, A&A, 576, A95

Janes K., 2000, Star Clusters, Murdin P., ed.

Jeans J. H., 1902, Philosophical Transactions of the Royal Society of London Series A, 199, 1

Jeffries R. D. et al., 2014, A&A, 563, A94

Ji J., Bregman J. N., 2015, ArXiv e-prints

Jimenez R., 1999, in Dark matter in Astrophysics and Particle Physics, Klapdor-Kleingrothaus H. V., Baudis L., eds., p. 170

Johnson C. I., Rich R. M., Pilachowski C. A., Caldwell N., Mateo M., Bailey, III J. I., Crane J. D., 2015, AJ, 150, 63

Kamann S. et al., 2016, A&A, 588, A149

Kayser A., Hilker M., Grebel E. K., Willemsen P. G., 2008, A&A, 486, 437

Kazantzidis S., Bullock J. S., Zentner A. R., Kravtsov A. V., Moustakas L. A., 2008, ApJ, 688, 254

Kimmig B., Seth A., Ivans I. I., Strader J., Caldwell N., Anderton T., Gregersen D., 2015, AJ, 149, 53

King I., 1962, AJ, 67, 471

King I. R., 1966, AJ, 71, 64

Klaassen P. D., Wilson C. D., 2007, ApJ, 663, 1092

Klessen R. S., 2011, in EAS Publications Series, Vol. 51, EAS Publications Series, Charbonnel C., Montmerle T., eds., pp. 133–167

Klessen R. S., 2011, in EAS Publications Series, Vol. 51, EAS Publications Series, Charbonnel C., Montmerle T., eds., pp. 133–167

Klessen R. S., Glover S. C. O., 2016, Star Formation in Galaxy Evolution: Connecting Numerical Models to Reality, Saas-Fee Advanced Course, Volume 43. ISBN 978-3-662-47889-9. Springer-Verlag Berlin Heidelberg, 2016, p. 85, 43, 85

Kolmogorov A., 1941, Akademiia Nauk SSSR Doklady, 30, 301

Konstantopoulos I. S. et al., 2013, AJ, 145, 137

Kraft R. P., Sneden C., Langer G. E., Prosser C. F., 1992, AJ, 104, 645

Kraus A. L., Hillenbrand L. A., 2007, The Astrophysical Journal, 662, 413

Krause M. G. H., Charbonnel C., Bastian N., Diehl R., 2016, A&A, 587, A53

Krauss L. M., Chaboyer B., 2003, Science, 299, 65

Kritsuk A. G., Lee C. T., Norman M. L., 2013, MNRAS, 436, 3247

Kruijssen J. M. D., 2014, Classical and Quantum Gravity, 31, 244006

Kruijssen J. M. D., 2015, MNRAS, 454, 1658

Krumholz M. R., 2014, Phys. Rep., 539, 49

Krumholz M. R., 2014, Phys. Rep., 539, 49

Krumholz M. R. et al., 2014, Protostars and Planets VI, 243

Krumholz M. R., Matzner C. D., 2009, ApJ, 703, 1352

Krumholz M. R., Thompson T. A., 2013, MNRAS, 434, 2329

Kruskal J. B., 1956, in Proceedings of the American Mathematical Society, 7

Kudryavtseva N. et al., 2012, ApJ, 750, L44

Kuhn M. A., Feigelson E. D., Getman K. V., Sills A., Bate M. R., Borissova J., 2015, ApJ, 812, 131

Kuiper R., Klahr H., Beuther H., Henning T., 2010, ApJ, 722, 1556

Lada C. J., 2010, Philosophical Transactions of the Royal Society of London Series A, 368, 713

Lada C. J., Lada E. A., 2003, ARA&A, 41, 57

Lada C. J., Margulis M., Dearborn D., 1984, ApJ, 285, 141

Lafrenière D., Jayawardhana R., Brandeker A., Ahmic M., van Kerkwijk M. H., 2008, The Astrophysical Journal, 683, 844

Lardo C. et al., 2015, A&A, 573, A115

Lardo C. et al., 2013, MNRAS, 433, 1941

Larsen S. S., 2002, AJ, 124, 1393

Larsen S. S., 2004, A&A, 416, 537

Larsen S. S., Brodie J. P., Strader J., 2012, A&A, 546, A53

Larsen S. S., Strader J., Brodie J. P., 2012, A&A, 544, L14

Larson R. B., 1968, PhD thesis, California Institute of Technology

Larson R. B., 1981, MNRAS, 194, 809

Law D. R., Majewski S. R., 2010, ApJ, 718, 1128

Lee J.-W., 2015, ApJS, 219, 7

Lee Y.-N., Hennebelle P., 2016, A&A, 591, A31

Lee Y.-W., Demarque P., Zinn R., 1994, ApJ, 423, 248

Lee Y.-W., Joo J.-M., Sohn Y.-J., Rey S.-C., Lee H.-C., Walker A. R., 1999, Nature, 402, 55

Lejeune T., Schaerer D., 2001, A&A, 366, 538

Li Z.-Y., Nakamura F., 2006, ApJ, 640, L187

Lightman A. P., Shapiro S. L., 1978, Reviews of Modern Physics, 50, 437

Lombardi M., Alves J., Lada C. J., 2010, A&A, 519, L7

Lopez L. A., Krumholz M. R., Bolatto A. D., Prochaska J. X., Ramirez-Ruiz E., 2011, ApJ, 731, 91

Lopez L. A., Krumholz M. R., Bolatto A. D., Prochaska J. X., Ramirez-Ruiz E., Castro D., 2014, ApJ, 795, 121

Lugger P. M., Cohn H., Grindlay J. E., Bailyn C. D., Hertz P., 1987, ApJ, 320, 482

Lynden-Bell D., 1967, MNRAS, 136, 101

Lynden-Bell D., 1967, MNRAS, 136, 101

Lynden-Bell D., Wood R., 1968, MNRAS, 138, 495

Mac Low M.-M., Klessen R. S., 2004, Reviews of Modern Physics, 76, 125

Mackey A. D., Gilmore G. F., 2003a, MNRAS, 338, 120

Mackey A. D., Gilmore G. F., 2003b, MNRAS, 338, 85

Mackey A. D., Gilmore G. F., 2004, MNRAS, 355, 504

Maíz-Apellániz J., 2001, ApJ, 563, 151

Majewski S. R., Patterson R. J., Dinescu D. I., Johnson W. Y., Ostheimer J. C., Kunkel W. E., Palma C., 2000, in Liege International Astrophysical Colloquia, Vol. 35, Liege International Astrophysical Colloquia, Noels A., Magain P., Caro D., Jehin E., Parmentier G., Thoul A. A., eds., p. 619

Makino J., Akiyama K., Sugimoto D., 1991, Ap&SS, 185, 63

Makino J., Hut P., Kaplan M., Saygın H., 2006, New A, 12, 124

Mapelli M., Bressan A., 2013, MNRAS, 430, 3120

Mapelli M., Zampieri L., Ripamonti E., Bressan A., 2013, MNRAS, 429, 2298

Mapelli M., Zampieri L., Ripamonti E., Bressan A., 2013, MNRAS, 429, 2298

Marín-Franch A. et al., 2009, ApJ, 694, 1498

Marino A. F. et al., 2015, MNRAS, 450, 815

Marino A. F., Milone A. P., Piotto G., Villanova S., Bedin L. R., Bellini A., Renzini A., 2009, A&A, 505, 1099

Martins F., Hillier D. J., Paumard T., Eisenhauer F., Ott T., Genzel R., 2008, A&A, 478, 219

Mashchenko S., Sills A., 2005, ApJ, 619, 258

Massari D. et al., 2014, ApJ, 795, 22

Mastrobuono-Battisti A., Perets H. B., 2013, ApJ, 779, 85

Mastrobuono-Battisti A., Perets H. B., Loeb A., 2014, ApJ, 796, 40

Mathieu R. D., 1984, ApJ, 284, 643

Matzner C. D., 2007, ApJ, 659, 1394

Matzner C. D., Jumper P. H., 2015, ApJ, 815, 68

McLeod A. F. et al., 2016, MNRAS, 462, 3537

McMillan S. L. W., Vesperini E., Portegies Zwart S. F., 2007, ApJ, 655, L45

Melena N. W., Massey P., Morrell N. I., Zangari A. M., 2008, AJ, 135, 878

Messier C., 1781, Catalogue des Nébuleuses & des amas d'Étoiles (Catalog of Nebulae and Star Clusters). Tech. rep.

Meylan G., Mayor M., 1986, A&A, 166, 122

Michell J., 1767, Philosophical Transactions of the Royal Society of London Series I, 57, 234

Miller G. E., Scalo J. M., 1978, PASP, 90, 506

Milone A. P. et al., 2013, ApJ, 767, 120

Milone A. P., Marino A. F., Piotto G., Bedin L. R., Anderson J., Aparicio A., Cassisi S., Rich R. M., 2012a, ApJ, 745, 27

Milone A. P. et al., 2015, MNRAS, 447, 927

Milone A. P. et al., 2012b, A&A, 540, A16

Milone A. P., Piotto G., Bedin L. R., Sarajedini A., 2008, Mem. Soc. Astron. Italiana, 79, 623

Milone A. P. et al., 2010, ApJ, 709, 1183

Milone A. P. et al., 2016, MNRAS

Milone A. P., Stetson P. B., Piotto G., Bedin L. R., Anderson J., Cassisi S., Salaris M., 2009, A&A, 503, 755

Milosavljević M., 2004, ApJ, 605, L13

Minniti D., 1995, AJ, 109, 1663

Moore B., 1996, ApJ, 461, L13

Moore B., Diemand J., Madau P., Zemp M., Stadel J., 2006, MNRAS, 368, 563

Morata O., Girart J. M., Estalella R., 2005, A&A, 435, 113

Moraux E., 2016, in EAS Publications Series, Vol. 80, EAS Publications Series, Moraux E., Lebreton Y., Charbonnel C., eds., pp. 73–114

Motte F., André P., Neri R., 1996, in The Role of Dust in the Formation of Stars, Käufl H. U., Siebenmorgen R., eds., p. 47

Mucciarelli A., Lapenna E., Massari D., Pancino E., Stetson P. B., Ferraro F. R., Lanzoni B., Lardo C., 2015, ApJ, 809, 128

Muench A. A., Lada E. A., Lada C. J., 2002a, in Bulletin of the American Astronomical Society, Vol. 34, American Astronomical Society Meeting Abstracts, p. 1210

Muench A. A., Lada E. A., Lada C. J., Alves J., 2002b, ApJ, 573, 366

Muno M. P. et al., 2006a, ApJ, 636, L41

Muno M. P., Law C., Clark J. S., Dougherty S. M., de Grijs R., Portegies Zwart S., Yusef-Zadeh F., 2006b, ApJ, 650, 203

Murray N., Quataert E., Thompson T. A., 2010, ApJ, 709, 191

Nakamura F., Li Z.-Y., 2014, ApJ, 783, 115

Nakamura F. et al., 2011, ApJ, 737, 56

Narayanan G., Snell R., Bemis A., 2012, MNRAS, 425, 2641

Nataf D. M., Gould A. P., Pinsonneault M. H., Udalski A., 2013, ApJ, 766, 77

Norris J. E., 2004, ApJ, 612, L25

Norris J. E., Da Costa G. S., 1995, ApJ, 447, 680

Noyola E., Baumgardt H., 2011, ApJ, 743, 52

Oey M. S., 2012, ArXiv e-prints

Oh S., Kroupa P., 2016, A&A, 590, A107

Olczak C., Spurzem R., Henning T., 2011, in IAU Symposium, Vol. 271, Astrophysical Dynamics: From Stars to Galaxies, Brummell N. H., Brun A. S., Miesch M. S., Ponty Y., eds., pp. 389–390

Olmi L. et al., 2013, A&A, 551, A111

Oort J. H., 1958, Ricerche Astronomiche, 5, 507

Padoan P., Federrath C., Chabrier G., Evans, II N. J., Johnstone D., Jørgensen J. K., McKee C. F., Nordlund Å., 2014, Protostars and Planets VI, 77

Padoan P., Nordlund Å., 2002, ApJ, 576, 870

Padoan P., Nordlund Å., 2011, ApJ, 741, L22

Pancino E., Carrera R., Rossetti E., Gallart C., 2010, A&A, 511, A56

Pancino E., Ferraro F. R., Bellazzini M., Piotto G., Zoccali M., 2000, ApJ, 534, L83

Pancino E., Galfo A., Ferraro F. R., Bellazzini M., 2007, ApJ, 661, L155

Pancino E., Mucciarelli A., Sbordone L., Bellazzini M., Pasquini L., Monaco L., Ferraro F. R., 2011, A&A, 527, A18

Pancino E., Rejkuba M., Zoccali M., Carrera R., 2010, A&A, 524, A44

Pang X., Grebel E. K., Allison R. J., Goodwin S. P., Altmann M., Harbeck D., Moffat A. F. J., Drissen L., 2013, ApJ, 764, 73

Pang X., Grebel E. K., Allison R. J., Goodwin S. P., Altmann M., Harbeck D., Moffat A. F. J., Drissen L., 2013, ApJ, 764, 73

Pang X., Shu C., 2010, in IAU Symposium, Vol. 266, Star Clusters: Basic Galactic Building Blocks Throughout Time and Space, de Grijs R., Lépine J. R. D., eds., pp. 482–482

Parker R. J., Dale J. E., 2013, MNRAS, 432, 986

Parker R. J., Dale J. E., 2015, MNRAS, 451, 3664

Parker R. J., Dale J. E., Ercolano B., 2015, MNRAS, 446, 4278

Parker R. J., Wright N. J., Goodwin S. P., Meyer M. R., 2014, MNRAS, 438, 620

Pasquato M., Chung C., 2016, ArXiv e-prints

Peebles P. J. E., 1984, ApJ, 277, 470

Pellegrini E. W., Baldwin J. A., Ferland G. J., 2011, ApJ, 738, 34

Perets H. B., Šubr L., 2012, ApJ, 751, 133

Peters T., Banerjee R., Klessen R. S., Mac Low M.-M., Galván-Madrid R., Keto E. R., 2010, ApJ, 711, 1017

Peters T. et al., 2016, ArXiv e-prints

Peterson R. C., 1980, ApJ, 237, L87

Pfalzner S., 2009, A&A, 498, L37

Piotto G. et al., 2012, ApJ, 760, 39

Piotto G. et al., 2005, ApJ, 621, 777

Piskunov A. E., Kharchenko N. V., Röser S., Schilbach E., Scholz R.-D., 2006, A&A, 445, 545

Piskunov A. E., Kharchenko N. V., Schilbach E., Röser S., Scholz R.-D., Zinnecker H., 2008, A&A, 487, 557

Porras A., Christopher M., Allen L., Di Francesco J., Megeath S. T., Myers P. C., 2003, AJ, 126, 1916

Portegies Zwart S. F., 2000, ApJ, 544, 437

Portegies Zwart S. F., McMillan S. L. W., 2002, ApJ, 576, 899

Portegies Zwart S. F., McMillan S. L. W., Gieles M., 2010, ARA&A, 48, 431

Portegies Zwart S. F., McMillan S. L. W., Hut P., Makino J., 2001, MNRAS, 321, 199

Portegies Zwart S. F., Verbunt F., 1996, A&A, 309, 179

Pryor C., Hartwick F. D. A., McClure R. D., Fletcher J. M., Kormendy J., 1986, AJ, 91, 546

Puzia T. H., Kissler-Patig M., Thomas D., Maraston C., Saglia R. P., Bender R., Goudfrooij P., Hempel M., 2005, A&A, 439, 997

Raskutti S., Ostriker E. C., Skinner M. A., 2016, ApJ, 829, 130

Read J. I., Goerdt T., Moore B., Pontzen A. P., Stadel J., Lake G., 2006, MNRAS, 373, 1451

Reddy A. B. S., Lambert D. L., Giridhar S., 2016, MNRAS, 463, 4366

Reipurth B., Guimares M. M., Connelley M. S., Bally J., 2007, The Astronomical Journal, 134, 2272

Renaud F., Agertz O., Gieles M., 2017, MNRAS, 465, 3622

Renaud F., Gieles M., Boily C. M., 2011, MNRAS, 418, 759

Renzini A., 2008, MNRAS, 391, 354

Renzini A., Fusi Pecci F., 1988, ARA&A, 26, 199

Rice T. S., Goodman A. A., Bergin E. A., Beaumont C., Dame T. M., 2016, ApJ, 822, 52

Richtler T., 2013, in Astronomical Society of the Pacific Conference Series, Vol. 470, 370 Years of Astronomy in Utrecht, Pugliese G., de Koter A., Wijburg M., eds., p. 327

Roberts P. H., 1962, ApJ, 136, 1108

Rogers H., Pittard J. M., 2013, MNRAS, 431, 1337

Röllig M. et al., 2011, A&A, 525, A8

Rosdahl J., Blaizot J., Aubert D., Stranex T., Teyssier R., 2013, MNRAS, 436, 2188

Rosdahl J., Teyssier R., 2015, MNRAS, 449, 4380

Rosen A., Bregman J. N., 1995, ApJ, 440, 634

Rosen A. L., Lopez L. A., Krumholz M. R., Ramirez-Ruiz E., 2014, MNRAS, 442, 2701

Röser S., Kharchenko N. V., Piskunov A. E., Schilbach E., Scholz R.-D., Zinnecker H., 2010, Astronomische Nachrichten, 331, 519

Rosolowsky E., 2005, PASP, 117, 1403

Ryon J. E. et al., 2015, MNRAS, 452, 525

Sabbi E. et al., 2012, ApJ, 754, L37

Salaris M., Weiss A., Percival S. M., 2004, A&A, 414, 163

Sana H., Momany Y., Gieles M., Carraro G., Beletsky Y., Ivanov V. D., de Silva G., James G., 2010, A&A, 515, A26

Sandage A., 1958, Ricerche Astronomiche, 5, 41

Sandell G., Knee L. B. G., 2001, ApJ, 546, L49

Sanner J., Brunzendorf J., Will J.-M., Geffert M., 2001, A&A, 369, 511

Santos M. R., 2003, in Extragalactic Globular Cluster Systems, Kissler-Patig M., ed., p. 348

Sarajedini A., 2009, in IAU Symposium, Vol. 258, The Ages of Stars, Mamajek E. E., Soderblom D. R., Wyse R. F. G., eds., pp. 221–232

Sarajedini A., Layden A. C., 1995, AJ, 109, 1086

Saviane I., da Costa G. S., Held E. V., Sommariva V., Gullieuszik M., Barbuy B., Ortolani S., 2012, A&A, 540, A27

Scheepmaker R. A., Haas M. R., Gieles M., Bastian N., Larsen S. S., Lamers H. J. G. L. M., 2007, A&A, 469, 925

Schilbach E., Kharchenko N. V., Piskunov A. E., Röser S., Scholz R.-D., 2006, A&A, 456, 523

Schilbach E., Röser S., 2008, A&A, 489, 105

Searle L., Zinn R., 1978, ApJ, 225, 357

Seth A., Agüeros M., Lee D., Basu-Zych A., 2008, ApJ, 678, 116

Shu F., 1991, Physics of Astrophysics, Vol. II: Gas Dynamics. University Science Books

Siess L., Dufour E., Forestini M., 2000, A&A, 358, 593

Silich S., Tenorio-Tagle G., 2013, ApJ, 765, 43

Sippel A. C., Hurley J. R., Madrid J. P., Harris W. E., 2012, MNRAS, 427, 167

Skinner M. A., Ostriker E. C., 2015, ApJ, 809, 187

Sneden C., Kraft R. P., Prosser C. F., Langer G. E., 1991, AJ, 102, 2001

Solomon P. M., Rivolo A. R., Barrett J., Yahil A., 1987, ApJ, 319, 730

Spera M., Capuzzo-Dolcetta R., 2015, ArXiv e-prints

Spera M., Mapelli M., Jeffries R. D., 2016, MNRAS, 460, 317

Spitzer L., 1978, Physical processes in the interstellar medium

Spitzer L., 1987, Dynamical evolution of globular clusters

Spitzer L., 1987, Dynamical evolution of globular clusters

Spitzer, Jr. L., 1958, ApJ, 127, 17

Spitzer, Jr. L., 1969, ApJ, 158, L139

Spitzer, Jr. L., 1975, in IAU Symposium, Vol. 69, Dynamics of the Solar Systems, Hayli A., ed., pp. 3–26

Stahler S. W., Palla F., 2005, The Formation of Stars. p. 865

Sternberg A., Hoffmann T. L., Pauldrach A. W. A., 2003, ApJ, 599, 1333

Stetson P. B., 1993, in Astronomical Society of the Pacific Conference Series, Vol. 48, The Globular Cluster-Galaxy Connection, Smith G. H., Brodie J. P., eds., p. 14

Stojimirović I., Narayanan G., Snell R. L., Bally J., 2006, ApJ, 649, 280

Stolte A., Brandner W., Brandl B., Zinnecker H., 2006, AJ, 132, 253

Stolte A., Brandner W., Brandl B., Zinnecker H., Grebel E. K., 2004, AJ, 128, 765

Stolte A., Brandner W., Grebel E. K., Lenzen R., Lagrange A.-M., 2005, ApJ, 628, L113

Stolte A., Brandner W., Grebel E. K., Lenzen R., Lagrange A.-M., 2005, ApJ, 628, L113

Stolte A., Grebel E. K., Brandner W., Figer D. F., 2002, A&A, 394, 459

Stolte A., Grebel E. K., Brandner W., Figer D. F., 2003, in Astronomical Society of the Pacific Conference Series, Vol. 287, Galactic Star Formation Across the Stellar Mass Spectrum, De Buizer J. M., van der Bliek N. S., eds., pp. 433–438

Stolte A. et al., 2015, A&A, 578, A4

Strader J., Brodie J. P., Cenarro A. J., Beasley M. A., Forbes D. A., 2005, AJ, 130, 1315

Strömgren B., 1939, ApJ, 89, 526

Sugimoto D., Makino J., 1989, PASJ, 41, 1117

Sung H., Bessell M. S., 2004, AJ, 127, 1014

Sutherland R. S., Dopita M. A., 1993, ApJS, 88, 253

Tan J. C., Krumholz M. R., McKee C. F., 2006, ApJ, 641, L121

Teyssier R., 2002, A&A, 385, 337

Toro E. F., 2009, Riemann solvers and numerical methods for fluid dynamics : a practical introduction. Springer, New York

Torres C. A. O., Quast G. R., Melo C. H. F., Sterzik M., de la Reza R., da Silva L., 2010, in IAU Symposium, Vol. 266, Star Clusters: Basic Galactic Building Blocks Throughout Time and Space, de Grijs R., Lépine J. R. D., eds., pp. 544–544

Tout C. A., Aarseth S. J., Pols O. R., Eggleton P. P., 1997, MNRAS, 291, 732

Townsley L. K. et al., 2011, ApJS, 194, 15

Townsley L. K., Broos P. S., Feigelson E. D., Brandl B. R., Chu Y.-H., Garmire G. P., Pavlov G. G., 2006, AJ, 131, 2140

Townsley L. K., Feigelson E. D., Montmerle T., Broos P. S., Chu Y.-H., Garmire G. P., 2003, ApJ, 593, 874

Trager S. C., King I. R., Djorgovski S., 1995, AJ, 109, 218

Trani A. A., Mapelli M., Bressan A., 2014, MNRAS, 445, 1967

Tremaine S. D., Ostriker J. P., Spitzer, Jr. L., 1975, ApJ, 196, 407

van den Bergh S., 1966, AJ, 71, 990

van den Bergh S., 1996, ApJ, 471, L31

van den Bergh S., 2008, AJ, 135, 1731

van den Bosch R., de Zeeuw T., Gebhardt K., Noyola E., van de Ven G., 2006, ApJ, 641, 852

Van Leer B., 1979, Journal of computational Physics, 32, 101

van Maanen A., 1945, ApJ, 102, 26

Vande Putte D., Garnier T. P., Ferreras I., Mignani R. P., Cropper M., 2010, MNRAS, 407, 2109

VandenBerg D. A., 2000, ApJS, 129, 315

Varri A. L., Bertin G., 2012, A&A, 540, A94

Verbunt F. W. M., 2007, Highlights of Astronomy, 14, 440

Verner D. A., Ferland G. J., Korista K. T., Yakovlev D. G., 1996, ApJ, 465, 487

Vesperini E., McMillan S., Portegies Zwart S., 2009, Ap&SS, 324, 277

Vesperini E., Varri A. L., McMillan S. L. W., Zepf S. E., 2014, MNRAS, 443, L79

Vesperini E., Varri A. L., McMillan S. L. W., Zepf S. E., 2014, MNRAS, 443, L79

Villanova S., Geisler D., Gratton R. G., Cassisi S., 2014, ApJ, 791, 107

Vink J. S., 2011, Ap&SS, 336, 163

Vink J. S., de Koter A., Lamers H. J. G. L. M., 2001, A&A, 369, 574

Walch S. K., Whitworth A. P., Bisbas T., Wünsch R., Hubber D., 2012, MNRAS, 427, 625

Walcher C. J. et al., 2005, ApJ, 618, 237

Wang P., Li Z.-Y., Abel T., Nakamura F., 2010, ApJ, 709, 27

Weaver R., McCray R., Castor J., Shapiro P., Moore R., 1977, ApJ, 218, 377

White R. E., Shawl S. J., 1987, ApJ, 317, 246

White S. D. M., 1978, MNRAS, 184, 185

Wielen R., 1971, Ap&SS, 13, 300

Wu Z.-Y., Zhou X., Ma J., Du C.-H., 2009, MNRAS, 399, 2146

Yong D., Grundahl F., 2008, ApJ, 672, L29

Yusef-Zadeh F., Law C., Wardle M., Wang Q. D., Fruscione A., Lang C. C., Cotera A., 2002, ApJ, 570, 665

Zinn R., 1985, ApJ, 293, 424

Zinn R., 1993, in Astronomical Society of the Pacific Conference Series, Vol. 48, The Globular Cluster-Galaxy Connection, Smith G. H., Brodie J. P., eds., p. 38

Zinnecker H., 1982, Annals of the New York Academy of Sciences, 395, 226

Zinnecker H., 2010, in IAU Symposium, Vol. 266, Star Clusters: Basic Galactic Building Blocks Throughout Time and Space, de Grijs R., Lépine J. R. D., eds., pp. 17–23

Acknowledgements

I thank my supervisor Prof. Dr. George Lake for his challenging discussions and unconventional ideas, which always pushed me to give my best and think out of the box.

I am very grateful to Dr. Michela Mapelli, for her very precious help at the start of my journey, introducing me to the world of star clusters and n-body dynamics.

A special thanks to Prof. Dr. Romain Teyssier who was always there when I needed help and taught me a lot about astrophysics and life, representing for me now an inspiring and outstanding scientist and human being, to which I will always look as a model.

The effort behind this thesis was equally shared with Dr. Michael Rieder, who always believed in me, especially when I did not anymore and kept motivating and loving me like none could have done better. I have no words to thank him, but the extent of my gratitude to him is measured by the real fact that without him I would have probably quit my PhD (multiple times).

Danke vielmal also to my inseparable officemate and friend, Dr. Andreas Bleuler, who showed me the way many times, with or without skis on, encouraging me when I was in difficulty, teaching me everything about his beloved sink particles, celebrating with me when I had a success and in general listening to a lot of cool music.

To the companion of many adventures, whether on a cliff in Elba or in Hawaii, or in a sleepless night at the Hive (when we were younger), to my official Lindy Hop leader: *Merci*! Dr. Valentin Perret has the merit of always made me feel good with his light and relaxed *joie de vivre*, of being southern-european with me in this teutonic country.

Furthermore, I would like to thank all the professors, post-docs and students (+Regina & Suzanne), which in these 4 years orbited around the Institute of Computational Science. Special mention to the group of people who really characterised my time at ICS, and whose leave made me clear it was time also for me to go: Drs. Simon Grimm, Volker Hoffmann, Irshad

Mohammed, Manuel Rabold, Davide Fiacconi, Valentina Tamburello and (soon to be doctor) Pawel Biernacki :).

An indefinite but very deep and honest thanks to all friends in Zürich, those part of the italian-connection and those belonging to the rest of the world.
To my best friends, in constant Whatsapp contact, Anna Bareato and Anna Salvioni, I owe big gratitude, for having been effectively always with me even living hundreds of kilometres away, anytime ready to bear my complaints and provide interesting solutions. Also for having become, unwillingly, a bit expert of astrophysics and informatics, when updating them about my project.

Tacit but fundamental thanks goes to my family, my mother Rita, my father Gianni and my brother Enrico, who constitute the reason of my strength and the core of my identity. Anything I achieved is only merit of the unshakeable, unconditional trust they have in me and the unique, paradisiac, funny, energising spirit I get when we are together: GRAZIE!